Universität Hamburg
DER FORSCHUNG | DER LEHRE | DER BILDUNG

mpsd
Max-Planck-Institut für
Struktur und Dynamik der Materie

First-Principles Calculation of Time-Resolved Excitations in 2D Materials: Core, Valence, and Vibrational Spectroscopies

Dissertation
zur Erlangung des Doktorgrades
an der Fakultät für Mathematik, Informatik und Naturwissenschaften
Fachbereich Physik
der Universität Hamburg

vorgelegt von
Mukhtar Muhammad Lawan, Msc.
aus Kano, Nigeria.

Hamburg
2024

Gutachter/innen der Dissertation:	Prof. Dr. Angel Rubio Dr. Hannes Hübener
Zusammensetzung der Prüfungskommission:	Prof. Dr. Daniela Pfannkuche Prof. Dr. Francesca Calegari Prof. Dr. Angel Rubio Prof. Dr. Umberto De Giovaninni Dr. Hannes Hübener
Vorsitzender der Prüfungskommission:	Prof. Dr. Daniela Pfannkuche
Datum der Disputation:	10. Oktober 2024
Vorsitzender Fach-Promotionsausschusses PHYSIK:	Prof. Dr. Markus Drescher
Leiter des Fachbereichs PHYSIK:	Prof. Dr. Wolfgang J. Parak
Dekan der Fakultät MIN:	Prof. Dr.-Ing. Norbert Ritter

Declaration on oath

I hereby declare and affirm that this doctoral dissertation is my own work and that I have not used any aids and sources other than those indicated.

If electronic resources based on generative artificial intelligence (gAI) were used in the course of writing this dissertation, I confirm that my own work was the main and value-adding contribution and that complete documentation of all resources used is available in accordance with good scientific practice. I am responsible for any erroneous or distorted content, incorrect references, violations of data protection and copyright law or plagiarism that may have been generated by the gAI.

Hamburg, den 11.09.2024

Für Habiba, Habiba und Habibah.
Mutter, Frau und Tochter

Preface

The work leading up to this monograph dissertation was conducted from January 2021 to October 2024 at the Max Planck Institute for the Structure and Dynamics of Matter (MPSD) and the University of Hamburg (UHH) under the supervision of Prof. Dr. Angel Rubio, Prof. Dr. Umberto De Giovaninni, and Dr. Hannes Hübener.

"This project has received funding from the European Union's Horizon 2020 research and innovation programme under the Marie Skłodowska-Curie grant agreement No. 860553."

Acknowledgements

I would like to express my deepest gratitude to everyone who supported and guided me throughout the course of this project and writing of this thesis.

First and foremost, I would like to thank my advisors, Prof. Dr. Angel Rubio, Dr. Hannes Hübener and Prof. Dr. Umberto De Giovaninni for their continuous support, patience, and insightful guidance for the past three years and ten months. Their expertise and dedication have been invaluable in shaping this work and my development as a researcher. I am also deeply grateful for their support during the birth of our daughter Habibah (Ikhlas).

I am also very grateful to my colleagues at the theory group, who provided a collaborative environment and offered helpful feedback throughout this project. Special thanks to Dr. Davis Welakuh, who welcomed me with open arms when I arrived. I would like to also extend my thanks to Dr. Kevin Lively and Prof. Dr. Shunsuke A. Sato for the detailed explanation on transient absorption and non-equilibrium dynamics. My appreciation goes to Dr. Nicolas Tancogne-Dejean and the Octopus team for their assistance with various techniques to navigate around the code. I will also like to thank my office mates-Alaa, WenWen, Afifa, Chongxiao and Christian-for creating a pleasant environment and the valuable discussions and joyful moments we shared.

I would also like to acknowledge the generous funding provided by the European union's Horizon 2020 research and innovation program through the Study of carrier transport in MAterials by time-Resolved specTroscopy with ultrashort soft X-ray light (SMART-X) Initial Training Network (ITN) project. This support was crucial in enabling me to come to Europe and pursue my research. I am deeply grateful to the colleagues and collaborators within these networks, whose contributions and guidance have greatly enriched my experience and work. Their involvement has been instrumental in the successful completion of this project. I am also very grateful to the International Max-Planck research school for Ultrafast imaging and structural dynamics (IMPRS-UFAST) graduate school for giving me the opportunity to be part of their program and for supporting my learning of the German language.

To my beloved wife, your unwavering love, encouragement, and patience have been my greatest source of strength. Your belief in me, even during the most challenging moments, has been invaluable, and I am forever grateful for your support.

To my parents and siblings, thank you for your endless sacrifices and for instilling in me the value of perseverance and hard work. Your guidance and encouragement have shaped me into the person I am today, and I could not have achieved this without your constant love and support.

Finally, to all who have contributed to my academic and personal growth, thank you for helping me reach this milestone.

Acronyms

a.u Atomic Units. 30, 68, 78, 80, 94

AES Auger electron spectroscopy. 17

ALDA Adiabatic Local Density Approximation. 52, 55, 79

ATAS Attosecond Transient Absorption Spectroscopy. 1, 3, 7, 8, 27, 77

BOA Born-Oppenheimer Approximation. 31–33, 45

DFKE Dynamical Franz-Keldysh Effect. 3, 86–88, 95, 100, 104, 105, 129, 130, XIII

DFPT Density Functional Perturbation Theory. 1, 4, 28, 44–46, 110, 111, 116, 117, 121, 124, 127, 130, XIV

DFT Density Functional Theory. 1, 4, 7, 28, 30, 34–36, 38, 39, 43, 44, 46, 47, 50, 51, 55, 57, 59, 66, 74, 75, 108, 115, 116, 127, 129, 130, 156

DFT+U DFT+U. 69, 70, 73–75, 129, XI, XV

DOS Density of States. 117, 118

EXAFS Extended X-ray Absorption Fine Structure. 19, 20

FGR Fermi Golden Rule. 25, 27

FKE Franz-Keldysh Effect. 87, 89, 95, 96, 104, XII

FT Fourier Transform. 24, 46, 56, 71, 78, 82–84, 86–88, 93, 99–102, 137, XII

GGA Generalized Gradient Approximation. 40, 41, 44, 108, 110, 116, 121

HF Hartree-Fock. 33–35

HK Hohenberg and Kohn. 35

KS Kohn-Sham. 37, 38, 44, 50–52, 54, 57, 67

LDA Local Density Approximation. 28, 39–41, 43, 44, 52, 55, 66, 69, 70, 73–75, 108, 110, 115, XI

PBE Perdew-Burke-Ernzerhof. 108, 110, 116, 121

PBM Parabolic Two Band Model. 97, 98, 102–105, 130, XIII, XVII

PP Pseudopotential. 44

RG Runge-Gross. 50

SE Schrödinger equation. 23, 31, 32

SFKE Static Franz-Keldysh Effect. 95

TAS Transient Absorption Spectroscopy. 1, 3, 28, 62, 82–86, 88, 95, 103–105, 129, XIII

TDDFT Time Dependent Density Functional Theory. 1, 3, 7, 8, 28, 30, 42, 47–52, 55, 57, 59, 62, 77, 88, 95, 103–105, 129, 130

TDKS Time Dependent Kohn-Sham. 26, 28, 50–52, 56, 59, 62, 64, 77, 153, 154, 156

TISE Time-Independent Schrödinger equation. 30, 33

XAS X-ray Absorption Spectroscopy. 18, 62, 66, 67, 69, 129

XC Exchange and Correlation. 39, 42, 43, 51, 52, 55, 66, 108, 110, 115, 116, 129

XES X-ray emmission. 17

XPS X-ray Photo-emmsission Spectroscopy. 17, 18

List of Figures

List of Tables

Contents

1 Abstract

The development of Attosecond Transient Absorption Spectroscopy (ATAS) based on pump-probe setups has been an area of active research for several decades. Recent advancements of tabletop laser sources, combined with the discovery of two-dimensional (2D) materials have intensified interest in this technique. ATAS is such a versatile and powerful technique that can be applied nearly to all states of matter including solids, liquids and gases. In solid state systems, ATAS enables precise measurements of a materials response or absorption while it interacts with a pump pulse, followed by a well controlled time-delayed probe pulse to probe the dynamics induced by the pump pulse. These measurement are typically performed as a function of pump-probe delay which shows the ultrafast electron dynamics and structural changes within the material. The ability of ATAS to capture nonlinear electron dynamics on attosecond time scales enables the exploration of various properties of matter, and making a corresponding numerical approach to the pump-probe scheme essential.

TAS can be accurately modeled using a numerical pump-probe scheme, employing real-time Time Dependent Density Functional Theory (TDDFT) to simulate light-induced electron dynamics in solids. In this thesis, we demonstrate how the numerical pump-probe calculations can be used for studying the non-equilibrium phenomena observed in time-resolved experiments, offering a accurate description of the transient optical properties of solids. By simulating the ultrafast electron dynamics in response to an external perturbation, these calculations provide a description of the underlying mechanism of light-induced electron dynamics in solids. Using this approach we show how the TAS is modelled for monolayer hBN using different configurations of pump pulse: linear, circular, two-color monochromatic and bichromatic counter rotating pulse induces non-linear equilibrium dynamics below the bandgap of this system. While the linear and circularly polarized pulses show features occurring with twice the applied pump frequency which are associated with the salient features of the Dynamical Franz Keldysh effect, we observed a highly nonlinear optical responses that oscillates with three times the pump frequency. The goal of this thesis is to understand the microscopic origin of these below gap transient features for the various pump pulse.

In addition to the numerical simulation, we develop a theory using two parabolic bands for the valence and conduction band states to investigate the microscopic origin of these transient features and compare to the latter first principles results. The parabolic two-band model allows proper description of the non-linear optical response of the monolayer hBN and does not only qualitatively reproduced the *ab-initio* results but also open a novel path to further analyse the nonequillibrium electron dynamics in solids.

Furthermore, we conduct a comprehensive study of the vibrational properties of various layers of MoS_2 under photoexcitation. Using Density Functional Theory (DFT) and constrained DFPT, we calculate the phonon frequencies of the low-frequency shear and interlayer breathing modes. Our findings are further quantified using an available open source tool capable of predicting the symmetry and optical activities of these vibrational modes from which we obtain a fan diagram of the optically active modes. Similarly, we investigate the effects of photodoping on these

layers and the phonon frequency shift of the shear and breathing modes. To probe these shifts, we discuss an experimental setup in which different layer of MoS_2 are optically excited by a Terahertz pump pulse, allowing for a detailed examination of the photodoping induced phonon frequency shift and their impact on the vibrational dynamics of the material and also to serve as a basis for the prediction of the theoretical results.

2 | Zusammenfassung

Die Entwicklung von ATAS auf der Grundlage von Pump-Probe-Anordnungen ist seit mehreren Jahrzehnten ein aktives Forschungsgebiet. Jüngste Fortschritte bei Tischlaserquellen in Verbindung mit der Entdeckung zweidimensionaler (2D) Materialien haben das Interesse an dieser Technik intensiviert. ATAS ist ein so vielseitiges und leistungsfähiges Verfahren, das auf nahezu alle Aggregatzustände, einschließlich Festkörper, Flüssigkeiten und Gase, angewendet werden kann. In Festkörpersystemen ermöglicht ATAS präzise Messungen der Absorption eines Materials, während es mit einem Pumpimpuls wechselwirkt, gefolgt von einem gut kontrollierten zeitverzögerten Probeimpuls, um die durch den Pumpimpuls induzierte Dynamik zu untersuchen. Diese Messungen werden in der Regel als Funktion des Delays zwischen Pump- und Probeimpuls durchgeführt, wodurch sich die ultraschnelle Elektronendynamik und die strukturellen Veränderungen innerhalb des Materials messen lässt. Die Fähigkeit von ATAS, die nichtlineare Elektronendynamik auf Attosekunden-Zeitskalen zu erfassen, ermöglicht die Erforschung verschiedener Eigenschaften der Materie, und ein entsprechender numerischer Ansatz für das Pump-Probe-Schema ist unerlässlich.

TAS kann mit Hilfe eines numerischen Pump-Probe-Schemas genau modelliert werden, wobei Echtzeit-TDDFT zur Simulation der lichtinduzierten Elektronendynamik in Festkörpern verwendet wird. In dieser Arbeit zeigen wir, wie die numerischen Pump-Probe-Berechnungen als Medium für die Untersuchung der Nicht-Gleichgewichtsphänomene dienen, die in den zeitaufgelösten Experimenten beobachtet werden, und eine genaue Beschreibung der vorübergehenden optischen Eigenschaften von Festkörpern bieten. Durch die Simulation der ultraschnellen Elektronendynamik als Reaktion auf eine externe Störung liefern diese Berechnungen den zugrunde liegenden Mechanismus der lichtinduzierten Elektronendynamik in Festkörpern. Mit diesem Ansatz zeigen wir, wie der TAS für einlagiges hBN unter Verwendung verschiedener Konfigurationen von Pumpimpulsen modelliert wird: lineare, zirkulare, monochromatische und bichromatische gegenläufig zirkular polarisierte Impulse induzieren eine nichtlineare Gleichgewichtsdynamik unterhalb der Bandlücke dieses Systems. Während die monochromatischen linearen und zirkular polarisierten Pulse Merkmale zeigen, die bei der doppelten Pumpfrequenz auftreten und mit den hervorstechenden Merkmalen des DFKE verbunden sind, beobachten wir eine hochgradig nichtlineare optische Reaktion, die mit der dreifachen Pumpfrequenz oszilliert. Das Ziel dieser Arbeit ist es, den mikroskopischen Ursprung dieser unter der Lücke liegenden transienten Merkmale für die verschiedenen Pumpimpulse zu verstehen.

Zusätzlich zur numerischen Simulation entwickeln wir eine Theorie, die zwei parabolische Bänder für die Valenz- und Leitungsbandzustände verwendet, um den mikroskopischen Ursprung dieser transienten Eigenschaften zu untersuchen und mit den Ergebnissen der *ab inito* Rechnugen zu vergleichen. Das parabolische Zweibandmodell ermöglicht somit eine angemessene Beschreibung der nichtlinearen optischen Reaktion des einschichtigen hBN und reproduziert nicht nur die Ergebnisse der *ab-initio*, sondern eröffnet auch einen neuen Weg zur weiteren Analyse der Nichtgleichgewichtselektronendynamik in Festkörpern.

Darüber hinaus präsentieren wir eine umfassende Studie über die Schwingungseigenschaften

verschiedener Schichten von MoS_2 unter Lasereinwirkung durchgeführt. Mit Hilfe von DFT und constrained DFPT berechnen wir die Phononfrequenzen der niederfrequenten Scher- und Zwischenschichtatmungsmoden. Unsere Ergebnisse werden mit Hilfe eines Open-Source-Tools weiter quantifiziert, das die Symmetrie und die optischen Aktivitäten dieser Schwingungsmoden vorhersagen kann, woraus wir ein Fächerdiagramm der optisch aktiven Moden erhalten. In ähnlicher Weise untersuchen wir die Auswirkungen der Photodotierung auf diese Schichten und die Phononenfrequenzverschiebung der Scher- und Atmungsmoden. Um diese Verschiebungen zu untersuchen, diskutieren wir einen Versuchsaufbau vor, bei dem verschiedene MoS_2-Schichten durch einen Terahertz-Pumpimpuls optisch angeregt werden. Dies ermöglicht eine detaillierte Untersuchung der durch Photodotierung induzierten Phononenfrequenzverschiebung und ihrer Auswirkungen auf die Schwingungsdynamik des Materials und dient auch als Grundlage für die Vorhersage der theoretischen Ergebnisse.

3 List of Publications

I **M. M. Lawan**, S. A. Sato, U. De Giovannini, H. Hübener, O. Neufeld and A. Rubio (2024), "Tailored-light driven ultrafast dynamical Franz Keldysh effect: higher order analysis and symmetry decomposition"; In preparation.

II **M. M. Lawan**, U. De Giovannini, H. Hübener, and A. Rubio (2024), "Terahertz peak shift in different layers of MoS_2 for shear and Interlayer breathing modes"; In preparation.

This page was intentionally left blank.

4 Introduction

> 'Read! In the name of your Lord who created. He created man from a clinging substance. Read! And your Lord is the Most Generous. Who taught by the pen. Taught man that which he knew not.'
>
> *Qur'an* $96 : 1 - 5$

In this chapter, the introduction unfolds, shedding light on the fundamental concepts that underpin this PhD project. Addressing the sources of certain nonlinear dynamics manifested in the transient absorption spectra of solids. Most parts of this thesis employs the framework of both DFT and TDDFT with their respective approximations.

4.1 General Introduction

In recent years, the field of ultrafast spectroscopy has witnessed remarkable advancements in unravelling the dynamics of molecular and material systems on unprecedented timescales. ATAS has emerged as a powerful technique for probing the ultrafast electron and nuclear dynamics in various systems with attosecond temporal resolution. With its ability to capture electron motion and energy transfer processes at the sub-femtosecond timescale, ATAS provides invaluable insights into fundamental processes governing light-matter interactions.

4.1.1 Attosecond Transient Absorption Spectroscopy

(ATAS) is an ultrafast spectroscopic technique that allows the investigation of electron and nuclear dynamics on attosecond timescales. There have been an extensive reviews of this topic in numerous literature [20–22]. This section provides a brief background on what ATAS entails. At the attosecond timescale (10^{-18}sec), it becomes possible to observe and investigate the ultrafast dynamics of electrons within atoms, molecules, and materials. Attosecond pulses in general are produced in non-linear process where a strong, few cycles Infra-red (IR) laser pulse interacts with a gas, this process known as High-Harmonic generation (HHG) [23–25] which allows the synchronization of the pump and probe pulses and thus paving way for performing transient absorption spectroscopy. The generation of attosecond-laser pulses using attosecond laser sources is usually described in a three-step model [25–27]: In the first step an intense laser pulse that is focused on the target material (usually a noble gas) ionizes the atoms or molecules, thus creating a plasma of free electrons. The free electrons are accelerated by the laser field

and subsequently driven back towards the parent ions. As they recombine with the ions, they release excess energy in the form of high-energy photons [28, 29]. The recombination process leads to the emission of photons with energies that are multiples of the original laser frequency. These higher harmonic frequencies correspond to shorter wavelengths and, consequently, to attosecond time scales. Finally, by filtering and isolating the desired higher harmonics, the emitted radiation can be shaped into an attosecond pulse with a duration on the order of a few hundred attoseconds [30]. In general, generating attosecond pulses requires precise control over the laser parameters, such as intensity, pulse duration, and phase, as well as careful selection of the target material. Achieving high-quality attosecond pulses often involves sophisticated experimental setups and advanced laser technologies. The first ATAS experiment was conducted by Hentschel et al. in 2001 [31] with a single cycle long X-ray attosecond pulse of 650 ± 150 *as*. Since the pioneering work of Hentschel et al. in 2001, there have been numerous subsequent experiments and advancements. Some of the noticeable experiments and advancements in the field of ATAS can be found in [32–34] amongst others.

4.1.2 Theory of Transient Absorption Spectroscopy

It is essential to describe the absorption process of the probe pulse after the pump pulse has changed the the electronic properties of the system. This section discusses the theoretical modelling employed using TDDFT for the calculations in this work. Here, we highlight the approach to treating the pump setup in a completely non-pertubative manner, with the assumption that the probe pulse has no temporal overlap with the pump pulse.

Response to an external perturbation

In general, a pump-probe experiment usually requires a setup that includes a pump pulse and a delayed probe pulse as depicted in the figure 4.1 below. Both pump and probe pulses are

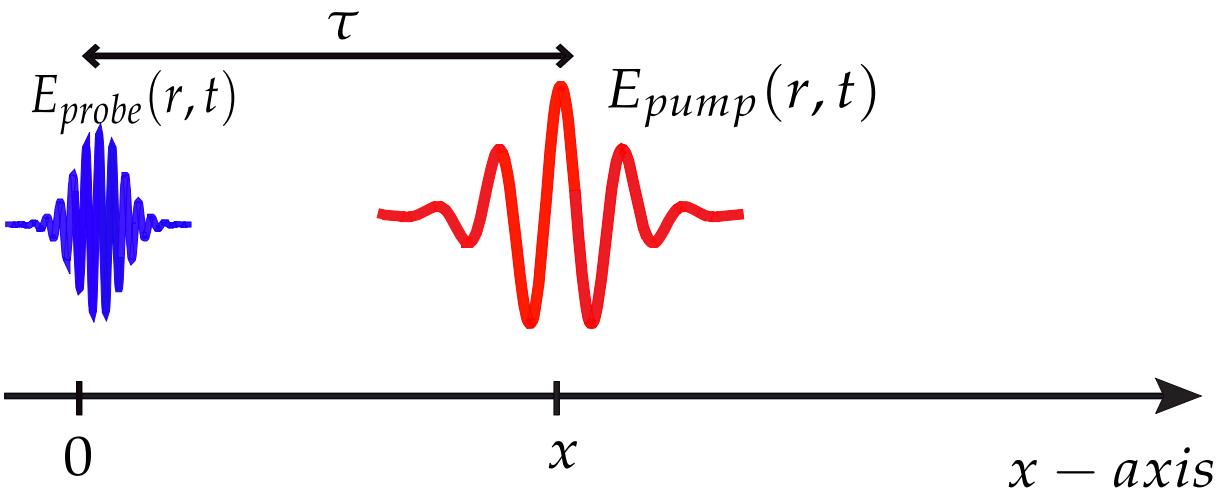

Figure 4.1: Pump-probe setup depicting pump and probe pulses propagating along the x axis as used in theoretical calculations.

propagating at vacuum speed of light c along the propagating axis. The electric field of the pump is given by $E_{pump}(r, t_{pu})$ and that of the probe, $E_{probe}(r, t_{pr})$ both centered at time $t_{pr} = t_{pu} = 0$.

Suppose both pump and probe are propagating along the x-axis as shown in the figure. At an instance of time, the total propagation time would be $t_{tot} = \frac{x}{c}$. The probe pulse is spatially centered at x and the target medium is also at x. In this setup, the time delay τ between the two pulses is then $\frac{x}{c}$, such that the pump pulse will be centered at the position x of the target medium (in our case an atom). The electric field of the pump pulse at x is then $E_{pump}(x, t_{pu})$ where $t_{pu} = t - \frac{x}{c}$ and that of the probe pulse is $E_{probe}(x, t_{pr})$.

To depict the absorption of the probe pulse and consequently analyse the polarization response of the electronic structure, it is imperative to solve the Schrödinger equation in a time-dependent manner following the method presented in [35]:

$$i\frac{\partial}{\partial t}|\Psi(t)\rangle = \hat{H}(t)|\Psi(t)\rangle \tag{4.1}$$

the time dependent Hamiltonian in the electric dipole approximation, can be formulated as

$$\hat{H}(t) = \hat{H}_0 - E_0 - E_{pu}(t)\hat{\mathcal{Z}} - E_{pr}\left(x, t_{pr}\right)\hat{\mathcal{Z}} \tag{4.2}$$

where $\hat{H}_0$ is the Hamiltonian of the unperturbed problem, E_0 is the ground state energy of the atom and $\hat{\mathcal{Z}}$ represents the z component of the electric dipole operator. To calculate and interpret the polarization response $P\left(x,t\right) = \langle\Psi(t)|\hat{\mathcal{Z}}|\Psi(t)\rangle$, it is helpful to initially derive an equation for $|\Psi(t)\rangle$ in terms of $E_{pr}\left(x,t\right)$. Let $\hat{\mathcal{U}}_{pu}(t,-\infty)$ represent the time evolution operator corresponding to the solution of the pump-only scenario. Hence,

$$|\Psi_{pu}(t)\rangle = \hat{\mathcal{U}}_{pu}(t,-\infty)|\Psi_0(t)\rangle \tag{4.3}$$

is the solution of the Schrödinger equation (4.1) for vanishing $E_{pr}\left(x,t\right)$. The eigenstate $|\Psi_0\rangle$ refers to the initial state of the atom postulated to be the lowest energy state. To derive the influence of the weak perturbation, we apply the time dependent perturbation theory, c.f. Appendix A, to the solution of the Schrödinger equation. The ansatz reads,

$$|\Psi(t)\rangle = |\Psi_{pu}(t)\rangle + |\Psi(t)\rangle^{(1)} \tag{4.4}$$

by inserting the ansatz Eq. (4.4) into Eq. (4.1), we have

$$i\frac{\partial}{\partial t}|\Psi(t)\rangle^{(1)} = \left[\hat{H}_0 - E_0 - E_{pu}(t)\hat{\mathcal{Z}}\right]|\Psi(t)\rangle^{(1)} - E_{pr}\left(x,t\right)\hat{\mathcal{Z}}\,|\Psi_{pu}(t)\rangle - E_{pr}\left(x,t\right)\hat{\mathcal{Z}}|\Psi(t)\rangle^{(1)} \tag{4.5}$$

Since the perturbation is only in the first order of the probe electric field E_{pr}, one can drop the last term of the previous equation, and upon integrating it, we obtain the expression for $|\Psi(t)\rangle^{(1)}$

$$|\Psi(t)\rangle^{(1)} = i\int_{-\infty}^{t}\hat{\mathcal{U}}_{pu}\left(t,t'\right)\hat{\mathcal{Z}}E_{pr}\left(x,t'+x/c\right)|\Psi_{pu}\left(t'\right)\rangle\,dt' \tag{4.6}$$

where $\hat{\mathcal{U}}_{pu}\left(t,t'\right) = \hat{\mathcal{U}}_{pu}(t,-\infty)\hat{\mathcal{U}}^{\dagger}_{pu}\left(t',-\infty\right)$. Utilizing this integral solution within the context of the first-order perturbation theory, the polarization response attributed to each atomic absorber can be expressed as follows

$$\begin{aligned} P\left(x,t\right) = n_0\Big\{&\Big\langle\Psi_{pu}(t)|\hat{\mathcal{Z}}|\Psi_{pu}(t)\Big\rangle + \Big\langle\Psi_{pu}(t)|\hat{\mathcal{Z}}|\Psi(t)^{(1)}\Big\rangle \\ &+ \Big\langle\Psi(t)^{(1)}|\hat{\mathcal{Z}}|\Psi_{pu}(t)\Big\rangle + \Big\langle\Psi(t)^{(1)}|\hat{\mathcal{Z}}|\Psi(t)^{(1)}\Big\rangle\Big\}. \end{aligned} \tag{4.7}$$

From the above equation, the first term shows the harmonic generation driven by the pump field. Polarization response is described by the second and third term, respectively. The last term is second order response from the probe field. As we make the assumption that harmonics originate solely from the pump pulse and that there is no temporal overlap with the probe pulse, the polarization response resulting from the absorbing component of the probe pulse can be formulated as follows

$$\begin{aligned} P_{(1)}(x,t) &= n_0 \left\langle \Psi_{pu}(t) | \hat{\mathcal{Z}} | \Psi(t)^{(1)} \right\rangle + \text{ c.c.} \\ &= i n_0 \int_{-\infty}^{t} E_{pr}\left(x, t' + x/c\right) \left\langle \Psi_{pu}(t) \left| \hat{\mathcal{Z}} \hat{\mathcal{U}}_{pu}\left(t,t'\right) \hat{\mathcal{Z}} \right| \Psi_{pu}\left(t'\right) \right\rangle dt' + c.c. \end{aligned} \tag{4.8}$$

In most parts of this work, a probe pulse with the shape of a delta function centered at $t' = \tau$ is used in the simulations. One can demonstrate how the polarization response can be defined if the electric field of the probe has such shape

$$E_{pr}\left(x, t' + x/c\right) = \delta(t' - \tau). \tag{4.9}$$

Therefore, the polarization in (4.8) becomes

$$\begin{aligned} P_{(1)}(x,t) &\propto i n_0 \int_{-\infty}^{t} \delta\left(t' - \tau\right) \left\langle \Psi_{pu}(t) \left| \hat{\mathcal{Z}} \hat{\mathcal{U}}_{pu}\left(t,t'\right) \hat{\mathcal{Z}} \right| \Psi_{pu}\left(t'\right) \right\rangle dt' + \text{ c.c.} \\ &\propto \left\langle \Psi_{pu}(t) \left| \hat{\mathcal{Z}} \hat{\mathcal{U}}_{pu}(t,\tau) \hat{\mathcal{Z}} \right| \Psi_{pu}(\tau) \right\rangle + c.c. \end{aligned} \tag{4.10}$$

The above equation shows how the polarization response is influenced not only by the state $|\Psi_{pu}\rangle$ at the time of the probe pulse τ, but also by the wave function $\langle\Psi_{pu}|$ and the time evolution operator $\hat{\mathcal{U}}_{pu}(t,\tau) > \tau$.

4.1.3 Response of absorbing medium after interacting with probe pulse

In the previous subsection, we have discussed how atoms respond when irradiated by a pump and probe pulse and shown how polarization response is determined by the wavefunction of the pump pulse. This part will explain how a probe pulse interacts with an absorbing medium as it travel through it. When light travels through an absorbing material, it interacts with the material, causing a variety of effects. In the last subsection we assumed that the probe pulse arrives after the target medium has been irradiated by the pump pulse, as described in [35], one can explicitly write the time evolution operator as

$$\hat{\mathcal{U}}_{pu}\left(t,t'\right) = e^{-i(\hat{H}_0 - E_0)(t-t')} \tag{4.11}$$

based on the assumption that no alteration of the electronic states excited through the absorption of the probe pulse. Similarly, we can express the electronic structure of the medium after interacting with pump pulse as an expansion of the eigenstates $|\phi_i\rangle$ with their eigenenergies as E_i and a time-independent expansion coefficient α_i, the eigenstate reads

$$|\Psi_{pu}(t)\rangle = \sum_i \alpha_i e^{-i(E_i - E_0)t} |\varphi_i\rangle \tag{4.12}$$

from the polarization we derived in Eq.(4.8), we substitute Eq.(4.11) and obtain the relation for the polarization as

$$\begin{aligned} P_{(1)}(x,t) =& in_0 \sum_{i,i'} \alpha_i^* \alpha_{i'} \sum_j \left\langle \varphi_i | \hat{\mathcal{Z}} | \varphi_j \right\rangle \left\langle \varphi_j | \hat{\mathcal{Z}} | \varphi_{i'} \right\rangle \cdot \\ & \int_{-\infty}^{t} E_{pr}\left(x,t'\right) e^{-i(E_j-E_i)(t-t')+i(E_i-E_{i'})t'} dt' + \text{ c.c.} \end{aligned} \tag{4.13}$$

where $|\varphi_j\rangle$ is the eigenstates of the Hamiltonian $\hat{H}_0$ with energies E_j. To obtain the response of the probe pulse E_{pr}, it is easier to solve the wave equation as obtained from Maxwell's equations.

$$\left(\frac{\partial^2}{\partial x^2} - \frac{\partial^2}{c^2 \partial t^2} \right) E_{pr}\left(x,t\right) = \frac{4\pi}{c^2} \frac{\partial^2}{\partial t^2} \left(P_{(1)}\left(x,t\right) + P_{(NL)}\left(x,t\right) \right). \tag{4.14}$$

The applied probe field which is a weak delta like perturbation can only induce excitation within the linear polarization regime, therefore, nonlinear polarization term $P_{NL}(x,t)$ can be neglected. It is convenient to describe the wave equation in frequency regime, hence taking the Fourier transform of the wave equation one obtains,

$$\frac{\partial^2}{\partial x^2} \widetilde{E}_{pr}(x,\omega) + \frac{2i\omega}{c} \frac{\partial}{\partial x} \widetilde{E}_{pr}(x,\omega) = -\frac{4\pi\omega^2}{c^2} \widetilde{P}_{(1)}(x,\omega), \tag{4.15}$$

where;

$$\begin{aligned} \widetilde{E}_{pr}(x,\omega) &= \frac{1}{2\pi} \int_0^\infty E_{pr}\left(x,t\right) e^{i\omega t} dt \\ \widetilde{P}_{(1)}(x,\omega) &= \frac{1}{2\pi} \int_0^\infty P_{(1)}\left(x,t\right) e^{i\omega t} dt \end{aligned} \tag{4.16}$$

As suggested in [36], the first term of Eq.(4.15) is negligible when utilizing the slowly changing amplitude approximation.

$$\frac{2i\omega}{c} \frac{\partial}{\partial x} \widetilde{E}_{pr}(x,\omega) = -\frac{4\pi\omega^2}{c^2} \widetilde{P}_{(1)}(x,\omega) \tag{4.17}$$

There are numerous ways to solve the wave equation above. One way is to employ analytical means only if the induced polarization response $\widetilde{P}_{(1)}(x,\omega)$ and the probe electric field $\widetilde{E}_{(1)}(x,\omega)$ are proportional. The proportionality concept is closely connected to the concept of linear susceptibility $\chi(x,\omega)$. To demonstrate the application of linear susceptibility concept, we have to calculate the value of $\widetilde{P}_{(1)}(x,\omega)$ assuming that the Fourier transform is restricted to only positive frequencies and also assuming that there is a certain life time and decaying rate Γ_j of the final states $|\varphi_j\rangle$. Therefore, the induced polarization in frequency regime can be expressed as

$$\begin{aligned} \widetilde{P}_{(1)}(x,\omega>0) =& in_0 \sum_{i,i'} \alpha_i^* \alpha_{i'} \sum_j \left\langle \varphi_i | \hat{\mathcal{Z}} | \varphi_j \right\rangle \left\langle \varphi_j | \hat{\mathcal{Z}} | \varphi_{i'} \right\rangle \cdot \\ & \left[\frac{1}{E_{i'} - E_j - i\Gamma_j/2 - \omega} \right] \widetilde{E}_{pr}\left(x, \omega + E_i - E_{i'}\right). \end{aligned} \tag{4.18}$$

Since in this work we usually use an ultrashort probe pulse with duration of less 300 attoseconds or even a delta function centered at t = τ, we can approximate the last part of the above equation as

$$\widetilde{E}_{pr}\left(x, \omega + E_i - E_{i'}\right) = \widetilde{E}_0(x) e^{i(\omega + E_i - E_{i'})t} \tag{4.19}$$

and finally we can express the polarization as;

$$\widetilde{P}_{(1)}(x,\omega>0,\tau) = in_0 \sum_{i,i'} \alpha_i^*(\tau)\alpha_{i'}(\tau) \sum_j \frac{\left\langle\varphi_i|\hat{\mathcal{Z}}|\varphi_j\right\rangle\left\langle\varphi_j|\hat{\mathcal{Z}}|\varphi_{i'}\right\rangle}{E_{i'} - E_j - i\Gamma_j/2 - \omega} \cdot \widetilde{E}_0(x)e^{i\omega\tau} \tag{4.20}$$

where $\alpha_i(\tau)$ are the time-dependent expansion coefficients. As mentioned, the linear response can be represented by a susceptibility known as the linear susceptibility χ which can be defined as;

$$\chi_{(1)}(\omega>0) = \frac{\widetilde{P}_{(1)}(x,\omega)}{\widetilde{E}_{pr}(x,\omega)} \tag{4.21}$$

upon inserting Eq.(4.20) into the above equation we obtain

$$\chi_{(1)}(\omega>0) == n_0 \sum_{i,i'} \alpha_i^*(\tau)\alpha_{i'}(\tau) \sum_j \frac{\left\langle\varphi_i|\hat{\mathcal{Z}}|\varphi_j\right\rangle\left\langle\varphi_j|\hat{\mathcal{Z}}|\varphi_{i'}\right\rangle}{E_{i'} - E_j - i\Gamma_j/2 - \omega}. \tag{4.22}$$

Finally, by leveraging the legitimacy of introducing the linear susceptibility, the wave equation (as depicted in 4.15), the resulting solution takes the form:

$$\widetilde{E}_{pr}(x,\omega) = \widetilde{E}_{pr}\left(x_0,\omega\right) e^{2\pi i\omega/c \int_{x_0}^{x} \chi_{(1)}(x',\omega)dx'}. \tag{4.23}$$

Similarly, we can express this solution in Eq. (4.23) in terms of the Intensity $\widetilde{I}_{pr}(L,\omega)$ as done experimentally, the expression reads

$$\widetilde{I}_{pr}(L,\omega) = \widetilde{I}_{pr}(0,\omega)e^{-4\pi\omega/c \int_0^L \mathrm{Im}[\chi_{(1)}(x',\omega)]dx'} \tag{4.24}$$

where L is the length of interaction volume. This is an important result and is refereed to as the Lambert Beer's law. For our target system (an atom), the probability of a single photon being absorbed can be described by the single-photon absorption cross section which reads;

$$\sigma_{(1)}(\omega) = 4\pi\omega/\left(cn_0\right) \mathrm{Im}\left[\chi_{(1)}(\omega)\right]. \tag{4.25}$$

This concept is essential in various applications and in Chapter 6, the cross section expressed here will be useful in the discussion of the optical conductivity.

4.1.4 Pump-probe Spectroscopy: an overview

Pump-probe spectroscopy has found application in characterizing rapid dynamics and relaxation rates of molecular systems in various environments, spanning from solutions [37–41], proteins and biological systems [42–47], to solids[48–51], and even in the gas phase [52–56]. The pump-probe technique usually relies on a Michelson-interferometer that utilizes femtosecond train pulses, which are not correlated [46]. One arm of the interferometer directs a strong beam, known as the pump pulse, to the sample to photo-excite the sample. On the other hand, the other arm of the interferometer introduces a delayed pulse, known as the probe, to the non-equilibrated sample to investigate the photo-induced changes caused by the pump pulse. The intensity I of the probe pulse is weaker than that of the pump pulse to avoid multiphoton processes, which are not desired in most of pump-probe spectroscopies. Pump-probe experiments

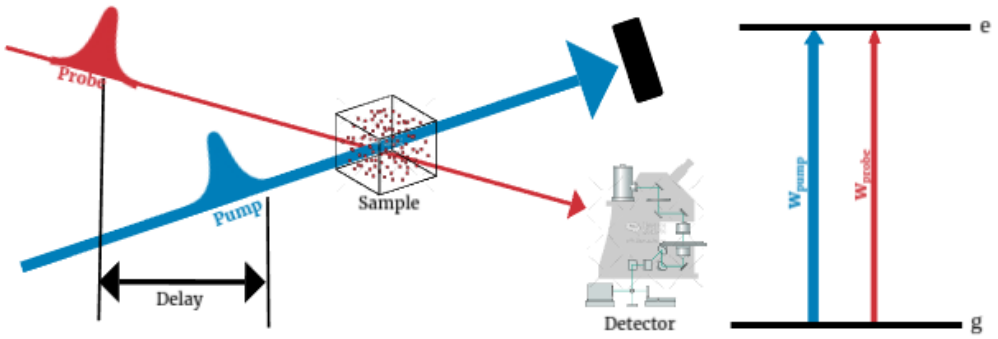

Figure 4.2: The fundamental setup for pump-probe experiments and the diagram depicting electronic energy levels. It's important to observe that the thickness of the lines represents the relative intensity of the laser pulses, with the probe intentionally kept weak to prevent undesired interference with the system.(*Adapted from* [1])

can be categorized based on the probe energy. When the probe pulse has the same energy as the pump pulse, the system is referred to as "degenerate". Conversely, if the probe pulse has a different energy from the pump pulse, the system is known as "non-degenerate" or a two-color pump-probe setup [57].

Since pump-probe spectroscopy is such a powerful tool used to study dynamical processes in physical systems, it requires the system to be perturbed from its equilibrium state. The perturbation is achieved using the pump pulse, which travels a shorter path to reach the sample first. The pump pulse can be manipulated in various ways, such as adjusting its energy, intensity, polarization, and duration, to excite the sample as desired. For instance, in the case of electron energy levels in an atom, if the energy of the pump pulse matches the energy difference between two levels, the atoms in the sample will absorb photons from the pump pulse, leading to an increase in the population of electrons in the higher energy level [58]. After the pump pulse has perturbed the sample, the probe pulse arrives at the sample with a controlled delay, determined by changing the path length difference between the pump and probe pulses. The probe pulse is then measured with a detector after it interacts with the sample. The key to deducing the physical state of the sample is observing the modulation of the probe pulse as it decays back to an equilibrium state following the perturbation from the pump pulse. For example, in the case of excited electrons in the atom, if many electrons are still in the excited state when the probe pulse arrives, most of the probe pulse will be transmitted rather than absorbed, due to Pauli blocking [59]. Conversely, if many of the previously excited electrons have already decayed by the time the probe pulse arrives, most of the probe pulse will be absorbed since many electrons have returned to the lower energy state. By measuring the intensity modulation of the probe pulse as a function of delay, the population dynamics of the electron energy levels can be described.

The dynamics of the photo induced samples can be monitored by varying the time delay between the pump and probe pulses. Therefore, this technique can be likened to snapshot-like spectroscopy, capturing the state of a specific system at a precise moment determined by the delay time between the pump and probe pulses [60]. This thesis primarily focuses on the absorption process in solids. The numerical pump-probe spectroscopy technique, which will be introduced in a subsequent chapter, will be utilized to analyze this process.

4.1.5 Theoretical Description of the Pulses

Understanding the properties and behavior of the pulses used in pump-probe spectroscopy is crucial for interpreting experiments and devising first-principles calculations for their description. For example, if we consider the electric field in time as shown in the figure (4.3) which can be described by the following equation

$$\begin{aligned} E(t) &= A(t) \cdot e^{i\varphi(t)} + c.c \\ \varphi(t) &= \omega_0 t + \phi(t) + CEP \end{aligned} \tag{4.26}$$

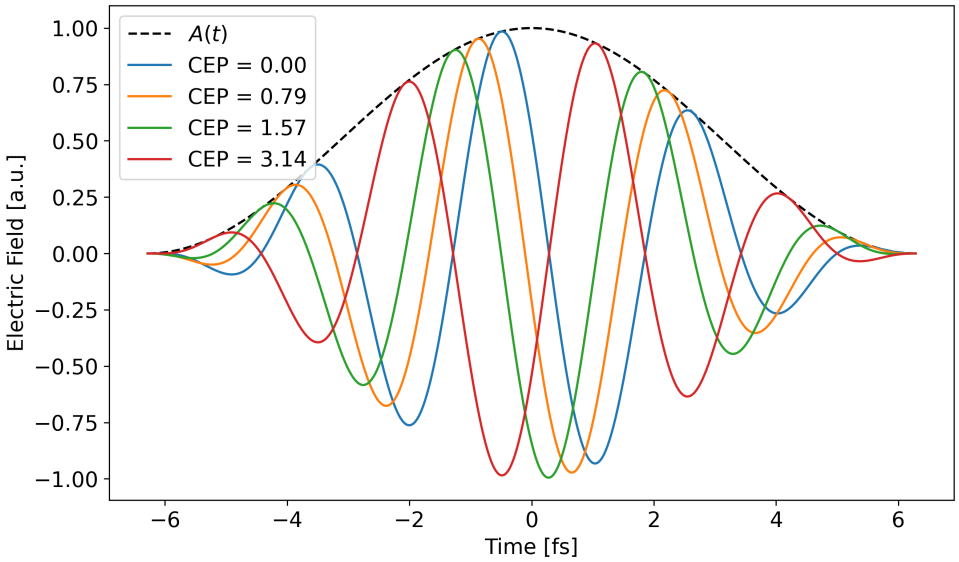

Figure 4.3: Depiction of electric field and its envelop in time domain. The dotted lines shows the envelop, while the solid blue, yellow, green, and red lines shows the CEPs at 0, $\frac{\pi}{4}$, $\frac{\pi}{2}$ and π respectively.

where $E(t)$ is the electric field, $A(t)$ is the envelop of the electric field and $\varphi(t)$ is the temporal phase. A common approach is to decompose the temporal phase $\varphi(t)$ into different components, which include the oscillations with the central frequency ω_0, additional phase components $\phi(t)$ and the carrier envelope phase offset (CEP). This separation helps in understanding the underlying dynamics of the system under study and facilitates the analysis of complex temporal waveforms. In some cases, the CEP is negligible especially with longer pulses but in pulse durations of only a few cycles, the CEP can play a crucial role as it has a substantial impact on the peak field strength and overall behavior of the field. Due to its influence, even small changes in the CEP can lead to significant alterations in the resulting pulse characteristics, making it a decisive factor in shaping the dynamics of ultrashort laser pulses.

4.1.6 Nonlinear Optics and Maxwells Equations

In the previous section we have described mostly linear optics where the material response and its effects on the light is independent of the intensity of the light. For low-intensity fields,

linear optical description holds well, and the classical optics description is accurate and can be used to describe linear phenomena. Since most of the process relevant in this thesis are beyond the linear optical limits, it is optimal to describe limits beyond it. To describe the non-linear optical limits we consider Maxwell's equations

$$\begin{aligned} \vec{\nabla} \cdot \vec{\mathbf{D}} &= \rho \\ \vec{\nabla} \cdot \vec{\mathbf{B}} &= 0 \\ \vec{\nabla} \times \vec{\mathbf{E}} &= -\frac{\partial \vec{\mathbf{B}}}{\partial t} \\ \vec{\nabla} \times \vec{\mathbf{H}} &= \vec{j} + \frac{\partial \vec{\mathbf{D}}}{\partial t} \end{aligned} \tag{4.27}$$

where $\vec{D} = \varepsilon_0 \vec{\mathbf{E}} + \vec{\mathbf{P}}$. Now, taking the curl of last two equations we obtain,

$$\begin{aligned} \vec{\nabla} \times \vec{\nabla} \times \vec{\mathbf{E}} &= -\mu_0 \frac{\partial^2 \vec{D}}{\partial t^2} \\ &= -\frac{1}{c^2} \frac{\partial^2 \vec{\mathbf{E}}}{\partial t^2} - \mu_0 \frac{\partial^2 \vec{P}}{\partial t^2} \\ &= -\frac{1}{c^2} \frac{\partial^2 \vec{\mathbf{E}}}{\partial t^2} - \mu_0 \frac{\partial^2}{\partial t^2} \left(\vec{P}_1 + \vec{P}_{NL} \right) \end{aligned} \tag{4.28}$$

using the identities

$$\begin{aligned} \vec{\nabla} \times \vec{\nabla} \times \vec{E} &= \vec{\nabla} \cdot (\vec{\nabla} \cdot \vec{E}) - \vec{\nabla}^2 E \\ \vec{P}_1 &= \epsilon_0 \chi_1 \vec{E} \\ n^2 &= 1 + \chi_{(1)} \end{aligned} \tag{4.29}$$

one obtains the nonlinear wave equation in its usual form, reading

$$\vec{\nabla}^2 \vec{E} = \frac{n^2}{c^2} \frac{\partial^2 \vec{E}}{\partial t^2} + \mu_0 \frac{\partial^2 \vec{P}_{NL}}{\partial t^2} \tag{4.30}$$

Even though $\rho = 0$ and $\vec{\nabla} \cdot \vec{D} = 0$ do not necessarily imply that $\vec{\nabla} \cdot \vec{E} = 0$, the quantity $\vec{\nabla} \cdot (\vec{\nabla} \cdot \vec{E})$ can often be neglected. The polarization can be expanded as a Taylor series expansion in order to have a better understanding and effects caused by the driving field

$$\begin{aligned} \vec{P} &= \epsilon_0 \left(\chi_1 \cdot \vec{E} + \chi_2 \cdot \vec{E}\vec{E} + \chi_3 \cdot \vec{E}\vec{E}\vec{E} + \ldots \right) = \\ &= \vec{P}_{(1)} + \vec{P}_{NL}. \end{aligned} \tag{4.31}$$

where χ_1 is the linear susceptibility tensor, χ_2 is lowest order non-linear susceptibility which is important in non-linear materials with no center of inversion, NL denotes non-linear. In the presence of light waves, the electrons in solids undergo oscillations around the ions, when subjected to an electric field. At low electric field intensities, these periodic oscillations are commonly known as the linear regime. However, under the influence of intense laser fields or large electric fields, the electrons deviate from the linear regime and display non-linear behavior. In this thesis the main consideration will be on the lowest order non-linear term given by the equation below

$$\vec{P}_{NL} = \epsilon_0 \left(\chi_2 \cdot \vec{E}\vec{E} \right) \tag{4.32}$$

As an example for the second order response of an incident field with more than one frequency

component,

$$\vec{E}(t) = \frac{1}{2}\left(\vec{E}_1 e^{i\omega_1 t} + \vec{E}_2 e^{i\omega_2 t} + cc.\right) \tag{4.33}$$

then the non linear term in (4.32) with the products of $\vec{E}\vec{E}$ produce two frequency terms $2\omega_1$ and $2\omega_2$ (frequency doubling) as well as $\omega_1 + 2\omega_2$ (frequency mixing), the non-linear polarization can be given by

$$\vec{P}_{NL} = \frac{1}{4}\epsilon_0\chi_1\left(\vec{E}_1^2 e^{i2\omega_1 t} + \vec{E}_2^2 e^{i2\omega_2 t} + 2\vec{E}_1\vec{E}_2 e^{i(\omega_1+\omega_2)t} + 2\vec{E}_1\vec{E}_2^* e^{i(\omega_1-\omega_2)t} + \vec{E}_1\vec{E}_1^* + \vec{E}_2\vec{E}_2^* + cc.\right) \tag{4.34}$$

From the above equation, we can visibly observe the second order frequency mixing, the second harmonic generation (SHG) from the frequency doubling.

4.2 Core-level Spectroscopy

In condensed matter, electrons can be categorized as core electrons and outer electrons (also known as valence electrons). Core electrons are confined within the atom, maintaining their attributes from the free atom state, regardless of the chemical environment and they are not involved in chemical bonding. Conversely, valence electrons are more spread out and contribute to interatomic bonding, leading to distinct properties in various materials, even when they share the same atomic origin. Core level spectroscopy involves exciting a core electron using incident photons or electrons. The resulting spectra, including photoemission, photoabsorption, fluorescence, and Auger electron emission, offer crucial insights into the characteristics of outer electrons and atomic structures [61].

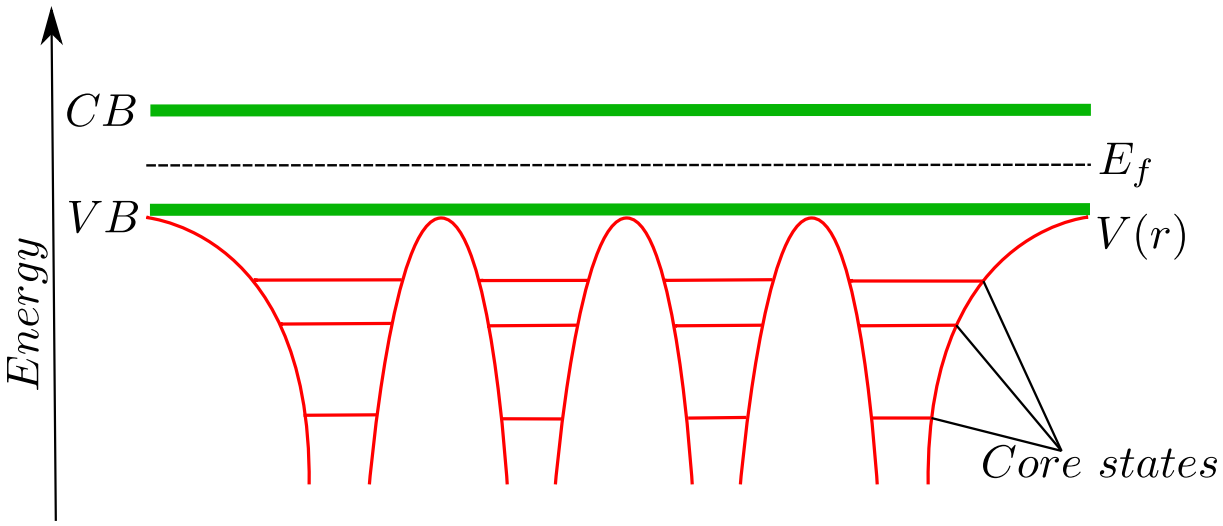

Figure 4.4: Schematic representation of core states in a periodic potential.

In core-level spectroscopy of solids, X-rays or UV light are used to excite the core electrons to an empty state, which are then emitted as photoelectrons. The energy of the emitted photoelectrons corresponds to the binding energy E_b of the core electrons in the solid. By measuring the binding energy of the core electrons, it is possible to determine the electronic structure of the solid, including the local chemical environment of the atoms and the occupation of the electronic states. X-ray absorption, along with other core level spectroscopies, demon-

strates a specificity that is unique to each element. Other types of core level spectroscopies are X-ray Photo-emmsission Spectroscopy (XPS), X-ray emmission (XES) and Auger electron spectroscopy (AES) among others. Figure 4.5 provides a schematic representation of the four listed above core level spectroscopies.

The terminology used in core level spectroscopies lacks uniformity. Traditionally, the principal quantum number is assigned a letter in alphabetical order, commencing with K. Within this principal quantum number, levels are sequentially numbered from higher to lower energies. In electronic structure calculations, core states are designated using orbital names. Here, the principal quantum number n receives a numerical identifier, while the angular quantum number l is represented by orbital labels such as s, p, d, and f, followed by alphabetical progression. For instance, absorption originating from a $1s$ core state is referred to as the K-edge. Table 4.1 shows various nomenclatures used for different core states.

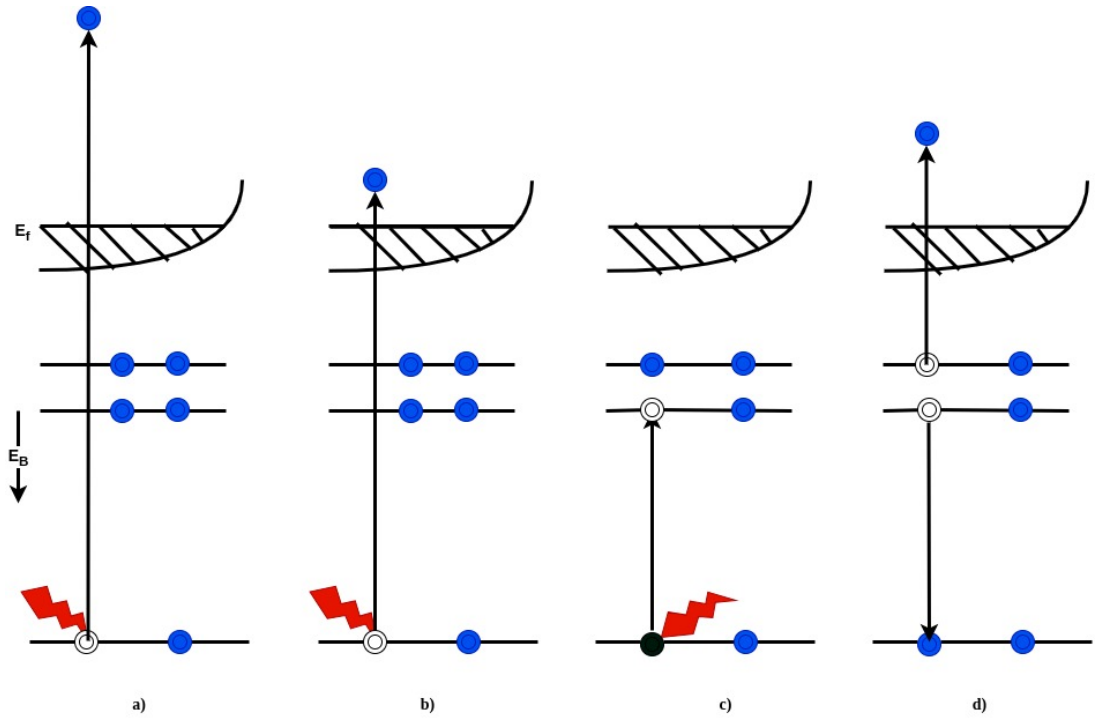

Figure 4.5: Schematic representation of different types of Core-level spectroscopies. (a) X-ray photoemission, (b) X-ray absorption, (c) X-ray emission and (d) Auger electron spectroscopy.

Core states	Spectroscopic name
$1s$,	K
$2s, 2p$	L_1, $L_{2,3}$
$3s, 3p, 3d$	$M_1, M_{2,3}, M_{4,5}$
$4s, 4p, 4d, 4f$	N_1, $N_{2,3}$, $N_{4,5}$, $N_{6,7}$

Table 4.1: Showing nomenclatures used in various X-ray spectroscopies.

X-rays were first identified by Wilhelm Konrad Röntgen in 1895 [62]. They possess wavelengths in the range of approximately 10 to 0.1 nanometers, classified into soft and hard X-ray categories. Soft X-rays are readily absorbed by air, whereas hard X-rays, with energies exceed-

ing 1 keV, can effectively penetrate both air and matter. Since their inception, X-rays have found extensive applications in both medical and natural sciences. This is primarily due to their capability to penetrate soft substances and their wavelengths, which closely match atomic dimensions. Consequently, X-rays have enabled the acquisition of diffraction patterns from well-ordered crystalline materials [63].

Other types of core-level spectroscopy, including ultraviolet photoelectron spectroscopy (UPS), and electron energy loss spectroscopy (EELS). Each of these techniques has its own advantages and disadvantages, and the choice of technique depends on the specific properties of the solid being studied and the information desired. XPS [64–66] is a widely used technique in core-level spectroscopy of solids. In this method, after excitation, the kinetic energy and angular distribution of the photoelectrons are measured to determine their binding energy E_b, which is related to the electronic structure of the solid. XPS is a surface sensitive technique, meaning it only probes the topmost layers of the solid, typically within a few nanometers of the surface. XPS is widely used to study the chemical composition and oxidation state of surfaces, as well as to determine the electronic structure of semiconductors and insulators. Furthermore electron energy loss Spectroscopy (EELS) [67, 68] is another technique used in core-level spectroscopy of solids. In this method, a beam of electrons is incident on a solid sample and the energy loss of the electrons is measured as they pass through the sample. EELS is a bulk-sensitive technique, meaning it can probe the electronic structure of the entire volume of the solid. EELS is particularly useful for studying the electronic structure of semiconductors and insulators.

4.2.1 X-ray Absorption Spectroscopy (XAS)

X-ray Absorption Spectroscopy involves irradiating a sample with X-rays and measuring the energy dependence of the X-ray absorption as it interacts with the sample [69–71]. X-ray Absorption Spectroscopy (XAS) provides insights various properties and local coordination environment of the atoms in materials, including electronic states, oxidation states, and coordination geometry. In most XAS experiments, the difference between the incoming laser pulse and the transmitted pulse is measured. The measured intensity is analogous to the Lambert-Beer law [72] and can be described as

$$I(E) = I_0(E)e^{(-\mu(E)\cdot d)} \tag{4.35}$$

where d is the thickness of the sample. As an illustration, Figure (4.6) shows the XAS spectra which show a 1s core state is excited with a sufficient X-ray energy to an empty unoccupied state. The XAS spectrum is closely related to the density of states (DOS). providing a detailed picture of the local electronic structure of the material. In general, XAS is often divided into two regions X-ray Absorption Near Edge Spectroscopy (XANES) and Extended X-ray Absorption Fine Structure (EXAFS), that we will discuss below.

XANES

X-ray absorption near edge Spectroscopy (XANES) [73–75] sometimes also referred to as Near-Edge X-ray absorption fine structure (NEXAFS) [76] gives a detailed information about the electronic state and coordination environment of metal atoms. In this technique, the energy

of the absorption edge at the K-edge increases as the electronic state rises [77]. In this kind of absorption, the atom get excited into an unoccupied states with one of the core electron leaving behind an empty hole (a so-called core hole)[1] while the excited electron occupies a level in the unoccupied state as depicted in Figure 4.6. From this procedure one can obtain an x-ray absorption spectrum.

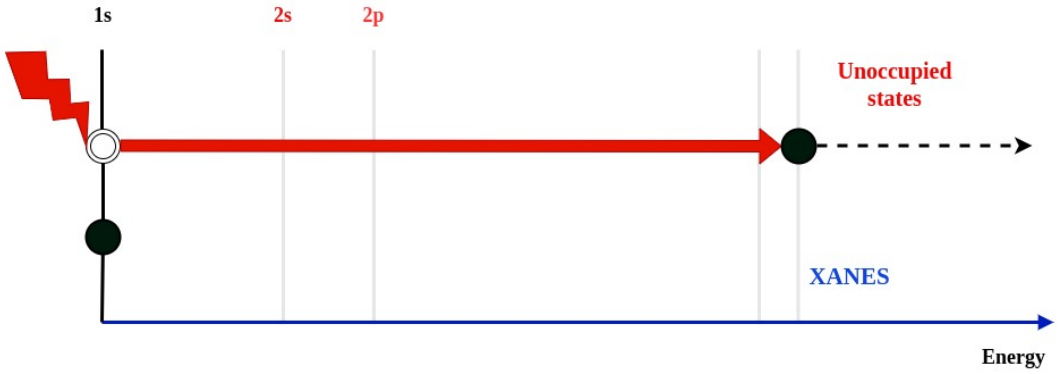

Figure 4.6: Schematic representation of x-ray absorption process in a solid or compound showing a 1s core state been excited for the core region to an empty state.

EXAFS

In Extended X-ray Absorption Fine Structure (EXAFS) [74, 78, 79], a sample is exposed to X-rays over a range of energies, typically spanning the X-ray absorption edge of a specific element of interest. The absorption of X-rays by the sample provides information about the local atomic environment around that element. As the X-rays are absorbed, electrons are excited from core energy levels to higher energy levels, resulting in the presence of absorption edges and fine structures in the X-ray absorption spectrum. The extended fine structure arises from the interaction between the absorbing atom and its neighboring atoms. These interactions result in constructive and destructive interferences of X-ray waves, leading to oscillations in the absorption spectrum as seen in the Figure 4.7.

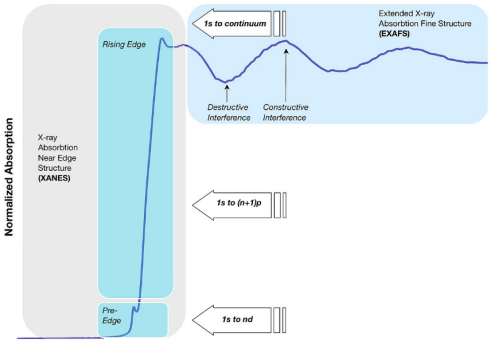

Figure 4.7: Schematic representation of an X-ray absorption spectrum depicting the two regions. Source M. Blank (2010) [2].

[1] A core-hole refers to an electron vacancy in the innermost electron shell (usually the K-shell) of an atom or a molecule. It is created when an electron from the core level is excited to a higher energy state or removed from the atom. It lives for $\approx 10^{-15}$ secs before it decays via radioactive or nonradioactive decay channels.

In the absorption process, any surplus energy is dissipated as kinetic energy related to motion in translation, which can also be observed through changes in the wavelength associated with the electron's wave-like behavior. The oscillations shown in the figure arise directly from the wave-like characteristics of the photoelectron, influenced by the velocity ν acquired due to the energy of the absorbed X-ray photon. This energy exceeds the binding or threshold energy of the electron. The kinetic energy of this photoelectron is given by the relation

$$(E - E_0) = \frac{1}{2} m_e v^2 \tag{4.36}$$

here E is the X-ray photon energy, E_0 is the ionization energy of the electrons, while m_e is the mass of the electron. Furthermore, one can express these modulations in terms of the photoelectron wave vector k, thus the expression is as follows

$$k = \frac{2\pi}{h}[2m_e(E - E_0)]^{1/2} \tag{4.37}$$

where the relation foe the wave vector $k = 2\pi/\lambda$ and lambda been the deBroglie wavelength ($\lambda = h/m_e v^2$) is used and h is the usual Planck's constant. By definition, the oscillatory part of the absorption spectrum can be described by the EXAFS fine-structure function $\chi(k)$, as

$$\chi(k) = \frac{\mu(k) - \mu_0(k)}{\mu_0(k)} \tag{4.38}$$

where $\mu(k)$ is the difference between the measured absorption coefficient and the absorption coefficient of the isolated atom and $\mu_0(k)$ is the pre-edge absorption. This is relation is as a result of the interference between the excited photoelectron wave and that of the backscattered wave from the neighbouring atoms.

In the context of a typical K-edge absorption, where a core electron of the 1s level undergoes excitation, the normalized EXAFS oscillations can be characterized by the following expression

$$\chi(\kappa) = \left(\frac{1}{\kappa}\right) \sum_j \left(N_j / R_j^2\right) \sinh(2\kappa R_j + \phi_j(\kappa)) \times A_j(\kappa) e^{\left(-2\sigma_j^2 \kappa^2\right)} e^{\left(-\frac{2R_j}{\lambda(\kappa)}\right)} \tag{4.39}$$

where $\lambda(k)$ is the mean free path, R_j is the distance between the central absorbing atom and other atoms in the j^{th} shell, N_j is the number of atoms in the j^{th} shell,the exponent is as a result of inelastic losses, $\phi_j(k)$ is the phase shift between the incident and backscattered wave, and $A_j(k)$ is the amplitude of the backscattered atom.

4.3 Properties of Solids

This section establishes the fundamental properties of solids, crucial for their behaviour, particularly under the influence of external perturbations. Since this thesis focuses on solid-state materials, knowing these basic characteristics is essential for understanding their diverse properties, including electronic (bandstructure, density of state), optical (absorption), and mechanical (phonon dispersion).

The distinctive trait of most types of solids is the orderly alignment of their atoms, resulting in a crystalline structure. Electrons within such a crystal experience a periodic attractive potential, which arises from the lattice ions as well as a repulsive interaction interaction with the other electrons. The description of the behavior of electrons in a periodic crystal lattice was first formulated by Felix Bloch in 1929 in his article [80] and is still the cornerstone of our understanding of electrons in solids.

4.3.1 Bloch's theorem and Bloch Functions

The Bloch theorem [80] provides a powerful framework to describe the electronic structure and properties of solids, paving the way for a deeper understanding of various phenomena such as electrical conductivity, magnetism, and optical properties. Bloch states $|n, k\rangle$ are defined by the quantum number n called the band index, k is the pseudo-momentum:

$$\psi_{nk}(\mathbf{r}) = \frac{1}{\sqrt{\Omega}} u_{nk}(\mathbf{r}) e^{i\mathbf{k}\cdot\mathbf{r}}. \tag{4.40}$$

where u_{nk} are the Bloch states and are cell periodic,Ω is the volume of the unit cell. The plane wave $e^{ik\cdot\mathbf{r}}$ is modulated by the periodicity of the lattice. The wavefunction can be expressed in reciprocal space as

$$\psi_{nk}(\mathbf{r}) = \frac{1}{\sqrt{N_k \Omega}} u_{nk}(\mathbf{G}) e^{i(\mathbf{k}+\mathbf{G})\cdot\mathbf{r}} \tag{4.41}$$

where

$$u_{nk}(\mathbf{G}) = \int_{\Omega} d^3 r e^{-i\mathbf{G}\mathbf{r}} u_{nk}(\mathbf{r}) \tag{4.42}$$

here also $u_{nk}(\mathbf{G})$ are still cell periodic, as the $e^{-i\mathbf{G}\mathbf{r}}$ must be periodic in the unit cell and N_k is the number of k-points considered. k-points, short for wave vector points, are a key concept in the study of crystalline materials. They are used to discretize the Brillouin zone, which is the first Brillouin zone in the reciprocal lattice of a crystal. The $\mathbf{G}$-vectors are the discrete reciprocal lattice of the crystal.

4.3.2 Reciprocal lattice

The reciprocal lattice is discussed due to its relevance in calculating the electronic band structure, which is introduced in the next subsection. By definition, the reciprocal lattice is a lattice in k-space which is related to the lattice of a crystal in real space. Given a crystal in real space is defined by the primitive lattice vectors $\mathbf{a}_1$, $\mathbf{a}_2$ and $\mathbf{a}_3$, the reciprocal lattice vectors are $\mathbf{b}_1$, $\mathbf{b}_2$ and $\mathbf{b}_3$ are defined as

$$\boldsymbol{b}_i = 2\pi \frac{\boldsymbol{a}_j \times \boldsymbol{a}_k}{\boldsymbol{a}_i \cdot (\boldsymbol{a}_j \times \boldsymbol{a}_k)} \quad \text{and} \quad \boldsymbol{a}_i = 2\pi \frac{\boldsymbol{b}_j \times \boldsymbol{b}_k}{\boldsymbol{b}_i \cdot (\boldsymbol{b}_j \times \boldsymbol{b}_k)}. \tag{4.43}$$

where

$$\boldsymbol{a}_i \cdot \boldsymbol{b}_j = 2\pi\delta_{ij}, \quad i, j = 1, 2, 3 \tag{4.44}$$

The reciprocal lattice vectors generate the reciprocal lattice, which consists of all points $\mathbf{G}$ that

can be expressed as a linear combinations of $\mathbf{b}_1$, $\mathbf{b}_2$ and $\mathbf{b}_3$

$$\mathbf{G} = h\mathbf{b}_1 + k\mathbf{b}_2 + l\mathbf{b}_3 \tag{4.45}$$

where h, k and l are all integers.

4.3.3 Energy Dispersion of electrons in Solids

In solid state physics, the study of the electronic bandstructure is of utmost important. The bandstructure of solids describes the range of energies that electrons can have within a solid material. It can be seen as a map of allowed and forbidden energy levels for the electrons in a crystal [5, 81]. Many optical, electrical, and even some magnetic properties of crystals can be explained in terms of their band structure. One particular quantity relevant to the band structure is the location of the Fermi energy. If the Fermi energy is located within the band gap E_g, the material is insulating (or semiconducting); otherwise, it is metallic [82]as illustrated in the Figure 4.8 below. Insulators have a very large bandgap, such that at room temperature, electrons cannot be excited across the gap. Essentially, free carrier absorption and intraband transitions occur only at high photon energies. In the case of semiconductors, the bandgap is small enough for excitation to occur. Hence, free carrier absorption can happen at room temperature due to excitation or doping. Furthermore, interband transitions can occur in the infrared or visible spectrum. In the case of metals, there is no bandgap, and interband transitions can easily occur while free carrier effects remain significant.

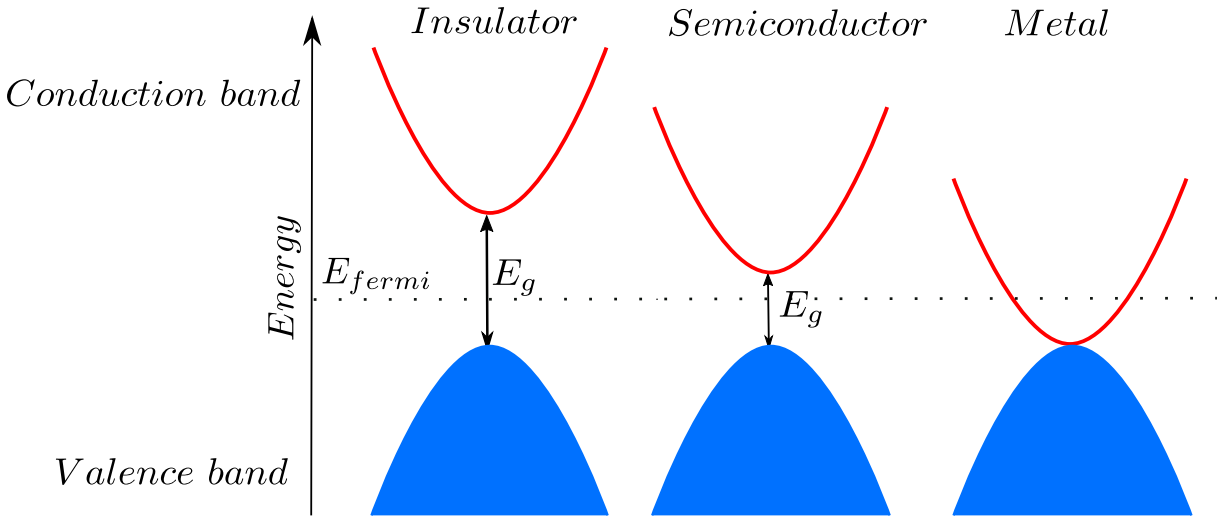

Figure 4.8: An illustration of the simplified model for classifying solids into Insulators (left), Semiconductors (middle) and metals, based on the position of the Fermi level. Figure adapted from [3].

Since we are dealing with a periodic potential $V(\vec{r}) = V(\vec{r} + \vec{R_n})$ that is weak enough for the electrons in the system to behave as if they are free electrons, the effect of this potential can be

handled using perturbation theory (c.f Appendix A). Within this weak potential limit, one can solve the Schrödinger equation (SE)

$$H\psi = E\psi \quad \text{with the Hamiltonian operator} \quad H = -\frac{\hbar^2}{2m}\nabla^2 + V(\vec{r}). \tag{4.46}$$

Applying time-independent perturbation theory (c.f Appendix A), we can express the energy E as

$$E(\vec{k}) = E^{(0)}(\vec{k}) + E^{(1)}(\vec{k}) + E^{(2)}(\vec{k}) + \dots \tag{4.47}$$

by taking the unperturbed solution such that $V(\vec{r}) = 0$ and $E^{(0)}(\vec{k})$ is the plane wave solution

$$E^{(0)}(\vec{k}) = \frac{\hbar^2 k^2}{2m} \tag{4.48}$$

The eigen functions of the Hamiltonian are the plane wave

$$\psi^{(0)}_{\vec{k}}(\vec{r}) = \frac{1}{\sqrt{\Omega}} e^{i\vec{k}\cdot\vec{r}} \tag{4.49}$$

where Ω is the volume of the unit cell. A plot of the electron energies described in Eq. (4.48) as a function of k is known as the *electronic band structure*. Figure 4.9 shows the bandstructure of a free electron in a one-dimensional lattice with a lattice constant a in an extended zone scheme. In most some cases, bandstructures are plotted in a reduced zone scheme (i.e $\frac{-\pi}{a} \leq 0 \leq \frac{\pi}{a}$).

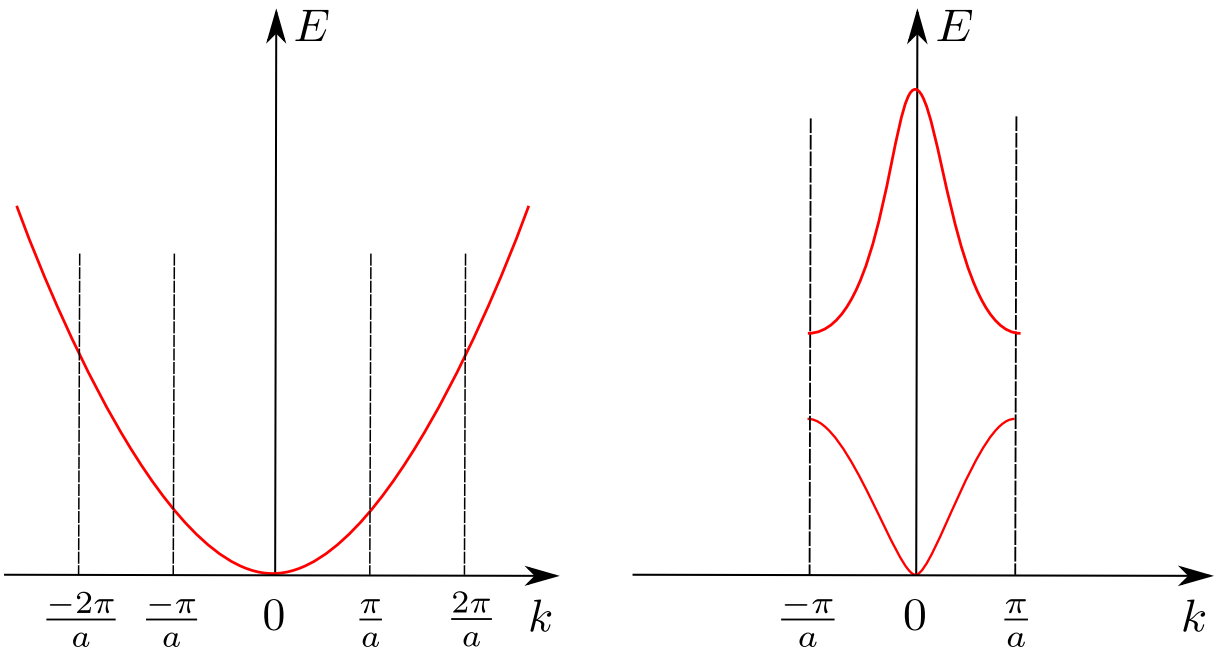

Figure 4.9: Example of the band structure of a free particle shown in the extended Brillouin zone scheme for a single band with the lowest energy. Figures reproduced from [4, 5].

From the perturbation theory, one can express the first order correction to the energy $E^{(1)}(\vec{k})$ as the diagonal matrix element

$$E^{(1)}(\vec{k}) = \left\langle \psi^{(0)}_{\vec{k}} | V(\vec{r}) | \psi^{(0)}_{\vec{k}} \right\rangle = \frac{1}{\Omega} \int_{\Omega} e^{-i\vec{k}\cdot\vec{r}} V(\vec{r}) e^{i\vec{k}\cdot\vec{r}} d^3r \tag{4.50}$$

The most interesting terms arise from the second order correction to the energy and are given by

$$E^{(2)}(\vec{k}) = \sum_{\vec{k'}}{}' \frac{\left|\left\langle \overrightarrow{k'}|V(\vec{r})|\vec{k}\right\rangle\right|^2}{E^{(0)}(\vec{k}) - E^{(0)}(\overrightarrow{k'})} \tag{4.51}$$

with the prime on the summation indicating that $\vec{k'} \neq \vec{k}$. By combing the first order correction to the energy and its FT with the second-order correction and its corresponding FT, one can give a proper description of the band structure in the reduced zone scheme [2].

4.3.4 Optical Transitions

In solids with appreciable bandgap (such as semiconductors or insulators), when interacting with light, the photon energy can increase and become comparable to the energy of the bandgap, enabling a conduction process to occur. A photon therefore needs to have a minimum energy to elevate an electron in a semiconductor or insulator from an occupied state in the valence band to an empty state in the conduction band, this kind of process, also known as **interband transition** presented schematically by the picture in figure 4.10, is the fundamental optical excitation process in these materials. This kind of transitions can either be **direct** [3] or an **indirect transition**. [4], where the additional momentum is supplied by the emission (or absorption) of another excitation process or quasiparticle in the solids, such as a phonon. The strength of transition depends on the interaction strength between the valence and conduction bands, which can be quantified by the magnitude of the momentum matrix elements connecting the valence band state v and the conduction band state c, the momentum matrix elements can be expressed as $\langle v|\vec{p}|c\rangle$. The whole process can be described by "Fermi's Golden rule" within time-dependent perturbation theory.

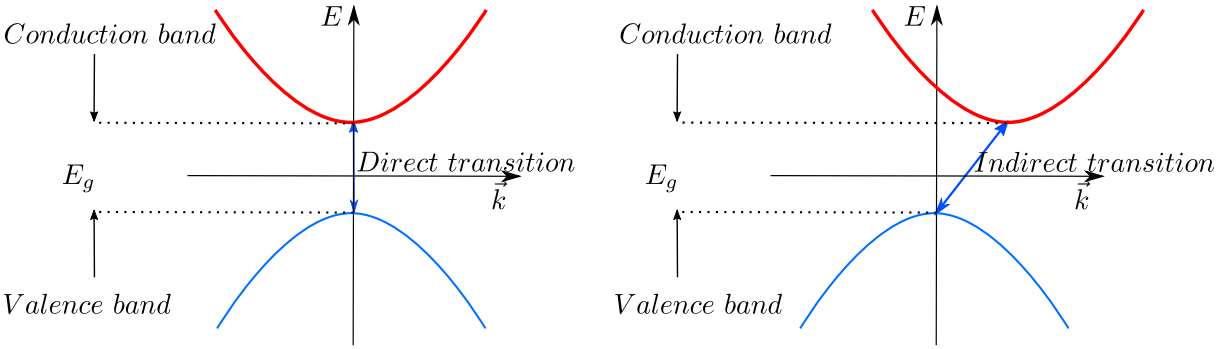

Figure 4.10: Representation of the semiconductor band structure illustrating a direct transition (depicted in the left plot) and an indirect transition (depicted in the right plot). In the direct transition, electrons move from the valence band to the conduction band without altering the crystal momentum (left), whereas in the indirect transition, the electron is transferred to the conduction band with a change in crystal momentum attributed to a phonon vector $\vec{q}$ (right).

[2] A rigorous proof of the quantities and a general description of the different regimes can be found in the lecture notes of M. S. Dresselhaus 6.732

[3] In direct transition, the crystal momentum $\vec{k}$ for both valence and conduction bands lies on the same symmetry point: $E_v(\vec{k}) \rightarrow E_c(\vec{k})$

[4] In indirect transition, a phonon is involved because the wave vectors $\vec{k}$ differs for both valence and conduction band by a phonon vector $\vec{q}$

4.3.5 Fermi Golden Rule

Thanks to the Fermi Golden Rule (FGR) [83], we can estimate the transition rate between quantum states due to the time dependent perturbation theory c.f Appendix A. The FGR will be used heavily in subsequent chapters to understand the optical properties solids. The FGR is related to the *transition probability per unit time* [84, 85] which gives us the transition probability as proportional to the time in which the perturbation acts. In c.f Appendix A, the Golden rule is derived in Eq. (A.19) in which we considered the system been exposed to the applied perturbation for a long period of time so that we can make a precise measurement of its state according to the Heisenberg uncertainty principle [86]. The uncertainty principle in energy reads

$$\Delta E \Delta t \approx h \tag{4.52}$$

and while the perturbation is applied, the uncertainty in energy becomes

$$\Delta E \approx \frac{h}{t}. \tag{4.53}$$

Now, the transition probability per unit time W_m for transition to a state m is given by

$$W_m = \frac{1}{t} \sum_{m' \approx m} |a_{m'}^{(1)}(t)|^2 \tag{4.54}$$

here, the calculation of the transition probability requires the summation to be carried out over a range of energy states consistent with the uncertainty principle in frequency; $\Delta_{cm'} \approx 2\pi/t$.

From c.f Appendix A, the relationship for the quantity $|a_{m'}^{(1)}(t)|$ is derived and shown in Eq.(A.22),

$$\left|a_m^{(1)}(t)\right|^2 = \left(\frac{|\langle m\,|\mathcal{H}'|\,\ell\rangle|^2}{\hbar^2}\right)\left(\frac{4\sin^2(\omega_{m\ell}t/2)}{\omega_{m\ell}^2}\right) \tag{4.55}$$

here $\mathcal{H}'$ is the perturbation, which is defined in next subsection and its connection with the momentum operator $\mathbf{p}$ is also shown. Upon substituting the above equation into Eq.(4.54) and replacing the summation with an integral over a small frequency range weighted by the density of states $\rho(E_m)$ one obtain

$$W_m = \frac{1}{\hbar^2 t}\int |4\mathcal{H}'_{m'\ell}|^2 \left(\frac{\sin^2(\omega_{m'\ell}t/2)}{\omega_{m'\ell}^2}\right)\rho(E_{m'})\,dE_{m'} \tag{4.56}$$

where $\mathcal{H}'_{m'\ell}$ is the matrix element $\langle m'|\mathcal{H}'|\ell\rangle$. But, the function $[sin^2(\omega' t/2)/\omega'^2]$ is oscillating continuously due to the nature of *sine* function, therefore one can integrate Eq.(4.56) over it with $dE = \hbar d\omega'$. The integral becomes

$$W_m \simeq \left(\frac{4\,|\mathcal{H}'_{m\ell}|^2\,\rho(E_m)}{t\hbar^2}\right)\int\left(\frac{\sin^2\frac{\omega' t}{2}}{\omega'^2}\right)\hbar d\omega' \tag{4.57}$$

by using the identity

$$\int_{-\infty}^{\infty}(sin^2(y)/y^2)dy = \pi \tag{4.58}$$

Eq.(4.57) becomes

$$W_m \cong (2\pi/\hbar)\left|\mathcal{H}'_{m\ell}\right|^2 \rho(E_m) \tag{4.59}$$

In solid-state physics, many important transitions involve a continuum of initial states and a continuum of final states [87]. Therefore, in this case the Fermi Golden Rule must be interpreted in terms of a joint density of states, whereby the initial and final states are separated by the photon energy $\hbar\omega$ inducing the transition. The probability per unit time that the photon energy $\hbar\omega$ is absorbed at a certain $\vec{k}$ point is thus given by

$$\boxed{W_{\vec{k}} \cong \frac{2\pi}{\hbar}\left|\langle v\left|\mathcal{H}'\right|c\rangle\right|^2 \delta\left[E_c(\vec{k}) - E_v(\vec{k}) - \hbar\omega\right]} \tag{4.60}$$

where $\mathcal{H}'$ is the matrix element for the electromagnetic perturbation between the valence v and conduction c band Bloch states at a certain wavevector k, the $\delta-$function $\delta[E_c - E_v - \hbar\omega]$ is for conservation of energy. This important result means that electrons in the valence band absorbs a photon energy $\hbar\omega$ and gets excited into the conduction band.

4.3.6 Hamiltonian in an Electromagnetic Field

We consider an unperturbed one-body Hamiltonian for a solid subjected to an electric field. Later, we will show how this Hamiltonian is used in conjunction with the Time Dependent Kohn-Sham (TDKS) equations to write down the equation of motion for solids. The unperturbed Hamiltonian can be described as

$$\mathcal{H}_0 = \frac{\boldsymbol{p}^2}{2m} + V(\boldsymbol{r}) \tag{4.61}$$

the electron magnetic field can be introduced in a form of vector potential $\boldsymbol{A}(\boldsymbol{r},t)$ and a scalar potential $\Phi(\boldsymbol{r},t)$. Using the *Coulomb gauge* [88], the vector potential and scalar potentials takes the following properties

$$\Phi = 0 \text{ and } \vec{\nabla}\cdot\boldsymbol{A} = 0 \tag{4.62}$$

In this gauge, we can express the electric and magnetic fields $(\boldsymbol{E},\boldsymbol{B})$ as

$$\boldsymbol{E} = -\frac{1}{c}\frac{\partial \boldsymbol{A}}{\partial t} \quad \text{and} \quad \boldsymbol{B} = \vec{\nabla}\times\boldsymbol{A} \tag{4.63}$$

To obtain the quantum mechanical Hamiltonian which will describe the motion of charge (-e) in an external electromagnetic field, we simply replace the electron momentum in Eq. (4.61) $\boldsymbol{p}$ with $\boldsymbol{p} + (e\boldsymbol{A}/c)$. The equation becomes

$$\mathcal{H} = \frac{1}{2m}[\boldsymbol{p} + (e\boldsymbol{A}/c)]^2 + V(\boldsymbol{r}) \tag{4.64}$$

here, the term $[\boldsymbol{p} + (e\boldsymbol{A}/c)]^2$ can be expanded as

$$\frac{1}{2m}\left(\boldsymbol{p} + \frac{e\boldsymbol{A}}{c}\right)^2 = \frac{p^2}{2m} + \frac{e}{2mc}\boldsymbol{A}\cdot\boldsymbol{p} + \frac{e}{2mc}\boldsymbol{p}\cdot\boldsymbol{A} + \frac{e^2A^2}{2mc^2} \tag{4.65}$$

Therefore, the equation becomes

$$\mathcal{H} = \frac{\boldsymbol{p}^2}{2m} + V(\boldsymbol{r}) + \frac{e}{2mc}\boldsymbol{A}\cdot\boldsymbol{p} + \frac{e}{2mc}\boldsymbol{p}\cdot\boldsymbol{A} + \frac{e^2A^2}{2mc^2} \tag{4.66}$$

Since our interest is to calculate linear optical properties, we can neglect the high order terms, i.e the last term of the above equation and using the conditions of the gauge invariance, the equation reduces to

$$\mathcal{H} = \frac{\boldsymbol{p}^2}{2m} + \frac{e}{mc}\boldsymbol{A}\cdot\boldsymbol{p} + V(\boldsymbol{r}) \tag{4.67}$$

From the above equation. one can deduce the one-electron Hamiltonian without optical fields as

$$\mathcal{H}_0 = \frac{\boldsymbol{p}^2}{2m} + V(\boldsymbol{r}) \tag{4.68}$$

and the perturbing Hamiltonian as;

$$\mathcal{H}' = \frac{e}{mc}\boldsymbol{A}\cdot\boldsymbol{p} \tag{4.69}$$

The terms in the above equation describes the interaction between the optical fields and a Bloch electron. To evaluate the optical properties of a solid, various approaches can be explored. Assuming that the vector potential $\mathbf{A}$ is sufficiently weak, we can apply FGR to calculate the transition probability per unit volume, R for an electron transitioning from a valence band state $|v\rangle$ to a conduction band state $|c\rangle$. This requires evaluating the matrix element $|\langle c|\mathcal{H}|v\rangle|^2$.

$$|\langle v|\mathcal{H}'|c\rangle|^2 = (e/mc)^2|\langle v|A\cdot\mathbf{p}|c\rangle|^2 \tag{4.70}$$

The Bloch functions for the electrons in the valence and conduction band states, as well as the vector potential, can be expressed respectively as

$$\begin{aligned} |\mathrm{c}\rangle &= u_{\mathrm{c},\boldsymbol{k}_\mathrm{c}}(\boldsymbol{r})e^{[\mathrm{i}(\boldsymbol{k}_\mathrm{c}\cdot\boldsymbol{r})]} \\ |\mathrm{v}\rangle &= u_{\mathrm{v},\boldsymbol{k}_\mathrm{v}}(\boldsymbol{r})e^{[\mathrm{i}(\boldsymbol{k}_\mathrm{v}\cdot\boldsymbol{r})]} \\ A &= -\frac{E}{2q}\, e^{[\mathrm{i}(\boldsymbol{q}\cdot\boldsymbol{r})-\omega t]+\mathrm{c.c}} \end{aligned} \tag{4.71}$$

Using these quantities, the matrix element on the right-hand side of Eq. (4.70) can be evaluated and integrated over space. After a little of algebraic manipulation and applying the electric dipole approximation [4], the matrix element simplifies to

$$|\langle v|\mathcal{H}'|c\rangle|^2 = (e/mc)^2|A|^2|P_{vc}|^2 \tag{4.72}$$

where P_{vc} is the momentum matrix element $\langle v|\mathbf{p}|c\rangle$.

4.4 Outline

The thesis is structured in the following way:

In this introductory Chapter 4, the foundational aspects of the research problem were introduced, that is ATAS. This chapter not only provides an introduction to theory underpinning ATAS but

also discusses atoms and system responses in the presence of external perturbations. Similarly, this chapter covers the basic properties of solids as well as the concept of light-matter interactions in solids. A more detailed discussion of light-matter interactions is provided in the subsequent chapters.

In Chapter 5 of this thesis, the essential theoretical methods are discussed. It commences with a description of the electronic structure problem and shows the significance of the Born-Oppenheimer approximation. This approximation serves as a pivotal tool, facilitating the differentiation between the electronic and nuclear degrees of freedom. Following this, the description of the most important methods involved in solving the electronic structure problem, which includes the Hartree Fock and the well-established DFT and its necessary approximations. Furthermore, the fundamentals of TDDFT are introduced, and its necessary approximation.

In Chapter 6, the theoretical foundation laid out in Chapter 5 were extended. The essential Hamiltonian for conducting real-time TDDFT calculations is derived and discussed. The approximations necessary for solving the TDKS on a real space grid are outlined. Furthermore, a detailed, step-by-step methodology demonstrating the calculation of optical conductivity σ is provided.

In Chapter 7, results are presented where TDDFT was used to calculate the equilibrium optical conductivity $\sigma(\omega)$ of monolayer hBN at the Boron K-edge. The calculations were performed using the LDA and DFT+U functionals and compared with existing literature. However, our results did not accurately reproduce the distinct excitonic peak observed at the Boron K-edge. To address this, we extended the investigation by calculating the conductivity using a supercell with a core-hole. Additionally, we explored the equilibrium conductivity variations by changing the polarization of the probe field. This comprehensive analysis provides insights into the complexities of the material's optical properties under different computational conditions.

In Chapter 8, we present the TAS calculations using various pump pulse configurations. Linear, colinear, circular and bicircular pump pulses are discussed, along with the origins of the nonlinear electron dynamics around the bandgap of monolayer hBN. Following this, we provide a theoretical analysis of the sub-bandgap features using the parabolic two-band model.

In Chapter 9, the results of the vibrational spectroscopy are presented. Using DFPT, we investigated the changes in the phonon dispersion relations of monolayer, bilayer and bulk MoS_2 due to photo-doping. Additionally, we examined the effects of photodoping on the shear and interlayer breathing modes across various layers. Finally, we calculated the Infrared spectra for these layers.

We conclude in Chapter 10 with a summary of the findings presented in the preceding chapters. Additionally, we provide a general discussion on future research directions, including the calculation of core and valence excitons and the simulation of X-TAS. Moreover, we discuss potential experiments at CNR Milano aimed at investigating the shear and interlayer breathing modes, as well as the corresponding phonon frequency shifts in various layers.

This page was intentionally left blank.

5 Theoretical Methods

5.1 Introduction

In this chapter, the theoretical background to the work done is presented, starting with an overview of DFT and its necessary approximations, followed by an introduction to TDDFT. This is just a short review of the well established theory. It is important to note that this review will not provide a detailed explanation of concepts that are thoroughly covered in most DFT and TDDFT textbooks. For an elaborate and detailed explanations, one can refer to the following textbooks and articles [89–97] and also the references that can be found in the context of this chapter. In the following chapter, it is important to note that Atomic Units (a.u) will be used unless stated otherwise. In particular $\hbar = m_e = e = 4\pi\epsilon_o = 1$.

5.2 Many Body Hamiltonian

Quantum mechanical systems are typically described using the non-relativistic many body Hamiltonian, which constitutes the fundamental characterization of such systems. The basic non-relativistic many body Hamiltonian is defined as

$$\hat{H} = \hat{T}_{\mathrm{I}} + \hat{T}_e + \hat{V}_{\mathrm{ii}} + \hat{V}_{\mathrm{ee}} + \hat{V}_{\mathrm{ie}} + \hat{V}_{\mathrm{ext}} \tag{5.1}$$

where $\hat{V}_{\mathrm{ext}}$ describes the external potential and the remaining terms are given by

$$\begin{aligned}
\hat{T}_I &= -\sum_l \frac{\nabla_l^2}{2M_l}, \\
\hat{V}_{ii} &= \frac{1}{2}\sum_{IJ} \frac{Z_l Z_J}{\left|\hat{\mathbf{R}}_l - \hat{\mathbf{R}}_J\right|} \\
\hat{T}_e &= -\sum_i \frac{\nabla_i^2}{2m} \\
\hat{V}_{ee} &= \frac{1}{2}\sum_{ij} \frac{1}{|\hat{\mathbf{r}}_i - \hat{\mathbf{r}}_j|} \\
\hat{V}_{el} &= \sum_{il} \frac{Z_l}{\left|\hat{\mathbf{r}}_i - \hat{\mathbf{R}}_l\right|}
\end{aligned} \tag{5.2}$$

where $\mathbf{r}_i$ describes the positions of the electrons, m is the electronic mass, $\hat{\mathbf{R}}_\mathbf{I}$, $\hat{\mathbf{M}}_\mathbf{I}$ and Z_I are the positions, masses and charges of the nuclei respectively. The groundstate properties of the material described by his Hamiltonian in Eq. (5.1) can be obtained by solving the corresponding Time-Independent Schrödinger equation (TISE)

$$H\Psi = E\Psi. \tag{5.3}$$

An analytical solutions of Eq. (5.3) can be found only for few limited cases. In practice one needs to solve the equation using various means of approximations. Even to solve the equation using computational methods is generally unfeasible as it is already computationally challenging to solve Eq. (5.3) for systems with more than two or three degrees of freedom. One of the commonly used practical approximations is the Born-Oppenheimer Approximation (BOA) [98–103].

5.3 Born-Oppenheimer Approximation

In 1927, the BOA was established by M. Born and R. Oppenheimer to simplify the difficulties in solving Eq. (5.3). It assumes that, due to the difference in mass between atoms and electrons, atomic and electronic motion happen on different time-scales and therefore, the general SE Eq. (5.3) can be separated into nuclear and electronic parts. Briefly, the solution of the equation is derived by starting with the definition of the electronic Hamiltonian as follows

$$\hat{H}_e = \hat{T}_e + \hat{V}_{\text{ii}} + \hat{V}_{\text{ee}} + \hat{V}_{\text{ie}} \tag{5.4}$$

Then, by substituting Eq. (5.4) into Eq. (5.3), we have a formal solution for the electronic part which is

$$\hat{H}_e \Phi_k(\mathbf{r}, \mathbf{R}) = E_k \Phi_k(\mathbf{r}, \mathbf{R}) \tag{5.5}$$

Here the $\mathbf{R}$ are *parameters*, and not operators, for the electronic wavefunction. The eigenfunctions of $\hat{H}_e$, $\{\Phi_k\}$ represents a complete basis sets in the electronic Hilbert space [104] and can used the to expand the eigenfunctions of the electronic Hamiltonian $\hat{H}_e$ denoted by Ψ_ν as,

$$\Psi_\nu = \sum_k \Phi_k(\mathbf{r}, \mathbf{R}) \chi_k(\mathbf{R}) \tag{5.6}$$

After substituting Eq. (5.6) into Eq. (5.3) and multiplying by $\Phi_l^*(\mathbf{r}, \mathbf{R})$ from left and integrating over the electronic coordinates $\mathbf{r}$. The electronic Hamiltonian H_e is a diagonal and is given by

$$\langle \Phi_{k'}(\mathbf{r}, \mathbf{R}) \, | H_{\text{e}} | \, \Phi_k(\mathbf{r}, \mathbf{R}) \rangle_{(\text{r})} = \delta_{k'k} E_k(\mathbf{R}) \tag{5.7}$$

and the electronic wave functions are orthogonal and given by

$$\langle \Phi_{k'}(\mathbf{r}, \text{R}) \mid \Phi_k(\mathbf{r}, \mathbf{R}) \rangle_{(\mathbf{r})} = \delta_{k'k} \tag{5.8}$$

This then yields to a set of coupled eigenvalue equations for the nuclear wave functions [105] and this takes the form of

$$[T_{\mathrm{n}} + E_{k'}(\mathbf{R}) - E]\,\chi_{k'}(\mathbf{R}) = \sum_{k} [\mathbb{F}_{\mathrm{n}}]_{k'k}\,\chi_k(\mathbf{R}) \tag{5.9}$$

which coupled to different electronic states k', k. The coupling between different electronic states occurs through the nuclear kinetic energy operator T_n and the coupling term is defined as

$$[\mathbb{F}_{\mathrm{n}}]_{k'k}\,(\mathbf{R}) = \langle \phi_{k'}(\mathbf{r};\mathbf{R})\,|T_{\mathrm{n}}|\,\phi_k(\mathbf{r};\mathbf{R})\rangle_{(\mathrm{r})} - T_{\mathrm{n}}\delta_{k'k} \tag{5.10}$$

The elimination of this non-adiabatic electronic coupling term is the core of the BOA, which leads to the nuclear SE for electronic states k'

$$[T_{\mathrm{n}} + E_{k'}(\mathbf{R})]\,\chi_{k'}(\mathbf{R}) = E\chi_{k'}(\mathbf{R}) \tag{5.11}$$

Similarly, the non adiabatic coupling terms are given by

$$[\mathbb{F}_{\mathrm{n}}]_{k'k}\,(\mathbf{R}) = -\sum_{A} \frac{\hbar^2}{2M_A}\left[2\,\langle \phi_{k'} \mid (\nabla_A \phi_k)\rangle_{(\mathrm{r})} \cdot \nabla_A + \left\langle \phi_{k'} \mid \left(\nabla_A^2 \phi_k\right)\right\rangle_{(\mathrm{r})}\right]. \tag{5.12}$$

The coupling terms are small due to the fact that the nuclear mass is very large. We can express the first term of the above equation as

$$\langle \phi_{k'} \mid (\nabla_A \phi_k)\rangle_{(\mathrm{r})} = \frac{\langle \phi_{k'}\,|[\boldsymbol{\nabla}_A, H_{\mathrm{e}}]|\,\phi_k\rangle_{(\mathrm{r})}}{E_k(\mathbf{R}) - E_{k'}(\mathbf{R})} \tag{5.13}$$

which shows that the coupling term Eq. (5.12) is small only when the electronic energies $E_k(\mathbf{R})$ and $E_{k'}(\mathbf{R})$ are far from each other. If this condition is fulfilled, then the BOA holds, else for certain geometries $\mathbf{R}$ the electronic energies $E_k(\mathbf{R})$ and $E_{k'}(\mathbf{R})$ may be degenerate and the approximation fails.

Solving Equations 5.3 has been explored by other methods which are more accurate, practical and efficient and is an area of active research within the community. The next sections in this chapter will discuss more on these techniques that have been employed to solve the electronic problem.

5.4 Methods to Solve Electronic Problems

In this section we start by highlighting numerous techniques and schemes that have been employed to solve the electronic structure problem. If we cannot find the analytical solution to the SE, a well known approach is the variational principle that allows to approximate the energy of the ground state of the system. The methodologies described in here are mainly within the scope of the variational principle [106–108]. The variational principle states that given a Hamiltonian, in this case an electronic Hamiltonian $\hat{H}_e$, the lowest energy eigenstate (i.e the ground state energy) E_0, is always less than or equal to the expectation value of $\hat{H}_e$ with a normalized trial wavefunction. That is

$$E_0 \leq \langle\psi|H|\psi\rangle. \tag{5.14}$$

Hence, by varying the normalized wavefunction until the expectation value of $\hat{H}_e$ is minimized, one can obtain approximations to the eigenfunctions and the ground state energy. Therefore, the variational principle formally reads

$$E_0 = \min_{\Phi} \left\langle \psi \left| \hat{H}_e \right| \psi \right\rangle \tag{5.15}$$

Most of the modern day methods and theories for calculating the lowest energy eigenstate are formally adapted from this principle.

5.5 Hatree Fock Method

From the above discussion for the BOA, it is still not possible to calculate the orbitals and energies exactly for anything but the most of simplest systems. For more complicated systems, one needs to resort to so higher approximations. One of the oldest methods, which lays the foundation for other methods and more pragmatic and advanced theories, is the Hartree-Fock (HF) method, which was established in 1928 [109–111]. The HF method gives an approximate solution to the TISE Eq. (5.3) using the Eq. (5.4) obtained from the aforementioned BOA.

The HF method is a type of wave function-based method used to describe the electronic structure of atoms, molecules, and solids. It is based on the idea that the total wave function of a many-electron system might be written as a product of single-electron wave functions, known as orbitals. In the Hartree scheme, one thus may make an ansatz for the eigenfunction as a product of orbitals

$$\Phi = \chi_1(\mathbf{X}_1)\chi_2(\mathbf{X}_1)...\chi_n(\mathbf{X}_n) \tag{5.16}$$

where the parametric dependence on $\mathbf{R}$ has been dropped for simplicity. $\mathbf{X}_j = (\mathbf{r}_j, m_{s,k})$ are the spatial and spin coordinates of the electron j, and χ_j represents a single-particle wave function, or spin-orbital. Since H_e does not depend explicitly on the spin variables, the spin-orbitals can be expressed as a product of a spin function, σ, and a spatial orbital, ψ_j, i.e.,

$$\chi_j\left(\mathbf{X}_j\right) = \psi_j\left(\mathbf{r}_j\right)\sigma\left(m_{s,k}\right) \tag{5.17}$$

The resulting energy expression, obtained by introducing Eq. (5.17) and (5.16) into Eq. (5.5) and integrating out the spin variables, reads as follows

$$\begin{aligned} E_{\mathrm{HA}} = & \sum_i^n \left[-\frac{1}{2}\int d\mathbf{r}\psi_i^*(\mathbf{r})\vec{\nabla}_i^2\psi_i(\mathbf{r})\right] \\ & + \sum_i^n \left[-\sum_I^N Z_I \int d\mathbf{r}\psi_i^*(\mathbf{r})\frac{1}{|\mathbf{r}-\mathbf{R}_I|}\psi_i(\mathbf{r})\right] \\ & + \sum_i^n \left[\frac{1}{2}\sum_{j\neq i}^n \iint d\mathbf{r}d\mathbf{r}\psi_i^*(\mathbf{r})\psi_j^*(\overrightarrow{r\prime})\frac{1}{|\mathbf{r}-\overrightarrow{r\prime}|}\psi_i(\mathbf{r})\psi_j(\overrightarrow{r\prime})\right], \end{aligned} \tag{5.18}$$

The three terms on the right-hand side of the equation correspond to the kinetic energy, electron-

nucleus electrostatic interaction energy, and electron-electron electrostatic interaction energy, respectively. The final term represents an effective single-particle potential energy that arises from the collective electrostatic interaction of each electron with the other electrons in the system. As this interaction is defined by the orbitals, which are the sought-after solution, Eq. (5.18) must be solved self-consistently. However, the approach in this form, the Hartree ansatz, suffers from the the fact that the wave function ansatz does not satisfy the Pauli exclusion principle [112, 113].

Slater [114] proposed a clever solution to overcome this problem and incorporate the anti-symmetric nature of the electronic wave function through construction. The proposed suggestion can be formulated as follows

$$\Phi = \frac{1}{\sqrt{n!}} \begin{vmatrix} \chi_1(\mathbf{X}_1) & \dots & \chi_n(\mathbf{X}_1) \\ \vdots & \ddots & \vdots \\ \chi_1(\mathbf{X}_n) & \dots & \chi_n(\mathbf{X}_n) \end{vmatrix} \tag{5.19}$$

where $|\bullet|$ stands for the determinant operation which fulfills the required symmetry. Subsequently, Fock [110] later proposed the use of this determinant as the ansatz for the wave function and applied the variational principle to find the electronic ground state, resulting in the HF method. The HF equations are solved self-consistently and yield a set of orthonormal orbitals and their corresponding orbital energies. The Slater determinant formed from the n orbitals with the lowest energy is then the HF ground state wave function Φ_o^{HF}, representing the best variational approximation to the ground state of a system in the single-determinant picture. Thus, the Hartree-Fock energy E_{HF}, is given by

$$\begin{aligned} E_{\mathrm{HF}} &= E_{\mathrm{HA}} - \frac{1}{2}\sum_{i,j\neq i}^{n}\left[\iint d\mathbf{r}d\mathbf{r}'\psi_i^*(\mathbf{r})\psi_j^*(\mathbf{r}')\frac{1}{|\mathbf{r}-\mathbf{r}'|}\psi_i(\mathbf{r}')\psi_j(\mathbf{r})\right] \\ &:= E_{\mathrm{HA}} + E_{\mathrm{xx}}, \end{aligned} \tag{5.20}$$

In the equation above, the exchange energy, denoted as E_{xx}, is defined. The sum over i and j runs only over the electrons with the same spin, and the spin variables have been integrated out. It is possible to include the terms where $i = j$ in the expression for E_{HF} because the terms coming from the electron-electron electrostatic interaction energy cancel exactly with the terms coming from the exchange energy. This cancellation ensures that the HF method is self-interaction free, meaning that an unphysical self-interaction energy resulting from a single electron interacting with its own charge density is eliminated. The HF method is important because it satisfies the Pauli exclusion principle [113], ensuring that no two electrons can occupy the same quantum state. Although it is able to recover more than 98% [115] of the exact total energy of the ground state, the remaining 2% corresponds to a significant amount of energy, much larger than the energy of chemical bonds. This residual energy is known as the correlation energy (E_c), which can be defined as the difference between the exact ground state energy (E_0) and the energy obtained from the HF method (E_{HF}).

The HF method is a widely used method for studying the electronic structure of atoms, molecules, and solids, and has been successful in predicting the properties of many atomic systems. However, despite failing to describe correlation effects, it also fails to capture certain physical phenomena, such as van der Waals interactions [116]. As a result, more advanced methods, such as DFT, are often used to improve upon the accuracy of the HF method. In the

next section, other electronic structure methods will be discussed to address the deficiencies of the HF method.

5.6 Density Functional Theory

In this section, a brief introduction of DFT which is a theoretical framework in physics and chemistry that is used to describe the electronic structure of matter is provided. It is based on the idea that the total energy of a many-electron system can be expressed as a functional of the electron density. By minimizing the total energy of the system with respect to the electron density, it is possible to obtain the ground state electron density and the corresponding ground state energy of the system. For a general description of this vast theoretical framework, the reader can look into [90, 107, 117].

In the 1950s and early 1960s, DFT was rigorously developed and began to be widely adopted. The contemporary theory of DFT was developed by Walter Kohn, John Perdew, and their colleagues during this period [118, 119]. The static DFT is based on the Hohenberg-Kohn theorem, which is discussed below.

5.6.1 The Hohenberg-Kohn Theorem

The Hohenberg and Kohn (HK) theorem for systems with non-degenerate ground-states reads as follows: *For a finite, interacting many-electron system there exists a one-to-one correspondence between the external potential* $v(r)$ *and the ground-state density* $n(r)$ [118, 120]. That is, the external potential is a unique functional of the ground-state density, $v([n], r)$, up to a trivial additive constant. The proof of this theorem employs a reductio ad absurdum approach. Let us consider a group of N interacting electrons with no spin, which is under the influence of an external potential $V(\mathbf{r})$. Typically, this potential is the Coulomb potential from the nuclei of the system. If this system has a unique ground state there is only one charge density $n(\mathbf{r})$ corresponding to a particular $V(\mathbf{r})$. However, in 1964, Hohenberg and Kohn proved the opposite, which was far from evident. They demonstrated that there is only one external potential $V(\mathbf{r})$ that can generate a specific ground-state charge density $n(\mathbf{r})$.

Let us consider a many-electron Hamiltonian $H = T+U+V$, with ground state wavefunction Ψ, T as the kinetic energy, U the electron-electron interaction, V the external potential. The charge density $n(\mathbf{r})$ is defined as

$$n(\mathbf{r}) = N \int |\Psi(\mathbf{r}, \mathbf{r}_2, \mathbf{r}_3, \ldots, \mathbf{r}_N)|^2 \, d\mathbf{r}_2 \ldots d\mathbf{r}_N. \tag{5.21}$$

Furthermore, let us consider now a different Hamiltonian $H' = T + U + V'$ (V and V' do not differ simply by a constant: $V - V' \neq$ const.), with ground state wavefunction Ψ' and energy E'. Let us assume that the ground state charge densities are the same: $n[V] = n'[V']$. Since Ψ is not the ground state of the potential V', then

$$\langle \Psi | H' | \Psi \rangle < E' \tag{5.22}$$

and therefore the following inequality holds

$$E' = \langle \Psi' \left| H' \right| \Psi' \rangle < \langle \Psi \left| H' \right| \Psi \rangle = \langle \Psi \left| H + V' - V \right| \Psi \rangle \tag{5.23}$$

that is,

$$E' < E + \int \left(V(\mathbf{r}) - V'(\mathbf{r}) \right) n(\mathbf{r}) d\mathbf{r} \tag{5.24}$$

The strict inequality in the equation is due to the fact that the wave functions Ψ and Ψ' are eigenstates of different Hamiltonians, hence they are different. If one were to reverse the primed and unprimed quantities, it would result in a contradiction. This proves that it is impossible for two different potentials to produce the same ground-state charge density.

In addition to that, most literature discusses a subtle point related to the existence of the potential that corresponds to a given ground state charge density, which is known as the V-representability problem. Additionally, various extensions of the Hohenberg and Kohn theorem are also made for a variety of systems including the systems with degenerate states as done in [121, 122] and also spin polarized systems [123] amongst others. Mermin also extended the theorems for finite systems in his article [124] where he shows that entropy and specific heat are indeed functionals of the ground state density.

A straightforward consequence of the first Hohenberg and Kohn theorem is that the ground state energy E is also uniquely determined by the ground-state charge density. In mathematical terms E is a functional $E[n(\mathbf{r})]$ of $n(\mathbf{r})$. The total energy of the system for a given density $n(\mathbf{r})$ is given by

$$E[n(\mathbf{r})] = \langle \Psi | T + U + V | \Psi \rangle = \langle \Psi | T + U | \Psi \rangle + \langle \Psi | V | \Psi \rangle = F[n(\mathbf{r})] + \int n(\mathbf{r}) V(\mathbf{r}) d\mathbf{r} \tag{5.25}$$

In DFT, the ground-state energy of a system of interacting electrons is described by a universal functional $F[n(\mathbf{r})]$, which depends only on the system's charge density $n(\mathbf{r})$, and not on the external potential $V(\mathbf{r})$. It is possible to minimize the ground-state energy by finding the corresponding ground-state charge density. However, the specific form of the functional $F[n(\mathbf{r})]$ is not known, making it challenging to apply this approach in practice. In the subsequent sections, methods for approximating the functional $F[n(\mathbf{r})]$ will be discussed to enable practical calculations using DFT. One year after the publication of the Hohenberg-Kohn theorem, Kohn and Sham [118] proposed a reformulation of the problem in a more practical form, which paved the way for practical applications of DFT.

5.6.2 The Kohn-Sham Theorem

The Kohn-Sham theorem states that *for any interacting electron system, there exists a non-interacting system with the same ground-state charge density $n(\mathbf{r})$, that yields the same expectation values for the total energy E and other observables of interest.* This non-interacting system is described by a set of single-particle equations with an effective potential, which depends on the ground-state charge density of the interacting system. For a system of non-interacting electrons, the ground-state charge density is representable as a sum over one-electron orbitals,the Kohn-Sham (KS) orbitals, $\psi_i(\mathbf{r})$

$$n(\mathbf{r}) = 2\sum_{i}^{N/2} |\psi_i(\mathbf{r})|^2 \tag{5.26}$$

where the index i runs from 1 to $N/2$ if we assume double occupancy of all states, and the KS orbitals are the solutions of the Schrödinger equation

$$\left(-\frac{\hbar^2}{2m}\nabla^2 + v_{KS}(\mathbf{r})\right)\psi_i(\mathbf{r}) = \epsilon_i\psi_i(\mathbf{r}) \tag{5.27}$$

Eq. (5.27) is known as the **Kohn-Sham equation**.

The existence of a unique potential $v_{KS}(\mathbf{r})$ having $n(\mathbf{r})$ as its ground state charge density is a consequence of the Hohenberg and Kohn theorem, which holds irrespective of the form of the electron-electron interaction U. The task at hand is to find the $v_{KS}(\mathbf{r})$ corresponding to a given density $n(\mathbf{r})$ in Eq. (5.27). One way to find this quantity is to use the variational principle [108] which was introduced in section 5.4.

5.6.3 Kohn-Sham equations and the variational principle

If we consider an arbitrary variation of the wavefunction $\psi_i(\mathbf{r})$ with the orthonomality constraint as stated in Eq. (**??**), the variation of the energy E must zero. This condition can be expressed as the functional derivative of the constrained functional with respect to the wavefunction ψ_i. This can be done in the following way

$$E' = E - \sum_{ij}\lambda_{ij}\left(\int \psi_i^*(\mathbf{r})\psi_j(\mathbf{r})d\mathbf{r} - \delta_{ij}\right) \tag{5.28}$$

where λ_{ij} are Lagrange multipliers. Taken the functional derivative of the Energy

$$\frac{\delta E'}{\delta\psi_i^*(\mathbf{r})} = \frac{\delta E'}{\delta\psi_i(\mathbf{r})} = 0. \tag{5.29}$$

The energy functional can be expressed in a more convenient form as follows

$$E = T_s[n(\mathbf{r})] + E_H[n(\mathbf{r})] + E_{xc}[n(\mathbf{r})] + \int n(\mathbf{r})V(\mathbf{r})d\mathbf{r} \tag{5.30}$$

In the above equation, the first term is the kinetic energy of the Non-interacting particle, and

it is given by

$$T_s[n(\mathbf{r})] = -\frac{\hbar^2}{2m} 2 \sum_i \int \psi_i^*(\mathbf{r}) \nabla^2 \psi_i(\mathbf{r}) d\mathbf{r} \tag{5.31}$$

the second term of Eq.(5.30) known as the Hartree energy which contains the electrostatic interaction between charges and can be expressed as

$$E_H[n(\mathbf{r})] = \frac{e^2}{2} \int \frac{n(\mathbf{r}) n(\mathbf{r}')}{|\mathbf{r} - \mathbf{r}'|} d\mathbf{r} d\mathbf{r}'. \tag{5.32}$$

The last term of the equation is the exchange and correlation energy which contains all the remaining terms. Our ignorance is hidden in this term and thus, one has to approximate it in real DFT calculations. In general we can express the Kohn-Sham equation as,

$$(H_{KS} - \epsilon_i)\, \psi_i(\mathbf{r}) = 0 \tag{5.33}$$

where H_{KS}, is called the Kohn-Sham Hamiltonian and is defined as

$$H_{KS} = -\frac{\hbar^2}{2m} \nabla^2 + v_H([\mathbf{n}(\mathbf{r})]) + v_{xc}([\mathbf{n}(\mathbf{r})]) + v(\mathbf{r}) \equiv -\frac{\hbar^2}{2m} \nabla^2 + v_{KS}([\mathbf{n}(\mathbf{r})]) \tag{5.34}$$

Where the exchange-correlation potential v_{xc} is given by

$$v_{xc}([\mathbf{n}(\mathbf{r})]) = \frac{\delta E_{xc}[n]}{\delta n(\mathbf{r})} \tag{5.35}$$

and the Hartree potential v_H is given by

$$v_H([\mathbf{n}(\mathbf{r})]) = \int \frac{n(\mathbf{r}')}{|\mathbf{r} - \mathbf{r}'|} d\mathbf{r}' \tag{5.36}$$

The KS orbitals can be obtained by self-consistently solving the KS equations Eq. (5.27) together with Eq. (5.26) and the KS potential [118]. A sketch of the Kohn-Sham scheme is shown in Figure 5.1.

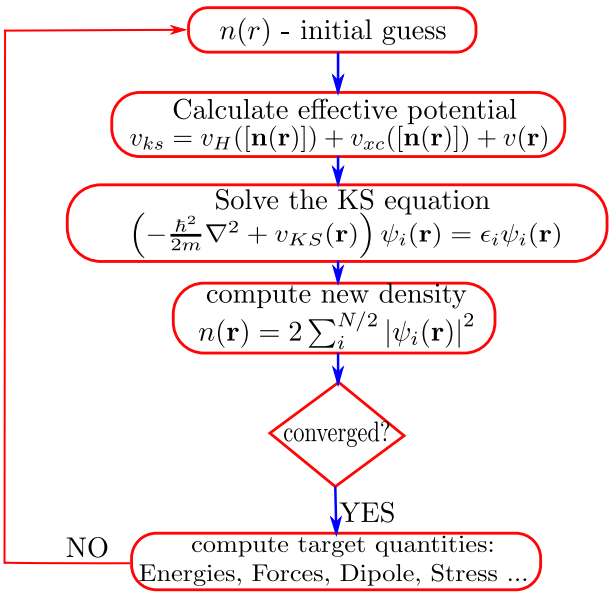

Figure 5.1: Schematic representation of the self-consistency cycle in Kohn-Sham DFT.

In practice, DFT calculations rely on approximations to the Exchange and Correlation (XC) functional in Eq. (5.37), the quality of which determines the accuracy of the result. The approximations to the XC functional can be found in wide variety of strategies such as empirical fitting [125], local scaling, mixing of exact and approximate exchange among others [126]. For more detailed references on the existing and widely used approximations to the functional, one can see [127]. Kohn and Perdew showed that the energy of a many-electron system could be expressed as a functional of the electron density, and that this functional could be approximated using the LDA [119]. The LDA has been widely used in DFT calculations and has been very successful in predicting the electronic structure of a variety of systems.

5.6.4 The Local Density Approximation (LDA)

One of the early approximations to the exchange-correlation functional is the LDA [119] [1]. The LDA is the most prominent approximation, which is widely used for different applications which ranges from molecules, solids, ions, atoms and clusters [128]. In LDA, the exchange-correlation energy is approximated as a function of the local electron density at each point in space. This means that the exchange-correlation energy at a given point is determined only by the density of electrons in the immediate vicinity of that point. LDA is a relatively simple and computationally efficient method, but it may not accurately capture the nonlocal effects of exchange and correlation. In this approximation, one can express the exchange-correlation energy functional as a functional of the electron density $n(\mathbf{r})$ as

$$E_{xc}[n] = \int n(\mathbf{r})\varepsilon_{xc}(n(\mathbf{r}))d^3\mathbf{r} \tag{5.37}$$

where $\varepsilon_{xc}(n(\mathbf{r}))$ is the exchange-correlation energy density. This energy density is approximated as a function of the local electron density $n(\mathbf{r})$ only, neglecting any dependence on the density gradient or higher order terms. Therefore, in practice, the exchange-correlation energy functional can be written as

$$E_{xc}^{LDA}[n] = \int n(\mathbf{r})\varepsilon_{xc}^{LDA}(n(\mathbf{r}))d^3\mathbf{r} \tag{5.38}$$

Now, since the effective potential that enters in the self-consistent KS equations requires the knowledge of the XC potential, we calculate the functional derivative of Eq. (5.37) and this produces the XC potential which reads

$$v_{xc}[n(\mathbf{r}] = \varepsilon_{xc}([n(\mathbf{r})]) + n(\mathbf{r})\frac{\delta\varepsilon_{xc}([n(\mathbf{r}])}{\delta n(\mathbf{r})} \tag{5.39}$$

while the LDA XC potential is expressed as,

$$v_{xc}^{LDA}[n(\mathbf{r}] = \varepsilon_{xc}^{LDA}([n(\mathbf{r})]) + n(\mathbf{r})\frac{\delta\varepsilon_{xc}^{LDA}([n(\mathbf{r}])}{\delta n(\mathbf{r})} \tag{5.40}$$

The expression for the exchange energy is

$$E_x^{LDA}[n] = -\frac{3}{4}\left(\frac{3}{\pi}\right)^{\frac{1}{3}}\left(\int n^{\frac{4}{3}}(r)dr\right)^{\frac{1}{2}} \tag{5.41}$$

[1] Unless stated otherwise, the majority of calculations in this thesis employ the Local Density Approximation (LDA).

The most commonly used LDA functionals are Perdew-Wang (PW91) [129], Ceperley-Alder (CA) [130], Vosko-Wilk-Nusair (VWN) [131] and Perdew-Zunger (PZ) [132] amongst others. While the LDA has been successful in many cases, it fails to capture certain physical phenomena, such as van der Waals interactions, underestimation of bandgap, in accurate description of excitation energies. It is also widely reported that LDA underestimates lattice constants by $\approx 2-3\%$ for metals and insulators [133–135]. In addition to the LDA, several other functionals have been proposed to address the limitations of the LDA. Some of these functionals include:

5.6.5 Generalized Gradient Approximation (GGA)

Generalized Gradient Approximation (GGA) referred to as *second* generation functionals is an improvement over the earlier discussed LDA and introduces the dependence of the exchange-correlation functional on the spatial gradients of the electron density. By including the gradient information, GGA provides a better description of the electronic structure and energetics compared to LDA [136]. GGA functionals are typically parameterized based on the analysis of experimental data or higher-level quantum mechanical calculations. The GGA functional can be expressed as the sum of the LDA exchange (E_x^{LDA}) and correlation (E_c) contributions

$$E_{xc}^{GGA} = E_x^{LDA} + E_c \tag{5.42}$$

The GGA functional can be briefly derived by introducing the electron density $n(\mathbf{r})$ and its gradient $\nabla n(\mathbf{r})$ to the exchange and correlation contributions. The exchange contribution can be expressed as

$$E_x = \int n(\mathbf{r})\epsilon_x(n(\mathbf{r}), \nabla n(\mathbf{r}))d\mathbf{r} \tag{5.43}$$

where ϵ_x represents exchange energy density functional that depends on the electron density and its gradient. Similarly, we can also express the correlation contribution as

$$E_c = \int n(\mathbf{r})\epsilon_c(n(\mathbf{r}), \nabla n(\mathbf{r}))d\mathbf{r} \tag{5.44}$$

The general form of GGA functionals takes the form

$$E_{xc}^{GGA}[n] = \int f^{GGA}(n(\mathbf{r}), \nabla n(\mathbf{r}))d\mathbf{r}. \tag{5.45}$$

Overall, due to flexibility of f^{GGA}, a diverse range of GGA functionals have been developed, forming a "zoo" of functionals. These functionals offer a wide range of validity depending on the specific system being studied. Within GGA the the exchange energy takes the form

$$E_x^{GGA}[n] = \int n(\mathbf{r})\epsilon_x(n(\mathbf{r})F_x^{GGA}(s)d\mathbf{r}. \tag{5.46}$$

Where $F_x^{GGA}(s)$ is the exchange enhancement factor which is a quantity that indicates the extent to which the exchange energy is enhanced compared to its value in LDA, given a specific electron density $n(\mathbf{r})$. It characterizes the improvement in the exchange contribution to the total energy beyond the LDA approximation. s is a dimensionless quantity given by

$$s = \frac{\nabla n(\mathbf{r})}{2(3\pi^2)^{1/3}n(\mathbf{r})^{4/3}}. \tag{5.47}$$

The choice of F_x^{GGA} differentiate one GGA from another. As an illustration for what $F_x(s)$ looks like, the two most prominent and most used GGA functionals are the Perdew-Burke-Ernzerhof (PBE) [137] and Revised Perdew-Burke-Ernzerhof (RPBE) [127, 138] functionals which we now briefly discussed since some calculations in this work were done using the PBE functionals. The F_x^{GGA} has the following forms for the two functionals,

$$F_x^{PBE}(s) = 1 + \kappa - \frac{\kappa}{1 + \mu s^2/k} \tag{5.48}$$

where κ and μ are quantities obtained by from physical constraints.

$$F_{\mathrm{x}}^{\mathrm{RPBE}}(r_s, \zeta) = 1 + \kappa - \frac{\kappa}{1 + \mu r_s/\zeta} - \frac{\mu r_s}{1 + \mu r_s/\zeta} \tag{5.49}$$

The parameters κ and ζ are constants that depend on the specific implementation of the RPBE functional. The parameter μ is defined as $\mu = \zeta/\sqrt{2}$. Some widely used gradient-corrected correlation functionals include PBE [137, 139], PW91 [129], Perdew86 (P86) [140] and Lee-Yang-Parr (LYP)[141].

5.6.6 meta-gga's

These sets of functionals are known as the *third* generation of functionals. They are an extension of the GGA functionals that incorporate additional information about the kinetic energy density of the electron system. They go beyond the local density and gradient of the electron density and consider the nonlocal kinetic energy density in their functional form. Meta-gga functionals introduce the use of the electron density $n(\mathbf{r})$, its gradient $\nabla n(\mathbf{r})$, and the Laplacian $\nabla^2 n(\mathbf{r})$ of the electron density in their expressions. By including higher-order derivatives of the electron density, these functionals aim to capture more accurate exchange and correlation effects in a wider range of systems and properties. Some examples of popular meta-gga functionals include TPSS (Tao, Perdew, Staroverov, and Scuseria) [142, 143] and M06 (Minnesota 06) [144, 145] functionals. The exact form of Meta-gga functionals can vary depending on the specific functional being used. However, in general, the expression for a Meta-gga functional can be written as

$$E_{\mathrm{XC}}^{\mathrm{Meta-gga}} = \int n(\mathbf{r}) \varepsilon_{\mathrm{X}}^{\mathrm{Meta-gga}} \left[n(\mathbf{r}), \nabla n(\mathbf{r}), \nabla^2 n(\mathbf{r}) \right] d\mathbf{r} + \int n(\mathbf{r}) \varepsilon_{\mathrm{C}}^{\mathrm{Meta-gga}} \left[n(\mathbf{r}), \nabla n(\mathbf{r}), \nabla^2 n(\mathbf{r}) \right] d\mathbf{r} \tag{5.50}$$

With the inclusion of nonlocal kinetic energy density, meta-gga's typically improve upon the accuracy of GGA. This allows meta-gga's to more accurately treat different quantities like chemical bonding, lattice parameter and Van der Waals interactions [146] compared to LDA and GGA.

5.6.7 Hybrid Functionals

Hybrid functionals are regarded as the *fourth* generation functionals. These functionals takes a portion of the exact exchange from Hartree-Fock theory (c.f Section 5.5) and mix it with the exchange-correlation functional. This combination aims to improve the description of both localized and delocalized electronic states, which can be challenging for purely local or semi-local

functionals. The general form of a hybrid functional can be written as;

$$E_{\mathrm{XC}}^{\mathrm{hybrid}} = (1-\alpha)E_{\mathrm{X}}^{\mathrm{HF}} + \alpha E_{\mathrm{X}}^{\mathrm{DFT}} + E_{\mathrm{C}}^{\mathrm{DFT}} \tag{5.51}$$

wherer $E_{\mathrm{X}}^{\mathrm{HF}}$ represents the exact exchange energy from Hartree-Fock theory, $E_{\mathrm{X}}^{\mathrm{DFT}}$ is the exchange energy from the exchange-correlation functional, and $E_{\mathrm{C}}^{\mathrm{DFT}}$ is the correlation energy from the exchange-correlation functional. The parameter α determines the fraction of exact exchange included in the hybrid functional. Different hybrid functionals use different values of α, typically ranging from 0 to 1, to balance the accuracy and computational efficiency. The most commonly used hybrid functionals in physics community are the PBE0 [147] and HSE [148] functionals. The PBE0 hybrid functional combines 25% of the exact exchange from Hartree-Fock theory with 75% of the exchange-correlation functional from the PBE functional. The expression for the PBE0 functional is as follows

$$E_{\mathrm{XC}}^{\mathrm{PBE0}} = 0.25E_{\mathrm{X}}^{\mathrm{HF}} + 0.75E_{\mathrm{X}}^{\mathrm{PBE}} + E_{\mathrm{C}}^{\mathrm{PBE}} \tag{5.52}$$

while the HSE functional combines a range-separated hybrid approach with the PBE exchange-correlation functional. It separates the long-range exchange interactions from the short-range exchange and correlation interactions. The HSE functional can be expressed as follows

$$E_{\mathrm{XC}}^{\mathrm{HSE}} = \alpha E_{\mathrm{X}}^{\mathrm{HF}}(\mathrm{SR}) + (1-\alpha)E_{\mathrm{X}}^{\mathrm{HF}}(\mathrm{LR}) + E_{\mathrm{C}}^{\mathrm{PBE}} \tag{5.53}$$

in the expression, the parameter α determines the range separation, with typical values ranging from 0.15 to 0.25 [149].

Another class of hybrid functional that have attracted interest lately is the *range-seperated hybrids* [150]. In this type of functionals, the Coulomb interaction is separated into a short-range (SR) and a long range (LR) part

$$\frac{1}{|\mathbf{r}-\mathbf{r}'|} = \frac{f\left(\mu\,|\mathbf{r}-\mathbf{r}'|\right)}{|\mathbf{r}-\mathbf{r}'|} + \frac{1-f\left(\mu\,|\mathbf{r}-\mathbf{r}'|\right)}{|\mathbf{r}-\mathbf{r}'|} \tag{5.54}$$

where f is a function and has the properties $f(\mu x \to 0) = 1$ and $f(\mu x \to 0) = \infty$. Some relevant examples are $f(\mu x) = e^{-\mu x}$ and $f(\mu x)$= erfc(μx). μ is the separation parameter and can be determined empirically or via physical arguments[151–153]. The resultant range-separated hybrid XC functional exhibits the following form

$$E_{xc} = E_X^{SR-DFA} + E_X^{LR-HF} + E_C^{DFA} \tag{5.55}$$

where DFA can be any form of the density-functional approximation (LDA or GGA). Range-separated hybrids excel in their ability to combine the accurate long-range asymptotic behavior of Hartree-Fock with the favorable short-range behavior of LDA or GGA. As a result, they exhibit notable enhancements in properties like the polarizabilities of extended molecules, bond dissociation, and crucially for TDDFT, excitation phenomena such as Rydberg and charge-transfer excitations.

5.6.8 DFT+U

LDA+U is a method that allows for a more realistic treatment of electronic interactions in systems where standard DFT might fail to capture the correct physics. The scheme is widely implemented in order to to correct the approximate DFT XC functional. The correction works similar to the standard LDA (described in subsection 5.6.4) and +U introduces a correction term to the LDA to account for the on-site Coulomb repulsion between electrons in localized orbitals (especially in correlated electronic states the d and f orbitals). The general form of the DFT+U energy functional (E_{LDA+U}) can be written as the summation of the LDA energy functional (E_{LDA}) and the energy that comes from the Hubbard functional (E_{Hub}) which describes the correlated states. This can be expressed as

$$E_{DFT+U}[n(\mathbf{r})] = E_{DFT}[n(\mathbf{r})] + E_{Hub}[\{n^I_{nm}\}] - E_{dc}[n^I] \tag{5.56}$$

where E_{DFT} is the standard DFT energy functional (LDA or GGA), n_{nm} are the localized orbitals occupation numbers which are identified by the atomic site I and state index m, E_{Hub} depends on the orbital occupancy n_{nm} and represents the energy correction according to the Hubbard model [154], E_{dc} is an extra term that accounts for the "double-counting" because of the addition of the Hubbard term [155, 156].

In essence, within DFT calculations, the primary obstacle lies in accurately determining the XC functional $E_{xc}[\mathbf{n}]$, as its exact form remains elusive. Consequently, different levels of approximations are employed, resulting in a hierarchical arrangement of DFT functionals. This hierarchy, depicted by the Jacob ladder [157] classification scheme in Figure 5.2, exhibits increasing complexity and computational cost as one ascends the ladder.

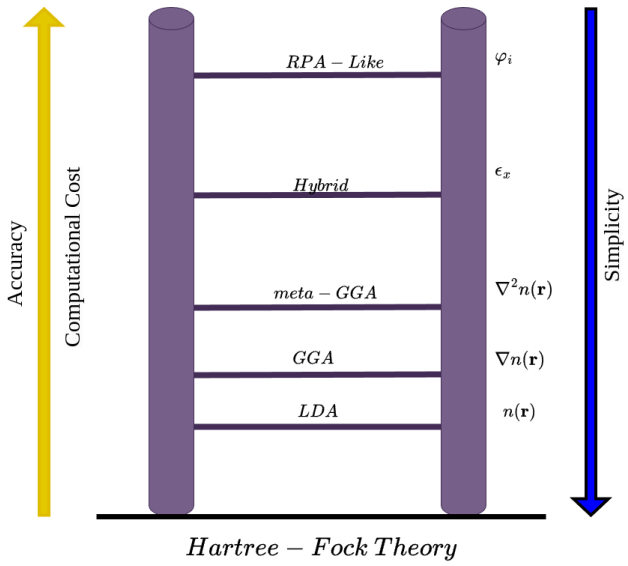

Figure 5.2: Jacob's Ladder: Hierarchy of Density-Functional Approximations. Higher rungs represents increasingly complex and accurate functionals. (Adapted from [6])

As illustrated in Figure 5.2, the Jacob's ladder analogy shows the historical development of XC functionals. Each rung represents a successive improvement in accuracy and complexity, reflecting the evolving nature of computational tools in electronic structure calculations. The ladder emphasizes the ongoing advancement in XC functionals, progressing from fundamental

approaches like LDA and GGA to more sophisticated meta-GGAs and hybrid functionals.

5.6.9 Pseudopotentials

To perform DFT in practice, the KS equations have to be treated numerically in various ways and one key ingredient to reducing complexity and improving efficiency is the use of pseudopotentials. These are essential in making large-scale and accurate calculations feasible. Pseudopotential (PP) or effective potentials are employed to simplify the description of the interaction between valence electrons and atomic nuclei in a solid or molecule. In a pseudopotential approach, the core electrons and their associated potentials are replaced by a smooth and weaker potential that acts on the valence electrons. This allows for a significant reduction in computational complexity, as the explicit treatment of core electrons can be computationally demanding. For calculations, where one is not interested in core excitations, one therefore freezes the core electrons and replaces the strong Coulomb potential in the core region by smoother potentials based on a combination of the nucleus and the influence of the core electrons. In this thesis pseduopotentials were generated with Troullier-Martins scheme [158] for calculations involving valence only and were used as implemented in the real space code **Octopus** [159–161] while for calculations using the plane-wave code Quantum Espresso (QE) [162–164] norm-conserving or ultrasoft pseudo-potentials were used.

5.6.10 All Electron Pseudopotentials

It is very hard to describe the strong Coulomb interaction in the core region of atoms with real space codes like **Octopus**. The easiest way to do so is by use of the all-electron pseudopotentials [165, 166]. In all-electron pseudopotentials, the core electrons are treated as valence-like electrons with modified potentials. This allows for a more accurate representation of the electron-electron and electron-nucleus interactions within the core region while still allowing for some degree of smoothness of the potential. By incorporating the core electrons explicitly, all-electron pseudopotentials can provide results for properties that depend on the behavior of these electrons. Compared to standard pseudopotentials, all-electron pseudopotentials require more computational resources since they involve a larger number of electrons. The utilization of pseudo-potentials is advantageous since it enables the reduction of the number of plane waves necessary to describe the system. This is achieved by substituting the real valence wavefunctions, which exhibit rapid variations near the nuclei, with smooth pseudo wave-functions that match the real valence wave-functions beyond a specific distance r_c from the nuclei as depicted in Figure 5.3 below.

5.7 Density Functional Perturbation Theory (DFPT)

DFPT is an extension of DFT. The aim of this method is to understand how a material responds to changes in its environment, such as lattice distortions, external electric fields, or other perturbations [167, 168]. Here, the theory related to the calculation of phonon dispersion curves as implemented in the open-source code **Quantum Espresso** (QE) is briefly described

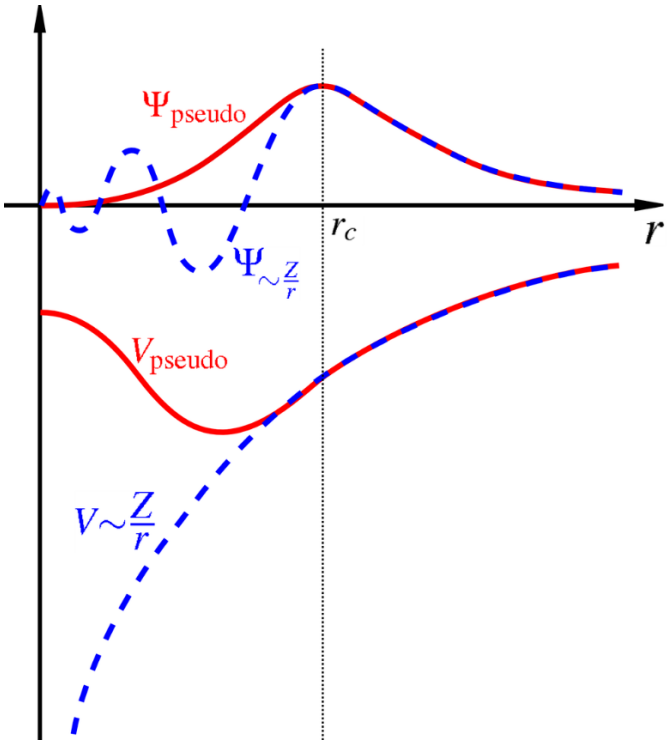

Figure 5.3: A schematic representation of the potentials and wave functions for both all-electron (solid lines) and pseudo electron (dashed lines) systems. The region where the all-electron and pseudo electron values coincide is indicated by the designated radius r_c (adapted from [7]).

[162–164].

Since we're dealing with a system of a periodic solid, we can describe the lattice position of an atom I by vectors $\boldsymbol{R_I}$ as

$$\boldsymbol{R_I} = \boldsymbol{R_\mu} + \boldsymbol{d_s} \tag{5.57}$$

whereby $\boldsymbol{R_\mu}$ denotes the linear combination of the unit cell lattice vectors $\mathbf{a_1}$, $\mathbf{a_2}$ and $\mathbf{a_3}$ and $\boldsymbol{d_s}$ is the position of the atoms in the unit cell. DFPT describes the behaviour of the electronic structure, when the atoms in the unit cell are displaced from their equilibrium position. The displacement of the atom I from equilibrium is given by, $\boldsymbol{u_I}$(t).

The potential energy of the atoms as they move within the potential energy surface can be described as

$$E_{tot}(\boldsymbol{R_I} + \boldsymbol{u_I}). \tag{5.58}$$

In this configuration, the electrons are assumed to be in the ground state (c.f. the BOA in sec. 5.3). If the displacements of the atoms is assumed to be small, the total energy E_{tot} can be expanded in Taylor series around the displacement $\boldsymbol{u_I}$ this is known as the *harmonic approximation*

$$E_{tot}\left(\mathbf{R_I} + \mathbf{u_I}\right) = E_{tot}\left(\mathbf{R_I}\right) + \sum_{I\alpha} \frac{\partial E_{tot}}{\partial \mathbf{u}_{I\alpha}} \mathbf{u}_{I\alpha} + \frac{1}{2} \sum_{I\alpha, J\beta} \frac{\partial^2 E_{tot}}{\partial \mathbf{u}_{I\alpha} \partial \mathbf{u}_{J\beta}} \mathbf{u}_{I\alpha} \mathbf{u}_{J\beta} + \ldots \tag{5.59}$$

where the derivatives are calculated at $\boldsymbol{u_I} = 0$ and α and β represents the Cartesian coordinates.

In order to calculate the equation of motion needed in DFPT, we assume that, at equilibrium, the derivative of the total energy with respect to the displacements $\boldsymbol{u_I}$ is zero i.e,

$$\frac{\partial E_{tot}}{\partial \mathbf{u_I}} = 0 \tag{5.60}$$

such that the ionic Hamiltonian becomes

$$H = \sum_{I\alpha} \frac{\mathbf{P}_{I\alpha}^2}{2M_I} + \frac{1}{2} \sum_{I\alpha, J\beta} \frac{\partial^2 E_{tot}}{\partial \mathbf{u}_{I\alpha} \partial \mathbf{u}_{J\beta}} \mathbf{u}_{I\alpha} \mathbf{u}_{J\beta} \tag{5.61}$$

where $\mathbf{P_I}$ is the momentum of the nuclei and the M_I are the corresponding masses. Classically, one can write the equation of motion of the nuclei as the solution of the Hamilton equations

$$\begin{aligned} \dot{\mathbf{u}}_{I\alpha} &= \frac{\partial H}{\partial \mathbf{P}_{I\alpha}} \\ \dot{\mathbf{P}}_{I\alpha} &= -\frac{\partial H}{\partial \mathbf{u}_{I\alpha}} \end{aligned} \tag{5.62}$$

From the Hamiltonian, we obtain

$$\begin{aligned} \dot{\mathbf{u}}_{I\alpha} &= \frac{\mathbf{P}_{I\alpha}}{M_I} \\ \dot{\mathbf{P}}_{I\alpha} &= -\sum_{J\beta} \frac{\partial^2 E_{tot}}{\partial \mathbf{u}_{I\alpha} \partial \mathbf{u}_{J\beta}} \mathbf{u}_{J\beta}. \end{aligned} \tag{5.63}$$

From these equation of motion, one can find the solution in the form of a phonon. Suppose we have a wave vector $\mathbf{q}$ as the vector describing the first Brillouin zone, one can express the displacement for each wave wave vector $\mathbf{q}$ as

$$\mathbf{u}_{\mu s\alpha}(t) = \frac{1}{\sqrt{M_s}} \mathrm{Re}\left[\mathbf{u}_{s\alpha}(\mathbf{q}) e^{i(\mathbf{q}\mathbf{R}_\mu - \omega_{\mathbf{q}} t)}\right] \tag{5.64}$$

The temporal variation is expressed through a phase factors, represented by $e^{(\pm i\omega_{\mathbf{q}} t)}$. The displacement of atoms within each unit cell, identified by the Bravais lattice symbolized as $\mathbf{R}_\mu$, can be derived from the atomic displacements in a single unit cell. Upon substituting the solution Eq. (5.64) into the equation of motion, one obtains the relation

$$\omega_{\mathbf{q}}^2 \mathbf{u}_{s\alpha}(\mathbf{q}) = \sum_{s'\beta} D_{s\alpha s'\beta}(\mathbf{q}) \mathbf{u}_{s'\beta}(\mathbf{q}) \tag{5.65}$$

where the quantity $D_{s\alpha s'\beta}(\mathbf{q})$ is defined as

$$D_{s\alpha s'\beta}(\mathbf{q}) = \frac{1}{\sqrt{M_s M_{s'}}} \sum_{\nu} \frac{\partial^2 E_{tot}}{\partial \mathbf{u}_{\mu s\alpha} \partial \mathbf{u}_{\nu s'\beta}} e^{iq(\mathbf{R}_\nu - \mathbf{R}_\mu)} \tag{5.66}$$

and it is known as the "Dynamical Matrix" which determines the equation for the normal modes or phonons. E_{tot} can be define in the context of DFT. In *ab-initio* calculations, usually the calculations are done on a grid of $\mathbf{q}$-points which form a regular lattice and covered the whole Brillouin zone. After the dynamical matrix is obtained, discrete FT are applied to interpolate it to arbitrary points in between. More details and derivations of other quantities and implementation of DFPT in the QE code can be found in [169–171].

5.8 Time-Dependent Density Functional Theory (TDDFT)

In the previous section 5.6, DFT [172] was presented in summary, which focuses on the electronic density distribution in the ground state and gives a proper description of the ground states properties of various systems. However, to properly describe the electronic properties and dynamics of many-body quantum systems, an extension of the ground-state formalism of DFT is essential. The framework of TDDFT is put forward by Eberhard K.U. Gross and Erich Runge [173–175] in their paper in 1984 [2]. In TDDFT, an external static potential of DFT is replaced by a time-dependent potential. Several comprehensive reviews on these subject of TDDFT can be found in numerous textbooks and other literatures. Some of these can be found in the references [174, 176–179].

The direct approach to solve the dynamics of time-dependent electronic systems is to solve the (non-relativistic) time-dependent Schrödinger equation for the many-electron wavefunction $\Psi(t)$

$$\hat{H}_{el}(t)\Psi(t) = i\frac{\partial\Psi(t)}{\partial t} \tag{5.67}$$

where $\hat{H}_{el}(t)$ is the Hamiltonian operator which can be described in 5.1. Here, the kinetic energy and the electron-electron repulsion, are, respectively given by

$$\hat{T} = -\frac{1}{2}\sum_{i=1}^{N}\nabla_i^2 \quad \text{and} \tag{5.68}$$

$$\hat{V}_{\text{ee}} = \frac{1}{2}\sum_{i\neq j}^{N}\frac{1}{|\boldsymbol{r}_i - \boldsymbol{r}_j|} \tag{5.69}$$

where the sum is over all pairs, and the factor of 1/2 avoids double counting. The "external potential" $\hat{V}_{ext}(t)$ [3] represents the potential the electrons experience due to any applied external field to the system. The one-body potential can be expressed as

$$\hat{V}_{\text{ext}} = \sum_{i=1}^{N} v_{\text{ext}}\left(\boldsymbol{r}_i, t\right) \tag{5.70}$$

For example, $v_{\text{ext}}\left(\boldsymbol{r}_i, t\right)$ can represent Coulomb interactions of the electrons with a set of nuclei, possibly moving along some classical path,

$$v_{\text{ext}}\left(\boldsymbol{r}_i, t\right) = -\sum_{v=1}^{N_n}\frac{Z_v}{|\boldsymbol{r} - \boldsymbol{R}_v(t)|} \tag{5.71}$$

where Z_v and R_v denote the charge and position of the nucleus v, and N_n stands for the total number of nuclei in the system. Another example is the interaction with external fields, such as a system illuminated by a laser beam. In the dipole approximation [180], we can express this interaction as follows

$$v_{ext}(\mathbf{r}, t) = Ef(t)\sin(\omega t)\mathbf{r}\cdot\alpha \tag{5.72}$$

where α, ω and E are the polarization, the frequency and the amplitude of the laser field

[2] The theory presented here forms part of section 6

[3] the external potential here is local, but the same equation 5.70 and formalism holds for a non-local potential, as for instance within the pseudo-potential approximation

respectively and $f(t)$ describes the envelop of the laser pulse. As the system evolves in time from some initial point (say $t = 0$), its density undergoes changes. The electron density at any given time can be formally described by

$$n(\boldsymbol{r}, t) = N \int \mathrm{d}^3 r_2 \ldots \int \mathrm{d}^3 r_N \left|\Psi\left(\boldsymbol{r}, \boldsymbol{r}_2, \ldots, \boldsymbol{r}_N, t\right)\right|^2 \tag{5.73}$$

where $n(\mathbf{r}, t)$ normalizes to the number of electrons N. The time-dependent Schrödinger equation 5.67 of many electron system with the Hamiltonian 5.1 can be used to describe the evolution of the system.

For a fixed initial state $|\Psi_0\rangle$ and external potential $v(\mathbf{r}, t)$, one wants to solve Eq. (5.67) with the Hamiltonian $\hat{H}_{el}(t)$. The resulting wavefunction depends on the initial state and the external potential given as $|\Psi\left([\Psi_0, v], t\right)\rangle$. Since the wavefunction has functional dependencies on the fixed initial state and external potential, the expectation value for an arbitrary operator $\hat{O}$ become a functional of $|\Psi_0\rangle$ and $v(\mathbf{r}, t)$. The observable can be written as

$$O\left([\Psi_0, v], t\right) = \left\langle \Psi\left([\Psi_0, v]; t\right) |\hat{O}| \Psi\left([\Psi_0, v], t\right) \right\rangle. \tag{5.74}$$

In order for TDDFT to be a comprehensive and accurate theory, it is necessary to identify a fundamental variable that can uniquely describe the physical wave-functions and their associated observables. When undergoing a functional-variable transformation from a fixed initial state, it is important to establish a one-to-one correspondence between the external variable $v(\mathbf{r}, t)$ and a chosen internal variable. In TDDFT, the internal variable that serves as the conjugate to the external potential is the electron density $n(\mathbf{r}, t)$. As every observable is characterized by $|\psi_0\rangle$ and $v(\mathbf{r}, t)$, the electron density is similarly labeled by these variables.

$$n\left([\Psi_0, v], \mathbf{r}, t\right) = \langle \Psi\left([\Psi_0, v], t\right) |\hat{n}(\mathbf{r})| \Psi\left([\Psi_0, v]; t\right) \rangle. \tag{5.75}$$

The foundation of any density-functional theory relies on the presence of a unique and well-defined mapping between a set of internal variables (such as the electron density) and external variables (such as the external potential). When the existence and uniqueness of this mapping are established, the functional dependence on the external variables in Eq. (5.75) can be replaced with a functional dependence on the fundamental internal variables. Consequently, in order to fully develop the theory of TDDFT, it is essential to provide a rigorous proof of the one-to-one mapping for a fixed initial state $|\psi_0\rangle$. This proof should demonstrate that

$$v(\mathbf{r}, t) \xrightarrow[\psi_0]{1:1} n(\mathbf{r}, t) \tag{5.76}$$

and was initially proven by Runge and Gross with the proof shown in the subsequent section.

5.8.1 Runge-Gross Theorem

The fundamental concept of TDDFT is to describe the dynamics of a many-electron quantum system exclusively using the time-dependent particle density $n(\mathbf{r}, t)$. In 1984, Erich Runge and Eberhard K.U. Gross established in their work [173] the existence of a one-to-one correspondence between the time-dependent density $n(\mathbf{r}, t)$ and the time-dependent external potential $v(\mathbf{r}, t)$ for a given initial state $\Psi(t_0)$. This result, known as the Runge-Gross (RG) theorem states that,

that for a given initial state $\Psi(t_0)$, there exists a unique one-to-one mapping between the time-dependent particle density $n(\mathbf{r},t)$ and the time-dependent external potential $v(\mathbf{r},t)$ in TDDFT. This means that the density $n(\mathbf{r},t)$ fully determines the external potential $v(\mathbf{r},t)$ and vice versa, allowing for the complete description of the time evolution of a many-electron quantum system. The proof of this theorem can be summarized as follows: Runge and Gross established that when starting from a shared initial state $\Psi(t_0)$ and evolving under the influence of distinct external potentials $v_{ext}(\mathbf{r},t)$ and $v'_{ext}(\mathbf{r},t)$, denoted by Hamiltonians $\hat{H}_{el}(t)$ and $\hat{H}'_{el}(t)$, the resulting solutions $\Psi(t)$ and $\Psi'(t)$ of the time-dependent Schrödinger equation will always lead to different electron density distributions $n(\mathbf{r},t)$ and $n'(\mathbf{r},t)$. This condition holds, provided that the two external potentials differ by more than a time-dependent constant function, i.e., $v_{ext}(\mathbf{r},t) \neq v'_{ext}(\mathbf{r},t)$. Assuming that the potentials can be expressed as analytic functions of time, these external potentials can be expanded using a Taylor series

$$v_{ext}(\mathbf{r},t) = \sum_{k=0}^{\infty} \frac{1}{k!} \frac{\partial^k v_k(\mathbf{r},t)}{\partial t^k}\bigg|_{t_0} (t-t_0)^k \,, \text{ and } v'_{ext}(\mathbf{r},t) = \sum_{k=0}^{\infty} \frac{1}{k!} \frac{\partial^k v'_k(\mathbf{r},t)}{\partial t^k}\bigg|_{t_0} (t-t_0)^k \,. \quad (5.77)$$

The requirement that the two external potentials deviate by more than a time-dependent constant, denoted as $c(t)$, ensures the existence of a non-negative integer $k \geq 0$. This integer guarantees that the Taylor coefficients in Equation (5.77) differ by more than a constant in the following manner

$$\frac{\partial^k v_k(\mathbf{r},t)}{\partial t^k}\bigg|_{t_0} - \frac{\partial^k v'_k(\mathbf{r},t)}{\partial t^k}\bigg|_{t_0} \neq \text{ const.} \quad (5.78)$$

The proof of the RG theorem employs the continuity equation from the time-dependent Schrödinger equation

$$\frac{\partial n(\mathbf{r},t)}{\partial t} = -\nabla \cdot \hat{\mathbf{j}}(\mathbf{r},t) \quad (5.79)$$

where $\mathbf{j}(\mathbf{r},t)$ is the paramagnetic current-density operator and given by

$$\hat{\mathbf{j}}(r) = \frac{\hbar}{2im_e} \sum_{i=1}^{N} [\nabla_i \delta(\mathbf{r}-\mathbf{r}_i) + \delta(\mathbf{r}-\mathbf{r}_i)\nabla_i] \quad (5.80)$$

The initial step of the proof confirms the uniqueness of the current densities. When considering two wave functions, $\Psi(t)$ and $\Psi'(t)$, evolving from a shared initial state, denoted as $\Psi(t_0)$, the difference in current densities is

$$\frac{\partial}{\partial t}\left[\hat{\mathbf{j}}(\mathbf{r},t) - \hat{\mathbf{j}}'(\mathbf{r},t)\right]\bigg|_{t_0} = -\frac{1}{m_e} n(\mathbf{r},t_0)\, \boldsymbol{\nabla}\left(v(\mathbf{r},t_0) - v'(\mathbf{r},t_0)\right) \quad (5.81)$$

From Equation (5.81), it becomes evident that the current operators $\hat{\mathbf{j}}(\mathbf{r},t)$ and $\hat{\mathbf{j}}'(\mathbf{r},t)$ will exhibit infinitesimal differences after time t_0 if the two potentials $v(\mathbf{r},t_0)$ and $v'(\mathbf{r},t_0)$ are distinct, as noted in [173]. Consequently, when the condition stated in Equation (5.81) is met for $k=0$, it implies that the right-hand side of Equation (5.81) is nonzero, and thus, the two current densities $\hat{\mathbf{j}}(\mathbf{r},t)$ and $\hat{\mathbf{j}}'(\mathbf{r},t)$ will inevitably diverge infinitesimally later than t_0. If the smallest integer k for which Equation (5.81) is met is greater than zero, it implies that the potentials are identical, up to a constant, at the initial time t_0 but deviate at a subsequent time $t > t_0$. To address this scenario, we apply the Heisenberg equations of motion (EOM) for the current-density in each

system which is valid for any operator $\hat{O}$,

$$\mathrm{i}\frac{d}{dt}\langle\Psi(t)|\hat{O}(t)|\Psi(t)\rangle = \left\langle \Psi(t) \left| \mathrm{i}\frac{\partial}{\partial t}\hat{O}(t) + [\hat{O}(t), \hat{H}(t)] \right| \Psi(t) \right\rangle \tag{5.82}$$

iteratively k times to Eq.(5.81), results to

$$\frac{\partial^{k+1}}{\partial t^{k+1}} \left[\hat{\mathbf{j}}(\mathbf{r},t) - \hat{\mathbf{j}}'(\mathbf{r},t)\right]\Big|_{t_0} = -\frac{1}{m_e} n\left(\mathbf{r},t_0\right) \nabla \left(v_k\left(\mathbf{r},t_0\right) - v_k'\left(\mathbf{r},t_0\right)\right) \tag{5.83}$$

where the potentials are assumed to be the same up to the k-th derivative. The right hand side of Eq. (5.83) differs from zero in accordance to Eq.(5.81) for the smallest integer k, which then implies that $\hat{\mathbf{j}}(\mathbf{r},t) \neq \hat{\mathbf{j}}'(\mathbf{r},t)$ for $t > t_0$. This proves that

$$\mathbf{j}(\mathbf{r},t) \xrightarrow[\psi_0]{1:1} v_{ext}(\mathbf{r},t). \tag{5.84}$$

Secondly, the next step demonstrates that $n(\mathbf{r},t) \neq n'(\mathbf{r},t)$ by using the continuity equation Eq.(5.79) and rewriting it for both primed and unprimed system and taking the difference, we get

$$\frac{\partial}{\partial t}\left[n(\boldsymbol{r},t) - n'(\boldsymbol{r},t)\right] = -\nabla \cdot \left[\hat{\boldsymbol{j}}(\boldsymbol{r},t) - \hat{\boldsymbol{j}}'(\boldsymbol{r},t)\right]. \tag{5.85}$$

As shown previously, we can express the kth time derivative of the external potential by taking the time derivative of 5.83 at $t = t_0$, hence we obtain

$$\begin{aligned} \frac{\partial^{k+2}}{\partial t^{k+2}}\left[n(\mathbf{r},t) - n'(\mathbf{r},t)\right]\Big|_{t_0} &= -\boldsymbol{\nabla} \cdot \frac{\partial^{k+1}}{\partial t^{k+1}}\left[\mathbf{j}(\mathbf{r},t) - \mathbf{j}'(\mathbf{r},t)\right]\Big|_{t_0} \\ &= -\boldsymbol{\nabla} \cdot \left(\frac{1}{m_e} n\left(\mathbf{r},t_0\right) \boldsymbol{\nabla}\left(v_k\left(\mathbf{r},t_0\right) - v_k'\left(\mathbf{r},t_0\right)\right)\right). \end{aligned} \tag{5.86}$$

Under the assumption that the quantity $n(\mathbf{r},t)\left|\nabla v^2(\mathbf{r},t)\right|$ decays more rapidly than $1/\mathbf{r}^2$ for large $\mathbf{r}$ in both the primed and unprimed systems, it can be demonstrated that the right-hand side of Equation (5.86) cannot be identically zero, as detailed in [173]. Consequently, the densities $n(\mathbf{r},t)$ and $n'(\mathbf{r},t)$ will exhibit differences infinitesimally later than t_0. Hence, it follows that the electronic density $n(\mathbf{r},t)$ uniquely determines the time-dependent potential $v(\mathbf{r},t)$ up to a purely time-dependent function $c(t)$. This concludes the proof of the Runge-Gross (RG) theorem.

5.8.2 Kohn-Sham system of TDDFT

In this subsection we discuss the Kohn-Sham system of TDDFT. The ground state DFT as introduced in section 5.6 is based on the central idea of Kohn-Sham where an interacting system is associated with an effective non-interacting KS system. The idea of the TDKS is to extend the concept of the ground-state KS system to describe the time evolution of the electronic states and properties in response to external perturbations. In the paper authored by Runge and Gross, they proposed employing an auxiliary system composed of independent particles as a means to simplify the task of determining the action. This approach leads to a time-dependent version

of the Kohn-Sham equations, which can be found in theorem 4 of [173]. The theorem can be summarised as follows. *The exact time-dependent density of the system can be computed from the single particle orbital* $\varphi_j(\mathbf{r},t)$ *fulfilling the time-dependent Schrödinger equation*

$$i\frac{\partial}{\partial t}\varphi_j(\boldsymbol{r},t) = \left[-\frac{\nabla^2}{2} + v_{\mathrm{KS}}(\boldsymbol{r},t)\right]\varphi_j(\boldsymbol{r},t) \tag{5.87}$$

where the Kohn-Sham one-particle potential is given by

$$v_{KS}(\mathbf{r},t) = v_{ext}(\mathbf{r},t) + v_H(\mathbf{r},t) + v_{xc}(\mathbf{r},t) \tag{5.88}$$

here, the first term is the external potential, the second term is the Hartree potential $v_H(\mathbf{r},t)$ that accounts for the classical electrostatic interaction between the electron and it can be described as

$$v_H(\mathbf{r},t) = \int d^3\mathbf{r}' \frac{n(\mathbf{r}',t)}{|\mathbf{r}-\mathbf{r}'|} \tag{5.89}$$

and the final component of the equation corresponds to the time-dependent exchange-correlation XC potential $v_{xc}(\mathbf{r},t)$, which describes many-body effects beyond the hartree potential and has to be approximated in practice just like in static DFT. One can express the XC potential as a functional derivation of the XC energy [181]

$$v_{xc}(\mathbf{r},t) = \frac{\delta E_{xc}}{\delta n(\mathbf{r},t)} \tag{5.90}$$

The electronic density $n(\mathbf{r},t)$ of of the interacting system is obtained from the time-dependent KS orbital. The density reads

$$n(\mathbf{r},t) = \sum_{j=1}^{N} |\varphi_j(\mathbf{r},t)|^2 \tag{5.91}$$

By solving these time-dependent equations (5.87), (5.88) and the (5.91) self-consistently, the TDKS approach allows for the calculation of a wide range of time-dependent properties and phenomena, such as excited states, optical spectra, and dynamic response of the system to external fields (e.g laser pulse). Just as in the case of DFT, the XC potential needs to be approximated in TDDFT. One of such approximations is the adiabatic approximation which is considered as one of the first and simplest of all TDDFT approximations.

5.8.3 Adiabatic Approximation

The adiabatic approximation assumes that the XC potential in TDDFT is instantaneous and solely determined by the density $n(\mathbf{r})$ at time t. The adiabatic approximation states that the response of the system to external perturbations occurs on a much longer timescale compared to the motion of electrons. Therefore, the electronic structure of the system is assumed to adapt slowly to changes in the external perturbation. In this approximation, the density at time t

is inserted into the ground state density functional and the TDKS equation can be simplified, allowing for efficient calculations of electronic excitations and spectra in a wide range of systems. Performing substitution of the LDA functional one obtains the so called Adiabatic Local Density Approximation (ALDA) [182].

$$v_{xc}^{ALDA}([n](\mathbf{r},t) = v_{\mathrm{xc}}^{LDA}((n),\mathbf{r})\Big|_{n(\mathbf{r})\to n(\mathbf{r},t)} \tag{5.92}$$

The ALDA assumes that the exchange-correlation kernel in TDDFT is the same as the one used in the ground-state LDA. It therefore simplifies the calculation of the frequency-dependent XC potential and response function. It should be noted that, the ALDA retains all the problems already present in the LDA as highlighted in section 5.6.4. Several other approximations are commonly used to simplify the calculations and make them computationally tractable. Example of such approximations include the Linear response approximation, Random phase approximation (RPA) amongst others.

5.9 Linear response of TDDFT

Our general interest is to calculate the electronic excitations by using TDDFT. We already established that the time-dependent density of a fully interacting system equals the time-dependent density of a non-interacting KS system within the scope of the available approximation for v_{xc}. By employing the principles of perturbation theory to the Kohn-Sham system, it becomes feasible to determine the induced quantities and establish a connection between the response functions of the fully-interacting system and those of the non-interacting system. When subjecting a system to a time-dependent external potential one typically distinguishes between the linear and the non-linear regime. In the case where the applied external potential is sufficiently strong compared to the internal interactions the pertubation is nonlinear and obtaining the complete solution of the TDKS equation becomes necessary [176, 183]. However, this can be computationally demanding, particularly for large systems. An example of such a regime is the study of molecules and atoms interacting with intense laser fields, where non-linear phenomena such as High-Harmonic Generation and multi-photon ionization occur. TDDFT has proven successful in describing these non-linear phenomena [184].

In this thesis, the calculations primarily focused on utilizing a weak external perturbation, as further elaborated in the subsequent Chapter 4 and in Chapter 6. In this context, the linear-density response of the system is sufficient for describing physical observables such as excitation energies and optical absorption spectra.

To begin the linear response treatment in TDDFT, we consider the effective potential v_{KS} as described in Eq. (5.88)

$$\hat{v}_{\mathrm{eff}}[n](\mathbf{r},t) = \hat{v}_{\mathrm{ext}}(\mathbf{r},t) + \int d^3\mathbf{r}' \frac{n\,(\mathbf{r}',t)}{|\mathbf{r}-\mathbf{r}'|} + \hat{v}_{\mathrm{xc}}[n(\mathbf{r},t)](\mathbf{r},t) \tag{5.93}$$

and small perturbation to the density of the system which reads

$$n(\mathbf{r},t) = n^{(0)}(\mathbf{r}) + n_{\mathrm{ind}}^{(1)}\,(\mathbf{r},t) \tag{5.94}$$

where $n^{(0)}(\mathbf{r})$ is the unperturbed density. Inserting the expression for the density into Eq. (5.93) which can be expanded as

$$\hat{v}_{\text{eff}}[n](\mathbf{r},t) = \hat{v}_{\text{eff}}^{(0)}(\mathbf{r},t) + \hat{v}_{\text{eff}}^{(1)}(\mathbf{r},t) \tag{5.95}$$

where

$$\begin{aligned} \hat{v}_{\text{eff}}^{(0)}(\mathbf{r},t) &= \hat{v}_{\text{xc}}^{(0)}(\mathbf{r},t) + \int d^3\mathbf{r}' \frac{n^{(0)}(\mathbf{r}',t)}{|\mathbf{r}-\mathbf{r}'|}, \\ \hat{v}_{\text{eff}}^{(1)}(\mathbf{r},t) &= \hat{v}_{\text{ext}}^{(1)}(\mathbf{r},t) + \hat{v}_{\text{xc}}^{(1)}(\mathbf{r},t) + \int d^3\mathbf{r}' \frac{n_{\text{ind}}^{(1)}(\mathbf{r}',t)}{|\mathbf{r}-\mathbf{r}'|}, \end{aligned} \tag{5.96}$$

Here the $\hat{v}_{\text{xc}}^{(i)}(\mathbf{r},t)$ are obtained by expanding $\hat{v}_{\text{xc}}[n]$ around the ground-state density

$$\hat{v}_{\text{xc}}[n](\mathbf{r},t) = \hat{v}_{\text{xc}}\left[n^{(0)}\right](\mathbf{r},t) + \int dt' \int d^3\mathbf{r}' f_{\text{xc}}(\mathbf{r},t,\mathbf{r}',t')\left(n^{(0)}(\mathbf{r}',t') + n_{\text{ind}}^{(1)}(\mathbf{r}',t')\right) \tag{5.97}$$

where

$$f_{\text{xc}}(\mathbf{r},t,\mathbf{r}',t') = \left.\frac{\delta \hat{v}_{\text{xc}}[n](\mathbf{r},t)}{\delta n(\mathbf{r}',t')}\right|_{n=n_0} \tag{5.98}$$

is called the exchange correlation *kernel* which generally only depends on both t and t' and is a functional of the ground state density, n_0. The f_{xc} is discussed in more details in Section 5.9.2.

5.9.1 Density-density response function

We begin with the variation of the first order induced density.

$$n_{\text{ind}}^{(1)}(\mathbf{r},t) = \int d^3\mathbf{r}' \int dt' \frac{\delta n_{\text{ind}}^{(1)}(\mathbf{r},t)}{\delta \hat{v}_{\text{ext}}^{(1)}(\mathbf{r},t')} \delta \hat{v}_{\text{ext}}^{(1)}(\mathbf{r},t') \tag{5.99}$$

The density induced as a result of the external potential, denoted as $n_{\text{ind}}^{(1)}(\mathbf{r},t)$, is connected to the first-order component of the external potential $\hat{v}_{\text{ext}}^{(1)}(\mathbf{r},t')$ through the density-density response function of the fully interacting system.

$$n_{\text{ind}}^{(1)}(\mathbf{r},t) = \int d^3\mathbf{r}' \int dt' \chi_{\rho\rho}^{(1)}(\mathbf{r},t,\mathbf{r}',t')\, \hat{v}_{\text{ext}}^{(1)}(\mathbf{r},t') \tag{5.100}$$

while the induced density of the non-interacting system is related to the first order part of the *effective* potential $v_{eff}^{(1)}$. Thus it reads

$$n_{\text{ind}}^{(1)}(\mathbf{r},t) = \int d^3\mathbf{r}' \int dt' \chi_0^{(1)}(\mathbf{r},t,\mathbf{r}',t')\, \hat{v}_{\text{eff}}^{(1)}(\mathbf{r},t') \tag{5.101}$$

$\chi_0^{(1)}(\mathbf{r},t,\mathbf{r}',t')$ is the KS density-density response function. We can rewrite the response function χ as

$$\chi\left(\mathbf{r},t,\mathbf{r}',t'\right)=\frac{n_{\mathrm{ind}}^{(1)}\left(\mathbf{r},t\right)}{\delta v_{\mathrm{ext}}^{(1)}\left(\mathbf{r}',t'\right)}=\int dt'\int d\mathbf{r}'\frac{n_{\mathrm{ind}}^{(1)}\left(\mathbf{r},t\right)}{\delta v_{\mathrm{eff}}^{(1)}\left(\mathbf{r}',t'\right)}\frac{\delta v_{\mathrm{eff}}^{(1)}\left(\mathbf{r}',t'\right)}{\delta v_{\mathrm{ext}}^{(1)}\left(\mathbf{r}',t'\right)} \tag{5.102}$$

Here

$$\delta v_{\mathrm{eff}}\left(\mathbf{r}',t'\right)=\delta v_{\mathrm{ext}}\left(\mathbf{r}',t'\right)+\delta v_{H}[n]\left(\mathbf{r}',t'\right)+\delta v_{xc}[n]\left(\mathbf{r}',t'\right) \tag{5.103}$$

where

$$\delta v_{H}[n]\left(\boldsymbol{r}',t'\right)=\int\mathrm{d}t''\int\mathrm{d}^{3}r''\frac{\delta\left(t'-t''\right)}{\left|\boldsymbol{r}'-\boldsymbol{r}''\right|}n_{ind}^{(1)}\left(\boldsymbol{r}'',t''\right) \tag{5.104}$$

By inserting the expression for the effective potential Eq. (5.93) into Eq. (5.101) and setting the RHS of the Eq. (5.101) equals the RHS of Eq. (5.102), we obtain

$$\begin{aligned}&\int\mathrm{d}t'\int\mathrm{d}^{3}r'\chi_{\rho\rho}^{(1)}\left(\boldsymbol{r},t,\boldsymbol{r}',t'\right)\delta v_{\mathrm{ext}}\ \left(\boldsymbol{r}',t'\right)=\\&\int\mathrm{d}t'\int\mathrm{d}^{3}r'\chi_{0}^{(1)}\left(\boldsymbol{r},t,\boldsymbol{r}',t'\right)\delta v_{\mathrm{ext}}\ \left(\boldsymbol{r}',t'\right)+\int\mathrm{d}t'\int\mathrm{d}^{3}r'\chi_{0}^{(1)}\left(\boldsymbol{r},t,\boldsymbol{r}',t'\right)\\&\times\int\mathrm{d}t''\int\mathrm{d}^{3}r''\left[\frac{\delta\left(t'-t''\right)}{\left|\boldsymbol{r}'-\boldsymbol{r}''\right|}+f_{\mathrm{xc}}\left[n\right]\left(\boldsymbol{r}',t'\boldsymbol{r}'',t''\right)\right]\\&\times\int\mathrm{d}t'''\int\mathrm{d}^{3}r'''\chi\left(\boldsymbol{r}'',t'',\boldsymbol{r}''',t'''\right)\delta v_{\mathrm{ext}}\ \left(\boldsymbol{r}''',t'''\right)\end{aligned} \tag{5.105}$$

The above expression Eq. (5.105) is the density response function in time domain and it is an intrinsic property of the fully interacting system. This equation is often referred to as **Dyson equation** [185]. The **Dyson equation** can be expressed in frequency space as

$$\begin{aligned}&\chi_{\rho\rho}^{(1)}\left(\boldsymbol{r},\boldsymbol{r}',\omega\right)=\chi_{0}^{(1)}\left(\boldsymbol{r},\boldsymbol{r}',\omega\right)+\int\mathrm{d}^{3}r''\int\mathrm{d}^{3}r'''\chi_{0}^{(1)}\left(\boldsymbol{r},\boldsymbol{r}'',\omega\right)\\&\times\left[\frac{1}{\left|\boldsymbol{r}''-\boldsymbol{r}'''\right|}+f_{\mathrm{xc}}\left[n\right]\left(\boldsymbol{r}'',\boldsymbol{r}''',\omega\right)\right]\chi_{\rho\rho}^{(1)}\left(\boldsymbol{r}''',\boldsymbol{r}',\omega\right).\end{aligned} \tag{5.106}$$

The Dyson equation provides an exact framework for describing the linear density response. The response function $\chi_{\rho\rho}^{(1)}$ plays a crucial role in calculating various measurable quantities, such as the dielectric function, in linear response. The KS response function is calculated directly from first-order perturbation theory and it has a poles at the transition frequencies. The strength of the poles is related to the optical absorption intensities. In frequency space the response function can be written as,

$$\begin{aligned}&\chi_{0}^{(1)}\left(\boldsymbol{r},\boldsymbol{r}',\omega\right)=\\&\lim_{\eta\to0^{+}}\sum_{j,i}\left(f_{i}-f_{j}\right)\left[\frac{\varphi_{i}^{*}(\boldsymbol{r})\varphi_{j}(\boldsymbol{r})\varphi_{i}\left(\boldsymbol{r}'\right)\varphi_{j}^{*}\left(\boldsymbol{r}'\right)}{\omega-\left(\varepsilon_{j}-\varepsilon_{i}\right)+\mathrm{i}\eta}-\frac{\varphi_{i}(\boldsymbol{r})\varphi_{j}^{*}(\boldsymbol{r})\varphi_{j}\left(\boldsymbol{r}'\right)\varphi_{i}^{*}\left(\boldsymbol{r}'\right)}{\omega-\left(\varepsilon_{i}-\varepsilon_{j}\right)+\mathrm{i}\eta}\right],\end{aligned} \tag{5.107}$$

where $\varphi_i(\boldsymbol{r})$ and $\varphi_j(\boldsymbol{r})$ are occupied and unoccupied KS orbitals, respectively, and ε_i and ε_j are the corresponding KS eigenvalues. Formally, the equation can be expressed as

$$\chi_{\rho\rho}^{(1)}=\left(1-\chi_{0}^{(1)}f_{\mathrm{Hxc}}\right)^{-1}\chi_{0}^{(1)} \tag{5.108}$$

where all the components of RHS of the equation are obtained from the ground-state KS calculations, and f_{Hxc} is the Hartree exchange correlation kernel.

5.9.2 The Exchange Correlation Kernel

In order to fully solve the Dyson equation Eq. (5.106), certain approximations are necessary. In practice, the XC kernel f_{xc} is unknown and needs to be approximated based on the available approximations for v_{xc}. The simplest approximation is to directly set f_{xc} to zero, corresponding to the the Random Phase Approximation (RPA) [178, 186].

$$f_{xc}^{RPA} = 0 \tag{5.109}$$

One of the simplest non-zero approximations to XC kernels is the LDA which however widely used due to its computational simplicity as described previously. In this approximation, one directly inserts the expression for the effective potential v_{eff}^{LDA} into the definition of the f_{xc} . The local and adiabatic TDLDA exchange-correlation kernel can then be derived as discussed in [178] and references within the article.

$$f_{xc}^{ALDA}\left(\mathbf{r}, t, \mathbf{r}', t'\right) = \delta\left(\mathbf{r} - \mathbf{r}'\right)\delta\left(t - t'\right) f_{xc}^{HEG}(n)\Big|_{n=n(\mathbf{r},t)} \tag{5.110}$$

where

$$f_{xc}^{HEG}(n) = \frac{d}{dn} v_{xc}^{HEG}(n) \tag{5.111}$$

is the derivative of the XC potential of the Homogeneous Electron Gas (HEG). The ALDA kernel is local both in the space and time coordinates [177] as well as frequency-independent. One major limitations of frequency-independent kernels is that they do not generate new poles and fail to describe the doubly excites states of the system [187]. Other kernels can be obtained from the DFT kernels with the aim to balance accuracy and computational efficiency by incorporating different levels of complexity in describing the XC effects. Both RPA and the TDLDA therefore have some shortcomings especially when describing optical properties of of extended systems. It well known that TDLDA fails to describe the optical properties of solids accurately, due to their neglect of the non-local and frequency-dependent nature of the excite state interaction, which becomes crucial in describing the optical response of solids accurately. To overcome this challenges, other approximations have been proposed, e.g. the $\alpha-$kernel [188, 189]. This kernel accounts for the *long-range* contribution (LRC) of the XC kernel. In reciprocal space one can express the static LRC kernel as

$$f_{xc}^{LRC}(\mathbf{q}) = -\frac{\alpha}{q^2} \tag{5.112}$$

where the parameter α is material dependent.

5.10 Methods to calculate response functions/linear response in TDDFT

In this section methods to numerically calculate linear response within the framework of TDDFT is presented. Since several methods have been developed to numerically perform the

calculation, here we only highlight the most relevant methods used. Some commonly used methods for calculating the density response of Eq. (5.105) are: the time-propagation [190], the Casida equation [191] and the frequency-dependent Sternheimer equations [160, 192].

5.10.1 The Time propagation Method for calculating linear response

The time-propagation method is a numerical approach used to solve the TDKS equation (5.87) and calculate the linear response of a system. It involves propagating the time-dependent Kohn-Sham orbitals or electron density (5.91) in time under the influence of an external perturbation. As an example, we demonstrate how to use the time-propagation method to calculate polarizability. Suppose we apply a small δ-like perturbation to our system at $t = 0$. The perturbation is of the form

$$v_{ext}(\mathbf{r}, t) = -e\mathbf{r} \cdot boldsymbol E\delta(t - t_0) \tag{5.113}$$

where $\boldsymbol{E}$ is the electric field strength. The strength of the perturbation is set to be weak enough such that it creates only excitation within the linear response regime. Taking the FT of the perturbation, we obtain

$$v_{ext}(\mathbf{r}, \omega) = -e\mathbf{r} \cdot \boldsymbol{E}\frac{1}{2\pi}\int_{-\infty}^{\infty} d\omega e^{i\omega t} \tag{5.114}$$

By simply replacing the ground state wavefunctions in the TDKS Hamiltonian $\varphi_j(\mathbf{r}, t)$ with

$$\begin{aligned}\varphi_j\left(\mathbf{r}, t\right) &= \exp\left\{-\mathrm{i}\int_{-\infty}^{\infty}\mathrm{d}t\left[\hat{H}_{\mathrm{KS}}(t) - e\boldsymbol{r}\cdot\boldsymbol{E}\delta(t)\right]\right\}\varphi_j\left(\boldsymbol{r}, t=0\right)\\ &= \exp(\mathrm{i}e\boldsymbol{r}\cdot\boldsymbol{E})\varphi_j\left(\boldsymbol{r}, t\right)\end{aligned} \tag{5.115}$$

and taking the propagation of the free oscillations in time one obtain the time-dependent dipole moment.

$$\boldsymbol{\mu}(t) = -e\int d^3r\ \mathbf{r}n(\mathbf{r}, t). \tag{5.116}$$

From the dipole moment one can deduce the dynamical polarizability tensor $\alpha(\omega)$.Taking the Fourier transform of Eq. (5.116) and expanding it in series, one obtain

$$\mu_i(\omega) = \mu_i(0) + \alpha_{ij}(\omega)E_k + ... \tag{5.117}$$

where $\mu_i(\omega)$ is the Fourier transform of the time-dependent dipole moment in direction i, and $\mu_i(0)$ is the static dipole moment.The dynamical polarizability tensor is given by

$$\alpha_{ij}(\omega) = \frac{1}{E_k}\int_0^{\infty}\mathrm{d}t\left[\mu_i(t) - \mu_i\left(0\right)\right]\mathrm{e}^{-\mathrm{i}\omega t} + ... \tag{5.118}$$

Hence, the absorption spectrum is directly related to the imaginary part of the diagonal component of the dynamic polarizability, denoted as $\Im[\alpha_{ij}(\omega)]$. Since the above equation involves involves integrating over an infinite amount of time which in practice one does not propagate over an infinite amount of time, one has to add a decaying function such that all excitations decay back to their initial state. Therefore, the dynamical polarizability is finally given by

$$\alpha_{ij}(\omega) = \frac{1}{E_k}\int_0^{\infty}\mathrm{d}t\left[\mu_i(t) - \mu_i\left(0\right)\right]\mathrm{e}^{-\mathrm{i}\omega t}\mathrm{e}^{\eta t} + ... \tag{5.119}$$

where η is the decaying rate. Finally the expression for the optical absorption cross section tensor can be be expressed as

$$\sigma(\omega) = \frac{4\pi\omega}{c}\Im[\alpha(\omega)] \tag{5.120}$$

In the next Chapter 6, the time propagation method is utilized to determine the optical conductivity $\sigma(\omega)$ and dielectric function $\epsilon(w)$ through numerical pump-probe calculations.

5.11 summary

This chapter reviewed methods for solving the electronic structure problem, beginning with the initial approximations used to address the many-body Schrödinger equation. We then introduced DFT in both its static and time-dependent forms, highlighting the key approximations required for each. In both approaches, the density n serves as the central quantity, from which the potential is derived. The potential, in turn, determines the wavefunctions, allowing for the calculation of the density. Using TDDFT, we derived and demonstrated the density response function χ for an *interacting* system, showing its connection to the *non-interacting* density response function of the KS auxiliary system. These non-interacting response functions are obtained from the ground state, which is determined by self-consistently solving the static KS equations of DFT. Finally, we showed methods used to calculate the response functions in TDDFT.

This page was intentionally left blank.

6 Theoretical Spectroscopy

6.1 Introduction

In this chapter, we build upon the theoretical foundations established in the preceding Chapter 5, where we explored the foundational theories of DFT and TDDFT. Extending this theoretical framework, we derive the necessary equations required for theoretical spectroscopy laying the groundwork for successful numerical calculations.

6.2 Model TDKS equation for solids

As described in section 5.8.2, the TDKS system is *a non-interacting* system which can be described by a single Slater determinant, whereby each orbital in the Slater determinant obeys the one-body Schrödinger like equation. The equation can be described as

$$i\frac{\partial}{\partial t}\varphi_j(\boldsymbol{r},t) = \left[\frac{\boldsymbol{p}^2}{2} + v_{\mathrm{KS}}(\boldsymbol{r},t)\right]\varphi_j(\boldsymbol{r},t) \tag{6.1}$$

where φ_j is the Kohn-Sham orbital, j is an orbital index, and v_{KS} is the one body potential that reproduces the identical density of the initial many-body system in Eq. (5.26). The components of v_{KS} remain the same as described in Eq. (5.88).

To practically simulate light-induced electron dynamics in solids, it is necessary to review the form of the TDKS equation in Eq. (6.1). First, the *dipole approximation* is applied to the electric field due to the slow variation of the electric field over the spatial extent of the atomic system. This approximation allows for a simplified treatment of the interactions. In this approximation the external potential can be written as

$$v_{ext}(\boldsymbol{r},t) = \mathbf{E}(t)\cdot\boldsymbol{r} \tag{6.2}$$

where $\mathbf{E}(t)$ is the time dependent spatially uniform electric field. To describe the Hamiltonian that is compatible with the symmetry of solids, another approximation is required. This is because, the dipole operator is not defined for periodic systems. The gauge transformation is applied to the eigenfunction in Eq. (6.1), expressed as

$$\varphi_j(\boldsymbol{r},t) = e^{-i\mathbf{A}(t)\cdot\mathbf{r}}\tilde{\varphi}_j(\boldsymbol{r},t) \tag{6.3}$$

with these approximations, the Eq.(6.1) can be rewritten as

$$i\frac{\partial}{\partial t}\tilde{\varphi}_j(\boldsymbol{r},t) = \Big[\frac{1}{2}(\boldsymbol{p}+\boldsymbol{A}(t))^2 + e^{-i\boldsymbol{A}(t)\cdot\boldsymbol{r}}v_{ion}(\boldsymbol{r},t)e^{i\boldsymbol{A}(t)\cdot\boldsymbol{r}} + v_H(\boldsymbol{r},t) + v_{xc}(\boldsymbol{r},t)\tilde{\varphi}_j(\boldsymbol{r},t)\Big] \tag{6.4}$$

where the v_{xc} and v_H maintain their usual definitions while v_{ion} is a spatially non-local operator due to the formulation of the pseudopotentials. $\mathbf{A}(t)$ is the vector potential which described the contribution of the electric field. The vector potential is related to the electric field by

$$\mathbf{A}(t) = -\int^t dt'\mathbf{E}(t'). \tag{6.5}$$

Therefore, the Hamiltonian described in Eq.(6.4) has the same periodicity as the ionic potential v_{ion} and also, the same symmetry as the crystals. To describe properly the contributions of the transformed eigen states, which can be described by using the time-dependent Bloch ansatz as described in subsection 4.3.1. Hence, the eigenstates becomes

$$\tilde{\varphi}_j(\boldsymbol{r},t) = e^{ik\cdot r}u_{bk}(\boldsymbol{r},t) \tag{6.6}$$

where the $u_{bk}(\boldsymbol{r},t)$ are the Bloch orbitals and also have the same periodicity as the ionic potential, they're labelled by the band index b as well as the wave vector k which replaces the orbital index j. With the above approximations, the time-dependent Kohn-Sham equation, as represented by Eq. (6.1) for the Bloch orbitals, can be reformulated as follows

$$i\frac{\partial}{\partial t}u_{bk}(\boldsymbol{r},t) = \hat{h}_{KS,k}(t)u_{bk}(\boldsymbol{r},t), \tag{6.7}$$

where the Hamiltonian $\hat{h}_{KS,k}(t)$ is given by

$$\boxed{\hat{h}_{KS,k}(t) = \frac{1}{2}(\mathbf{p}+\mathbf{k}+\mathbf{A}(\mathbf{t}))^2 + +e^{-i(\boldsymbol{A}(t)+\mathbf{k})\cdot\boldsymbol{r}}v_{ion}(\boldsymbol{r},t)e^{i(\boldsymbol{A}(t)+\mathbf{k})\cdot\boldsymbol{r}} + v_H(\boldsymbol{r},t) + v_{xc}(\boldsymbol{r},t)} \tag{6.8}$$

The enclosed equation represents the crucial equation of motion employed to describe the electron dynamics induced by light in solids. Solving the time-dependent Kohn-Sham equations 6.8 entails addressing an initial value problem, where the primary objective is to numerically time propagate the initial state until reaching a specified final time t_f.

6.2.1 Numerical Considerations

To effectively solve the time-dependent Kohn-Sham equations 6.8 involves employing a numerical approach that takes into consideration factors like computational costs, precision, and the characteristics of the dynamics. The real-space code **Octopus** [159–161, 193] is utilized for this purpose, incorporating the real space grid representation as outlined in [194–198], and orbital basis expansion [199]. Further details about these methodologies can be found in c.f Appendix C.

In real-time electron dynamics calculations, the time-dependent Kohn-Sham equations in Bloch orbitals can be rewritten in the integral form, which can be expressed as

$$u_{bk}(\boldsymbol{r}, t_f) = \hat{U}(t_f, t) u_{bk}(\boldsymbol{r}, t) \tag{6.9}$$

where $\hat{U}$ is the time-evolution operator and is defined as

$$\hat{U}(t', t) = \hat{T} exp\left[-i \int_t^{t'} d\tau \hat{h}_{KS}(\tau)\right] \tag{6.10}$$

$\hat{T}$ is the time-ordering operator. The exponent in the given expression cannot be directly applied, necessitating an appropriate approximation. Likewise, to minimize the error stemming from the propagation from the initial time t to a specific time t_f, we partition the time interval into smaller sub-intervals of length Δt. Therefore, the Bloch functions are then propagated from $t \to t + \Delta t$, also from $t + \Delta t \to t + 2\Delta t$ and so on. One of such approximations to the exponential, is the direct expansion of the exponential in power series of Δt. This gives us

$$\hat{U}(t + \Delta t, t) \approx \sum_{l=0}^{k} \frac{[-i\Delta t \hat{h}_{KS}(t + \Delta t/2)]^l}{l!} + \mathcal{O}\left(\Delta t^{k+1}\right) \tag{6.11}$$

The above equation Eq. (6.11) regrettably lacks a crucial property of the Kohn-Sham time-evolution operator: unitarity. In order to fulfill this unitarity, alot of propagation methods have been proposed and here the mid-point rule [200] is applied to estimate the integral in the exponential. The mid-point rule allows us to use the Hamiltonian at $t + \Delta t$. The time propagation can be expressed as

$$u_{bk}(\boldsymbol{r}, t + \Delta t) \approx \exp\left[-i\Delta t \hat{h}_{KS,\mathbf{k}}(t + \Delta t/2)\right] u_{bk}(\boldsymbol{r}, t) \tag{6.12}$$

where Δt is the smaller sub-intervals in time. In practice, we employ the fourth order Taylor expansion of Eq. (6.12)

$$u_{b\boldsymbol{k}}(\boldsymbol{r}, t + \Delta t) \approx \sum_{n=0}^{4} \frac{1}{n!} \left(-i\Delta t \hat{h}_{KS,\boldsymbol{k}}\left(t + \frac{\Delta t}{2}\right)\right)^n u_{b\boldsymbol{k}}(\boldsymbol{r}, t) \tag{6.13}$$

The process of time-propagation in this context can only be described through matrix operations on the state vectors. This paved way for performing the time-propagation in real-space grid representation.

Another way of performing the time propagation is by the use of the time reversal symmetry based propagator. In this method, time propagating backwards with $\Delta t/2$ beginning from $u_{b\boldsymbol{k}}(\boldsymbol{r}, t + \Delta t)$ or propagating forwards in time with $\Delta t/2$ starting from $u_{b\boldsymbol{k}}(\boldsymbol{r}, t)$ must yield identical results. The propagator can be expressed as

$$u_{b\boldsymbol{k}}(\boldsymbol{r}, t+\Delta t) = \exp\{-i\frac{\Delta t}{2}\hat{h}_{KS,\mathbf{k}}(t+\Delta t)\} \times \exp\{-i\frac{\Delta t}{2}\hat{h}_{KS,\mathbf{k}}\} \tag{6.14}$$

this form of propagator is known as the *enforced time-reversal symmetry* (ETRS) propagator. Other forms of propagators include Approximated Enforced Time-Reversal Symmetry (AETRS) which is a modified version of ETRS, Magnus expansions, Commutator-Free Magnus Expansions, the Runge–Kutta Schemes and so on. Details of these forms of propagators can be found in [201, 202].

6.2.2 Absorption Spectra from Time-Evolution

Our goal is to obtain the optical absorption spectra using TDDFT by time propagating the TDKS equation using the method proposed by Yabana and Bertsch in [194]. Throughout this thesis, this methodology is applied for all TDDFT computations due to its simplicity and directness unless stated otherwise. The "kick" technique was employed, which involves perturbing the system under investigation with a weak δ-like perturbation, to compute the equilibrium optical conductivity, TAS as well as the Tr-XAS.

To obtain the optical conductivity, we have to solve the Eq.(6.8) with the outlined approximations. The most important result we obtain is the time-dependent induced electric current. The total electric current can be described as

$$\boldsymbol{J}(t) = -\frac{1}{\Omega}\sum_{b}\int_{BZ} d\boldsymbol{k} f_{b\boldsymbol{k}} \int_{\Omega} d\boldsymbol{r} u^{*}_{b\boldsymbol{k}}(\boldsymbol{r}, t)\boldsymbol{\pi}_{\boldsymbol{k}}(t) u_{b\boldsymbol{k}}(\boldsymbol{r}, t) \tag{6.15}$$

where Ω is the volume of the unit-cell, f_{bk} is the occupation factor for each orbital, b is the band index and k is the wave-vector and π_k is the kinetic momentum which can be defined as

$$\begin{aligned} \boldsymbol{\pi}_{\boldsymbol{k}}(t) &= \frac{1}{i}\left[\boldsymbol{r}, \hat{h}_{KS,\boldsymbol{k}}(t)\right] \\ &= \boldsymbol{p} + \boldsymbol{k} + \boldsymbol{A}(t) + \frac{1}{i}\left[\boldsymbol{r}, e^{-i(\boldsymbol{A}(t)+\boldsymbol{k})\cdot\boldsymbol{r}} v_{ion}(\boldsymbol{r}, t) e^{i(\boldsymbol{A}(t)+\boldsymbol{k})\cdot\boldsymbol{r}}\right]. \end{aligned} \tag{6.16}$$

where the contribution of the ionic potential is included due to the nonlocality of the pseudopotential. Derivation of the electric current can be found in c.f Appendix C.

To calculate the equilibrium optical properties of the system under investigation, we applied weak perturbation of the form

$$\boldsymbol{E}(t) = E_0 \boldsymbol{e}_x \delta(t) \tag{6.17}$$

with E_0 been the strength of the perturbation, $\boldsymbol{e}_x$ is the unit vector along the x-direction. When the perturbation is applied in one direction, it produces a force in another direction due to the an isotropic nature of constant energy surfaces in solids. The induced current density in time domain is related to the applied perturbation by the linear tensorial relation

$$\boldsymbol{J}_\alpha(t) = \sum_{\beta=[x,y,z]} \int_{-\infty}^{t} dt' \sigma_{\alpha\beta}(t-t')\boldsymbol{E}_\beta(t') \tag{6.18}$$

where $\boldsymbol{J}_\alpha(t)$ is the α-component of the total current $\boldsymbol{J}$(t), $\boldsymbol{E}_\beta(t)$ is the β-component of the electric field $\boldsymbol{E}$(t), the optical conductivity tensor $\sigma_{\alpha\beta}$ is a second rank tensor. For free electrons in an isotropic medium, the optical conductivity tensor has only diagonal elements, however generally it and can be written as

$$\sigma = \begin{pmatrix} \sigma_{xx} & \sigma_{xy} & \sigma_{xz} \\ \sigma_{yx} & \sigma_{yy} & \sigma_{yz} \\ \sigma_{zx} & \sigma_{zy} & \sigma_{zz} \end{pmatrix} \tag{6.19}$$

By taking the Fourier transformation of Eq. (6.18), the optical conductivity σ is related to the current and electric field via the following equation

$$\boldsymbol{J}_\alpha(\omega) = \sum_{\beta=[x,y,z]} \sigma_{\alpha\beta}(\omega)\boldsymbol{E}_\beta(\omega) \tag{6.20}$$

The equation above is significant and will be utilized in calculating the static and transient optical conductivity of hBN in the next section. As an example, the x-component of the optical conductivity can be obtained using the equation below.

$$\sigma_x(\omega) = \frac{\boldsymbol{J}_x(\omega)}{\boldsymbol{E}_{0,x}(\omega)} \tag{6.21}$$

Using this relationship, one can also evaluate the Imaginary part of the dielectric function $\epsilon(\omega)$ of a solid using the following expression

$$\Im\epsilon(\omega) = 1 + \frac{4\pi i}{\omega}\sigma(\omega). \tag{6.22}$$

6.3 Summary

In this chapter, we showed the necessary equations to perform numerical simulations for a system of solid. We begin by outlining the model TDKS equation for solids and the numerical approximations that forms the basis of our computational approach. The methods and approximations are crucial for modelling the optical properties our system. Furthermore, we establish the essential relationship between the time-dependent induced current and the electric field, which is pivotal for determining the optical conductivity $\sigma(\omega)$. This connection provides a better understanding on on how our system response to an external field can be analyzed.

This page was intentionally left blank.

7 Equilibrium X-ray Absorption Spectrum of 2D hBN

7.1 Introduction

Two-dimensional (2D) materials have garnered considerable attention in recent years due to their unique electronic, thermal and optical properties. Among these materials, hexagonal boron nitride (hBN) stands out as a promising candidate for a wide range of applications, including as a dielectric in nanoelectronic devices and as a substrate for graphene-based systems. Understanding the electronic structure and excitations of hBN is crucial for harnessing its potential.

As described in Chapter 4, one powerful tool for probing the electronic structure of materials is XAS, a versatile technique that can provide insights into the unoccupied electronic states. In particular, the equilibrium X-ray absorption spectrum of hBN offers a window into its electronic excitations and the dynamics of its charge carriers.

In this chapter, we study the equilibrium X-ray absorption spectrum of monolayer and bulk hBN using DFT and the model equations described in Chapter 6 as implemented in octopus code. Additionally, we investigate the impact of different approximations to the XC functional and other theoretical approaches, shedding light on the challenges and opportunities associated with modeling the electronic excitations in this unique 2D material.

7.2 Hexagonal Boron Nitride

Hexagonal Boron Nitride (hBN) exhibits a honeycomb structure very similar to that of graphene, with sp^2 hybridized Boron and Nitrogen atoms alternatively bonded together in a basal plane as shown in figure 7.1. This unique structure of hBN leads to some properties, such as high chemical and thermal stabilities, enhanced thermal and electrical conductivity [203, 204]. Thus hBN have attracted increasing attention in many fields and have been used in various applications such as dielectrics, substrates, deep UV light emitters and other applications. However, unlike graphene the polar covalent B-N bond reduced electron delocalization and created a large bandgap ($\approx 6eV$) in the ultraviolet (UV) region, making hBN a wide bandgap material.

We begin by calculating the electronic properties of monolayer and bulk hBN using DFT as implemented in the octopus code, by determining their electronic bandstructures. The XC effects have been treated approximately with the LDA functional. The lattice constant and the bandgaps obtained are reported in the Table 7.1 below. The structural parameters shows good agreement with both experimental and other theoretical results [205, 206] with an average error of approximately 1%. The bandstructures, calculated using the equilibrium lattice parameters, are presented in Figure 7.2. For the monolayer, the direct LDA bandgap is calculated to be

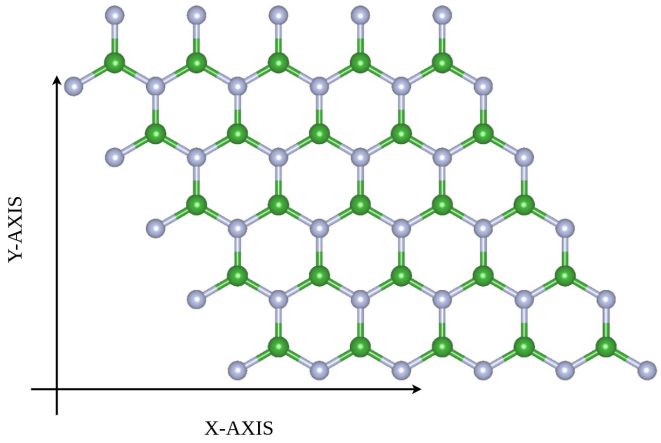

Figure 7.1: Atomic Configuration of Bulk hBN. The green coloured balls are the Boron atoms while silver coloured are Nitrogen atoms.

	a(Å)	c	$E_g(eV)$
Monolayer	2.520	—	4.62
Bulk	2.502	7.707	4.45

Table 7.1: Calculated lattice constants in Å, bandgap E_g (eV) for monolayer and bulk hBN.

4.62eV at the K point as illustrated in the Figure 7.2 (a). Similarly, Figure 7.2 (b) shows the calculated bandstructure of bulk phase, showing an indirect bandgap of 4.45eV between the H and M point. These values are in close agreement with previously reported data in [206, 207].

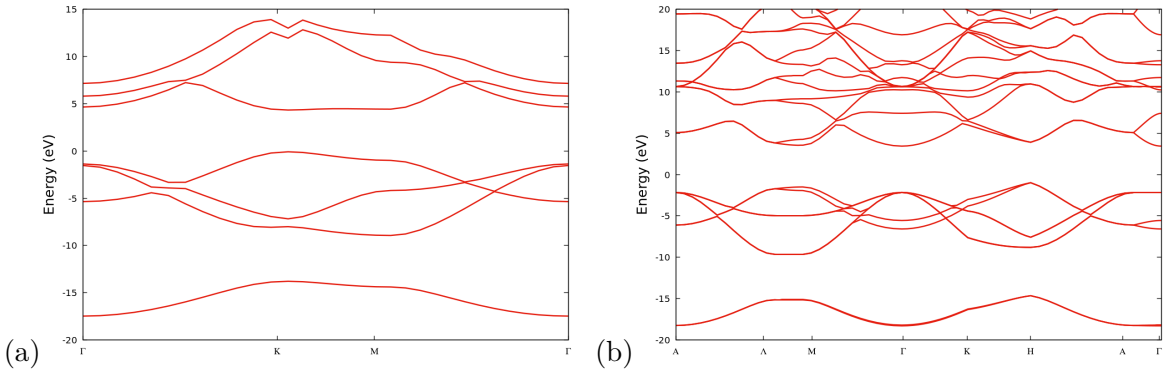

Figure 7.2: Electronic bandstructure of (a) monolayer, and (b) bulk hexagonal BN.

In their article Arenal *et al.*. [8] studied the B K-edge using the high-angular-resolution electron energy loss spectroscopy (EELS) in hBN. The study demonstrated the absorption spectrum of B K-edge with the associated features as shown in Figure 7.3. The main feature in the absorption spectrum is the narrow and intense peak at 192eV which is the main core excitonic peak in XAS experiments.

To calculate the equilibrium optical properties of hBN, we first calculate the ground state properties and then evaluate the time evolution of the KS orbitals, to obtain the XAS of hBN both in monolayer and bulk phase. To simulate the equilibrium optical properties we use a vector potential of the form

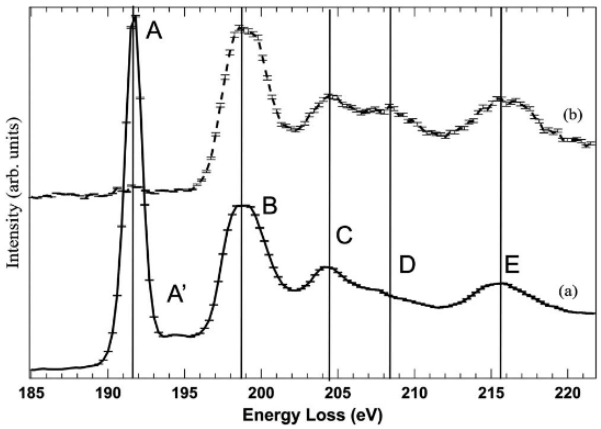

Figure 7.3: Boron K-edge EELS absorption spectra. Figure taken from [8].

$$\boldsymbol{A}(t) = -E_{0,x}\boldsymbol{e}_x\Theta(t) \tag{7.1}$$

with $\Theta(t)$ being the Heaviside step function, the field strength E_0 is set to be 8×10^{-4}a.u which is weak enough to induce distortion only within the linear regime. The wavefunctions are presented on a real-space grid with a spacing of $\Delta x = 0.20$ a.u. The box size L = 30a.u in monolayer, pulse duration T_f = 10fs, and a time steps $\Delta t = 0.01$ a.u were employed in all calculations presented in this section. The unit cell of monolayer hBN consist of two atoms with D_{3h} symmetry while the bulk consist of four atoms with D_{6h} symmetry. The Brillouin zone is discretized into $33 \times 33 \times 1$ $\boldsymbol{k}$-points in both cases.

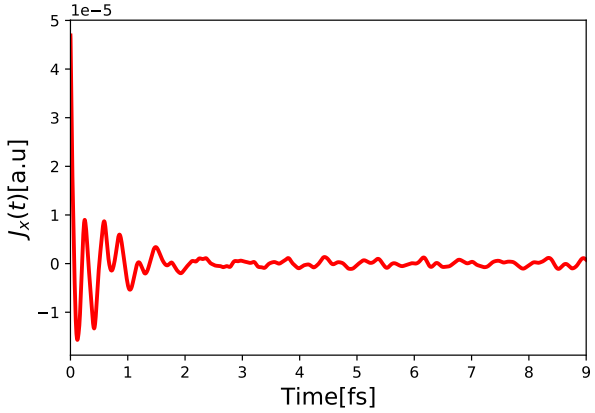

Figure 7.4: Linear response calculation for Bulk hBN. The figure shows an electric current induced by an impulsive distortion at t = 0.

Figure 7.4 shows the x-component of the time-dependent induced current Eq. (6.15) by the vector potential. The current is suddenly induced at $t = 0fs$ and shows oscillatory behaviour until the end of the pulse. With the time-dependent induced current, the optical conductivity $\sigma(\omega)$ as shown in Eq. (6.20) is obtained.

Figure 7.5 shows the real part of optical conductivity $\sigma(\omega)$ at the Boron K-edge for the in-plane direction alongside the EELS experimental data (red dotted points). The B K-edge is obtained by simulating the 1s core-level using the *all-electron* framework with the delta-like

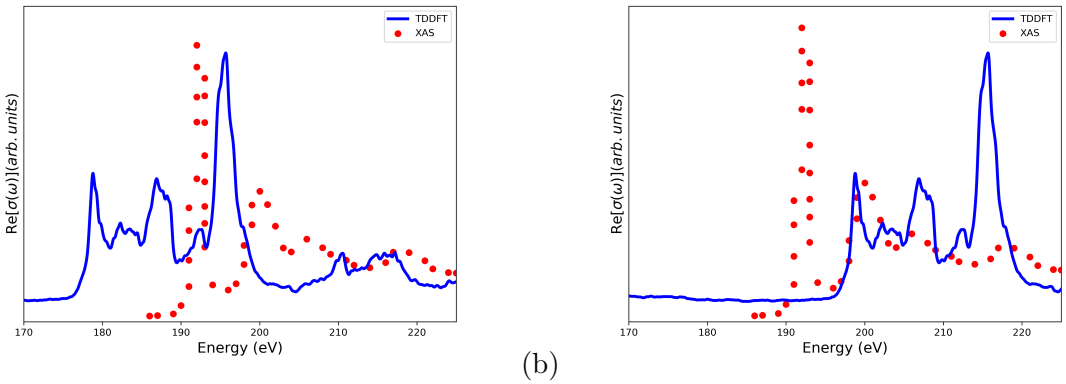

Figure 7.5: Linear response calculation for bulk hBN. Figure (a) shows the real part of equilibrium optical conductivity $\sigma(\omega)$ at the Boron K-edge obtained by an impulsive distortion at $t = 0$ in blue curve compared to the EELS spectra in red dotted lines. (b) The theoretical B K-edge shifted so that the $1s \rightarrow \pi^*$ is aligned with the experimental data.

distribution. The 1s core electron is described by a delta charge which is placed on a grid point. The remaining atoms are treated with a pseudopotential [1]. The main feature in the figure is the peak occurring at approximately 177eV, primarily associated with $1s \rightarrow \pi^*(2P_z)$ transitions while the second peak is associated to the $1s \rightarrow \sigma^*$. Similarly, the remaining peaks are as a result of the antibonding involving the N-$2s$ orbitals and B-$2p_{xy}$. Notably, in this bulk hBN, the π^* peak is relatively weak due to the orthogonal orientation of the electronic vector with respect to the polarization of the electric field, resulting in its diminished appearance. In contrast, various XAS experiments and theoretical investigations, such as those cited in [8, 203, 208, 209], typically place this peak within the energy range of 190eV $\rightarrow$ 192eV, characterizing it as a very strong excitonic peak—a bound state formed by an electron-hole pair as depicted by the spectra in the plot. Furthermore, in some experiments [210], the π^* resonance excitonic peak undergoes a split due to electron-phonon coupling. Our results show peaks at lower energies compared to experimental/calculated values and completely omits the excitonic peak. This discrepancy can be attributed to a well-known issue associated with the LDA, which tends to underestimate the bandgaps of materials, as elaborated in Section 5.6. Since the K-edge absorption involves transition from the $1s$ core state of the B atom to an unoccupied states, the LDA does not explicitly account for core-hole effects thus leading to an inaccurate description of the K-edge.

Describing core excitons poses significant challenges when employing a real-space code such as Octopus [195]. To address these challenges, we explore the possibility to use (TD)DFT+U, as described in [211], particularly because our material exhibits correlation effects. Given the localization of electrons, DFT+U accurately gives a good representation of the electronic structure contributed by core. On top of the same setting as described above, we calculate the equilibrium absorption spectrum at the B K-edge with (TD)DFT+U with the calculated values of the effective U for the core-levels and other states as shown in Table 7.2.

The Figure 7.6 shows the absorption spectrum, demonstrating the real part of the optical conductivity computed using DFT+U, and they are compared with the LDA results. A noticeable difference emerges when we compare the DFT+U outcomes with those obtained through

[1] An example of the input file for such calculation is provided in c.f Appendix F

Element	Orbitals	Effective U (eV)
B	1s	116.5652
B	2s	0.074694
B	2p	0.005986
N	2s	12.23099
N	2p	7.361936

Table 7.2: The effective values of U for the core-levels and other states from the DFT+U calculations.

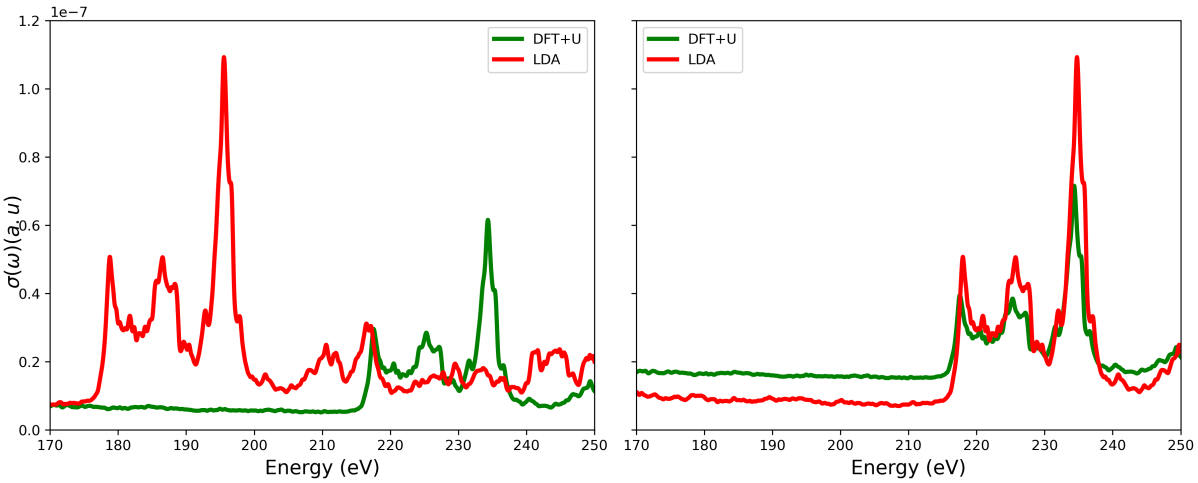

Figure 7.6: Comparison of the equilibrium optical conductivity $\sigma(\omega)$ between the DFT+U approach and the results obtained from LDA. The green solid line shows the absorption spectrum obtained by LDA+U while the red solid line is obtained from LDA. The peak at 177eV is shifted by almost 40eV in the LDA+U calculation as shown in the right side combined plot.

LDA. Specifically, the DFT+U result exhibit an overestimation of the K-edge, with the primary peak occurring at approximately 218eV. Likewise, the DFT+U approach falls short as well in capturing the excitonic peak occurring at approximately 192eV. In general, the characteristics observed in both calculations are nearly identical, except for the overestimation of the energy of the K-edge.

In order to calculate the core excitons in our system, challenges were encountered when using the DFT+U approach. To overcome these challenges, we used another method known as the "supercell approach". This methods involves expanding the lattice by creating a larger supercell, which comprises of multiple unit cells. Within the supercell, we introduce a core hole, which serves as a placeholder for the excited electron. The presence of the core hole allows us to simulate excitonic behavior within the supercell by calculating the optical conductivity with the core hole. The core atom is treated as an all electron with a delta charge distribution while the remaining atoms are treated with a pseudopotential. The core-hole modelled in this supercell approach is then screened by all the valence electrons in the neighbouring atoms.

To determine the equilibrium optical conductivity $\sigma(\omega)$ through this method, we utilized a supercell with dimensions of $3 \times 3 \times 3$ for the bulk phase and the size of the supercell is found to be sufficiently large to decrease the core-hole to core-hole interactions. This supercell consisted

of 108 atoms. A k-point sampling of $3 \times 3 \times 1$ was used to sample the Brillouin zone effectively while in the unitcell, the k-point sampling of $9 \times 9 \times 3$ was used.

For the excitation of electronic dynamics within the supercell, we employed a probe pulse. This pulse, polarized along the x-axis, had a central frequency of $\omega = 177$eV and was characterized by a $\sin^4$ envelope function. The envelop function is defined as

$$\mathbf{A}(t) = -\frac{E_0}{\omega}\mathbf{e_x}(sin^4(\frac{\pi}{s}t))(1 - \Theta(t - s)) \tag{7.2}$$

where s is the width of the pulse in time domain, Θ is the Heaviside step function. The vector potential and electric field are shown in Figure 7.7 with a duration of $10fs$. The field strength E_0 is set to 8×10^{-4}a.u and with an Intensity $I = 1.3 \times 10^{13} W/cm^2$.

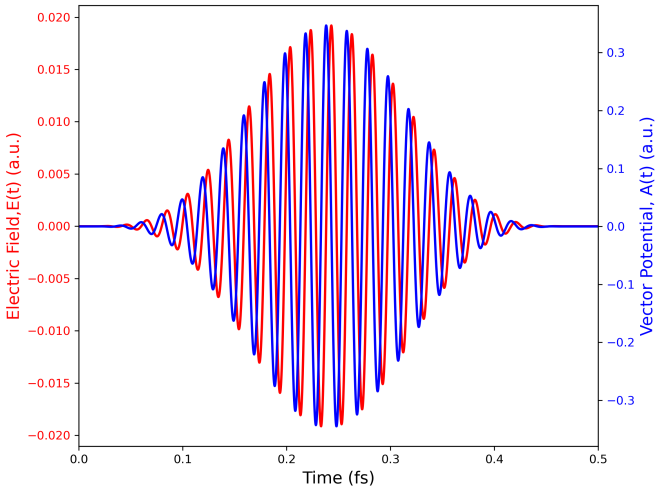

Figure 7.7: Time profile of the Vector potential and the electric field from the sin^4 envelop probe pulse in Eq. (7.2). The vector potential is used to obtain the equilibrium optical conductivity.

At the initial time, i.e $t = 0$, the probe pulse excites the electron dynamics within the system. This results in the inducing of the time-dependent current Eq. (6.15) as shown in Figure 7.8.

Figure 7.8 shows the time-dependent induced current by the probe pulse after interacting with the system. In panel (a), the total current is shown for the whole duration of the probe pulse. In panel (b) the induced current is shown until 0.5fs, the current shows oscillatory behaviour from $t = 0$, i.e. is is largely following the pulse coherently. while in panel (c), the current is shown until the end of the pulse and showing the sustained oscillations at the excited eigenmodes of the system. Using Eq. (6.20), we take the FT of the current and the electric field and subsequently evaluate the real part of the optical conductivity $\sigma(\omega)$.

Figure 7.9 shows the Fourier transform of the induced current and vector potential. The FT of the field shows the pulse is centered at around the absorption edge and an appearance of a sharp peak at in the FT of the current at around 177eV. Applying Eq. (6.21), we obtain the real part of the optical conductivity $\sigma(\omega)$ at B K-edge for the $3 \times 3 \times 3$ supercell.

Figure 7.10 shows the optical conductivity of hBN using the supercell approach. The K-edge is at 177 eV. The plot shows that the peaks in the optical conductivity of the $3 \times 3 \times 3$ supercell

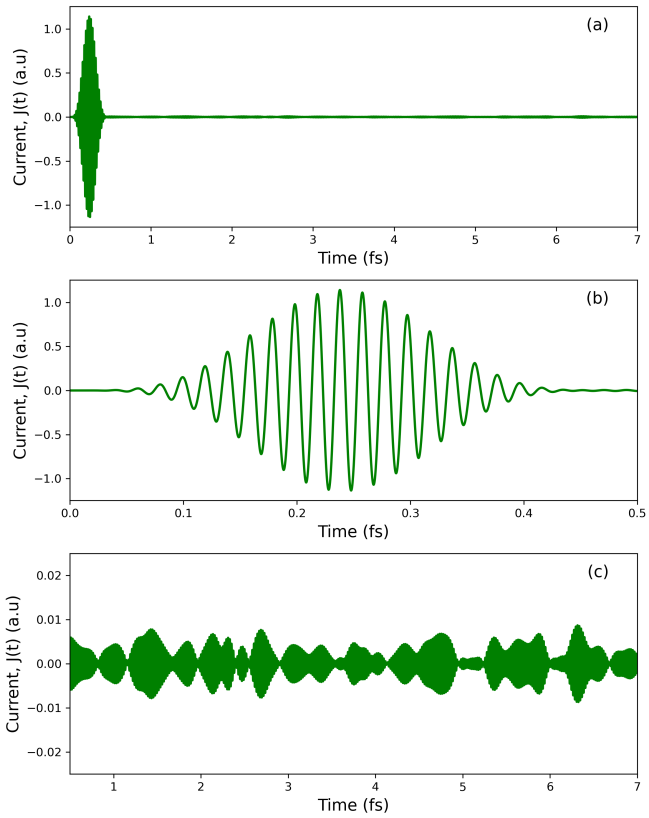

Figure 7.8: Time-Dependent Current Induced by the sin^4 probe pulse at $t = 0$ in the supercell approach. In (a), the total current for the whole duration of the pulse. (b) shows zoomed-in view of the total current from 0 to 0.5fs and (c) zoomed-in view of the total current from 0.5fs to 7fs. Current is induced at $t = 0$ and exhibits oscillatory behavior throughout the pulse's duration.

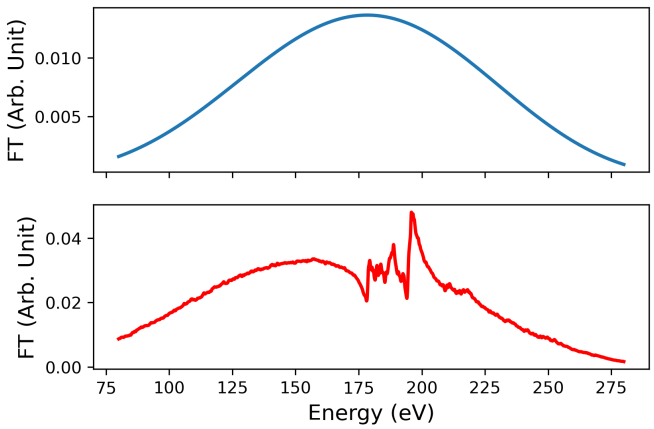

Figure 7.9: Fourier transforms of vector potential (blue solid line) and the time-dependent current induced (red solid line) by the cos^4 probe pulse at $t = 0$ in the supercell approach.

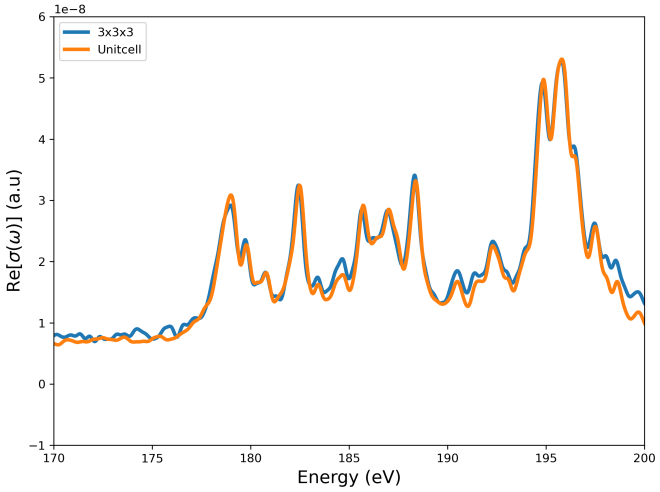

Figure 7.10: Comparison of the optical conductivity of a unit cell and a $3 \times 3 \times 3$ supercell for bulk hBN. The K-edge of the supercell is at a slightly lower energy than the K-edge of the unit cell.

are a marginally higher in intensity than the optical conductivity of the unit cell at all energies. This is because the $3 \times 3 \times 3$ supercell is 27 times larger than the unit cell and therefore has more valence states. The K-edge of the $3 \times 3 \times 3$ supercell shows pre-edges at a slightly lower energy than the K-edge of the unit cell. This is because the $3 \times 3 \times 3$ supercell has a slightly different electronic structure than the unit cell. Overall, both the unit cell and the supercell K-edges looks identical. One noticeable defect of the supercell approach is the inability to capture the excitonic peak at the K-edge.

In a final attempt, we explored different probe pulse polarization following the calculations using LDA, DFT+U, and the supercell approach. The vector potential is defined in Eq. (7.1). The Figure 7.11 below shows the equilibrium optical conductivity of bulk hBN for probe polarizations in plane and at an angle of 40°.

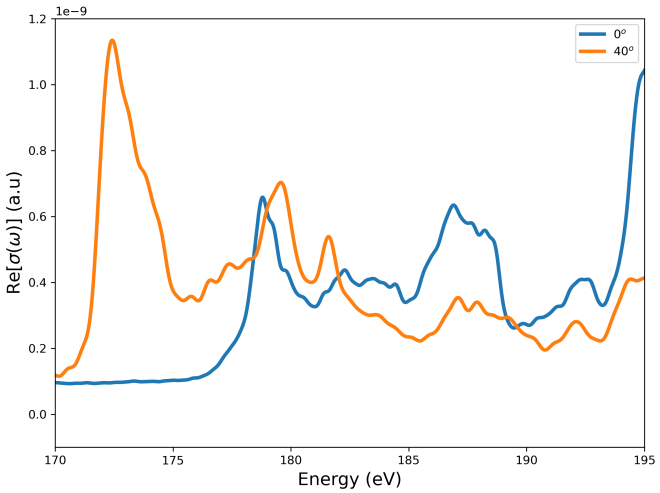

Figure 7.11: Equilibrium optical conductivity of hBN for different probe polarizations.

From the figure, the absorption peak at 177eV exhibits an energy shift of $\approx$ 6eV when the field is polarized at an angle of 40° and its at much higher intensity when compared to the in

plane polarization. This is due to the combinations of other components of $\sigma_{\alpha\beta}$ as defined in 6.19 where α, β are Cartesian coordinates. This shift in energy and increase in intensity of the peak, suggest that the transitions are sensitive to the polarization of the field. Here also, the sought after excitonic peak is

In the investigation to understand the electronic properties of hBN, accurately calculating the equilibrium spectrum at the B K-edge has proven to be a formidable challenge. Several computational methods were explored, such as the DFT within LDA, the use of DFT+U and the supercell with a core hole. Despite these efforts, challenges persist. Initially we employed the LDA to calculate the absorption spectrum , but it fails to describe the correct physics due to its inability to describe strongly correlated electrons. Subsequently, to address this issue, the DFT+U was applied, this method also failed short in describing the strongly excitonic peak at K-edge. Another difficulty encountered during the simulations is the convergence with respect to spacing i.e the grid problem. A large value of the grid spacing was employed thus making it difficult to capture the rapid changes of the core electron around the nuclei. To calculate the correct values, convergence with respect to the spacing is required to a much smaller value but this comes at a much larger computational cost.

7.3 Summary

In studying the equilibrium optical conductivity at the Boron K-edge, we employed various computational methods, including DFT, LDA, DFT+U, and the supercell approach with a core-hole. However, these methods presented several formidable challenges that affected our ability to reproduce experimental results in [8] and others.

The LDA shows a peak at 177eV, which, while capturing some features, remained significantly lower than the experimentally observed values of 190eV $\rightarrow$ 192eV. On the other hand, DFT+U, although displaying promising accuracy, overestimated the K-edge peak,the π^* peak is positioned at approximately 218eV. Unfortunately, the supercell approach also failed to produce the sought-after excitonic peak, further adding to the difficulties of our research. Additionally, the issue of convergence concerning grid spacing introduced yet another hurdle in our calculations. These challenges underscore the complexities of precisely describing core excitons in the Boron K-edge spectra within the approximations explored.

Our ongoing efforts include exploring alternative approaches to tackle these challenges, and hybrid functionals have shown potential. However, due to their considerable computational cost, they remain an avenue for future investigation.

This page was intentionally left blank.

8 Simulating Transient Absorption Spectroscopy with TDDFT

8.1 Introduction

In Chapter 5 and 6, the necessary theory needed to perform the calculations using the pump-probe scheme as highlighted in 4.1.4 is described. One of the most preferred and used techniques in order to study different dynamical behaviours of atoms as well as molecules are such pump-probe experiments.

In most attosecond experiments, an XUV attosecond pulse and a corresponding more intense and longer (Hundreds of femtoseconds) NIR or visible pulse is used for its generation. This laser pulse is used to investigate the light-induced non-equillibrium dynamics in solids. However, due to the complex nature of the electronic structure of solids; ATAS tend to provide a complex experimental data, therefore it is often not straightforward to interpret the output data from the experiment. A corresponding theoretical investigation is needed in order to understand the underlying physics behind the experimental data.

TDDFT in principle meets all the requirements needed to investigate this complex experimental outputs. In this section, we demonstrate how the TDDFT electron dynamics simulation is extended to the attosecond time scale to study electron dynamics in solids.

8.2 Numerical pump-probe calculations

In the preceding Chapter 6, the modeling of the TDKS equation to compute the equilibrium optical properties of solids in response to a weak, delta-like perturbation has been demonstrated. Here we extend explorations beyond linear response calculations and into the regime of nonlinear optical phenomena.

In this section, we will employ numerical pump-probe calculations to mimic experimental pump-probe techniques. The numerical pump-probe approach is very similar to the linear response approach calculation. Here, the electron dynamics is induced by the pump and probe electric fields, $\boldsymbol{E}_{pump}(t)$ and $\boldsymbol{E}_{probe}(t)$ respectively. These pulses trigger the electron dynamics and the induced current is evaluated. The induced current can be named as *pump-probe current* and denoted by $\boldsymbol{J}_{pump-probe}(t)$.

Numerical pump probe calculations are thus performed in three steps.

1. Simulate electron dynamics using only the pump pulse, denoted as $\boldsymbol{E}_{pump}(t)$. Evaluate the induced current as $\boldsymbol{J}_{pump}(t)$.

2. Simulate pump-probe electron dynamics by considering both the pump pulse, $\boldsymbol{E}_{pump}(t)$, and the probe pulse, $\boldsymbol{E}_{probe}(t)$. Evaluate the induced current as $\boldsymbol{J}_{pump-probe}(t)$.

3. Extract the probe electric field induced by the probe pulse, $\boldsymbol{E}_{probe}(t)$, in the presence of the pump pulse, $\boldsymbol{E}_{pump}(t)$ and the probe current $\boldsymbol{J}_{probe}(t)$. The probe electric field and the probe current can be defined as the difference between the pump-probe electric field and the pump electric field, as well as the difference between the pump-probe induced current and the pump-induced current.

$$\boldsymbol{J}_{probe}(t) = \boldsymbol{J}_{pump-probe}(t) - \boldsymbol{J}_{pump}(t) \tag{8.1}$$

$$\boldsymbol{E}_{probe}(t) = \boldsymbol{E}_{pump-probe}(t) - \boldsymbol{E}_{pump}(t) \tag{8.2}$$

With these steps, one can analyze the probe current $\boldsymbol{J}_{probe}(t)$ and the probe electric field $\boldsymbol{E}_{probe}(t)$ to evaluate the transient optical properties of solids in the presence of pump fields. The numerical pump probe calculations are performed with a time delay T_{delay} between the pump and probe pulses, this allows one to evaluate the transient optical properties by evaluating the transient optical conductivity. The transient optical conductivity is given by

$$\sigma^{T}_{\alpha\beta}(\omega, T_{probe}) = \frac{\boldsymbol{J}_{probe,\alpha}(\omega)}{\boldsymbol{E}_{probe,\beta}(\omega)} \tag{8.3}$$

where $\boldsymbol{J}_{probe,\alpha}(\omega)$ and $\boldsymbol{E}_{probe,\beta}(\omega)$ are the α-components of the FT of the probe electric field $\boldsymbol{E}_{probe}(\omega)$ and the probe current $\boldsymbol{J}_{probe}(\omega)$ respectively. The FT are given by

$$\sigma^{T}_{\alpha\beta}(\omega, T_{probe}) = \frac{\int dt\ \mathbf{J}_{probe}(t) e^{i\omega t - \gamma t'}}{\int dt\ \mathbf{E}_{probe}(t) e^{i\omega t - \gamma t'}} \tag{8.4}$$

where γ is the damping factor and T_{probe} is the central time of the probe pulse. Unlike the linear response calculations conducted in equilibrium, the transient conductivity influenced by the pump pulse is not solely dependent on the central time of the probe pulse. This variance arises because the pump pulse disrupts time translation symmetry. Consequently, one can explore the dynamics of transient optical properties in the time domain by adjusting the time delay between the pump and probe pulses as highlighted in the steps to perform numerical pump-probe calculations.

In performing the numerical pump probe calculations, we consider the hexagonal unit cell of monolayer hBN, which comprises 1 Boron and 1 Nitrogen atom. The Brillouin zone is divided into a 36^2 grid points in k space and a vacuum L of 50 a.u in real space is added to break periodicity in the out-of-plane direction. To compute the time evolution, we employ a fourth-order Taylor expansion of the operator $exp[-ih_{ks}(t)\Delta t/\hbar]$ and use a time step of $\Delta t = 0.08$ a.u. The computation involves a total of 50,000 time steps. Due to finite time propagation in the FT, we employed a damping of 250meV to reduce the numerical noise. Similarly, three different configurations of pump pulses were employed: a linear pump pulse, a colinear pump, a circular pump and a bicircular pump.

8.2.1 Linear Pump

Before performing the pump-probe calculations, the equilibrium spectrum at the valence is first obtained using Eq. (6.21). The equilibrium time-dependent induced current is then obtained using the probe pulse only whose vector potential is defined in Eq. (7.1) at time $t = 0$. The induced probe current $J_{probe}(t)$ is shown in Figure 8.1 (a) below. The equilibrium conductivity is calculated from probe current using Eq. (6.21) and it is shown in Figure 8.1 (b).

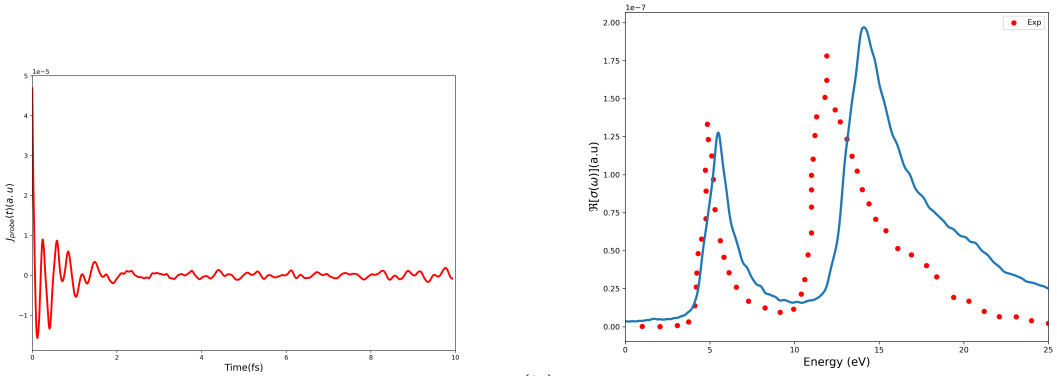

(a) (b)

Figure 8.1: Linear response calculation for monolayer hBN. Figure (a) Time-dependent induced current by the probe pulse at time $t = 0$. (b) Real part of equilibrium optical conductivity $\Re[\sigma(\omega)]$ of Monolayer hBN (solid blue line) with the experimental data (in red dots). The experimental spectra is shifted to align with the theoretical result. The experimental results are reproduced from [9].

Figure 8.1 (b) shows the corresponding optical conductivity of monolayer hBN alongside the experimental data. The calculated absorption spectrum shows two peaks at around 5eV and 15eV. The peak in the optical conductivity at around 5eV is due to the excitation of electrons from the valence band to the conduction band with the optical bandgap obtained to be 4.45eV. The experimental results shows the optical gap at around 5eV. There's a very good agreement with the experimental result and theoretical calculations. It is ideal to note that excitonic effects in this calculations are not taken into account even though they play a crucial role in the optical absorption of hBN. This is due to the fact that the ALDA functional is used in this calculation and it does not give a proper description of excitonic effects, therefore, the excitonic contribution is completely omitted. From the figure, our calculations shows a peak at the absorption zone exhibits a broad character. This peak, consistent with experimental observations and other theoretical calculations (such as BSE or GW) is associated with highest oscillator strength and correspond to a strong excitonic peak [212–215].

We commenced the numerical pump-probe calculations by employing the linear pump as our starting point. The linear pump is distinguished by its vector potential of the form

$$\boldsymbol{A}_{pump}(t) = -\frac{\boldsymbol{E}_{pump}}{\omega_{pump}}\mathbf{e}_x f(t)(1 - \Theta(t - T_{pump})) \times \Theta(t - t_0) \tag{8.5}$$

where $f(t)$ is the envelop of the pulse. we employed a Gaussiansimulant (sine squared) envelope

so that the pulse starts and ends with zero for numerical stability. The envelope is given by

$$f(t) = \frac{sin(\pi(t - t_0))}{T_{pump}}^{|\frac{\pi(t-t_0)/T_{pump}}{\sigma}|} \tag{8.6}$$

where $\boldsymbol{E}_{pump}$ is the peak electric field, the peak field strength is set to $I = 1.5 \times 10^{12}\ W/cm^2$, with a frequency of $\omega_{pump} = 0.8266eV$, a full width of half maximum of $\sigma = 0.75$, and a pulse duration of 40fs.

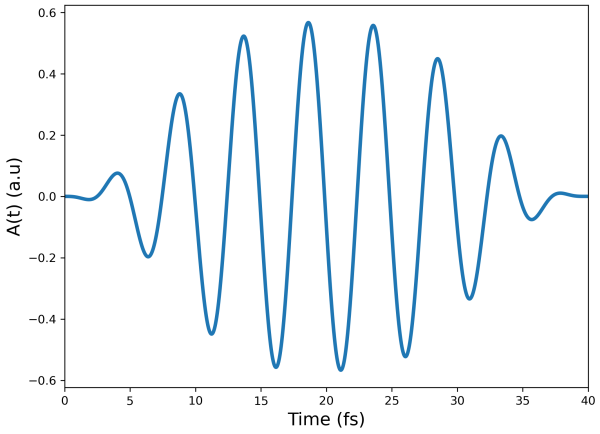

Figure 8.2: Time profile of the vector potential used for linear pump calculations. The Intensity is set to $I = 1.5 \times 10^{12}\ W/cm^2$, with a frequency of $\omega_{pump} = 0.8266eV$ and a pulse duration of $40fs$.

As for the probe vector potential, the following impulsive distortion was employed

$$\mathbf{A}_{probe}(t) = -E_{probe}\mathbf{e}_x\Theta(t - T_{delay}) \tag{8.7}$$

where $\Theta(t)$ is the Heaviside step function. The strength of the probe field E_{probe} is set to 8×10^{-4}a.u which is weak enough to excite only within the linear response regime. The time delay between the pump and the probe pulses is denoted as T_{delay}.

Next, we compute the transient optical properties of hBN using the numerical pump-probe scheme as described above. The pump and the probe are polarized in the x-direction which is perpendicular to B-N bond.

Figure 8.3 shows the real part of the transient optical conductivity of monolayer hBN. Here, the time profile of the applied vector potential is shown until its maximum at 20fs. The color map displays the changes in the real part of the optical conductivity. The horizontal axis represents the time delay, the vertical axis corresponds to energy, and the color scale indicates the difference between the optical conductivity obtained with the pump-probe $\sigma^T(\omega, T_{delay})$ and the probe alone $\sigma^T(\omega, 0)$. In the figure one can see below gap oscillatory features with the energy dispersion around the gap (4.45eV). In time domain, the frequency of the oscillations is twice the applied pump frequency ω_{pump}.

Additionally, calculations were conducted by systematically changing the intensity I of the pump pulse, spanning a range from 1.0×10^{11} to 5.0×10^{12} W/cm^2. The resulting transient absorption spectra corresponding to each distinct intensity are presented in Figure 8.4 (a) - (d).

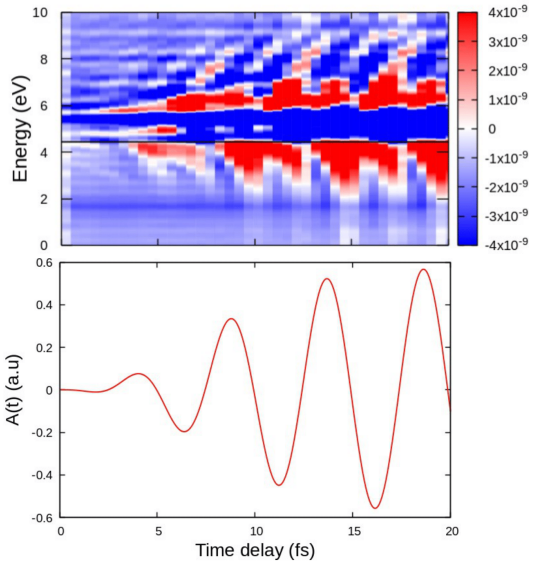

Figure 8.3: The upper plot shows the real part of the transient optical conductivity $\sigma^T(\omega)$ with the black solid line indicating the bandgap, while the lower plot displays the time profile of the vector potential till its maxima at around 20fs.

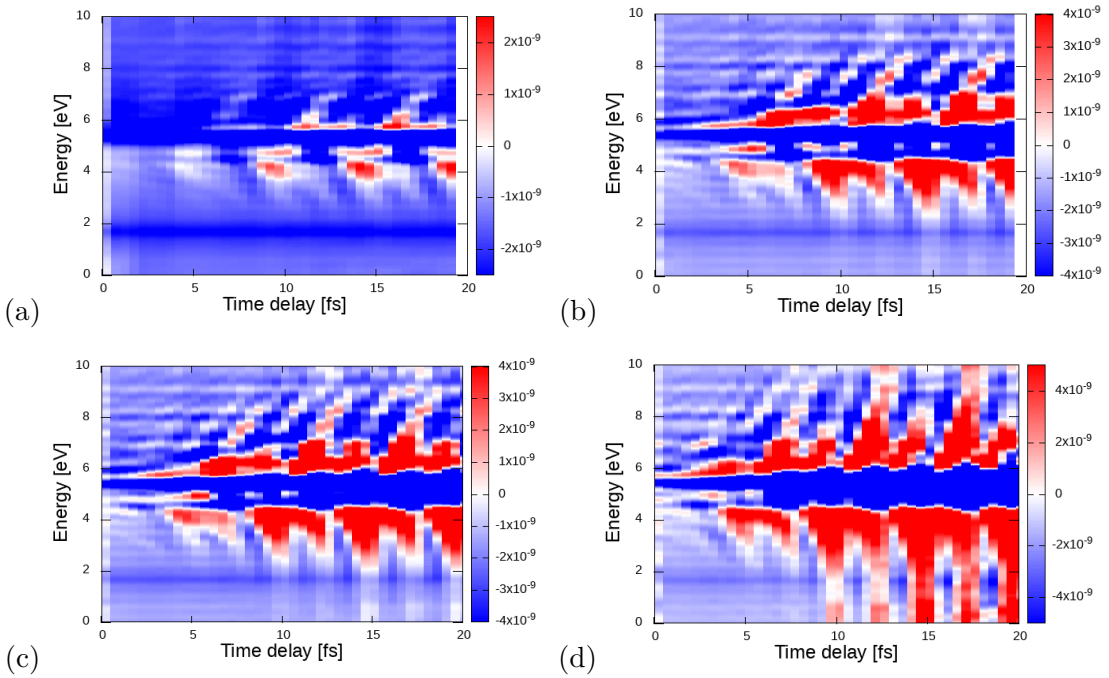

Figure 8.4: Transient Absorption Spectrum (TAS) from the transient optical conductivity $\Delta\sigma(\omega, T_{delay})$ of h-BN computed for peak pump intensity I of (a) 1.0×10^{11} W/cm^2, (b) 1.0×10^{12} W/cm^2, (c) 1.5×10^{12} W/cm^2, and (d) 5.0×10^{12} W/cm^2 with frequency ω_{pump} of 0.8266eV by numerical pump probe calculations.

From the figures, we can distinctly observe below gap oscillatory features. As noted above, the below gap features oscillates with twice the frequency of the pump ($2\omega_{pump}$). The oscillatory features below the gap are more pronounced with the increase in intensity. The occurrence of the $2\omega_{pump}$ oscillation can be attributed to the material's inversion symmetry in the pump-probe direction. This symmetry prohibits even-order nonlinear responses since materials with inversion symmetry are required to exhibit identical responses regardless of the electric field's sign along a symmetry direction. The observed features are also associated with the pump-induced interband transitions and also, the dynamical Franz-Keldysh effect (DFKE) [1] [216, 217]. In the subsequent subsection, the derivation of the general formula for the Franz-Keldysh effect is presented and used to analyse the non-linear below the bandgap features observed.

In order to investigate the origin of the observed dynamical features in the TAS 8.4, we performed an FT analysis of the the results by taking $|F[\sigma(\omega, T_{delay})]|^2$. Figure 8.5 displays the FT components of the time dependent modulation of the transient optical conductivity in Figure 8.4. From the figures one can observe that at lower intensity, the extent of modulation is notably subdued. Nevertheless, with the increase in intensity, the modulation's frequency-dependent characteristics become increasingly clear, thus confirming the presence of oscillatory features related to below-gap excitation with $2\omega_{pump}$ frequency, which aligns with the observations in the transient absorption spectra in Figure 8.4. The other features in the figures that are not in the Harmonics are due to the pump intensity.

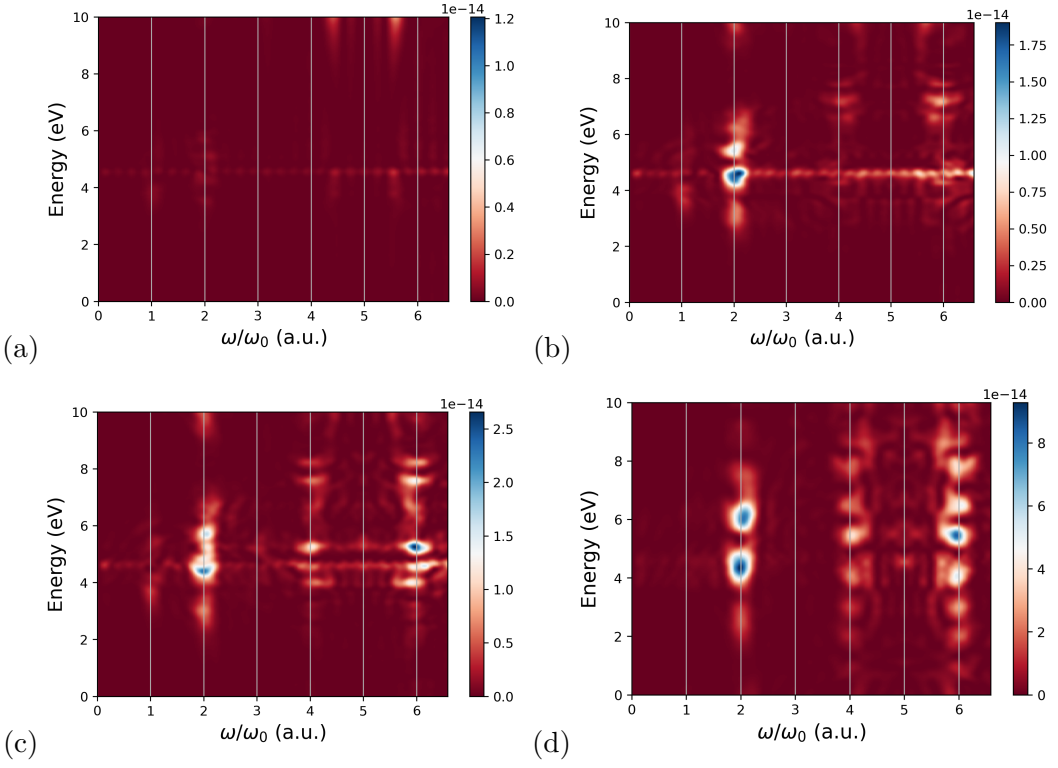

Figure 8.5: Fourier transforms of the TAS obtained under linear pump intensities of 1.0×10^{11} W/cm^2, 1.0×10^{12} W/cm^2, 1.5×10^{12} W/cm^2 & 5×10^{12} W/cm^2. Pump and probe are polarized in plane and ω_{pump} of 0.8266eV.

[1] The Franz Keldysh effect is simply an application of either static or time varying electric field to system which bends the crystal potential and accelerates the electron-hole pair. If this process occurs using only a static field, then the effect is known as Static Franz-Keldysh effect. If the static field is replaced by a time dependent electric field, the response of the system is then described by the Dynamical Franz-Keldysh effect.

8.2.2 Colinear Pump

Next, we use a colinear pump to perform the numerical pump-probe simulations. The colinear pulses comprises of a combination of two linearly polarized pulses along the same axes. The numerical pump-probe simulations were conducted using two-color pulses, where one comprises a fundamental pulse with frequencies of $\omega_{pump} = 0.83$eV and $2\omega_{pump} = 1.65$eV, and the another case that features $\omega_{pump} = 0.62$eV and its corresponding $2\omega_{pump} = 1.24$eV. The intensity of the pump pulse is set to $I = 1.5 \times 10^{12}\ W/cm^2$ in both cases. Both two-color pulses exhibit the same waveform and have the same pulse duration. The vector potential associated with the colinearly polarized two-color pulse is defined as follows

$$\mathbf{A}_{pump}^{\omega-2\omega}(t) = -\frac{E_{pump}}{w_{pump}}\mathbf{e}_x f(t)(sin(\omega t - \phi) + \frac{1}{2}sin(2\omega t)) \tag{8.8}$$

where $f(t)$ is envelop which is defined in Eq. (8.6), ϕ is the relative phase between the two colour lasers. The pump intensity is set to $I = 1.5 \times 10^{12}\ W/cm^2$.

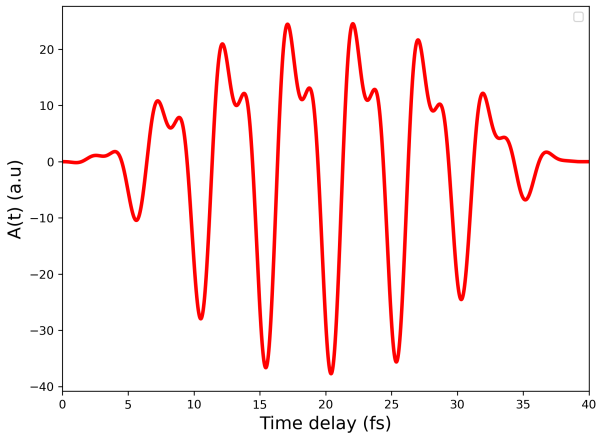

Figure 8.6: Time profile of the two-color laser vector potential in Eq. (8.8) with the phase $\phi = \pi/2$.

The vector potential in Eq. (8.8) breaks the time-reversal and inversion symmetries as explained in [218, 219]. As for the probe pulse, we use the same one as before, defined in Eq. (8.7). The TAS is presented in Figure 8.7 and its corresponding FT's. From the TAS, one can observe energy dispersion around the bandgap with a clear oscillatory features below the gap. These features arise directly from the breaking of time-reversal and inversion symmetry, leading to oscillatory patterns below the gap in the time domain, characterized by a frequency of $3\omega_{pump}$. Such distinctive attributes may be indicative of the dynamical Franz-Keldysh effect (DFKE). From the FT's, it indicates an energy dependent even and odd harmonics. This observation provides clear evidence of photoabsorption occurring below the bandgap, consequently affirming the presence of $3\omega_{pump}$ oscillatory features as observed in the TAS. This points towards a novel multicolour feature of the DFKE, where the oscillations do not occur with twice the fundamental frequency, but instead as a $3\omega_{pump}$ feature.

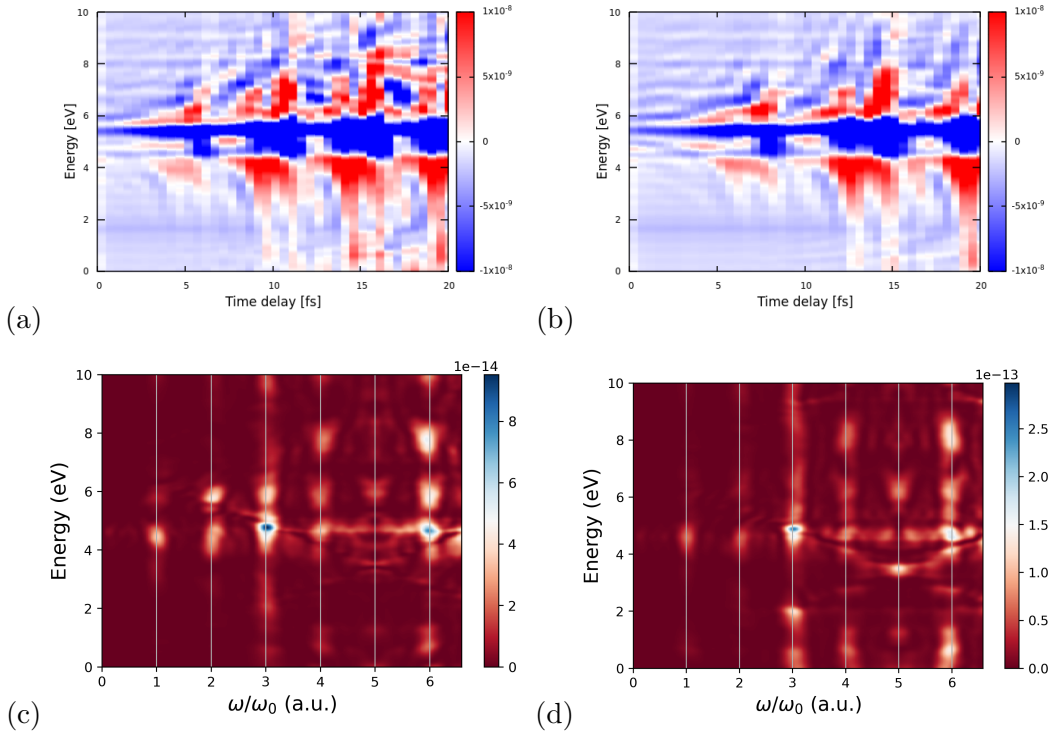

Figure 8.7: Transient Absorption Spectrum (TAS) using two-color pump pulses with an intensity of $1.5 \times 10^{12}\ W/cm^2$. Both pump and probe are polarized in-plane. (a) TAS with fundamental frequencies of 0.83 eV and 1.65 eV; (b) its corresponding Fourier transform; (c) TAS with pump frequencies of 0.62 eV and 1.24 eV; (d) its corresponding Fourier transform.

8.2.3 Circular pump

Next, we demonstrate the use of a circularly polarized pulse to perform the numerical simulation. The circularly polarized pulse typically carries an angular momentum, and the interaction with the system can create a distinction between the clockwise or anticlockwise rotations, thereby breaking the time reversal symmetry [220]. The pulse consists of right-handed circularly polarized light with the vector potential given by Eq. (8.9). The frequency of pulse is set to $\omega_{pump} = 0.866eV$ with an intensity of $1.5 \times 10^{12}\ W/cm^2$. The pulse duration is as indicated in the linear case and the probe pulse is defined in Eq. (8.7).

$$\boldsymbol{A}_{pump}(t) = -\frac{\boldsymbol{E}_{pump}}{\omega_{pump}} f(t) \sin(\omega t - \phi)(1 - \Theta(t - t_0)) \times \Theta\,(t - t_0) \tag{8.9}$$

where $f(t)$ is the envelop of the pulse as defined in Eq. (8.6). Keeping the frequency of the pump pulse the same, we calculate the TAS for a different intensity set to $5 \times 10^{12}\ W/cm^2$. Figure 8.8 shows the TAS and the corresponding of FT's. Similar to the features observed in the linear case, we also observed the below gap oscillatory features here. In the time domain, the features oscillates with twice the pump frequency $2\omega_{pump}$. Despite the pump pulse breaking the time reversal symmetry, the below gap features remains distinct. With increase in intensity, additional features appear around 12-20fs and this is due to free carrier absorption. The FT in panels (c) and (d) also confirms the below gap oscillatory features with strong peaks at the second harmonics and a much intense peak with increase in intensity of the pump pulse.

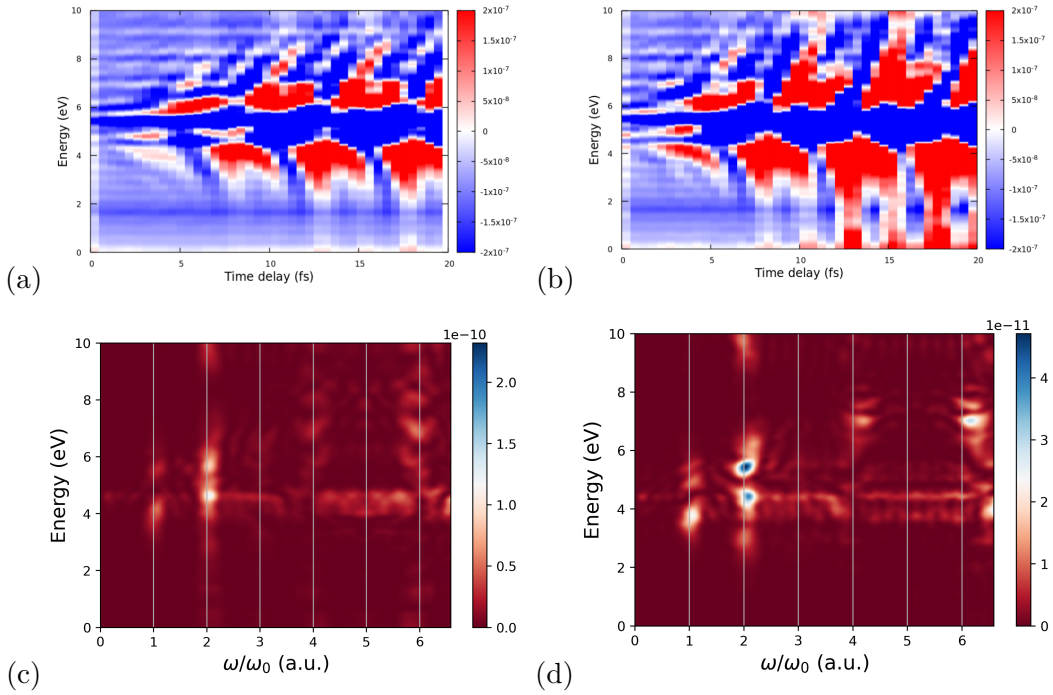

Figure 8.8: Transient Absorption Spectrum (TAS) using circular pump pulse. (a) TAS with fundamental frequency of 0.83 eV and Intensity of 1.5×10^{12} W/cm^2; (b) its corresponding Fourier transform; (c) TAS with pump frequency of 0.83 eV and Intensity of 5×10^{12} W/cm^2; (d) its corresponding Fourier transform.

8.2.4 Bicircular Pump

In their article [221], an all-optical, non-element-specific technique was proposed by by employing strong non-resonant fields to manipulate the valley degree of freedom in two-dimensional hBN with broken inversion symmetry. A weak circularly polarized field resonant with the direct bandgap of the material was used to excite the K and K' valleys selectively. It is also revealed that using the model proposed, one of the valleys (either K or K') will experience a bandgap closure and thus leading to light-induced topological phase transition that occurs at specific values of intensity and wavelength of the driving bicircular field. To investigate the origin of these features, we use numerical pump-probe calculations and calculate the TAS to measures the changes in absorption of the monolayer hBN as a function of time after the pump pulse is applied.

Here, we obtained the *bicircular* field by combining two-counter rotating circularly polarized pulses at fundamental frequency (ω) and its second harmonic (2ω) frequencies respectively. This creates a rotating electric field that can excite the sample into a coherent state. The total electric fields is formed with a threefold rotational symmetry as shown in Figure 8.9. The fundamental field (ω) is rotating in a counter-clockwise, while the corresponding second harmonic field (2ω) is rotating in clockwise direction. The vector potential of the pump is of the form

$$\begin{aligned} \boldsymbol{A}_{pump}(t) = -\frac{\boldsymbol{E}_{pump}}{\omega_{pump}} f(t)\sin(\omega t - \phi)(1 - \Theta(t - t_0)) \times \Theta(t - t_0) + \\ \frac{\boldsymbol{E}_{pump}}{2\omega_{pump}} f(t)\sin(2\omega t)\,(1 - \Theta(t - t_0)) \times \Theta(t - t_0)) \end{aligned} \tag{8.10}$$

where $f(t)$ is the envelop of the pulse as defined in Eq. (8.6). The intensity of the pump pulse is set to $5 \times 10^{12}\ W/cm^2$, with a frequency $\omega_{pump} = 0.68eV$, the phase factor ϕ is changed such that we control the orientation of the field with respect to either the Boron or the Nitrogen sublattice or in between. The probe vector potential remains the same as describe in Eq. (8.7). Figure 8.9 shows the Lissajous figure generated by the vector potential 8.10 oriented in sublattice of the hexagonal lattice. The relative phase ϕ used in the calculations are $\phi = \pi$ and, $\phi = 3\pi/2$ respectively.

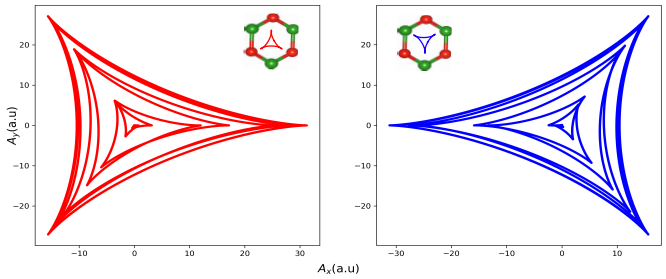

Figure 8.9: Lissajous curve: The curve drawn by the vector potential amplitude of the bicircular field, with polarization during pump $\phi = \pi$ (left plot) and, $\phi = 3\pi/2$ (right plot) respectively. The trefoil has the symmetry of one of the sublattices. The green ball represents the Nitrogen atoms while the red ball are the Boron atoms.

Figure 8.10 shows the calculated TAS with the bicircular pump field for field orientations $\phi = \pi$ and $\phi = 3\pi/2$ and their corresponding FTs. In the complex TAS, there are noticeable oscillations present below the bandgap. These oscillatory characteristics exhibit a periodicity at thrice the frequency of the applied pump $3\omega_{pump}$. They also display an extended, persistent behavior, with a long-lasting non-decaying tail that extends deeply into the bandgap region, particularly in the time range from 15 to 20 fs. With the change in orientation of the field, the observed features are less pronounced even though the oscillatory features observed maintain the $3\omega_{pump}$ frequency. The FT of the transient absorption spectrum reveals the frequencies of the vibrational modes. In the FT one can observe a combination of even and odd harmonics and a broad band of absorption at frequencies below the gap and also at higher frequencies, which corresponds to the below gap excitation as well as the excited state absorption of the monolayer hBN and we again observe the characteristic $3\omega_{pump}$ feature of the multicolour DFKE. Overall, the observed features are however not consistent with a bandgap closure nor induced a topological phase transition.

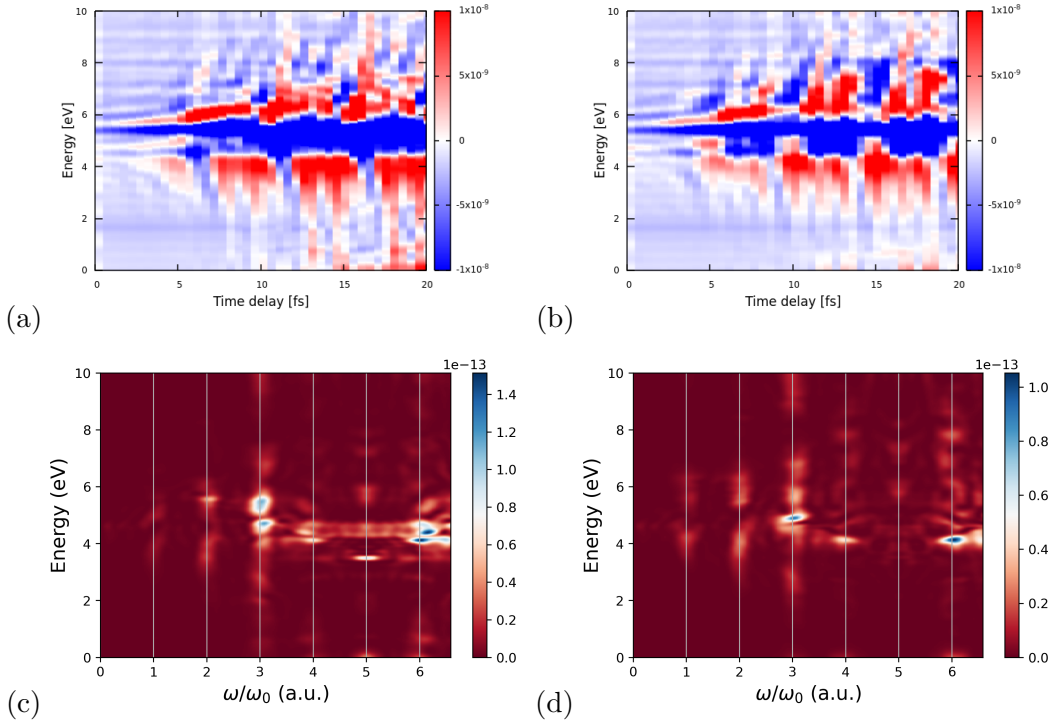

Figure 8.10: Transient Absorption Spectrum (TAS) calculated with the *bicircular* field with intensity of 5×10^{12} W/cm^2 with frequency $\omega = 0.68$eV. (a) TAS with field oriented at $\phi = \pi$ & (c) its corresponding Fourier transform (b) TAS with pump field oriented at $\phi = 3\pi/2$ & (d) its corresponding Fourier transform

8.2.5 The *multicolor* DFKE Signatures

As noted before, the almost universal signature of the DFKE are the $2\omega_{pump}$ oscillations in the TAS induced by the pump pulse [222]. Consistent with these observation, we also observed the $2\omega_{pump}$ oscillatory features for the monochromatic linear and circular pump pulses respectively. However, in the In the case of the multicolor driven fields, i.e colinear and bicircular, we here observe oscillatory features with $3\omega_{pump}$ frequency. To the best of our knowledge these signatures have not yet been discussed in the literature and seem to contradict at first glance what is known about the DFKE. In the next section we will carry out a detailed analysis of the FKE and DFKE, however, here we already postulate that the such 3ω behaviour is the unique signal of the multicolour driving and hence can be defined as the *multicolour* DFKE. A first insight into the mechanism behind these signatures can be gained from analysing the power spectra of the driving pulse. To this end we calculate the electric field from the vector potentials in Eq. 8.8 and Eq. 8.10 using the relation 8.16, and evaluate the FT of the square of the vector potential $\mathrm{FT}(|\vec{A}(t)|^2)$. Figure 8.11 shows FT analysis of the square of the vector potential for two-color colinear and bicircular pump pulse in panel (a) and (b) respectively. The peaks in the FT shows the $\omega, 2\omega, 3\omega$ frequency components of the pump pulse. The 3ω components dominates the temporal resolution of the pulses.

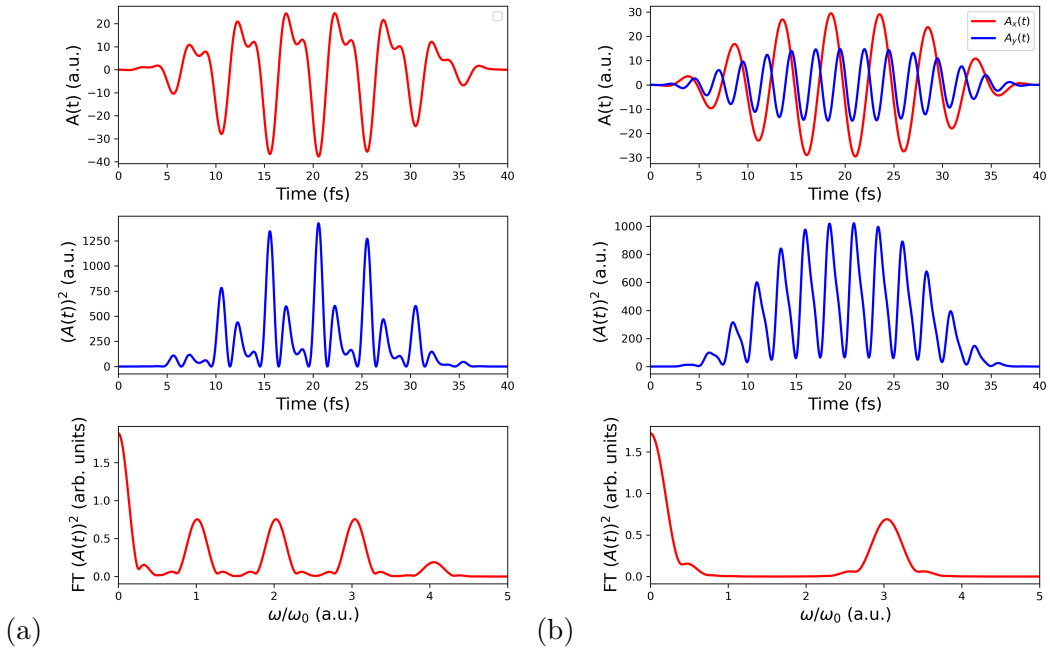

Figure 8.11: FT of the square of the vector potential $|\boldsymbol{A(t)}|^2$ for (a) colinear pump pulse and (b) bicircular pump. Note that $\omega_{pump} = 0.83$ eV for colinear and $\omega_{pump} = 0.68$ eV for bicircular.

Similarly, we evaluate the FT of the square modulus of the driving field $[\boldsymbol{E(t)^2}]$ for the bichromatic pulses and compare it the monochromatic case. Figure 8.12 shows the FT of the driving monochromatic pulse in (a) and bichromatic pulse in (b). In the linear (monochromatic) we observe a very strong 2ω peak. In contrast, the bichromatic colinear case shows a combination of $\omega, 2\omega, 3\omega$ and 4ω frequency components, with a dominant 3ω peak. For the bicircular case, we observe a distinct 3ω peak which occurs due to the 3-fold symmetry of driving pulse. The pulse beats only three times per period, these 3-fold oscillations, modulated by the driving pulses, induce the 3ω oscillations in the TAS. This analysis supports the macroscopic origin of the 3ω transient multicolor DFKE signatures observed in the TAS from TDDFT simulations.

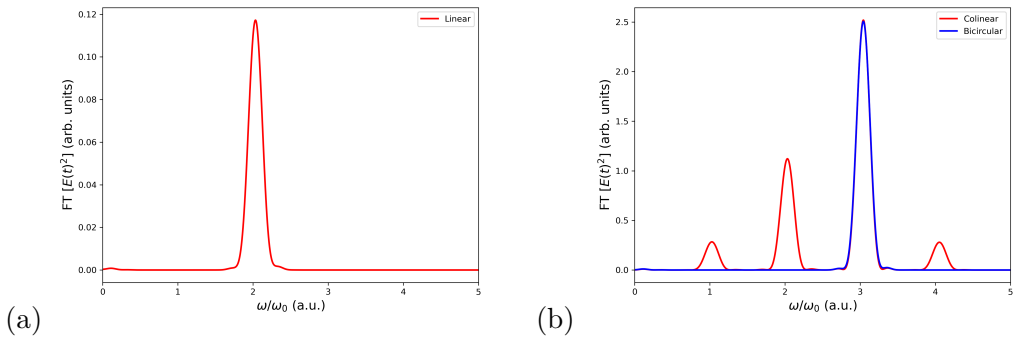

Figure 8.12: FT of the square of the electric field $|\boldsymbol{E(t)}|^2$ for (a) colinear pump pulse and (b) bicircular pump.

8.3 Franz-Keldysh Effect

The Franz-Keldysh effect predicted by Franz and Keldysh in 1958 [223, 224] describes the modification of the electronic band structure near the bandgap of a material when an electric field (such as an applied voltage or an intense laser field) is present. It leads to changes in the absorption and optical properties of the material. The effect can be observed as a shift in the absorption edge of the material when an external electric field is applied. When the electric field is applied, it results in an exponential tail below the bandgap and a characteristic oscillatory feature above the gap, which is understood as photon assisted-tunnelling of electrons from the valence band to the conduction band. The absorption spectrum $\alpha(\hbar\omega)$ under these conditions as defined in [10] is given by

$$\alpha(\hbar\omega) \propto \left|\tilde{E}_0\right|^{1/3} \left(\tilde{\omega}(\mathrm{Ai}(-\tilde{\omega}))^2 + (\mathrm{Ai}'(-\tilde{\omega}))^2\right) \tag{8.11}$$

where $\tilde{E}_0$ is the strength of the field, Ai is the airy functions, $\tilde{\omega}$ is the applied frequency and is given by

$$\tilde{\omega} = \frac{\hbar\omega - E_g}{E_b} \left(\frac{E_b}{e r_B \left|\tilde{E}_0\right|}\right)^{2/3} \tag{8.12}$$

Here the field strength E_0 is set to $5.14220652 \times 10^{11} V/m$ (Corresponding to an Intensity of $I = 1.5 \times 10^{12} W/cm^2$, the exciton binding energy $E_b = 8$meV, exciton Bohr radius is $r_B = 20$nm, bandgap $E_g = 4.45$eV, the photon energy $\hbar\omega = 0.25eV$ was employed to evaluate Eq. (8.12) and Eq. (8.11).

In Figure 8.13, the absorption spectra of monolayer hBN are depicted under the influence of a static field, as described by Eq. (8.11) and Eq. (8.12). The plot features gray areas representing the zero-field absorption spectrum, while the blue oscillatory lines illustrate an exponential, non-decaying tail. These oscillations occur for frequencies ω both below and above the bandgap, characterizing the phenomena of Franz-Keldysh effects. The Franz-Keldysh effect is distinguished by two fundamental features: the static and dynamical aspects. In the context of our study, we have derived and considered both cases to comprehensively explore their implications and relevance to our results.

8.3.1 Static FKE

We develop an analytical model to understand the observed FKE behaviours in the pump-probe numerical calculations. To do this, we examine the dynamics of electrons subjected to both pump and probe fields, a scenario that can be aptly characterized by the time-dependent Schrödinger equation.

$$i\frac{\partial}{\partial t}\varphi_i(\vec{r},t) = \left[\frac{1}{2m_e}\left(\vec{p} + \frac{e}{c}\vec{A}(t)\right)^2 + v(\vec{r})\right]\varphi_i(\vec{r},t) \tag{8.13}$$

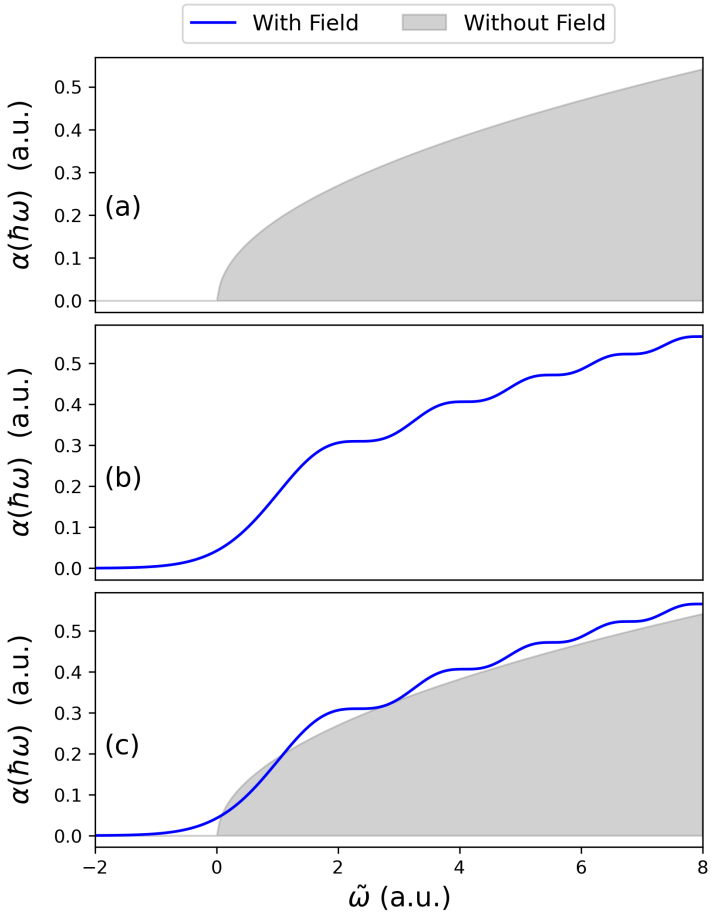

Figure 8.13: A typical absorption spectra of solids under the influence of a static electric field. **(*a*)** The grey area shows the zero field absorption spectrum. **(*b*)** The blue curve displays the exponential tail for frequencies below the gap and an oscillatory behaviour above the gap, and **(*c*)** the absorption spectra with static field (grey area) and without field (blue curve). The plot is reproduced from [10].

where $\vec{r}$ is time-independent potential that characterizes the lattice periodic potential, $\vec{A}(t)$ is the time-dependent vector potential. The solution of the above equation can be described by the time dependent Bloch functions $u_{n\vec{k}}(\vec{r},t)$ as $\varphi_i(\vec{r},t) = e^{i\vec{k}\cdot\vec{r}}u_{n\vec{k}}(\vec{r},t)$. Eq. (8.13) can be rewritten in terms of the Bloch orbitals as

$$i\frac{\partial}{\partial t}u_{n\vec{k}}(\vec{r},t) = \hat{h}_{\vec{k}_p(t)}u_{nk}(\vec{r},t) \tag{8.14}$$

where $\hat{h}_{\vec{K}(t)}$ is the Hamiltonian which is given by,

$$\hat{h}_{\vec{k}_p(t)} = \left[\frac{1}{2m_e}(\vec{p}+\vec{k})^2 + v(\vec{r})\right] \tag{8.15}$$

The crystal momentum is shifted by the vector potential as $\vec{k}_p(t) = \vec{k} + e\vec{A}_p(t)/\hbar c$. Where the vector potential is given by

$$\vec{A}(t) = -c\int_{-\infty}^{t}\vec{E}(t')dt' \tag{8.16}$$

The eigen states can be described interms of Houston function [225] [2]. The Houston function can be expressed as

$$w_{n\vec{k}}(\vec{r},t) = u_{n\vec{k}_p(t)}(\vec{r})e^{-i\int^t dt'\epsilon_{n\vec{k}_p(t')}} \tag{8.17}$$

The solution of Eq. (8.13) under the presence of both pump and probe with the vector potential $\vec{A}(t) = \vec{A}_{pump}(t) + \vec{A}_{probe}(t)$ can be expressed in terms of the Bloch function as

$$u_{n\vec{k}}(\vec{r},t) = w_{n\vec{k}}(\vec{r},t) + \sum_m C^{\vec{k}}_{nm}(t)w_{m\vec{k}}(\vec{r},t) \tag{8.18}$$

we substitute Eq. (8.17) into Eq. (8.18) and we have,

$$u_{n\vec{k}}(\vec{r},t) = u_{n\vec{k}_p(t)}(\vec{r})e^{-i\int^t dt'\epsilon_{n\vec{k}_p(t')}} + \sum_m C^{\vec{k}}_{nm}(t)w_{m\vec{k}}(\vec{r},t) \tag{8.19}$$

where $C^{\vec{k}}_{nm}(t)$ are time dependent coefficients. Substituting the the above equation into Eq. (8.14), the equation becomes,

$$\begin{aligned} i\frac{\partial}{\partial t}\left[u_{n\vec{k}_p(t)}(\vec{r})e^{-i\int^t dt'\epsilon_{n\vec{k}_p(t')}} + \sum_m C^{\vec{k}}_{nm}(t)w_{m\vec{k}}(\vec{r},t)\right] = \\ \hat{h}_{\vec{k}_p(t)}\left[u_{n\vec{k}_p(t)}(\vec{r})e^{-i\int^t dt'\epsilon_{n\vec{k}_p(t')}} + \sum_m C^{\vec{k}}_{nm}(t)w_{m\vec{k}}(\vec{r},t)\right] \end{aligned} \tag{8.20}$$

Next we substituting Equation (8.17) into the above equation, we obtain

$$\begin{aligned} i\frac{\partial}{\partial t}\left[u_{n\vec{k}_p(t)}(\vec{r})e^{-i\int^t dt'\epsilon_{n\vec{k}_p(t')}} + \sum_m C^{\vec{k}}_{nm}(t)u_{m\vec{k}_p(t)}(\vec{r})e^{-i\int^t dt'\epsilon_{m\vec{k}_p(t')}}\right] = \\ \hat{h}_{\vec{k}_p(t)}\left[u_{n\vec{k}_p(t)}(\vec{r})e^{-i\int^t dt'\epsilon_{n\vec{k}_p(t')}} + \sum_m C^{\vec{k}}_{nm}(t)u_{m\vec{k}_p(t)}(\vec{r})e^{-i\int^t dt'\epsilon_{m\vec{k}_p(t')}}\right] \end{aligned} \tag{8.21}$$

[2] The Houston states describes the electron dynamics in a moving frame in which the lattice momentum is prescribed by the vector potential.

Then the RHS of Eq. (8.21) can be further expanded as

$$i\left[\frac{\partial u_{n\vec{k}_p(t)}(\vec{r})e^{-i\int^t dt'\epsilon_{n\vec{k}_p(t')}}}{\partial t}+\frac{\partial\sum_m C^{\vec{k}}_{nm}(t)}{\partial t}u_{m\vec{k}_p(t)}(\vec{r})e^{-i\int^t dt'\epsilon_{m\vec{k}_p(t')}}+\frac{\partial u_{m\vec{k}_p(t)}(\vec{r})e^{-i\int^t dt'\epsilon_{m\vec{k}_p(t')}}}{\partial t}\sum_m C^{\vec{k}}_{nm}(t)\right]$$
$$=\hat{h}_{\vec{k}_p(t)}\left[u_{n\vec{k}_p(t)}(\vec{r})e^{-i\int^t dt'\epsilon_{n\vec{k}_p(t')}}+\sum_m C^{\vec{k}}_{nm}(t)u_{m\vec{k}_p(t)}(\vec{r})e^{-i\int^t dt'\epsilon_{m\vec{k}_p(t')}}\right] \tag{8.22}$$

By employing time-dependent perturbation theory, as outlined in c.f Appendix (A), we determine the value of the time-dependent coefficient $C^{\vec{k}}_{nm}(t)$. [3]

$$C^{\vec{k}}_{nm}(t)=-\frac{ie}{m_e c}\int_{-\infty}^{t}dt'\vec{P}^{\vec{k}}_{mn}(t')\vec{A}_p(t')-\delta_{mn}\frac{ie}{m_e c}\int_{-\infty}^{t}dt'\vec{k}_p(t')\vec{A}_p(t') \tag{8.23}$$

where $\vec{P}^{\vec{k}}_{mn}(t')$ is the momentum matrix operator and is defined as

$$\begin{aligned}\vec{P}^{\vec{k}}_{mn}(t')&=\int_V d\vec{r}w^*_{m\vec{k}}(\vec{r},t)\vec{p}w_{m\vec{k}}(\vec{r},t)\\&=\vec{p}_{mn\vec{k}_{p(t)}}e^{-i\int_\infty^t dt'\ (\epsilon_{m\vec{k}_p(t')}\ -\ \epsilon_{n\vec{k}_p(t')})}\end{aligned} \tag{8.24}$$

where the matrix element in the static basis is given by

$$\vec{p}_{mn\vec{k}}=\int_V d\vec{r}u^*_{m\vec{k}}(\vec{r})\vec{p}u_{m\vec{k}}(\vec{r}). \tag{8.25}$$

8.3.2 Time-dependent Current

The subsequent step entails the computation of a crucial quantity, namely the time-dependent current induced by both the pump and probe pulses. The induced current can be determined via

$$\vec{J}(t)=\frac{-i\hbar}{m}\left[u^*_{nk}(\vec{r},t)\nabla u_{nk}(\vec{r},t)\right] \tag{8.26}$$

After a series of algebraic manipulations [4], the calculated expression for the total induced current is determined to be

$$\vec{J}(t)=-\frac{e}{m_e V}\int_V d\vec{r}\times\sum_{n\vec{k}}R_e\left\{u^*_{n\vec{k}}\left[\vec{p}+\vec{k}_{p(t)}+\frac{e}{c}\vec{A}_p(t)\right]u_{n\vec{k}}\right\} \tag{8.27}$$

This total current is expressed as a combined contribution from both the pump and the probe $\vec{J}(t)=\vec{J}_{pump}+\vec{J}_{probe}$. The pump contribution is given by

$$\vec{J}_{pump}=-\frac{e}{m_e V}\sum_{n\vec{k}}\int_V d\vec{r}\,\mathrm{Re}\left\{w^*_{n\vec{k}}\left[\vec{p}+\vec{k}_{p(t)}\right]w_{n\vec{k}}\right\} \tag{8.28}$$

[3] refer to the appendix for a detailed step-by-step derivation of this coefficient.
[4] The detailed steps of this calculation can be found in c.f Appendix C section for reference.

while the probe contribution is

$$\vec{J}_{\text{probe}}(t) = -\frac{e^2}{m_e c} n_e \vec{A}_{probe}(t) + \frac{e^2}{m_e^2 c V}\int_{-\infty}^{t} dt' \times \sum_{n\neq n',\vec{k}'} \text{Im}\left\{\vec{P}^{\vec{k}}_{nn'}(t)\left[\vec{P}^{\vec{k}}_{nn'}(t')\cdot\vec{A}_{probe}(t')\right]\vec{E}(t)\right\} \tag{8.29}$$

here the valence electrons have an average density described by n_e. $\vec{E}$(t) is the electric field of the probe. Since the probe induced current has a linear relation with the probe field, we can apply linear response theory to obtain the optical conductivity. Eq. (6.21) gives the linear relation between the induced current and the optical conductivity. In time domain, the optical conductivity can be expressed as;

$$\sigma_{\alpha\beta}(t,t') = \frac{e^2}{m_e} n_e \delta_{\alpha\beta} - \frac{e^2}{m_e V}\int_{t'}^{t} dt'' \sum_{n\neq n',\vec{k}} \text{Im}\left[(p_\alpha)_{nn'\vec{k}_{p(t)}}(p_\beta)_{n'n\vec{k}_p(t'')} \times e^{-i\int_{t''}^{t} d\tau\left\{\varepsilon_{n'\vec{k}_p(\tau)}-\varepsilon_{n\vec{k}_p(\tau)}\right\}}\right] \tag{8.30}$$

α, β are the Cartesian indices. The orbitals in the above equation can be expressed as the occupied valence band and the unoccupied conduction band by assuming that the bands are parabolic. The excitation energies of the valence and conduction bands can be defined as

$$\begin{aligned}\epsilon_{v,\vec{k}} &= -\frac{\vec{k}^2}{2m_v},\\ \epsilon_{c,\vec{k}} &= \epsilon_g + \frac{\vec{k}^2}{2m_c},\end{aligned} \tag{8.31}$$

and

$$\epsilon_{c,\vec{k}} - \epsilon_{v,\vec{k}} \approx \frac{k^2}{2\mu} + \epsilon_g \tag{8.32}$$

where ϵ_g is the band gap and μ is the reduced mass.

The optical conductivity under the static electric field (weak delta like impulsive distortion $E(t) = E_0\delta(t-t_0)$ can be evaluated by taking the FT of Eq. (8.30) and Eq. (8.29) and taking the ratio between the two as stated in Eq. (6.20).

$$\begin{aligned}\tilde{\sigma}_{\alpha\beta}(\omega) =& \frac{ie^2 n_e}{m_e\omega}\delta_{\alpha\beta} + \frac{e^2}{m_e^2\omega V}\int_0^\infty dt e^{i\omega t}\sum_{\vec{k}}\\ &\times\Big[(p_\alpha)_{vc\vec{k}-e\vec{E}t/2}(p_\beta)_{cv\vec{k}+e\vec{E}t/2}\, e^{-i\left\{(\epsilon_k+\epsilon_g)t+\frac{c^2E^2}{24\mu}t^3\right\}}\\ &-(p_\beta)_{vc\vec{k}+e\vec{E}t/2}(p_\alpha)_{cv\vec{k}-e\vec{E}t/2}\, e^{i\left\{(\epsilon_k+\epsilon_g)t+\frac{c^2E^2}{24\mu}t^3\right\}}\Big]\end{aligned} \tag{8.33}$$

Since the σ is a tensorial quantity, we only consider the real part of the diagonal elements of $\sigma_{\alpha\beta}$. Integrating the above equation withe respect to t, we obtain,

$$\text{Re}\,\tilde{\sigma}_{\alpha\alpha}(\omega) = \frac{\pi e^2}{m_e^2\omega V}|(p_\alpha)_{vc}|^2\sum_{\vec{k}}\left(\frac{8\mu}{e^2E^2}\right)^{1/3}\times \text{Ai}\left[(\epsilon_k+\epsilon_g-\omega)\left(\frac{8\mu}{e^2E^2}\right)^{1/3}\right] \tag{8.34}$$

where Ai is the airy functions, and $\epsilon_k = k^2/2\mu$. Upon integrating the equation with respect to k we obtain the relation for real part of the diagonal element of the optical conductivity as;

$$\mathrm{Re}\,\tilde{\sigma}_{\alpha\alpha}(\omega) = \frac{(2\mu)^{3/2}e^2}{2m_e^2\omega}\left|(p_\alpha)_{vc}\right|^2\sqrt{\Theta} \quad \times\left\{-\frac{\epsilon_g-\omega}{\Theta}\mathrm{Ai}^2\left(\frac{\epsilon_g-\omega}{\Theta}\right)+\mathrm{Ai}'^2\left(\frac{\epsilon_g-\omega}{\Theta}\right)\right\} \tag{8.35}$$

with $(\Theta = e^2E^2/2\mu)^{1/3}$. The real part of the optical conductivity without the electric field as defined in the reference [4] is given by

$$\mathrm{Re}\,\sigma(\omega) = \frac{\frac{\left(2e^2(2\mu)^{3/2}\right)}{m_e^2\hbar}\left|p_{vc}\right|^2 E_g^{-3/2}\left(\hbar\omega/E_g\right)^{-2}\left(\hbar\omega/E_g-1\right)^{1/2}\times\omega}{4\pi} \tag{8.36}$$

where E_g is the bandgap, μ is the reduced mass between electron and hole pair. To evaluate the static properties, $E_g = 4.45\mathrm{eV}$, $\mu = 0.54m_e$, the matrix element $p_\alpha = 0.925a.u.$

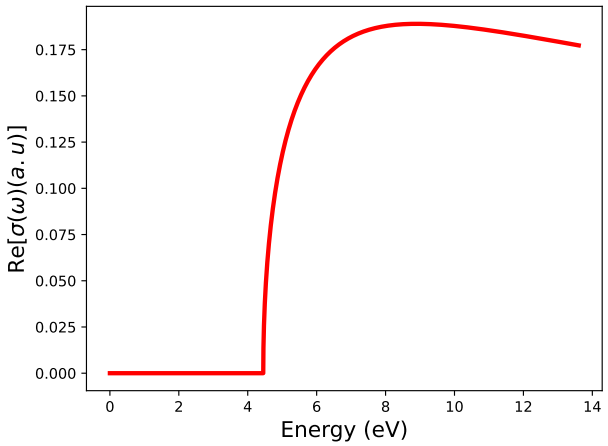

Figure 8.14: Real part of the Optical conductivity Eq. (8.36) of monolayer hBN without electric field. The sharp peak at 4.45 eV corresponds to the bandgap, indicating that photons with an energy of 4.45 eV or more can be absorbed.

Figure 8.14 show the optical conductivity obtained by evaluating Eq. (8.36). The plot shows a sharp peak at around 4.45 eV, which corresponds to the bandgap. This peak indicates that photons with an energy of 4.45 eV or more can be absorbed by exciting electrons from the valence band to the conduction band, while absorption does not occur below the bandgap.

Utilizing the optical conductivity derived from the electric field in Eq. (8.35), we employ the expression to calculate the conductivity for various intensities of the linear pump pulse.

Figure 8.15 illustrates the optical conductivity calculated using Eq. (8.35) for a pump pulse intensity of $I = 1.5\times10^{12}W/cm^2$. The red curve in the first plot indicates absorption occurring only at the bandgap and above it. In contrast, the blue curve exhibits absorption below the gap and displays oscillatory features above the gap. The second plot **(b)** represents the difference between the two aforementioned conductivity profiles in **(a)**. The time-averaged modulation reveals the emergence of absorption below the bandgap and a reduction in absorption above the bandgap. Additionally, a decrease in oscillations above the gap is observed.

We performed multiple evaluation of the Eq. (8.35) at different intensities of the time profile

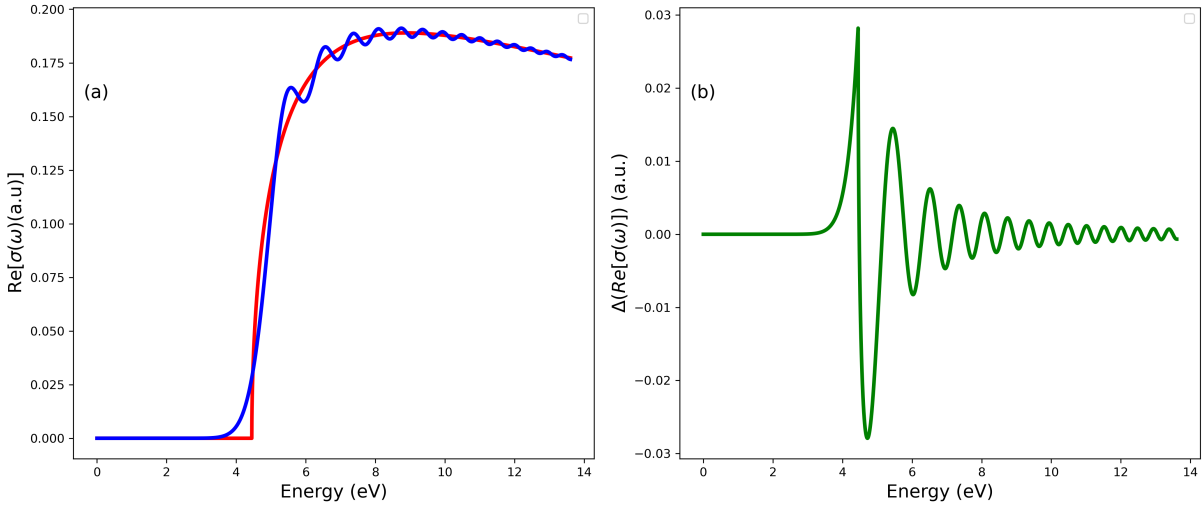

Figure 8.15: (a) Real part of the Optical conductivity of monolayer hBN computed with electric field (blue curve) and without electric field (red curve). The peak at 4.45 eV corresponds to the bandgap, while the blue curve shows an absorption below the gap and an oscillatory behaviour above the gap. **(b)** displays the difference $\mathrm{Re}(\sigma(\omega, E) - \sigma(\omega))$ between the field free and the field induced modulations.

of the linear pump pulse as well as the colinear pump and we obtained the TAS. Figure 8.16 shows the TAS obtained by the FKE static model for the intensities considered. The figure shows the changes in the real part of the optical conductivity caused by the pump field. In the figure, it is possible to recognise the oscillatory features below and above the gap even for the smallest intensity of $I = 1.0 \times 10^{11} W/cm^2$. As the intensity increases, the features become more pronounced, and the oscillatory patterns oscillate with twice the applied pump frequency. Notably, a distinct difference is observed between these results and those obtained using TDDFT as illustrated in 8.4. In contrast to the TDDFT case, the tail below the gap does not extend as deeply into the gap. This discrepancy suggests that the features identified in the TDDFT results are attributed to the specific characteristics of the DFKE, even though the estimation by the Static Franz-Keldysh Effect (SFKE) is relatively close.

Figure 8.17 shows the results obtained using the colinear pump pulse with the intensity of $I = 1.5 \times 10^{12} W/cm^2$ for a fundamental pump frequency of 0.83 and $0.62eV$. The results obtained with the colinear pump are also attributed to the characteristics of the SFKE even though the features oscillates with $3\omega_{pump}$ frequency as observed in Figure 8.7. This is due to the fact that the non-decaying tail below the gap does not extend deeply into the gap as observed in the TDDFT case.

8.3.3 Dynamical FKE

Next we consider a case where the pump electric field is periodic in time. Since we have shown in the previous section that the SFKE is as a result of intra-band transition due to the static electric field. Hence, the modification optical properties arising from intra-band transitions induced by oscillating electric fields can be referred to as the DFKE. Here also, we use the parabolic two band model to investigate the observed features in the TDDFT results.

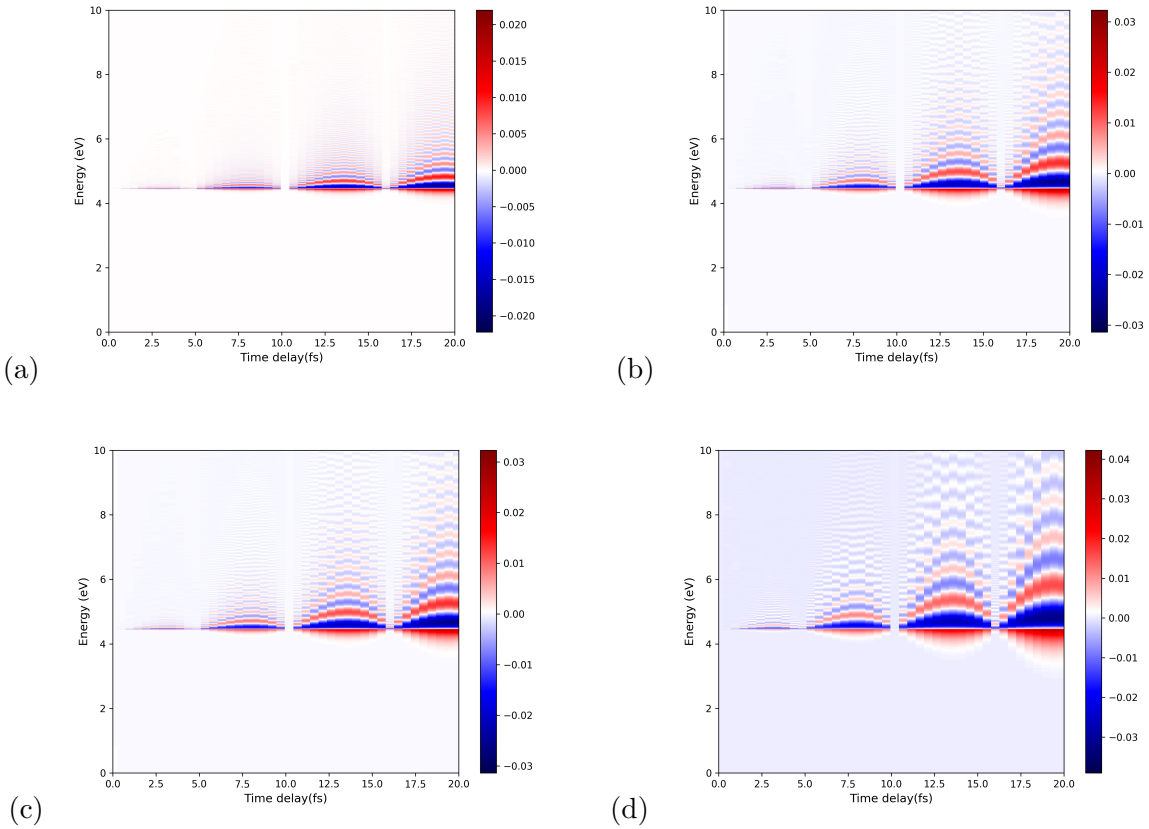

Figure 8.16: TAS calculated with the static FKE model for pump intensities of (a) $1.0 \times 10^{11}\ W/cm^2$, (b) $1.0 \times 10^{12}\ W/cm^2$, (c) $1.5 \times 10^{12}\ W/cm^2$ & (d) $5 \times 10^{12}\ W/cm^2$.

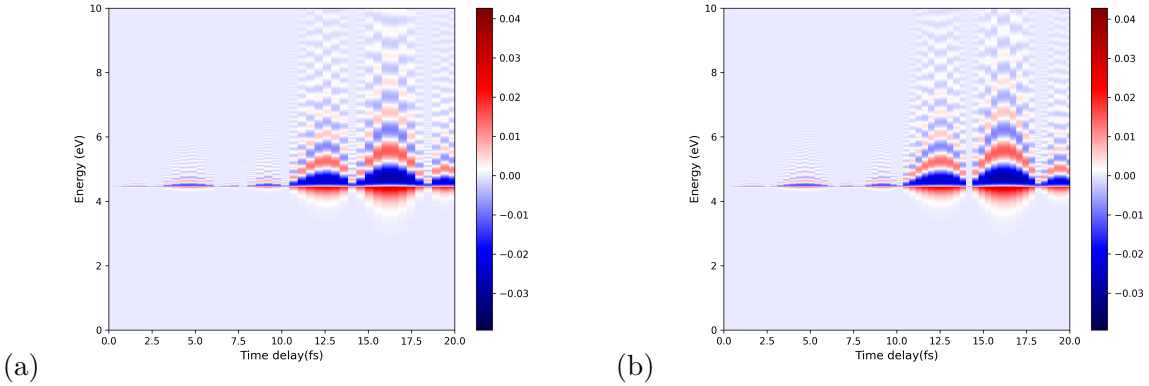

Figure 8.17: TAS calculated with the static FKE model with a colinear pump pulse for the intensities of $I = 1.5 \times 10^{12}\ W/cm^2$ for frequency of (a) $\omega = 0.83eV$ and (b) $\omega = 0.62eV$.

8.3.4 Parabolic Two Band Model (PBM)

To develop the PBM, we begin with the one-body Schrödinger equation in the following form

$$i\hbar\frac{\partial}{\partial t}u_{b\vec{k}}(\vec{r},t)=\left[\frac{1}{2}\left\{\vec{p}+\hbar\vec{k}+\frac{e}{c}A(t)\right\}^2+v(r)\right]u_{b\vec{k}}(\vec{r},t) \tag{8.37}$$

which can the be written in another form as

$$ih\frac{\partial}{\partial t}u_{b\vec{k}}(\vec{r},t)=\hat{h}_{\vec{K}(t)}u_{bk}(\vec{r},t) \tag{8.38}$$

where $u_{b\vec{k}}(\vec{r},t)$ is a time-dependent Bloch state from 4.3.1, and $v(\vec{r})$ is a one-body potential that has the same periodicity as the crystal. The crystal momentum is shifted by the vector potential $\vec{A}(t)$ with $\vec{K}(t)=\vec{k}+e\vec{A}(t)/\hbar c$. The Bloch functions can be expressed by using the time dependent basis set, the Houston states [225, 226], we can write the eigen states in the Houston basis as

$$u^H_{b\vec{k}}(\vec{r},t)=e^{-\frac{i}{\hbar}\int^t dt'\epsilon_{b\vec{K}(t')}}u^S_{b\vec{K}(t)}(\vec{r}) \tag{8.39}$$

where $\epsilon_{b\vec{K}(t)}$ and $u^S_{b\vec{K}(t)}(\vec{r})$ are an eigenvalue and the eigenstate of the instantaneous Hamiltonian $\hat{h}_{\vec{K}(t)}$, respectively.

The Houston states describes the electron dynamics in a moving frame in which the lattice momentum is prescribed by the vector potential $\vec{A}(t)$ and $\epsilon_{b\vec{K}(t)}$ describes the motion of the electron on each band.

We can express the time-dependent Schrödinger equation using the Houston basis as follows

$$\hat{h}_{\vec{K}(t)}u^S_{b\vec{K}(t)}(\vec{r})=\epsilon_{b\vec{K}(t)}u^S_{b\vec{K}(t)}(\vec{r}) \tag{8.40}$$

To characterize the two-state system, the eigenstates are represented as a linear combination of two Houston states. One corresponds to the valence state, while the other characterizes the conduction states. This is given by

$$u_{\vec{k}}(\vec{r},t)=c_{v\vec{k}}(t)u^H_{v\vec{k}}(\vec{r},t)+c_{c\vec{k}}(t)u^H_{c\vec{k}}(\vec{r},t) \tag{8.41}$$

Subsequently, we substitute the expressions from Eq. (8.41) into Eq. (8.38) alongside (8.39), resulting in

$$i\hbar\frac{\partial}{\partial t}\left[c_{v\vec{k}}(t)u^H_{v\vec{k}}(\vec{r},t)+c_{c\vec{k}}(t)u^H_{c\vec{k}}(\vec{r},t)\right]=\hat{h}_{\vec{K}(t)}\left[c_{v\vec{k}}(t)u^H_{v\vec{k}}(\vec{r},t)+c_{c\vec{k}}(t)u^H_{c\vec{k}}(\vec{r},t)\right] \tag{8.42}$$

After some algebraic manipulations, the details of which can be found in c.f Appendix D, we

arrived at

$$\begin{aligned} &i\hbar\dot{c}_{v\vec{k}}\, e^{-\frac{i}{\hbar}\int^t dt' \epsilon_{v\vec{K}(t')}} u^S_{v\vec{K}(t)}(\vec{r}) + i\hbar c_{v\vec{k}}\, e^{-\frac{i}{\hbar}\int^t dt' \epsilon_{v\vec{K}(t')}} \frac{\partial u^S_{v\vec{K}(t)}(\vec{r})}{\partial t} + \\ &i\hbar\dot{c}_{c\vec{k}}\, e^{-\frac{i}{\hbar}\int^t dt' \epsilon_{c\vec{K}(t')}} u^S_{c\vec{K}(t)}(\vec{r}) + i\hbar c_{c\vec{k}}\, e^{-\frac{i}{\hbar}\int^t dt' \epsilon_{c\vec{K}(t')}} \frac{\partial u^S_{c\vec{K}(t)}(\vec{r})}{\partial t} = 0 \end{aligned} \tag{8.43}$$

and again, performing more rigorous algebraic manipulations, we arrive at the following equation in matrix form

$$i\hbar\frac{d}{dt}\begin{pmatrix} c_{v\vec{k}}(t) \\ c_{c\vec{k}}(t) \end{pmatrix} = \begin{pmatrix} 0 & h_{vc,\vec{k}}(t) \\ h^*_{vc,\vec{k}}(t) & 0 \end{pmatrix}\begin{pmatrix} c_{v\vec{k}}(t) \\ c_{c\vec{k}}(t) \end{pmatrix} \tag{8.44}$$

where the off-diagonal terms are defined as follows

$$\boxed{h_{vc,\vec{k}}(t) = -i\frac{\vec{p}_{vc,\vec{K}(t)}}{\epsilon_{v,\vec{K}(t)} - \epsilon_{c,\vec{K}(t)}} \cdot \frac{e}{m}\vec{E}(t) e^{-\frac{1}{\hbar}\int^t dt' \left\{\epsilon_{c,\vec{K}(t')} - \epsilon_{v,\vec{K}(t')}\right\}}} \tag{8.45}$$

and the matrix element is thus given by

$$\vec{p}_{vc,\vec{K}(t)} = \int_\Omega d\vec{r} u^{S,*}_{v\vec{K}(t)}(\vec{r})\vec{p}u^S_{c\vec{K}(t)}(\vec{r}), \tag{8.46}$$

where Ω is a volume of the unit-cell.

The model is simplified by making two distinct approximations namely

1. Parabolic band approximation
2. Uniform matrix-element approximation

The utilization of the parabolic band approximation enables the characterization of the electronic structure through the expressions of energy eigenstates as defined in Eq. (8.31). On the other hand, the uniform matrix approximation permits the neglect of the k-dependence of the matrix element.

$$\vec{p}_{vc,\vec{K}(t)} = \vec{p}_{vc} \tag{8.47}$$

An essential outcome of this model is the ability to calculate the time-dependent induced current by the pulse. The derivation of the current is presented in the next subsection.

8.3.5 Time Dependent Current for the PBM

As the current is a spatial integral quantity, the contributions from both the valence and conduction band states are identical. Therefore, the total current induced by the laser field is computed using [5]

[5] Step by step derivation of this quantity in c.f Appendix C

$$J(t) = \frac{-i\hbar}{m}\left[u_k^*(\vec{r},t)\nabla u_k(\vec{r},t)\right] \tag{8.48}$$

$u_k(\vec{r},t)$ is defined in Eq. (8.39),

$$u_k(\vec{r},t) = c_{v\vec{k}}(t)e^{-\frac{i}{\hbar}\int^t dt' \epsilon_{v\vec{K}(t')}} u^S_{v\vec{K}(t)}(\vec{r}) + c_{c\vec{k}}(t)e^{-\frac{i}{\hbar}\int^t dt' \epsilon_{c\vec{K}(t')}} u^S_{c\vec{K}(t)}(\vec{r}) \tag{8.49}$$

it complex conjugate is then given by,

$$u_k^*(\vec{r},t) = c^*_{v\vec{k}}(t)e^{\frac{i}{\hbar}\int^t dt' \epsilon_{v\vec{K}(t')}} u^{*S}_{c\vec{K}(t)}(\vec{r}) + c^*_{c\vec{k}}(t)e^{\frac{i}{\hbar}\int^t dt' \epsilon_{c\vec{K}(t')}} u^{*S}_{c\vec{K}(t)}(\vec{r}) \tag{8.50}$$

putting $\vec{p} = -i\hbar\nabla$, Eq. (8.49) and Eq. (8.50) into Eq. (8.48), and integrating the electric current averaged over the unit cell one obtain

$$J(t) = \frac{1}{m}\cdot\frac{1}{V}\int_V d\vec{k}\int d\vec{r}\Big[c^*_{v\vec{k}}(t)c_{v\vec{k}}(t)u^{*S}_{v\vec{K}(t)}(\vec{r})\vec{p}u^S_{v\vec{K}(t)}(\vec{r}) + c^*_{v\vec{k}}(t)c_{c\vec{k}}(t)e^{\frac{i}{\hbar}\int^t dt'\left\{\epsilon_{c,\vec{K}(t')}-\epsilon_{v,\vec{K}(t')}\right\}}u^{*S}_{v\vec{K}(t)}(\vec{r})$$
$$\vec{p}u^S_{c\vec{K}(t)}(\vec{r}) + c^*_{c\vec{k}}(t)c_{v\vec{k}}(t)e^{\frac{i}{\hbar}\int^t dt'\left\{\epsilon_{c,\vec{K}(t')}-\epsilon_{v,\vec{K}(t')}\right\}}u^{*S}_{c\vec{K}(t)}(\vec{r})\vec{p}u^S_{v\vec{K}(t)}(\vec{r}) + c^*_{c\vec{k}}(t)c_{c\vec{k}}(t)u^{*S}_{c\vec{K}(t)}(\vec{r})\vec{p}u^S_{c\vec{K}(t)}(\vec{r})\Big] \tag{8.51}$$

Solving the above equation and performing some algebraic expressions, assuming that the probe field is applied in z-direction, the induced current by probe pulse is calculated to be

$$\boxed{J_z(t>T) = \frac{e}{m}\cdot\frac{2E_0}{(2\pi)^3}\int d\vec{k}\,\frac{1}{\hbar}\frac{|p_{vc}|^2}{(\epsilon_{c,\vec{k}}-\epsilon_{v,\vec{k}})}e^{\frac{i}{\hbar}\int_T^t dt'\left\{\epsilon_{c,\vec{k}}-\epsilon_{v,\vec{k}}\right\}} + \text{ c.c.}} \tag{8.52}$$

Equation (8.52) represents the total current induced by the probe when the probe is applied in the z-direction. Once the time-dependent current is obtained, the next property to calculate is the optical conductivity $\sigma(\omega)$.

8.3.6 Optical Conductivity from PBM

To calculate the optical conductivity ($\sigma(\omega)$), we considered the electron dynamics under a weak perturbing electric field $\vec{E}(t)$.

$$\vec{E}(t) = E_0\vec{e}_z\delta(t-T), \tag{8.53}$$

whose FT is then

$$E_z(w) = \int_{t=-\infty}^{\infty} dt\ E_0\vec{e}_z\delta(t-T)e^{i\omega t-\gamma t} \tag{8.54}$$

and

$$E_z(w) = E_0 e^{i\omega T-\gamma T} \tag{8.55}$$

To obtain the optical conductivity, we apply the Eq. (6.21), but first we have to take the FT of the time-dependent current in Eq. (8.52). The FT is given by

$$J_z(w) = \frac{e}{m} \cdot \frac{2E_0}{(2\pi)^3} \int d\vec{k}\, \frac{1}{\hbar} \frac{|p_{vc}|^2}{(\epsilon_{c,\vec{k}} - \epsilon_{v,\vec{k}})} \int_T^\infty dt\; e^{\frac{i}{\hbar}\int_T^t dt' \left\{\epsilon_{c,\vec{k}} - \epsilon_{v,\vec{k}}\right\}} e^{i\omega t - \gamma t} + \text{ c.c.} \tag{8.56}$$

Subsequently, by calculating the ratios of the FT, one derives the optical conductivity ($\sigma(\omega)$) expressed as

$$\sigma(\omega) = \left(\frac{2\pi e^2}{m^2\omega}\right) |p_{vc,}|^2 D_j(\hbar\omega) \tag{8.57}$$

where $D_j(\hbar\omega)$ is the joint density of states and its given by

$$D_j(\hbar\omega) = \frac{1}{(2\pi)^3} \int d\vec{k} \delta\left(\epsilon_{c,\vec{k}} - \epsilon_{v,\vec{k}} - \hbar\omega\right) \tag{8.58}$$

Equation (8.58) can be referred to as "Static Joint Density of States (SJDOS)" since we use a static electric field to calculate it. DFKE is mainly associated with a time-dependent electric field, therefore the static JDOS needs to be extended. The JDOS can be described as transition rate between different states, given the system's Hamiltonian and the coupling between the initial and final states. In Heisenberg picture, we can express the JDOS as

$$\begin{aligned} D_j(\omega) &= \frac{1}{(2\pi)^3} \int d\vec{k} \delta\left(\epsilon_{c,\vec{k}} - \epsilon_{v,\vec{k}}, \vec{k}\right) \\ &= \frac{1}{(2\pi)^3} \frac{1}{\pi} \Re\left[\int dt e^{i\omega t} \int d\vec{k} \left\langle \Phi_0 \left| \hat{a}^\dagger_{v,\vec{k}}(t) \hat{a}_{c,\vec{k}}(t) \hat{a}^\dagger_{c,\vec{k}}(0) \hat{a}_{v,\vec{k}}(0) \right| \Phi_0 \right\rangle\right] \end{aligned} \tag{8.59}$$

where $|\Phi_0\rangle$ describes the ground-state of the many-body wavefunction which occupies the valence band, $\hat{a}^\dagger_{b,\vec{k}}(t)$ is a creation operator that creates an electron at a specific band b and a certain k-point $\vec{k}$ at a time t.

The SJDOS under the influence of the time-dependent vector potential $\vec{A}(t)$ can be expressed as, assuming that the vector potential can induce only intra-band transitions and not inter-band ones.

$$\begin{aligned} D_{d-j}(\omega, T) &= \frac{1}{(2\pi)^3} \frac{1}{\pi} \Re\left[\int dt e^{i\omega(t-T)} \int d\vec{k} \right. \\ &\quad \left. \times \left\langle \Phi_0 \left| \hat{a}^\dagger_{v,\vec{K}(t+T)}(t+T) \hat{a}_{c,\vec{K}(t+T)}(t+T) \hat{a}^\dagger_{c,\vec{K}(T)}(T) \hat{a}_{v,\vec{K}(T)}(T) \right| \Phi_0 \right\rangle\right] \\ &= \frac{1}{(2\pi)^3} \frac{1}{\pi} \Re\left[\int dt e^{i\omega(t-T)} \int d\vec{k} e^{-i\int_T^t dt' \left\{\epsilon_{c,\vec{K}(t')} - \epsilon_{v,\vec{K}(t')}\right\}}\right]. \end{aligned} \tag{8.60}$$

The above equation is very relevant in what we are trying to describe. The equation describes various dynamics which involves the following,

1. At a specific momentum $\vec{K}(t)$, an electron-hole pair is created.
2. The electron-hole pair created evolved from the specific momentum at $\vec{K}(t)$ to $\vec{K}(t+T)$ by the intra-band transition.

3. Finally, the created electron-hole pair is annihilated.

Hence, Equation (8.60) represents the "Dynamical Joint Density of States (D-JDOS)", depicting a spectrum of electron-hole pairs generated at a specific time T in response to a time-dependent vector potential $\vec{A}(t)$.

If we calculate the D-JDOS under the influence of a monochromatic electric field, $\vec{E}(t) = E_0 \cos(w_0 t)$, the D-JDOS can be formulated as follows

$$D_{d-j-\text{ dyn}}(\omega) = \frac{1}{4\pi}\Theta^{1/2}(2m_r)^{3/2}\left[\frac{\epsilon_g-\omega}{\Theta}\text{Ai}^2\left(\frac{\epsilon_g-\omega}{\Theta}\right) - \text{Ai}^2\left(\frac{\epsilon_g-\omega}{\Theta}\right)\right]. \tag{8.61}$$

After deriving various quantities, numerical simulations were performed by solving Eq. (8.44) to determine the values of the time-dependent coefficients $C_{v,k}(t)$ and $C_{c,k}(t)$. Similarly, we obtain the numerical solution of the time-dependent induced current as described in Eq. (8.48). Initially, the equilibrium optical conductivity $\sigma(\omega)$ was calculated by applying only a probe pulse. The vector potential of the probe pulse is defined by a cos^2 envelope, as outlined in Eq. (8.62), with a strength of $E_{probe} = 3.6 \times 10^8$ V/m, and a frequency $\omega_{probe} = 4.55eV$ which is resonant with the gap, with a pulse duration of 1fs. The vector potential employed is of the form

$$\boldsymbol{A}_{\text{probe}}(t) = -\frac{E_{\text{probe}}}{\omega_{\text{probe}}}\boldsymbol{e}_a \sin\left(\omega_{\text{probe}}\ (t - T_{\text{delay}})\right) \times \cos^2\left(\frac{\pi}{T_{\text{probe}}}\left(t - 0.5 \times T_{\text{probe}} - T_{\text{delay}}\right)\right) \tag{8.62}$$

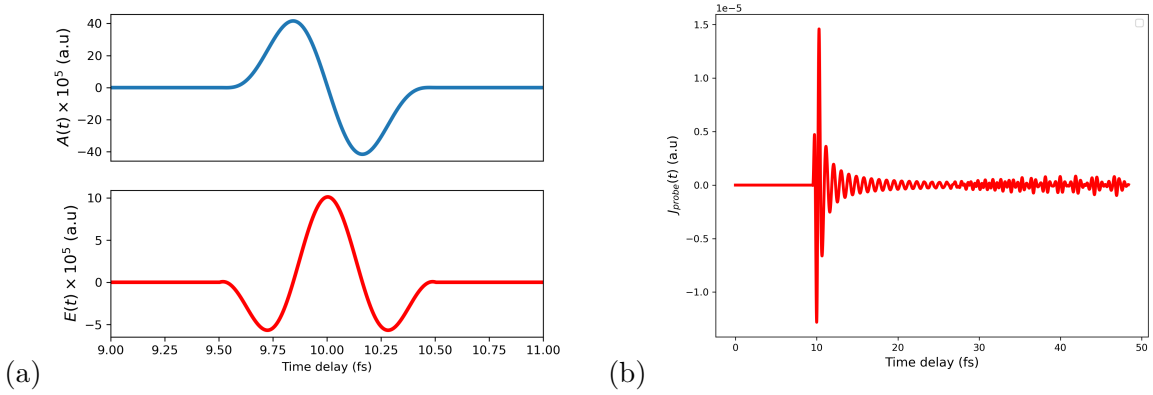

(a) (b)

Figure 8.18: (a) The upper plot shows the vector potential and lower plot displays the electric field of the probe pulse, (b) shows the time-dependent induced current by the probe pulse.

Figure 8.18 panel (a) shows the vector potential $\mathbf{A}_{\text{probe}}(t)$ and electric field of the probe pulse. The time-dependent current $\mathbf{E}_{\text{probe}}(t)$ induced by the probe pulse is shown in panel (b) of Figure 8.18. The current is induced at the time the probe field is applied and it shows oscillations until the end of the pulse.

The equilibrium optical conductivity $\sigma(\omega)$ is determined by obtaining the FT of the probe

current and probe electric field, followed by calculating the ratio of their respective FTs as stated in Eq. (6.21). The FT of the current and probe electric field are shown in panel (a) of Figure 8.19. The blue curve in the upper panel shows the FT of the probe electric field while the red curve in the lower panel shows the FT of the time-dependent induced current. The the equilibrium optical conductivity $\sigma(\omega)$ computed with the PBM is shown in panel (b) of the figure. The plot in panel (b) vividly showcases a distinct absorption peak located at around 4.45 eV, aligning precisely with the bandgap of the system corresponding to an increase in absorption.

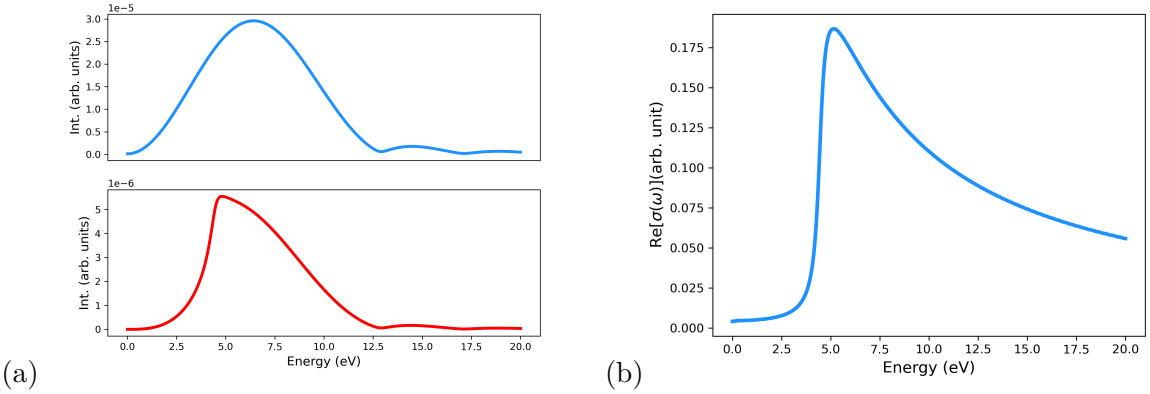

Figure 8.19: (a) FT of $\mathbf{E}_{probe}(t)$ and $\mathbf{J}_{probe}(t)$, and (b) Real part of optical conductivity computed using the PBM in the presence of the probe field.

To obtain the transient optical conductivity $\sigma^T(\omega)$, we simulate the electron dynamics in the presence of both pump and probe pulses. We followed the numerical pump-probe steps as depicted in Section 8.2. The vector potential of the pump and the probe is defined as

$$\boldsymbol{A}_{\text{pump}}\,(t) = -\frac{E_{\text{pump}}}{\omega_{\text{pump}}}\boldsymbol{e}_a \sin\left(\omega_{\text{pump}}\,\left(t - 0.5 \times T_{\text{pulse}}\right)\right) \cos^4\left(\frac{\pi}{T_{\text{pump}}}(t - 0.5 \times T_{\text{pulse}})\right) \tag{8.63}$$

the duration $-T_{\text{pump}}\,/2 < t < T_{\text{pump}}\,/2$ and zero outside, and

$$\boldsymbol{A}_{\text{probe}}\,(t) = -\frac{E_{\text{probe}}}{\omega_{\text{probe}}}\boldsymbol{e}_a \sin\left(\omega_{\text{probe}}\,\left(t - T_{\text{delay}}\,\right)\right) \times \cos^2\left(\frac{\pi}{T_{\text{probe}}}\,(t - 0.5 \times T_{\text{probe}} - T_{\text{delay}}\,)\right) \tag{8.64}$$

In Figure 8.20, the temporal profiles of electric fields $\vec{E}(t)$ and the resulting time-dependent induced currents $\vec{J}(t)$ for a time delay of $T_{delay} = 0$ fs are presented. The field strength E_{pump} is set at $3.6 \times 10^{10}\ V/m$ ($I = 1.5 \times 10^{12}\ W/cm^2$), with a mean frequency $\omega_{pump} = 1.55$ eV. The probe pulse is applied when the pump field reaches its peak magnitude. The probe pulse E_{probe} has a strength of $3.6 \times 10^8 V/m$, which is 100 times smaller, sufficiently inducing responses within the linear regime. Its frequency, ω_{probe}, is resonant with the bandgap at 4.45 eV. The pump pulse duration T_{pump} is set to 20 fs, while the probe pulse duration T_{probe} is set to 1 fs.

In the left panels of the Figure 8.20, electric fields are depicted: (a) shows pump-probe pulses only $\vec{E}_{pump}(t) + \vec{E}_{probe}(t)$, (b) displays pump pulse only $\vec{E}_{pump}(t)$, and (c) illustrates the probe pulse $\vec{E}_{probe}(t)$, obtained by taking the difference between (a) and (b). On the right panels, induced currents are shown: (d) features pump and probe pulses $\vec{J}_{pump}(t) + \vec{J}_{probe}(t)$, (e) shows

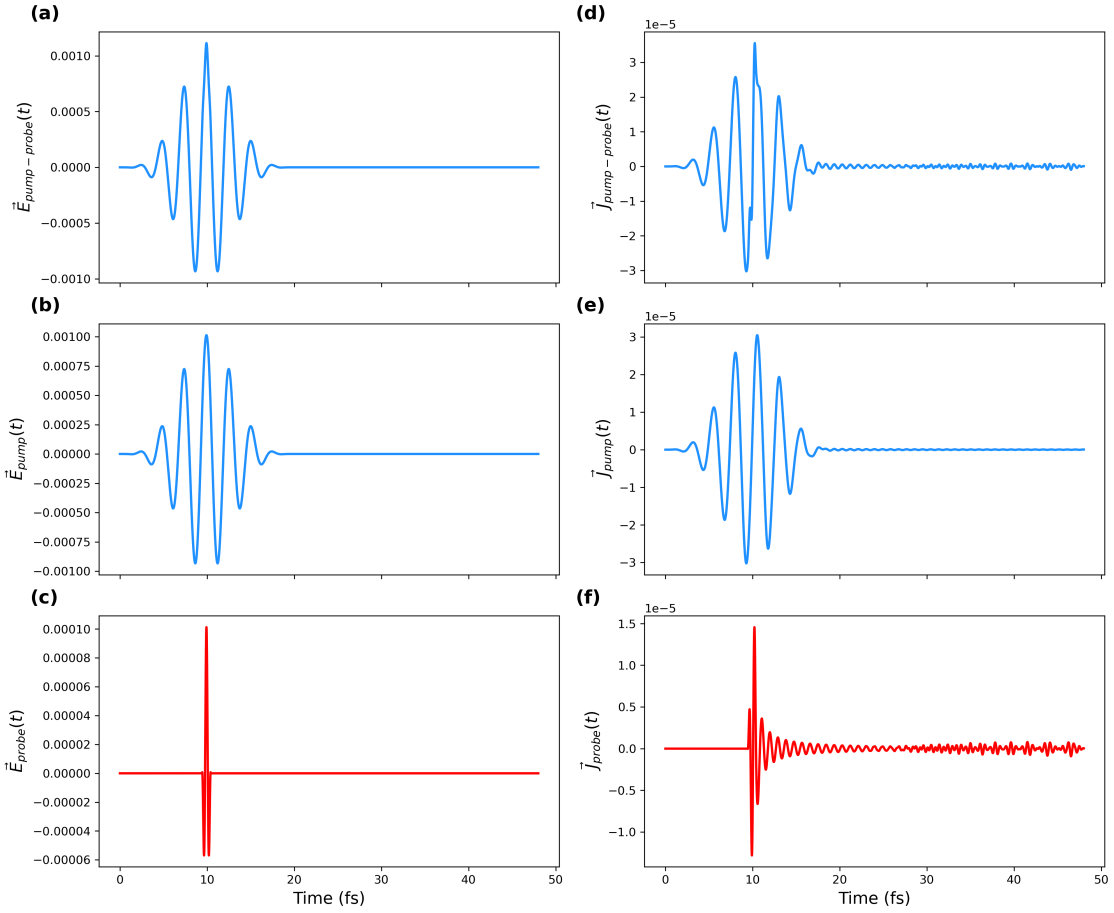

Figure 8.20: In the left panels, (a) displays the electric field of both pump and probe pulses, (b) illustrates the electric field of the pump pulse only, and (c) represents the probe pulse, obtained as the difference between the pump-probe and pump-only. Meanwhile, the right panels showcase the induced current, with (d) by the combined pump and probe pulses, (e) by the pump pulse alone, and (f) the difference between the currents illustrated in (d) and (e).

pump pulse only $\vec{J}_{pump}(t)$, and (f) represents the difference of the currents in (d) and (e) to obtain the probe current $\vec{J}_{probe}(t) = \vec{J}_{pump-probe}(t) - \vec{J}_{pump}(t)$. The next step is to repeat the simulations by changing the time delay between the pump and the probe to evaluate the transient optical conductivity $\sigma^T(\omega, T_{delay})$ and obtain the TAS.

We were thus able obtain the full TAS spectra of the PBM as shown in Figure 8.21. These results show that the physics governing the simulated TAS spectra in section 8.2 are well captured by the independent response of electrons in simple parabolic bands. In the figure, panels (c) and (g) shows the TAS for the monochromatic linearly polarised and circularly polarised pulses respectively. We observe the appearance of transient features that oscillate with twice the applied pump frequency $2\omega_{pump}$ throughout the duration of pulse. The main features are observed around the gap (i.e 4.45eV). Similarly, a V-shaped energy dispersion can be seen, originating around the gap and referred to as the 'fishbone' structure [227]. These feature also follows the pump adiabatically. The results from the PBM shows very good agreement with the features observed in TDDFT results described in section 8.2.

Panels (d) and (h) shows the TAS obtained using two-colour colinear and bicircular pulses

obtained using the PBM. Here, we also observed the below gap transient oscillatory features that oscillates with $3\omega_{pump}$ frequency in time domain. The results demonstrates the signatures of the *multicolor* DFKE, which are well reproduced by the parabolic two-band model as seen in the TDDFT calculation in section 8.2. The PBM results thus confirm the dominant role of the *multicolor* DFKE.

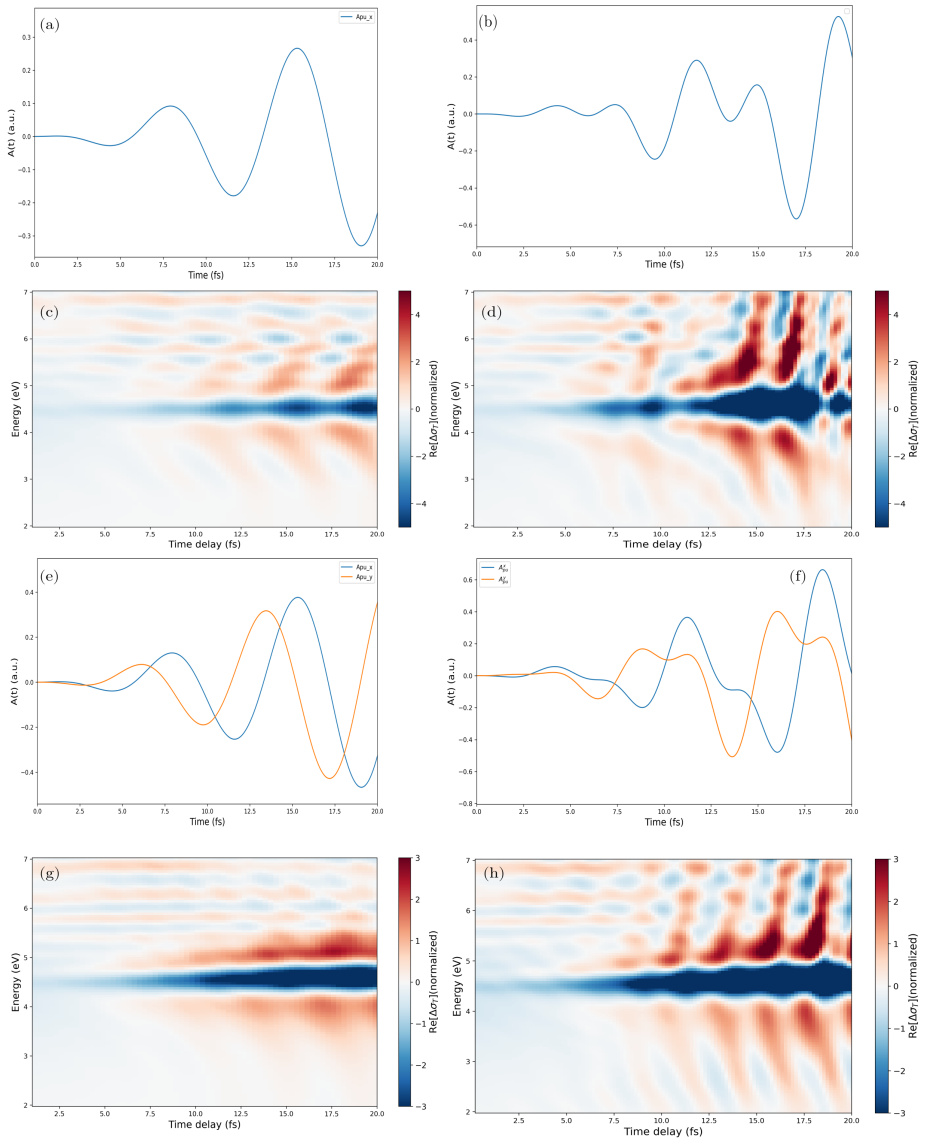

Figure 8.21: TAS of the PBM. Panels (a) and (e) shows the vector potential of the pump field corresponding a monochromatic linearly polarized and circularly polarised pump respectively. Panels (c) and (g) the corresponding differential transient absorption spectrum $\sigma(\omega, T_{delay}) - \sigma(\omega, 0)$ showing the characteristic "fishbone" structure and the 2ω periodicity that is associated with the DFKE. Panels (b) and (f) shows the vector potential of the two-colour colinear and bicircular pump field, while panels (d) and (h) shows the corresponding differential transient absorption spectrum $\sigma(\omega, T_{delay}) - \sigma(\omega, 0)$ with the 3ω periodicity that shows the signature of the multicolour DFKE.

The analysis in terms of the FKE and DFKE shows that it is above all the intra-band motion of these electrons that is responsible for the main spectroscopic features. The analysis further shows, that 3ω periodicity of the in gap structures in the spectra that we here assign as the signature of the multicolour DFKE is as well a purely independent electron response and stems

from their the intraband motions. These results confirm previous conjectures about the character and content of TAS in semiconductors and above all allow to generalizes the interpretation of these features in terms of the power-spectra of the multicolour pump fields.

8.4 Conclusion

In summary, we performed numerical pump-probe TDDFT simulations to obtain the TAS of monolayer hBN using different configurations of the pump pulse namely, the linear, colinear, circular and bicircular pump pulses. The results shows an oscillatory behaviour below the band gap, characterised by a V-shaped energy dispersion known as the 'fishbone' structure. The observed oscillatory features oscillates with twice the pump frequency $2\omega_{pump}$ for the linear and circularly polarized pulses, respectively. Studies have shown that this features are related to in the intraband motion of charges and known as the DFKE.

In the multicolour monochromatic colinear pulse and bicircular pulses, we observed that the frequency oscillates with three times the pump frequency $3\omega_{pump}$. These signatures, which have not been previously discussed in the literature, can be seen as the unique signals of the multicolor driving fields. Therefore, we define these features as the *multicolor* DFKE.

To gain full insight into the microscopic origin of the *multicolor* DFKE, we derived and demonstrate the use of a simple PBM. The main features observed in the TDDFT simulations are accurately reproduced by the PBM. The qualitative agreement between the TDDFT results and those obtained by PBM shows dominant role of intraband motion.

This page was intentionally left blank.

9 Phonon Dynamics in MoS_2 under optical doping

9.1 Introduction

In the previous chapter 5, the theoretical foundations for the calculation of phonons dynamics was highlighted. This include those quantum mechanical quantities that govern lattice vibrations in crystalline materials. Here the main focus is on the phonon dispersion of molybdenum disulfide (MoS_2). MoS_2, a member of the transition metal dichalcogenide (TMD) family, has garnered considerable attention due to its exceptional electronic, optical, and thermal properties. Beyond its 2D structure, this material exhibits distinctive phonon dispersion characteristics that hold the key to understanding its behavior under different conditions and for various applications. Here, we will focus on the investigation of how phonon dispersion relation changes with under the influence of photo doping.

Photo doping, often referred to as photo-induced charge transfer is an interesting approach. In this method, an electron in the occupied valence band, which is not ionized under equilibrium conditions, becomes ionized when exposed to irradiation. This causes the electron electron to be excited into the empty conduction band, leading to a change in the concentration of carriers. Several studies have shown that photo doping of layered materials or TMD's can enhance their optical properties and boost their applications in optoelectronic devices [228]. MoS_2 has been proposed as an ideal candidate for optoelectronic applications due to its distinct bandgap (direct in monolayer or indirect in bulk), exceptional charge mobility, high thermal rigidity and extremely low dissipation of power [47, 229]. Therefore, understanding these novel properties could lead to a better understanding and improvement of the application of these material in those devices.

9.2 Lattice Dynamics

The structure of MoS_2 consists of layers with covalent bonds between sulfur and molybdenum (S–Mo–S), which are further held together by weak van der Waals (vdW) interactions between adjacent sulfur-sulfur (S–S) layers. Illustrated in Figure 9.1, the layers of sulfur and molybdenum atoms exhibit a hexagonal arrangement, with each molybdenum atom positioned at the center of a trigonal prism formed by six sulfur atoms [230]. Such arrangements of atoms allows three different possible stacking configurations which include $1T$, $2H$ and $3R$. The $2H$ and $3R$ occurs naturally and have a trigonal prismatic atomic coordination [231]. The $3R$ configuration exhibits rhombohedral symmetry characterized by three S-Mo-S units. On the other hand, the $2H$-MoS_2

variant displays hexagonal symmetry, featuring two S-Mo-S units per unit cell. The $1T$ type, identified as a metastable structure in the early 1990s, showcases octahedral coordination with tetragonal symmetry, containing only one S-Mo-S unit as a repeating cell. Both the 1T and $3R$ types are considered metastable and can transition to the $2H$-MoS_2 structure when subjected to heating [232–235]. Subsequently, all of the bulk MoS_2 crystals discussed henceforth in this part are of the $2H$-MoS_2 structure whose Bravais lattice is hexagonal and with a space group of $P6_3/mmc$ (D^4_{6h} in Schönfließ notation). The unit cell is characterized by the lattice constant a (in-plane lattice constant) and c (out-of-plane lattice constant or vacuum). The basis vectors are given by

$$\begin{aligned} \vec{a_1} &= (\frac{1}{2}a, -\frac{\sqrt{3}}{2}a, 0) \\ \vec{a_2} &= (\frac{1}{2}a, \frac{\sqrt{3}}{2}a, 0) \\ \vec{a_3} &= (0, 0, c) \end{aligned} \tag{9.1}$$

In the case of monolayer, it consists of a single Mo atom and two S atoms. In this monolayer atomic configuration, the inversion symmetry is broken and the space group changes to $P\bar{6}m2(D^1_{3h}$ symmorphic group). By incorporating another S-Mo-S layer, a bilayer is formed with a symmetry group of $P\bar{3}m1(D^3_{3d}$ symmorphic group) and other layers are constructed in the same manner. As a result, odd-numbered layers has the same symmetry as that of a monolayer i.e, the absence of inversion symmetry while an even-numbered ones have the same symmetry as a bilayer with an inversion symmetry.

The geometry optimization of different layers of MoS_2 is the first step to perform before performing any calculation to obtain either the bandstructure or the phonon dispersion, a critical process to find the equilibrium structures of few layers of MoS_2. Figure 9.1 shows the atomic configuration of monolayer and bulk phase of MoS_2. The open source computational toolkit Quantum Espresso (QE) was employed to perform these geometry optimizations within the framework of DFT with an ultrasoft pseudopotential. The XC effects was treated within LDA for the monolayer and bulk case while the GGA in the form form of Perdew-Burke-Ernzerhof (PBE) was used for the remaining layers. Through various sets of self-consistent calculations, convergence threshold for energy is set to $10^{-9}eV$. All the atomic coordinates and lattice constants are optimized with Broyden–Fletcher–Goldfarb–Shanno (BFGS) algorithm [236, 237] and convergence was attained for key parameters, including k-points, lattice parameters, and plane-wave kinetic energy cutoffs(ecutwfs).

Layers	**Monolayer**	**Bilayer**	**Trilayer**	**Four layer**	**Five layer**	**Bulk**
a(Å)	3.194(3.125)	3.180(3.126)	3.190	3.192	3.192	3.142(3.127)
c(Å)	12.53(12.066)	13.378	32.12	43.196	50.381	12.058(12.066)

Table 9.1: Converged Lattice Parameters for various layers of MoS_2. The values in brackets are obtained from [14–16].

The table 9.1 shown above displays the optimized lattice parameters for different layers of MoS_2 for the electronics properties and phonon dispersion calculations, alongside corresponding values obtained from relevant literature sources as listed in the caption.

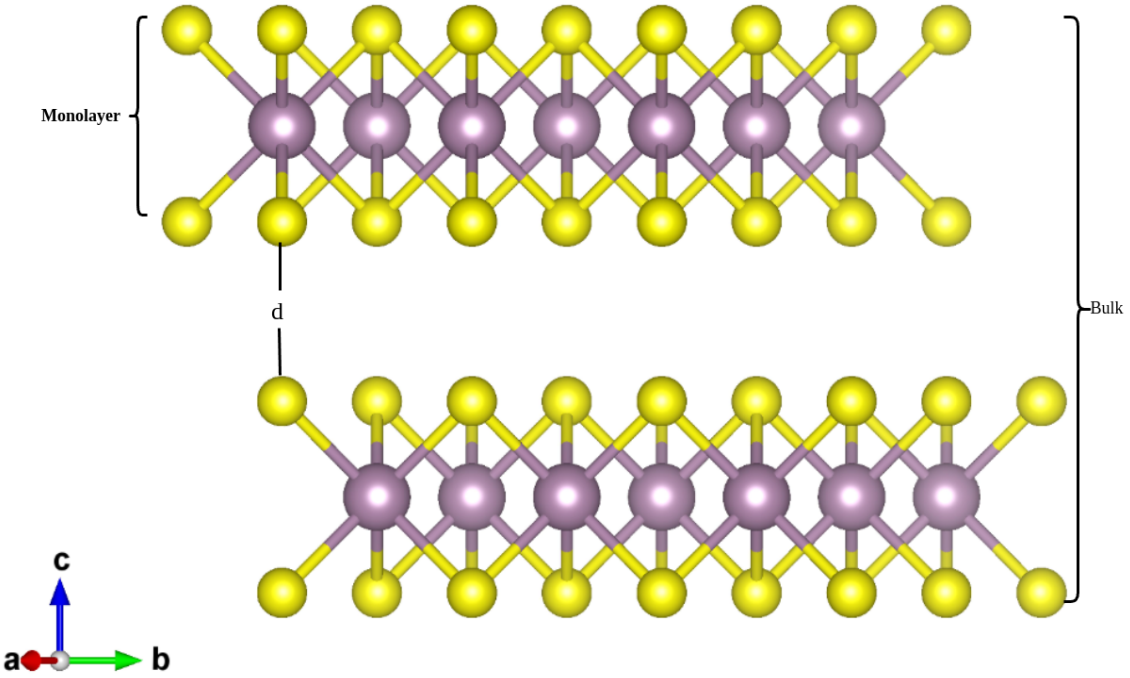

Figure 9.1: Atomic configuration of single layer and bulk phase of MoS_2. The interlayer distance is denoted d.

9.2.1 Electronic Band Structures

With the optimized lattice parameters, k-points and energy cutoff, the electronic band structures for the various layers were computed. In these calculations, the following k-points and energy cutoff for each atomic configurations were employed:

1. **Monolayer Configuration**: A Monkhorst-Pack k-point mesh of $18 \times 18 \times 1$ k-points grid are used to sample the Brillouin zone and set the energy cutoff at 100Ry and charge density of 800Ry and a Gaussian smearing with a smearing width of 10meV.

2. **Bilayer and Trilayer Configuration**: For the bilayer and trilayer atomic configurations, the choice is a $24 \times 24 \times 1$ k-points grid, accompanied by an energy cutoff of 80Ry and charge density of 640Ry.

3. **Four layer and Five layer Configuration**: For the four layer and five layer atomic configurations, the choice is a $18 \times 18 \times 1k$-points grid, and an energy cutoff of 80Ry and charge density of 640Ry.

4. **Bulk Configuration**: When dealing with bulk, our approach uses a $12 \times 12 \times 4$ k-points grid to sample the Brillouin zone and utilizes an energy cutoff of 80Ry charge density of 640Ry.

Figure 9.2 illustrates the bandstructures of different MoS_2 layers. In panel (a), the Monolayer MoS_2 is identified as a direct bandgap semiconductor with a bandgap energy of 1.88eV at the K-point. Panel (b) presents the Bilayer MoS_2, which exhibits an indirect bandgap of 1.2eV, spanning from Γ to K-point. The Bulk MoS_2 configuration, shown in panel (c), demonstrates

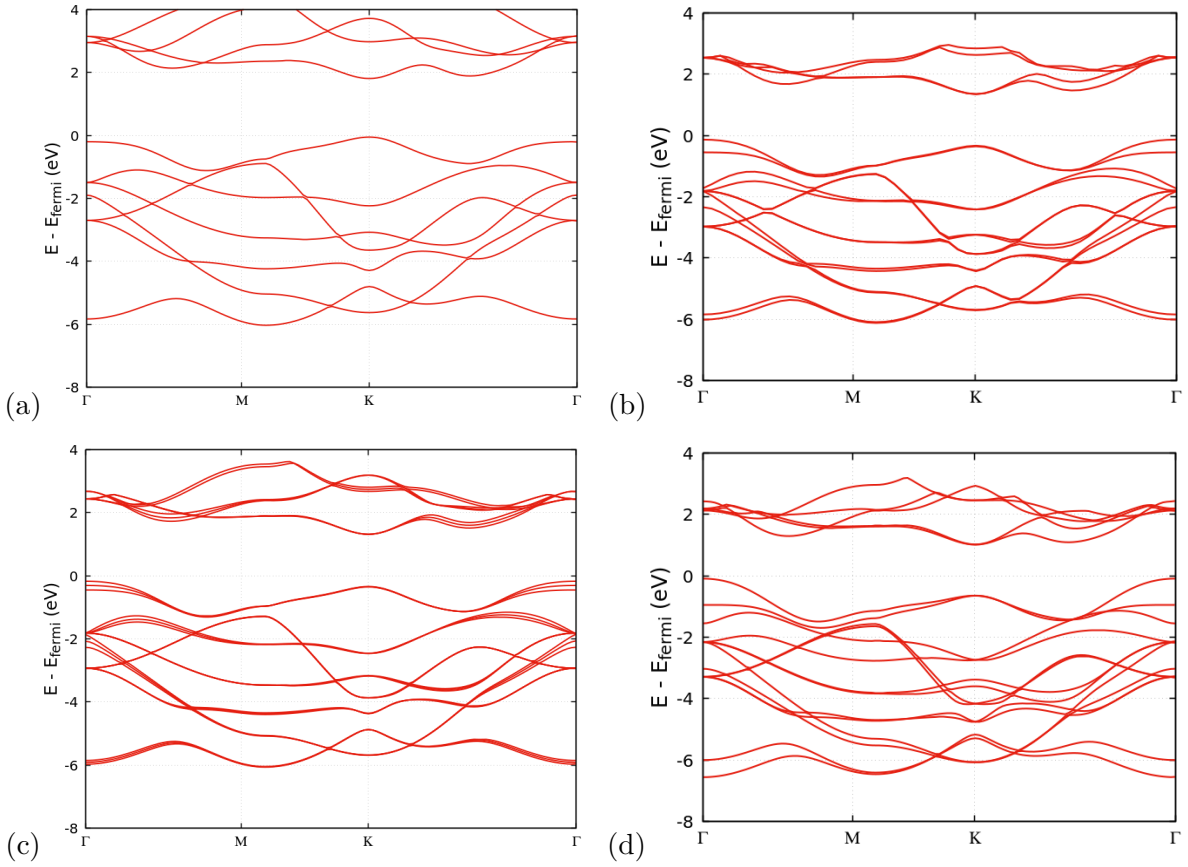

Figure 9.2: Electronic Band structures of different layer of MoS_2 for (a) Monolayer, (b) Bilayer, (c) Trilayer, and (d) Bulk.

Layers	Monolayer	Bilayer	Trilayer	Bulk
E_g(eV)	1.88(1.90)	1.20(1.31)	1.80(1.59)	1.18(1.20)

Table 9.2: Bandgap values of different layers of MoS_2. Values in parentheses are the experimental values from [17, 18].

characteristics of an indirect bandgap semiconductor, featuring a bandgap energy of 1.18eV. This indirect bandgap originates from the top of the valence band at the Γ point and extends to the bottom of the conduction band, encompassing the Γ and K-point regions. Additionally, a direct optical bandgap is observed at the K-point. Lastly, for the trilayer MoS_2 shown in panel (d), it shows an indirect bandgap with an energy value of 1.80eV. The calculated values reported here are in an excellent agreement with experimental and other theoretical results presented in the articles referenced in the figure caption.

9.3 Phonon Dispersion

After obtaining the equilibrium geometry for various layers and the bulk phase, phonon calculations were performed. The calculations were performed within the framework DFPT as implemented in the open source code QE [168, 238], within the LDA and GGA in form of PBE as approximations to the XC functional is employed in Norm-conserving pseudopotential through-

out the calculations. For the DFPT self-consistent iterations, a high convergence threshold of $1 \times 10^{-18} eV$, and a mixing factor 0.4 were employed for all phonon calculations in order to compute the dynamical matrix, from which the phonon frequencies and oscillation amplitudes are extracted [239].

9.3.1 Monolayer

In the case of monolayer, the vacuum value of $c = 12.53$Å was used which is enough to consider the interlayer interaction negligible and also gives a good description of both covalent and non-covalent interatomic bonding in the system. The phonon frequencies ω were calculated using Eq. (5.65) with a $\boldsymbol{q}$-grid points of $3 \times 3 \times 1$. The character of the modes, their direction of displacement, the atoms involved are presented in the table 9.3 below.

The phonon dispersion of monolayer MoS_2 in the high-symmetry direction $\Gamma - M - K - \Gamma$ is shown in Figure 9.4 and its comparison with experimental results alongside the phonon DOS. The phonon dispersion is characterized by two major bands that consist of nine branches: Three acoustic modes-namely the transverse acoustic (TA), longitudinal acoustic (LA) and the out-of-plane transverse acoustic (ZA)-and six optical modes. The acoustic modes are the lower frequency modes and are separated from the higher frequency modes by a frequency of $46 cm^{-1}$. Both acoustic and optical phonon modes have a linear dispersion at low momentum, which indicates that the phonons behave like free particles at low momentum. From the figure, one can also observe a band crossing of the acoustic modes just before the M point and between M and K points respectively. The dispersion curve demonstrates a good agreement with the experimental data (depicted by red dotted lines), particularly capturing the characteristics of the low-frequency acoustic modes. The higher frequency modes, particularly the A_2'' mode, exhibit a slightly lower frequency in comparison. Nevertheless, there is an overall excellent agreement between the DFPT results and the experimental data.

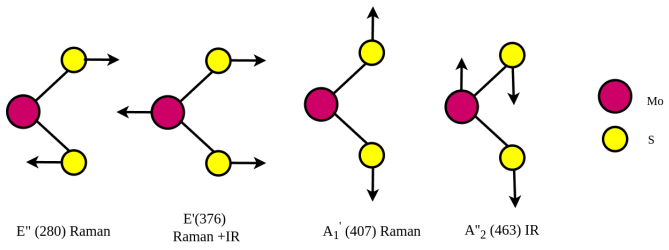

Figure 9.3: Sketch of the Atomic displacement vectors of the optical phonon modes E″ (Raman-active), E′ (Raman+IR), A_1' (Raman) and A_2'' (Infrared-active) at the Γ point showing the direction of displacements, involved atoms and their respective frequencies in cm^{-1}.

The frequencies of the phonon modes at the Γ point, their symmetry and characters as well the experimental values are shown in Table 9.3 below.

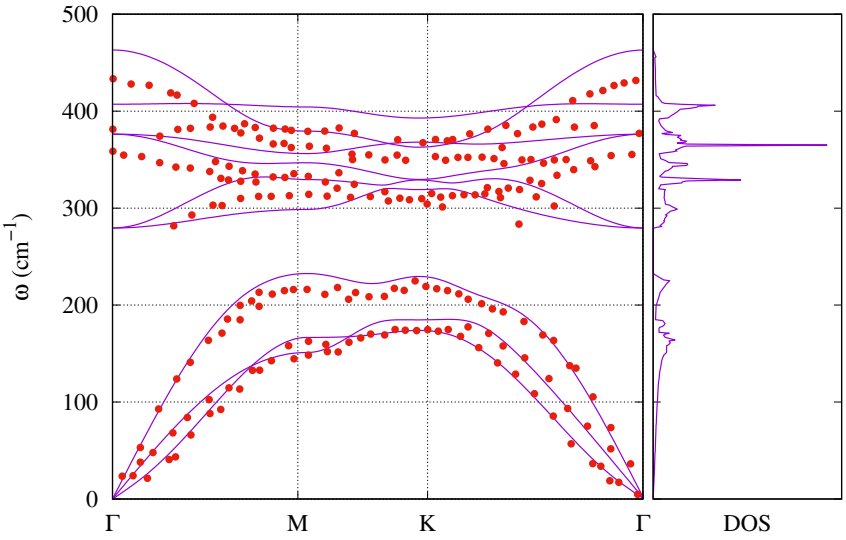

Figure 9.4: Comparison between the phonon dispersion curve of monolayer MoS_2 along the high symmetry path $\Gamma - M - K - \Gamma$ and experimental data (depicted by red dotted lines) and the phonon DOS. The experimental data is reproduced from the literature [11].

Modes	ω (cm^{-1})	ω (THz)	Exp.(cm^{-1})	D_{3h}	Character	Atoms	Direction
1	0.000	0.000	0.0	A_2	Acoustic	Mo + S	Out of plane
2	0.000	0.000	0.0	"	Acoustic	"	"
3	0.000	0.000	0.0	"	Acoustic	"	"
4	279.463	8.378	280.1	E″	Raman	S	In plane
5	279.463	8.378	280.1	E″	Raman	S	In plane
6	376.294	11.281	357.7	E′	Raman	Mo + S	In plane
7	376.294	11.281	357.7	E′	Raman	Mo + S	In plane
8	407.102	12.205	400.112	A_1	Raman	S	Out of plane
9	463.059	13.882	450.311	A_2″	Infrared	Mo + S	Out of plane

Table 9.3: Phonon Frequencies at Γ point for monolayer MoS_2 and experiment values obtained from [11].

9.3.2 Bilayer

To obtain the phonon dispersion for bilayer MoS_2, the relaxed structure was used and the calculated phonon dispersion alongside the experimental data is shown in figure 9.5 below. The phonon dispersion is calculated with q-grid points of $3 \times 3 \times 1$ in the Phonon-BZ employing the same convergence criterion as mentioned above. From the figure, there are in total 18 phonon modes which include three acoustic branches consisting of the following: one longitudinal acoustic mode (LA), the other is transverse acoustic mode (ZA) and the last one is the flexural acoustic mode (ZA) and the rest been higher frequency optical phonon modes. AT the M point, the LA mode has a value of $236cm^{-1}$ while it reaches a value of almost $240cm^{-1}$ at the K-point. One can also notice that there are no degeneracies at either M or K points but we noticed a band crossing between LA and TA branches between the Γ and M points and halfway between M and K point. The separation gap between the lower frequency modes and higher frequency modes is calculated to be around $45cm^{-1}$. Overall, as seen from the figure, there is a general

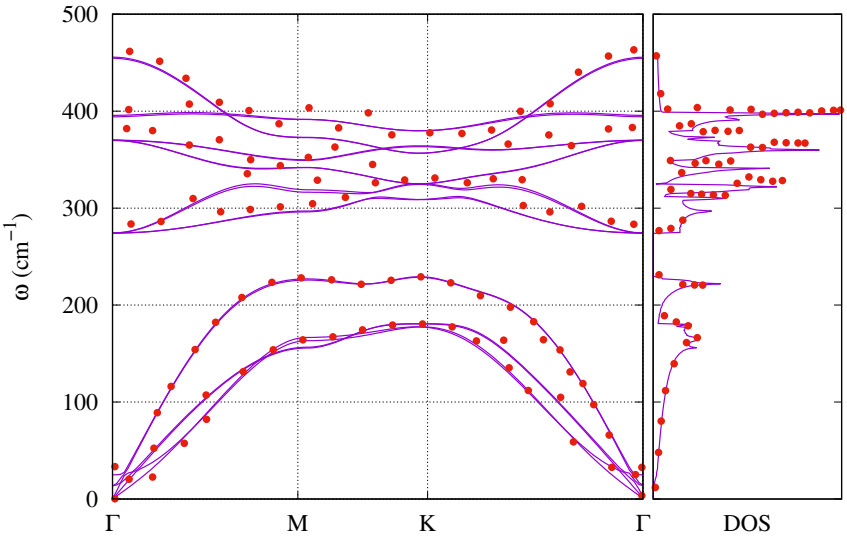

Figure 9.5: Phonon dispersion for Bilayer MoS_2 alongside the experimental results which are the data points extracted from [12].

agreement between the results and previous results in [240–242]. The phonon frequencies, the character of the phonon modes and their direction of vibration can be found in the Table 9.4 below.

Modes	ω (cm^{-1})	ω (THz)	Exp.(cm^{-1})	D_{6h}	Character	Atoms	Direction
1	0.000	0.000	0.00	A_{2u}	Acoustic	Mo+S	Out of plane
2	0.000	0.000		A_{2u}	Acoustic	Mo+S	Out of plane
3	0.000	0.000		A_{2u}	Acoustic	Mo+S	Out of plane
4	15.634	0.469	16.2	$E^2{}_{2g}$	Raman	Mo+S	In plane
5	15.634	0.469		$E^2{}_{2g}$	Raman	Mo+S	In plane
6	26.209	0.786	28.7	$B^2{}_{2g}$	Raman	Mo+S	Out of plane
7	274.275	8.223	287.1	$E^2{}_{2g}$	Raman	S	In plane
8	274.275	8.223		$E^2{}_{2g}$	Raman	S	In plane
9	274.492	8.229	288.0	$B^2{}_{2g}$	Inactive	S	In plane
10	274.492	8.229		E_{2u}	Inactive	S	In plane
11	369.908	11.090	378.7	$E^1{}_{2g}$	Raman	Mo+S	In plane
12	369.908	11.090		$E^1{}_{2g}$	Raman	Mo+S	In plane
13	370.234	11.099	384.8	E_{1u}	Infrared	S	In plane
14	370.234	11.099		E_{1g}	Infrared	S	In plane
15	394.202	11.818	404.3	B_{1u}	Inactive	S	Out of plane
16	395.639	11.861	405.1	A_{1g}	Raman	S	Out of plane
17	454.604	13.629	464.0	A_{2u}	Infrared	Mo+S	Out of plane
18	455.755	13.663	465.5	$B^1{}_{2g}$	Inactive	Mo+S	Out of plane

Table 9.4: Phonon Frequencies at the Γ Point of bilayer MoS_2. This table compares the calculated phonon frequencies at the Γ point of bilayer MoS_2 with the corresponding experimental values obtained from [12].

9.3.3 Bulk

Next, the phonon dispersion of bulk $2H - MoS_2$ is presented. The phonon dispersion of bulk MoS_2 is shown in Figure 9.6. The phonon dispersion is characterized by three acoustic modes (ZA, TA, and LA) and 15 optical modes (E_{1g}, E_{1u}, E_{2g}, and A_{1g}) giving rise to a total of 18 phonon modes. At the Γ point, the phonon modes can be represented in an irreducible form as

$$\Gamma_{2H} = A_{1g} \oplus 2A_{2u} \oplus 2B_{2g} \oplus B_{1u} \oplus E_{1g} \oplus 2E_{1u} \oplus 2E_{2g} \oplus E_{2u}$$

The phonon dispersion is anisotropic, meaning that the phonon frequencies depend on the direction of propagation of the phonons. The highest frequency optical modes (E_{1g} and E_{2g}) are observed at the K point in the Brillouin zone, while the lowest frequency optical mode (E_{1u}) is observed at the Γ point in the Brillouin zone. The low-frequency optical modes are found around $35.92cm^{-1}$ and $56.45cm^{-1}$. The high-frequency optical modes are separated from the low-frequency modes by a gap of $\approx 45cm^{-1}$.

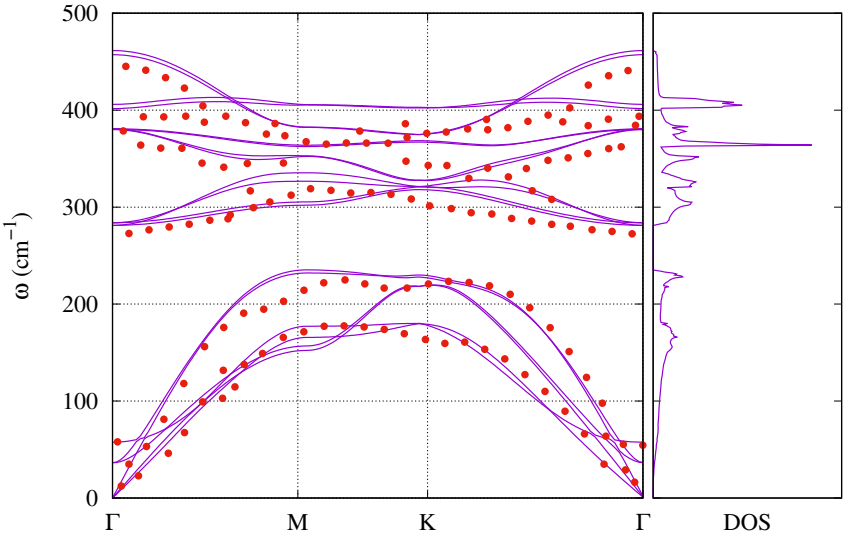

Figure 9.6: Plot of phonon dispersion curve of bulk MoS_2 along high symmetry directions $\Gamma - M - K - \Gamma$. Circles in red represents experimental measurements reproduced from [13].

From the phonon dispersion, one can see the ZA mode showing a q^2 dependence which is analogous to the ZA mode found in graphene. The nature of the ZA mode is due to the direct consequence of the point-symmetry group [243]. From the figure, one can also observe the slight splitting of the in plane $E^1{}_{2g}$ ($380.08cm^{-1}$) and E_{1u} ($380.83cm^{-1}$). This splitting is known as the Davydov splitting and in MoS_2, the experimental value of the splitting is reported to be around $1cm^{-1}$ [244]. The frequency of the Davydov pairs is small due to the fact that the interactions between the layers is weak. As reported by Ghosh *et al.* [245], the frequency of the E_{1u} mode is expected to be lower than that of the $E^1{}_{2g}$ because the sulfur atoms in different layers vibrate in opposite directions, creating an additional spring between them, which should increase the $E^1{}_{2g}$ mode frequency. However, experimental results has shown the opposite behaviour [13, 244]. Our results is consistent with the experiment which suggest that the splitting of these two modes is not only due to weak interlayer interactions but also due to the increase in self-interaction of the Coulomb part in the potential.

Modes	ω (cm^{-1})	ω (THz)	Exp (cm^{-1})	D_{6h}	Character	Atoms	Direction
1	0.000	0.000	0.00	A_{2u}	Acoustic	Mo+S	Out of plane
2	0.000	0.000		A_{2u}	Acoustic	Mo+S	Out of plane
3	0.000	0.000		A_{2u}	Acoustic	Mo+S	Out of plane
4	36.425	1.092	33.0	$E^2{}_{2g}$	Raman	Mo+S	In plane
5	36.425	1.092		$E^2{}_{2g}$	Raman	Mo+S	In plane
6	57.588	1.726	55.2	$B^2{}_{2g}$	Inactive	Mo+S	Out of plane
7	281.177	8.429	287.0	E_{2u}	Inactive	S	In plane
8	281.177	8.429		E_{2u}	Inactive	S	In plane
9	283.861	8.510	288.7	E_{1g}	Raman	S	In plane
10	283.861	8.510		E_{1g}	Raman	S	In plane
11	380.079	11.394	383.0	$E^1{}_{2g}$	Raman	Mo+S	In plane
12	380.079	11.394		$E^1{}_{2g}$	Raman	Mo+S	In plane
13	380.835	11.417	384.0	E_{1u}	Infrared	S	In plane
14	380.835	11.417		E_{1u}	Infrared	S	In plane
15	401.592	12.039	401.3	B_{1u}	Inactive	S	Out of plane
16	405.940	12.170	407.0	A_{1g}	Raman	S	Out of plane
17	457.202	13.707	462.0	A_{2u}	Infrared	Mo+S	Out of plane
18	461.453	13.834	467.1	$B^1{}_{2g}$	Inactive	Mo+S	Out of plane

Table 9.5: Phonon Frequencies of bulk MoS_2. The table shows the frequencies of each phonon mode at the Γ point alongside the experimental frequencies obtained from [19].

Table 9.5 presents calculated phonon frequencies at the Γ point for bulk MoS_2, alongside experimental values [19, 246]. Our results exhibit good qualitative agreement with other DFT calculations [14] and inelastic neutron scattering (INS) experiments [247], although calculations using PBE+D3 show slightly lower frequencies compared to our LDA results. Despite the absence of van der Waals corrections in our approach, our phonon frequencies closely match Raman measurements, differing by only a few cm^{-1}. Notably, discrepancies are more pronounced in acoustic and lower-energy optical modes. Achieving comprehensive agreement across the phonon dispersion curve requires an improved XC functional that can accurately capture both the strong in-plane covalent bonding and the weaker interlayer non-covalent interactions observed in MoS_2. The atomic displacement patterns of the atoms are shown in Figure 9.7.

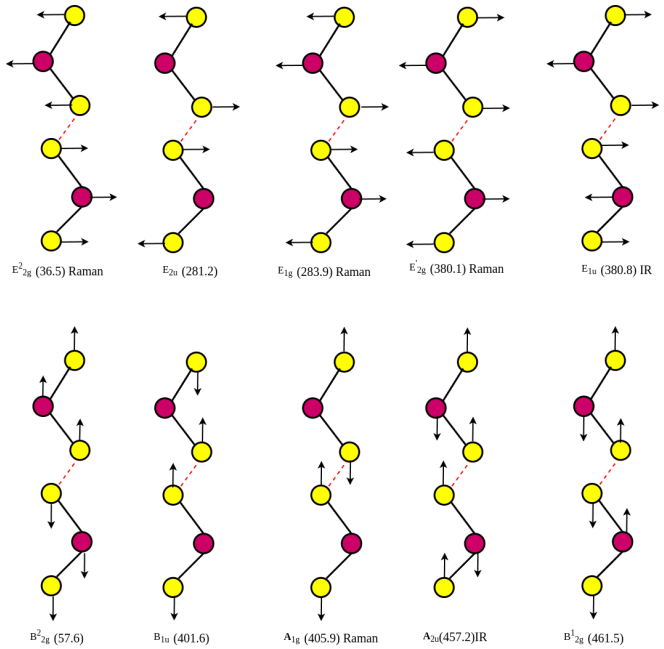

Figure 9.7: This sketch illustrates the optical phonon modes of bulk MoS_2. The first five modes represent vibrations with polarization parallel to the layers, while the remaining modes depict perpendicular polarization. The phonon frequencies are indicated in cm^{-1}.

9.4 Photoexcitation Dynamics

The theory discussed in 5.7 is subsequently applied to perform simulations on different layers of MoS_2 and the results are presented here. *Ab-initio* calculations have been performed within DFT using norm-conserving pseudopotential [158] to describe the electron-ion interaction for equilibrium calculations. The kinetic energy cut-off is the same as to what was previously reported in 9.2.1. For the XC potential, the GGA in form of PBE formulation was used in all cases considered. In the case of photo-excited calculations we used cDFPT as described in [248]. In the cDFPT approach, where a system of both electrons and holes are present, the chemical potential is a measure of the energy required to add an additional electron or hole in to the system. To do this, two distinct chemical potentials are defined: one for the thermalized electrons and one for thermalized holes. Here we employed two separate Fermi-Dirac distributions-one for the thermalized electrons and one for the thermalized holes. The two quasi-Fermi surfaces [1] are dealt with using the smearing method. The smearing parameter σ for the two Fermi-Dirac distributions, the lattice parameters after relaxation and number of photoexcited electrons for each layer is stated in the table 9.6 below. To calculate the phonon frequencies for the photoexcited case, a $\mathbf{q}$-grid points of $3 \times 3 \times 1$ was employed in both bilayer and bulk phase.

Table 9.6 compares the calculated lattice parameters obtained using the cDFPT approach with their equilibrium values. Here, photoexcitation induces slight changes in the lattice parameters for monolayer, bilayer and bulk phase. In the monolayer case, the lattice constant is increased by 0.13%, while in the bilayer case, the lattice parameter is increased by 0.06%. The bulk case shows an increase in the lattice parameter by 1.20%. These changes are attributed to

[1] Quasi-Fermi levels represents the energy distributions of electrons and holes, respectively.

Layer	a(Å)	c(Å)	$\sigma(eV)$	$n_e(e/atom)$
Monolayer	3.196 (3.192)	12.50 (12.53)	0.05	0.01
Bilayer	3.182 (3.180)	20.007 (13.378)	0.05	0.01
Bulk	3.180 (3.142)	13.17 (12.058)	0.05	0.01

Table 9.6: Lattice parameters (equilibrium lattice parameters), smearing and number of photoexcited electrons in the cDFPT approach for various layers.

electronic rearrangements that modify the interatomic forces, leading to a shift in the equilibrium atomic positions and, consequently, a change in the overall lattice parameters [249].

First, we employed the cDFPT approach to calculate the phonon frequencies of bilayer MoS_2 and compared them to the equilibrium ones. The phonon dispersion curve for the photoexcited with respect to the unexcited are presented in the figure 9.8 below. In the figure, the dispersion curves appears similar, but there are notable differences. The photoexcited case shows a slight shift in the phonon frequencies compared to the unexcited one, especially in the $E^2{}_{2g}$ and the $B^2{}_{2g}$ phonon modes [2]. The difference in the phonon frequencies indicates that photoexcitation modifies the lattice dynamics and phonon properties, resulting in the softening of these phonon modes. Similarly, there are some changes also in the optical branches. These changes in the curve suggest a modification in the electronic structure and perhaps electron-phonon coupling upon photoexcitation. We will discuss the shear and interlayer breathing modes in more details in the next section. Furthermore, the corresponding Density of States (DOS) also appears similar however there are some notable changes in the intensity of some of the peaks but overall appearances of the peaks in both cases looks the same. The changes in the intensity and positions of the peaks is as a results of the changes in the phonon population distribution [250, 251].

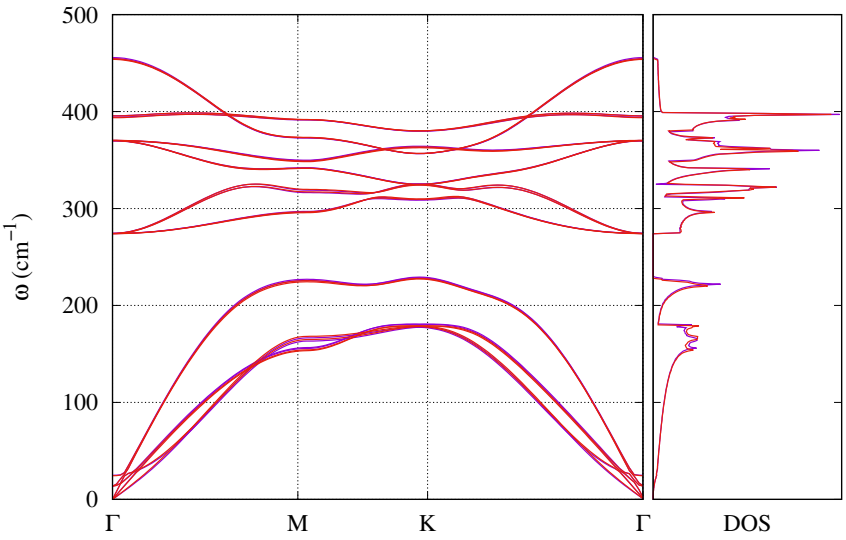

Figure 9.8: Phonon Dispersion: Comparison between photoexcited (Red curve) and equilibrium (Blue curve) phonon dispersion relations of bilayer MoS_2.

The table 9.7 below lists the phonon frequencies for both the photoexcited and unexcited cases for each phonon mode. From the shear ($E^2{}_{2g}$) mode, we observe a phonon frequency shift

[2] These modes are referred to as the shear and interlayer breathing modes in bilayer and bulk

of 0.216THz which corresponds to 31.5% increase at this photocarrier concentration while for the interlayer breathing mode ($B^2{}_{2g}$), the phonon frequency shift is 0.074THz corresponding to 8.6% increase. This frequency shifts suggest a change in the interlayer interactions and bonding strengths. In addition, the frequency shifts suggests that photoexcitation weakens or strengthens certain interlayer forces.

Mode	ω (THz)	ω (cm^{-1})	ω_{n_e} (THz)	ω_{n_e} (cm^{-1})	Character
1	0.000	0.000	0.000	0.000	A_{2u}
2	0.000	0.000	0.000	0.000	
3	0.000	0.000	0.000	0.000	
4	0.469	15.634	0.685	22.835	$E^2{}_{2g}$
5	0.469	15.634	0.685	22.835	
6	0.786	26.209	0.860	28.682	$B^2{}_{2g}$
7	8.223	274.275	8.212	273.933	E_{2u}
8	8.223	274.275	8.212	273.933	
9	8.229	274.492	8.219	274.150	E_{1g}
10	8.229	274.492	8.219	274.150	
11	11.090	369.908	11.100	370.270	$E^1{}_{2g}$
12	11.090	369.908	11.100	370.270	
13	11.099	370.234	11.109	370.569	E_{1u}
14	11.099	370.234	11.109	370.569	
15	11.818	394.202	11.801	393.624	B_{1u}
16	11.861	395.639	11.857	395.504	A_{1g}
17	13.629	454.604	13.610	453.967	A_{2u}
18	13.663	455.755	13.627	454.562	$B^1{}_{2g}$

Table 9.7: Phonon Frequencies at Γ point for equilibrium and photoexcited (ω_{n_e}) bilayer MoS_2.

Next, we study the vibration response of bulk MoS_2 under photoexcitation. The phonon dispersion of photoexcited bulk MoS_2 alongside the corresponding DOS is calculated, and the phonon frequencies for the respective cases are compared. The phonon dispersion curves are presented in the figure below 9.9. The phonon frequencies are also listed in the table 9.8 below. The dispersion curves demonstrate good agreement between the photoexcited and unexcited cases, although a noticeable difference can be observed. The shear ($E^2{}_{2g}$) and breathing modes ($B^2{}_{2g}$) exhibit significant frequency shifts, with the shear mode showing a shift of 0.032THz and the breathing mode showing a frequency shift of -0.008THz which shows $\approx 0.48\%$ softening of the mode already at this photocarrier concentration. The softening of these mode can be attributed to many factors relating to the materials electronic and lattice structure. The breathing modes which involves out-of-plane vibrations, is particularly sensitive to changes in interlayer coupling. Photoexcitation can weaken these interlayer interactions, leading to a reduction in the frequency of the breathing mode [252–254].

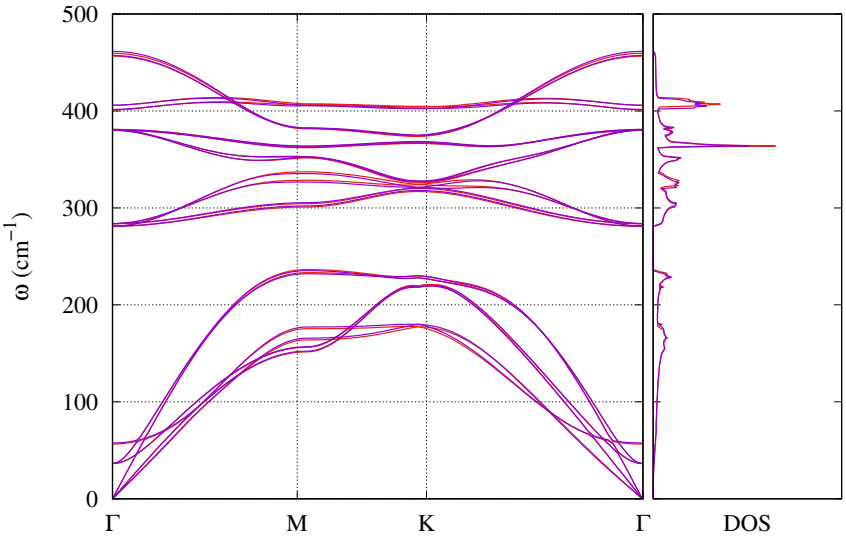

Figure 9.9: Phonon Dispersion: Comparison between photoexcited (Red curve) and equilibrium (Blue curve) phonon dispersion relations of bulk MoS_2 along the high symmetry lines.

Mode	ω (THz)	ω (cm^{-1})	ω_{n_e} (THz)	ω_{n_e} (cm^{-1})	Character
1	0.000	0.000	0.000	0.000	A_{2u}
2	0.000	0.000	0.000	0.000	
3	0.000	0.000	0.000	0.000	
4	1.092	36.425	1.124	37.495	$E^2{}_{2g}$
5	1.092	36.425	1.124	37.495	
6	1.726	57.588	1.718	57.312	$B^2{}_{2g}$
7	8.429	281.177	8.410	280.513	E_{2u}
8	8.429	281.177	8.410	280.513	
9	8.510	283.861	8.489	283.146	E_{1g}
10	8.510	283.861	8.489	283.146	
11	11.394	380.079	11.396	380.135	$E^1{}_{2g}$
12	11.394	380.079	11.396	380.135	
13	11.417	380.835	11.419	380.904	E_{1u}
14	11.417	380.835	11.419	380.904	
15	12.039	401.592	12.032	401.346	B_{1u}
16	12.170	405.940	12.173	406.036	A_{1g}
17	13.707	457.202	13.690	456.662	A_{2u}
18	13.834	461.453	13.779	459.603	$B^1{}_{2g}$

Table 9.8: Phonon Frequencies at Γ point for equilibrium and photoexcited (ω_{n_e}) bulk MoS_2.

9.5 Shear and Breathing Modes

In layered materials like MoS_2, photoexcitation can influence the behavior of specific vibrational modes. Bilayer and bulk phases exhibit two interlayer optical phonon modes: the Raman-active E^2_{2g} (shear mode) that vibrates in-plane and the optically inactive B^2_{2g} (breathing mode) that vibrates out-of-plane. These modes typically consist of N-1 doubly degenerate interlayer shear modes and N-1 interlayer breathing modes, where N represents the number of layers. When the number of layers (N) is odd, the interlayer breathing modes can be classified as either Raman-active (A'_1) or IR-active (A''_2). Meanwhile, the interlayer shear modes can be either Raman-active (E″) or both Raman-active and IR-active (E′). For even N, the interlayer shear modes are either Raman-active (E_g) or IR-active (E_u), while the interlayer breathing mode can be either Raman-active (A_{1g}) or IR-active (A_{2u}). Table 9.9 below summarised these phonon modes in MoS_2, while the Figure 9.10 shows the depiction of the low frequency shear and breathing modes in bulk MoS_2, along with their direction of displacement and frequencies.

	Shear modes		Breathing modes	
Bulk	$E^2{}_{2g}$ (R)			$B^2{}_{2g}$ (inactive)
Odd layers	E′ (I+R)	E″ (R)	A'_1 (R)	A''_2 (I)
Even layers	E_g (R)	E_u (I)	A_{1g} (R)	A_{2u} (I)

Table 9.9: Vibrational modes in bulk and few layers of MoS_2.

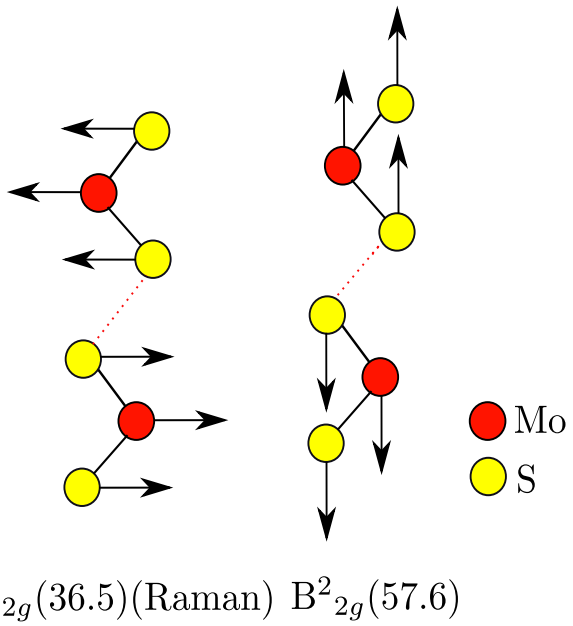

Figure 9.10: Illustration of shear (in plane) and interlayer breathing (out of plane) modes in bulk MoS_2 showing their direction of displacement and character. The phonon frequencies are indicated in cm^{-1}.

The aim here is to predict the signatures of the shear and interlayer breathing modes in various layers of MoS_2 upon photoexcitation, as would occur in an experiment where few-layer of MoS_2 crystals are prepared using the liquid exfoliation technique [255]. This exfoliation technique has been described as one of the most efficient method in producing cleanest and highly crystalline and atomic thin nanosheets. The prepared bulk sample should have a thickness of 200nm while other layers are peeled off from the bulk crystal. These MoS_2 layers will then

excited using an ultrafast optical pump with a central frequency of $400nm$ and a pulse duration of $100fs$. The pump excites the electron dynamics, and then a weak probe pulse with a duration $1ps$ will be applied at a certain time delay to probe the resulting changes. The pump fluence is set to $48\mu J/cm^{-1}$. The experiments are been carried out by Eugenio Cinquanta's group at CNR in Milano, and the resulting data, as well as a detailed comparison with our results, will be the subject of a forthcoming publication.

To quantify the experimental results, we performed simulations using cDFPT as implemented in revised version of QE package with the GGA in form of PBE. Highly accurate convergence threshold is employed throughout the calculations. With the optimized structures and self consistent wavefunctions, the phonon frequencies at the Γ point were calculated employing a mixing factor of 0.4 and a high convergence threshold of $10^{-18}eV$ for all layers.

The phonon frequency shift of the shear mode is reported in Table 9.10 while that of the breathing mode is reported in Table 9.11 for the various layers. Figure 9.11 shows the calculated phonon frequencies at the Γ point as a function of photo doping for the layers considered. The figures indicate a linear increase in phonon frequencies with increasing photodoping for most layer, with the exception of the fourlayer structure which shows a blue shift of frequencies of the shear modes.

		Layers				
		Bilayer	Trilayer	Fourlayer	Fivelayer	Bulk
	f_0(THz)	0.468708	0.312865	0.481257	0.433503	1.091984
$n_e(e/atom)$	$df_0 = f' - f_0$					
0.01	df_0(THz)	0.216	0.042	0.050	0.002	0.032
0.03	df_0(THz)	0.535	0.070	0.303	0.033	0.090
0.06	df_0(THz)	0.843	0.160	0.554	0.403	0.170
0.09	df_0(THz)	1.094	0.202	0.753	0.587	0.234

Table 9.10: Shear mode phonon frequency shift ($df_0 = f' - f_0$) for different layers of MoS_2 at different photodoping levels (n_e). Here, f_0 represents the equilibrium shear mode frequency.

		Layers				
		Bilayer	Trilayer	Fourlayer	Fivelayer	Bulk
	f_0(THz)	0.785725	0.524936	0.828020	0.635961	1.726431
$n_e(e/atom)$	$df_0 = f' - f_0$					
0.01	df_0(THz)	0.070	0.007	-0.155	0.021	-0.008
0.03	df_0(THz)	0.258	0.017	-0.136	0.095	-0.030
0.06	df_0(THz)	0.478	0.034	-0.205	0.113	0.004
0.09	df_0(THz)	0.691	0.064	-0.053	0.187	0.004

Table 9.11: Breathing mode phonon frequency shift ($df_0 = f' - f_0$) for different layers of MoS_2 at different photodoping levels (n_e).

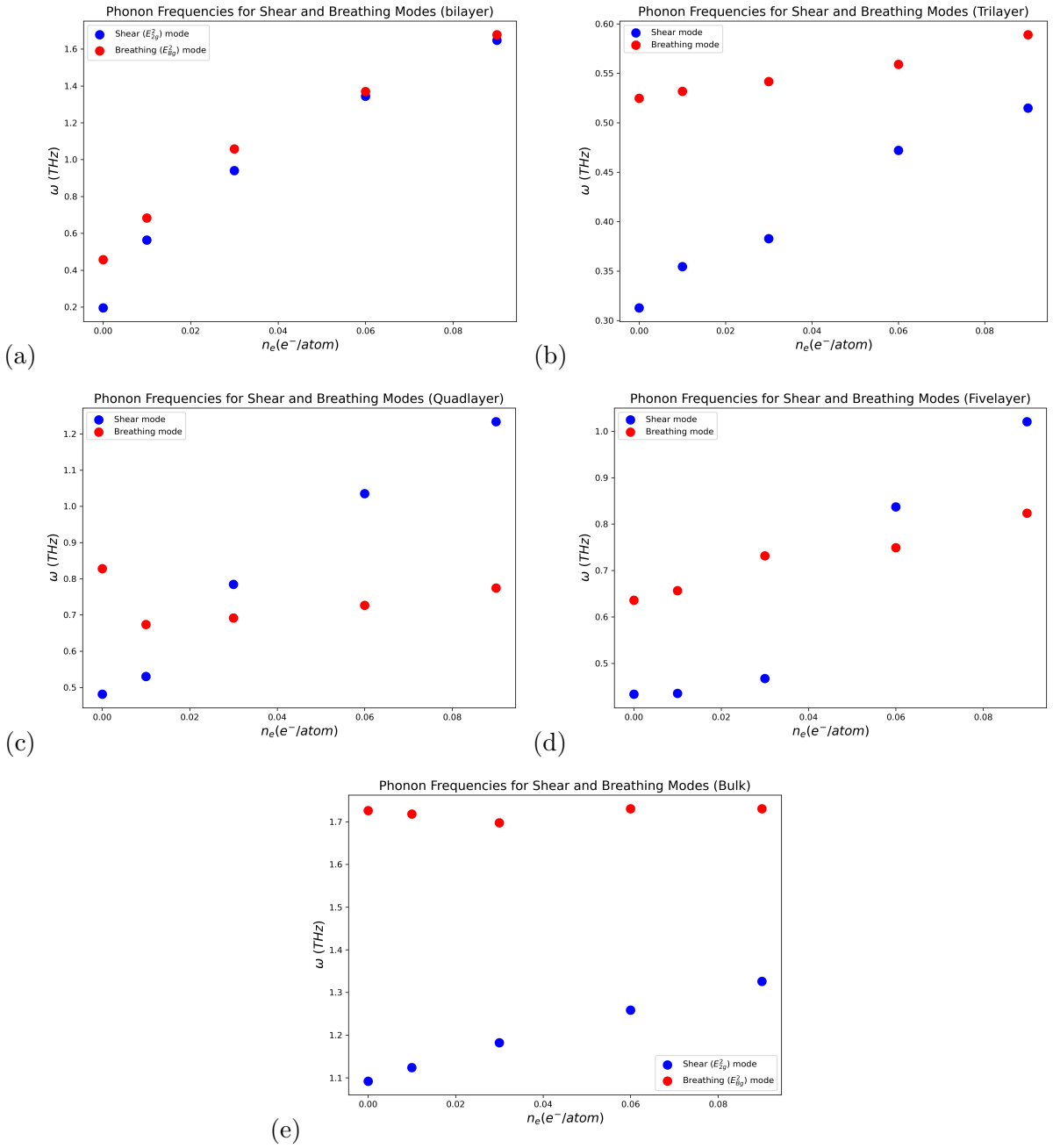

Figure 9.11: Phonon frequencies for shear and breathing modes in (a) bilayer, (b) trilayer, (c) four-layer, (d) five-layer, and (e) bulk MoS_2 as a function of photoexcitation.

In the layer distribution of the samples available to the experimental group at CNR Milano, the most dominant layer is the fivelayer which contribute to about 60% of the total sample and we assume the following distribution of layers as shown in the Figure 9.12. We further explored this layer by performing simulation to determine the total number of excited electrons (n_{ex}) at the end of the pump pulse. The fivelayer was excited with a pulse characterized by a sine-squared envelop for a duration of 100fs, with a frequency of 400nm and an Intensity of $1.413 \times 10^9\ W/cm^2$. The n_{ex} at the end of the pulse is 0.6 electrons. In total, the system contains 90 electrons, making n_{ex} corresponds to $\approx 0.67\%$ of the electrons. In the fivelayer MoS_2 system, which contains a total of 15 atoms, the number of excited electrons per atom ($n_e(e/atom)$) is 0.04. Hence this value corresponds to the photodoping at the given fluence. We obtain the phonon frequencies at photocarrier concentration ranging from $0.02 - 0.10 e/atom$. The phonon frequencies of the shear and breathing modes are shown in the table 9.12 while the frequency shift are listed in table 9.13.

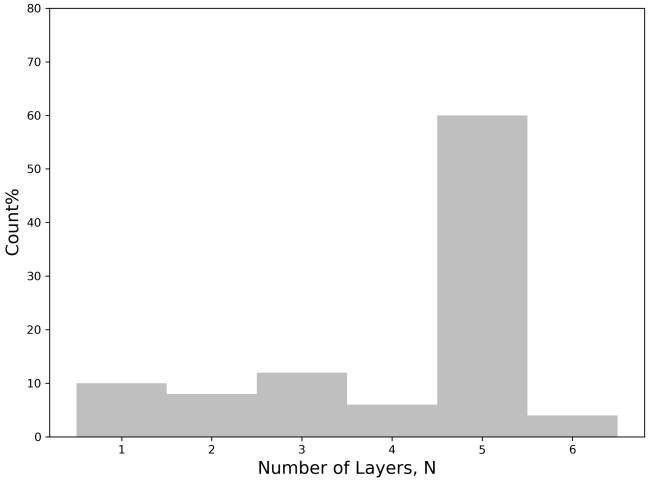

Figure 9.12: Distribution of number of layers (N) from the bulk sample. The plot highlights fivelayer distribution as the most dominant layer of the bulk configuration.

$n_e(e/atom)$	0.02	0.04	0.06	0.08	0.10
Shear	0.441	0.514	0.837	0.882	1.036
Breathing	0.698	0.744	0.769	0.778	0.846

Table 9.12: Shear and interlayer breathing mode phonon frequency (in THz) for different values of photoexcitation in fivelayer MoS_2.

$n_e(e/atom)$	0.02	0.04	0.06	0.08	0.10
Shear	0.007	0.080	0.403	0.448	0.602
Breathing	0.062	0.108	0.133	0.142	0.210

Table 9.13: Shear and interlayer breathing mode phonon frequency shifts (Δf_0) (in THz) for different values of photoexcitation in five-layer MoS_2.

Figure 9.13 (a) shows the relationship between phonon frequencies of shear and breathing mode with respect to the photo carrier concentration. For the shear modes, there is a linear increase in phonon frequencies as photodoping increases. Similarly, the breathing modes also show an increase in the phonon frequencies with increasing photodoping, although the relationship appears to be less linear compared to the shear mode. Meanwhile, Figure 9.13 (b) displays

the phonon frequency shift (Δf_0) of the shear and breathing modes.

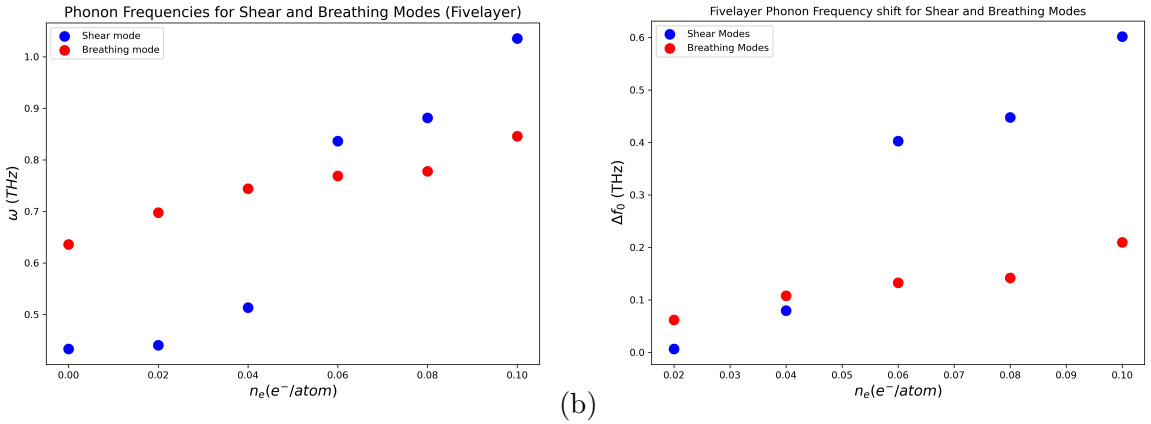

(a) (b)

Figure 9.13: (a) Phonon frequencies of shear and breathing modes (b) Phonon frequency shift (Δf_0) of shear and breathing modes in five-layer MoS_2 for different values of photocarrier concentration.

We quantified our equilibrium phonon frequencies for the shear and breathing modes using the online platform on the Materials Cloud [256], developed by Marzari *et al.*, following the theoretical methods described in [257]. The computed frequencies were obtained using a force constants tensor with $K_{xx} = 1.33\times10^{19}\ N/m^3$ and $K_{zz} = 3.743\times10^{19} N/m^3$ to fit the equilibrium phonon frequencies.

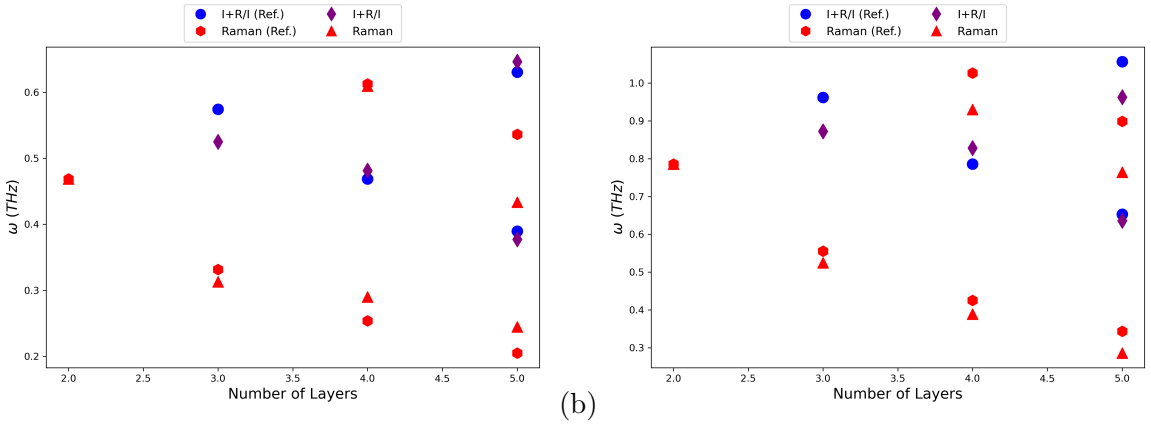

(a) (b)

Figure 9.14: Fan diagram: (a) **Shear modes**: The green triangles (Raman) and purple diamonds (Infrared) represents the equilibrium frequencies obtained using the DFPT. The red hexagons and the blue circles indicated frequencies obtained from the online tool. (b) **Breathing modes:** The green triangles represents Raman-active modes, while purple diamonds indicate modes that are active either Infrared + Raman or Raman only.

Figure 9.14 shows the fan diagram [258], comparing the normal mode frequencies for shear and interlayer breathing modes between our results and those obtained using the open source online tool [256]. The figure shows excellent agreement for both shear and breathing modes between the two sets of results, with the exception of the shear mode (Infrared) in the trilayer, where our results underestimate the phonon frequency.

9.5.1 Infrared Spectra

We are not in the position to combine all the information to make predictions on the pump induced changes to the low energy IR spectra of multilayer MoS_2 with different sample compositions. Here, we compute the Infrared (IR) spectra based on the phonon dispersion calculations. It is important to note that for these IR calculations, certain parameters were adjusted to address constraints within the QE code, including the removal of smearing. The spectra were calculated using norm-conserving pseudopotentials, and the equilibrium case was analyzed to obtain the intensities of the IR modes. For the photo-doped case, we employed the model shown in Eq. 9.2 to fit the intensities and reproduce the IR spectra. The acoustic sum rule was not applied in the IR spectra calculations.

$$\alpha(\omega) = \Im\left[\sum_{i=1}^{2} \frac{a_i}{\omega - \omega_i + i\eta}\right] \tag{9.2}$$

where a_i is the intensity of the IR peaks calculated from QE, ω is the phonon frequency and η is the broadening, with a broadening value of 0.035 eV used in this case.

Figure 9.15 show the IR spectra for 3, 4, and 5 layer MoS_2 configurations. In panels (a) and (b) the IR/R spectra for 3 layer configurations and the corresponding difference between the equilibrium and doped. The first peak (blue) at 0.313THz corresponds to the shear mode in the equilibrium case while the second peak (red) at $\approx$ 0.356THz corresponding to the shear mode in the doped case. The most intense peaks corresponds to the breathing mode in both cases. The breathing mode in the doped case shows marginally higher intensity at the peak which shows doping enhances the IR response of the mode.

Panels (c) and (d) shows the IR spectra for the 4 layer configuration in both cases and the corresponding difference between the spectra. The first peak corresponds to the shear modes in both cases. Here also we can observe the blue shift of the phonon frequencies of the shear modes. The breathing modes in the doped case shows a red shift of the phonon frequencies which confirms the softening of the IR mode as reported in 9.11.

Panels (e) and (f) show the IR spectra for the 5 layer configuration, which we assume to be the most dominant layer among the distribution. As in the previous cases, the first peaks correspond to the shear modes in both the doped and equilibrium states, while the second peaks represent the breathing modes. Both the shear and breathing modes exhibit a blue shift in the phonon frequencies, indicating a hardening of the vibrational modes due to doping.

Finally, Figure 9.16 (a) shows the combined IR spectra of a sample with a combined 3,4 and 5 layer composition, according to the distribution given in Figure 9.12, both in its equilibrium and doped states. The first sets of peaks at lower frequencies corresponds to the shear modes, while the second set of more intense peaks corresponds to the breathing modes. Panel (b) shows the difference between the spectra for the equilibrium and doped, showing the frequency shifts and intensity changes due to photodoping. This final result constitutes the prediction of an experiment, probing the low energy redistribution of phonons upon photodoping. As of finalisation of this thesis such experiments are currently being performed at CNR Milano and are used as a guide for experimentalists on laser parameters and energy scales. The final comparison will then both be a validation of the theory and serve as the basis for the interpretation of results

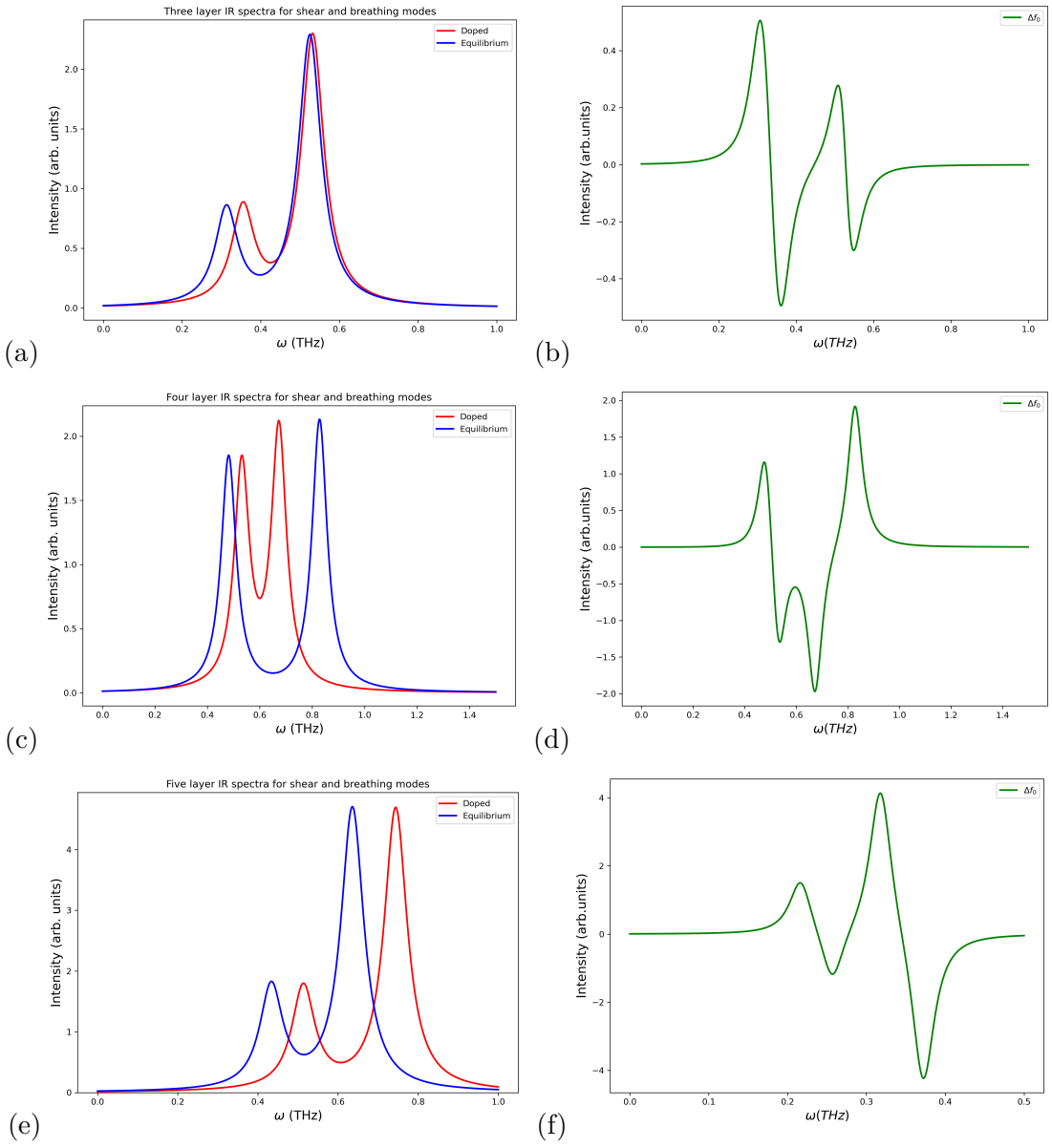

Figure 9.15: IR spectra (a) Three layer configuration, (b) difference between equilibrium and doped, (c) four-layer configuration, (d) difference between equilibrium and doped, (e) five-layer configuration, and (f) difference between equilibrium and doped.

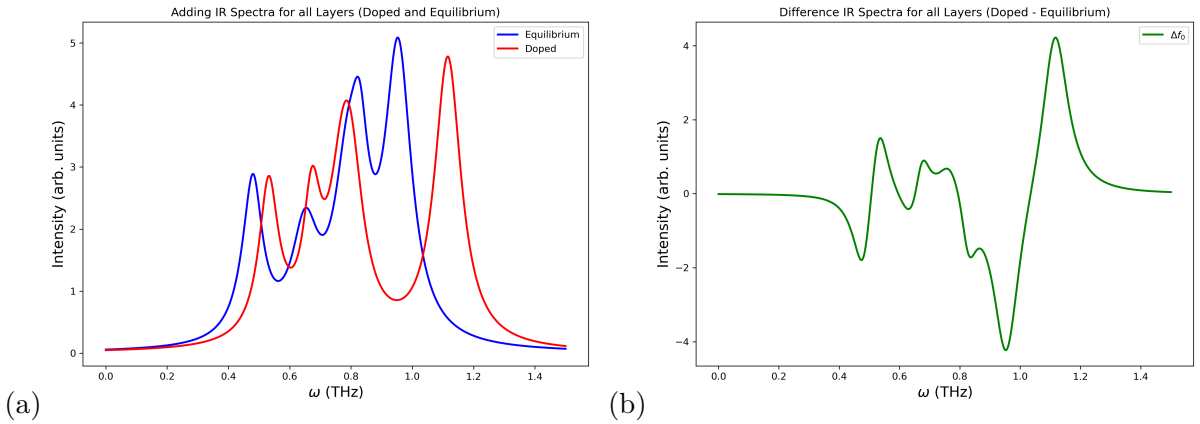

(a) (b)

Figure 9.16: (a) Combined IR spectra for 3, 4 and 5 layer configurations for the shear and interlayer breathing modes, (b) The difference between the doped and equilibrium combine spectra.

in terms of disentangling the layer contributions and the unambiguous assignment of the spectral features.

9.6 Conclusion

In this chapter, we utilized DFT and cDFPT to investigate the phonon frequency shift in different layers of MoS_2 due to photodoping, with a focus on the low frequency shear and interlayer breathing modes. Based on the available sample at CNR Milano, the most dominant layer of the bulk configuration is the five layer system. Both shear and interlayer breathing modes in this system shows an increase in phonon frequencies with photodoping, indicating a blue shift. Additionally, we calculated the IR spectra of 3, 4 and 5 layer configurations, which provides a further insight into the vibrational properties across these layers. The results provide a valuable predictions for future experimental investigations of the layer dependent phonon behaviour in MoS_2.

This page was intentionally left blank.

10 | Summary, Conclusion and Outlook

I gotta stop somewhere - I'll leave you something to imagine.

Richard Feynman - Symphony of Science

In this thesis, the we have studied how to systems response to an external perturbation by applying real time TDDFT as implemented in the octopus code to calculate various observables and non-linear quantum mechanical effects in solid systems. While TDDFT gives a proper description of systems in their ground state, here we demonstrate how TDDFT can be applied to study time resolved phenomena using the numerical pump-probe technique to mimic the time-resolved pump-probe experiments.

In the first part of this thesis, we discuss the development of attosecond transient absorption spectroscopy (TAS) over time and introduce the fundamental concepts necessary for conducting pump-probe experiments. Additionally, we explore some basic properties of solid-state systems, focusing on hexagonal boron nitride (hBN) and molybdenum disulfide (MoS_2), as these materials are central to the research presented in this work.

The second part of this work presents an extension of the TDDFT to accurately describe the response of solid systems to external perturbations. We demonstrate that applying a small perturbation within the linear response regime can effectively induce excitations, allowing us to establish the necessary relationship between the time-dependent induced current and the external perturbation, which is essential in evaluating the optical conductivity.

We performed XAS calculations focusing on the boron K-edge. Our results reveals a prominent feature corresponding to the $1s \rightarrow \pi^*$ transition peak at an energy of 175eV. In contrast, the experimental observations typically report as a strong excitonic peak occurring in the energy range of 190 $\rightarrow$ 192 eV, indicating a significant difference between the theoretical and experimental findings. We further investigated the K-edge spectra using various approximations to DFT such as DFT+U which also fails to capture the excitonic peak accurately. These findings suggest limitations in the current theoretical approaches for modelling the excitonic effect in the XAS and highlights needs for more advanced methods and approximations to the XC functional and use of more ad-hoc functionals like the hybrid functional or another XC kernel f_{xc} to achieve a better agreement with experimental data.

In the third part of this thesis, we utilized the real-time electron dynamics simulation within the framework of TDDFT to calculate the TAS using a numerical pump-probe technique. We explored four different configuration of the pump pulses: linear, circular, two-colour monochromatic colinear, and bichromatic counter rotating pulses. For the linear and circular pulses, we observed non linear electron dynamics below the bandgap of hBN characterized by oscillatory features below the gap. These observed features oscillates with twice the pump frequency and are the salient feature of the DFKE.

In contrast, unique features were observed when employing the monochromatic colinear pulse and bichromatic counter rotating pulse. The below gap oscillations in these cases occur with three times the applied pump frequency, making it this is the first time that these features are observed. We attribute these behaviour to the *multicolor* DFKE. Further experiment is required to validate the theoretical findings and perhaps it could lead to new and fascinating discoveries about the transient features observed.

To investigate the microscopic origin of these features, we developed a PBM. The results from this model not only successfully reproduced the TDDFT results but also provide insights into the underlying mechanism, which are driven by the intraband transition of electrons.

The final part of this work focuses on the vibrational properties of different layers of MoS_2. We employed DFT and cDFPT, as implemented in the Quantum Espresso code to calculate phonon dispersion curves and their corresponding phonon frequencies. Our investigation centered on the low frequency shear and interlayer breathing modes, examining their behaviour in response to the photodoping. In 3 layer and 5 layer configurations, we observed a hardening of both the shear and interlayer breathing modes, while the 4 layer configuration shows a phonon softening of the breathing mode. These phonon hardenening/softening is attributed to the increase in interlayer interaction and modification of the electronic structure.

We quantified our result with the online tool and proposed a novel experiment to be conducted at CNR Milano. This experiment will serve as a benchmark for validating the theoretical results and will contribute to a future publication.

This page was intentionally left blank.

A | Time Dependent Perturbation Theory

A.1 General formulation

In this section, we derive a very useful result for estimating the transition rates between different quantum states utilizing the time dependent perturbation theory. Continuing the formal advancement in understanding the optical characteristics of solids requires us to address the quantum mechanical treatment of the impact of time-dependent electromagnetic fields. The significant scenario to consider involves external fields that follow a sinusoidal time variation. In most real-world scenarios, these external fields are relatively weak, enabling their treatment through perturbation theory. In application of time-dependent perturbation theory one can express the total Hamiltonian $\mathcal{H}$ as:

$$\mathcal{H} = \mathcal{H}_0 + \mathcal{H}'(t) \tag{A.1}$$

where $\mathcal{H}_0$ is the unperturbed Hamiltonian and $\mathcal{H}'(t)$ is the applied time-dependent perturbation. Here I assumed that I know how to solve the unperturbed time independent problem for its eigenvalues E_n and corresponding eigenfunctions u_n.

$$\mathcal{H}_0 u_n = E_n u_n \tag{A.2}$$

Because the perturbing Hamiltonian $\mathcal{H}'(t)$ possesses explicit time dependence, the concept of "energy" no longer remains a "constant of the motion". As we no longer have stationary solutions that are independent of time, we must utilize the time-dependent version of Schrödinger's equation, given by:

$$i\hbar\frac{\partial\psi}{\partial t} = \mathcal{H}\psi = \left(\mathcal{H}_0 + \mathcal{H}'\right)\psi \tag{A.3}$$

Now, if the perturbation term $\mathcal{H}'(t)$ is not added to the Hamiltonian, one can use the ansazts for the eigenstates

$$\psi(\vec{r},t) = u_n(\vec{r})e^{-iE_nt/\hbar} \tag{A.4}$$

where $u_n(\vec{r})$ is independent of time and its the solution of Eq. (A.2). Hence, the time dependence of $\psi(\vec{r},t)$ is encapsulated within the phase factor $e^{-iE_nt/\hbar}$.In the case where $\mathcal{H}'(t) = 0$, it promptly results in:

$$i\hbar\frac{\partial\psi}{\partial t} = E_n\psi \tag{A.5}$$

which results in the time-independent Schrödinger equation. With the presence of the perturbation, the time dependent eigen states $\psi(\vec{r},t)$ can be expanded in terms of the complete set $u_n(\vec{r})e^{-iE_nt/\hbar}$. Therefore, the eigen states becomes

$$\psi(\vec{r},t) = \sum_n a_n(t)u_n(\vec{r})e^{-iE_nt/\hbar} \tag{A.6}$$

where $a_n(t)$ are the time-dependent expansion coefficients. Now, upon substituting Eq.(A.6)

into Eq.(A.3), one obtain the following expression:

$$\begin{aligned} i\hbar \sum_n \dot{a}_n(t) u_n e^{-iE_n t/\hbar} + \sum_n a_n(t) u_n E_n e^{-iE_n t/\hbar} &= \sum_n a_n(t) \left[\mathcal{H}_0 + \mathcal{H}'(t)\right] u_n e^{-iE_n t/\hbar} \\ &= \sum_n a_n(t) \left[E_n + \mathcal{H}'(t)\right] u_n e^{-iE_n t/\hbar} \end{aligned} \tag{A.7}$$

where $\dot{a}_n(t)$ denotes the time derivative $da_n(t)/dt$. From Eq. (A.2), one can clearly see that the second term on the LHS of Eq.(A.7) cancels out by the first term on the RHS. We have

$$i\hbar \sum_n \dot{a}_n(t) u_n e^{-iE_n t/\hbar} = \sum_n a_n(t) \mathcal{H}'(t) u_n e^{-iE_n t/\hbar} \tag{A.8}$$

Now, the trick is to multiply the LHS of Eq.(A.8) with by $u_m^*(\vec{r})$ and integrate over all space and utilizing the orthogonality condition of the eigen functions

$$\int u_m^*(\vec{r}) u_n(\vec{r}) d^3r = \delta_{m,k} \tag{A.9}$$

we obtain

$$i\hbar \dot{a}_m e^{-iE_m t/\hbar} = \sum_n a_n \left\langle m \left| \mathcal{H}'(t) \right| n \right\rangle e^{-iE_n t/\hbar} \tag{A.10}$$

where the matrix element can be expressed as

$$\left\langle m \left| \mathcal{H}'(t) \right| n \right\rangle = \int u_m^*(\vec{r}) \mathcal{H}'(t) u_n(\vec{r}) d^3r. \tag{A.11}$$

Since the perturbing Hamiltonian $\mathcal{H}'(t)$ is time-dependent, the matrix element also have to be time-dependent altyhough it is important to note that the matrix element is computed between states that are stationary. Therefoe, Eq.(A.8) becomes

$$i\hbar \dot{a}_m(t) = \sum_n a_n(t) \left\langle m \left| \mathcal{H}'(t) \right| n \right\rangle e^{i(E_m - E_n)t/\hbar} \tag{A.12}$$

Upon setting

$$\hbar\omega_{mn} = E_m - E_n \tag{A.13}$$

we obtain this expression for the time derivative of the time-depedent coefficient

$$\dot{a}_m(t) = \frac{1}{i\hbar} \sum_n a_n(t) e^{i\omega_{mn} t} \left\langle m \left| \mathcal{H}'(t) \right| n \right\rangle \tag{A.14}$$

where ω_{mn} is the Bohr frequency between states m and n and the matrix element is taken between the eigenfunctions of the unperturbed Hamiltonian $\mathcal{H}_0$.

Up to this point, no perturbation theory has been applied, and the result presented in Equation A.14 remains exact. It's worth observing that the unperturbed Hamiltonian is conspicuously absent from Equation A.14. Nonetheless, its energy eigenvalues are present within the frequency ω_{mn}, and its eigenfunctions are incorporated in the matrix element $\left\langle m \left| \mathcal{H}'(t) \right| n \right\rangle$. If we apply the perturbation theory, we assume that the matrix element $\langle m|\mathcal{H}(t)|n\rangle$ to be small, this allows us to to represent each time-dependent amplitude as an expansion utilizing perturbation theory.

Thus, the expression for the expansion reads

$$a_n = a_n^{(0)} + a_n^{(1)} + a_n^{(2)} + \cdots = \sum_{i=0}^{\infty} a_n^{(i)} \tag{A.15}$$

where the superscript shows the order of the terms. Here, $a_n^{(0)}$ is the zero o^{th} order term and $a_n^{(i)}$ is the i^{th} order correction to a_n. Now, utilizing Eq.(A.14) we can see that the time-dependet coefficient $a_m(t)$ varies with time only due to the time-dependent perturbation. Therefore, the zeroth $\left(0^{\text{th}}\right.$ order perturbation theory) must vanish due to no time dependence. Hence

$$\dot{a}_m^{(0)} = 0 \tag{A.16}$$

and the first order correction is then given by

$$\dot{a}_m^{(1)} = 1/i\hbar \sum_n a_n^{(0)} \langle m | \mathcal{H}'(t) | n \rangle e^{i\omega_{mn}t} \tag{A.17}$$

Now, suppose we start from an eigen state say $n = \ell$, only the first order term $a_\ell^{(0)}$ will be sufficiently large, all other higher order terms will decay gradually and therefore they can be neglected in the sum. Hence, the first order perturbation theory give us

$$\dot{a}_m^{(1)} = \frac{1}{i\hbar} a_\ell^{(0)} \langle m | \mathcal{H}' | \ell \rangle e^{i\omega_{m\ell}t} \tag{A.18}$$

where $a_\ell^{(0)}$ is approximately unity.

In many relevant scenarios, the integration over the time variable can be carried out, yielding $a_m^{(1)}$ rather than its time derivative. There are two straightforward cases where integration can be accomplished:

1. The perturbing hamiltonian $\mathcal{H}'$ remains constant but is introduced at a specific time $(t = 0)$. One can observe the amplitudes of the wave function in different states after the perturbation has been active for some time $t > 0$.

2. The perturbing Hamiltonian $\mathcal{H}'$ possesses sinusoidal time dependence with a frequency ω. This applies to all resonant phenomena. First, let's focus on case (1) above.

Upon integrating Eq.(A.18) we have

$$a_m^{(1)}(t) = \frac{1}{i\hbar} \int_0^t \langle m | \mathcal{H}' | \ell \rangle e^{i\omega_{m\ell}t'} dt' = \frac{\langle m | \mathcal{H}' | \ell \rangle}{i\hbar} \frac{\left[e^{i\omega_{m\ell}t} - 1\right]}{i\omega_{m\ell}} \tag{A.19}$$

For the case (2), suppose we consider the Hamiltonian with explicit time dependence as

$$\mathcal{H}'(t) = \mathcal{H}'(0) e^{\pm i\omega t} \tag{A.20}$$

we perform same technique as we did in case (1) i.e by integrating Eq.(A.18) with the Hamiltonian to obtain the amplitude $a_m^{(1)(t)}$ as

$$a_m^{(1)}(t) = \frac{1}{i\hbar} \langle m | \mathcal{H}'(0) | \ell \rangle \int_0^t e^{i(\omega_{m\ell} \pm \omega)t'} dt' = \frac{1}{i\hbar} \langle m | \mathcal{H}'(0) | \ell \rangle \frac{e^{i(\omega_{m\ell} \pm \omega)t} - 1}{i\left(\omega_{m\ell} \pm \omega\right)} \tag{A.21}$$

from this relation, we can also calculate the probability of finding the system in a state m after a certain time t has elapsed after the perturbation by simply taking the $|a_m^{(1)}(t)|^2$. From Eq.(A.19), one can obtain

$$\begin{aligned}\left|a_m^{(1)}(t)\right|^2 &= \left(\frac{|\langle m\,|\mathcal{H}'|\,\ell\rangle|^2}{\hbar^2}\right)\left(\frac{\left|e^{i\omega_{m\ell}t}-1\right|^2}{\omega_{m\ell}^2}\right)\\ \left|a_m^{(1)}(t)\right|^2 &= \left(\frac{|\langle m\,|\mathcal{H}'|\,\ell\rangle|^2}{\hbar^2}\right)\left(\frac{4\sin^2\left(\omega_{m\ell}t/2\right)}{\omega_{m\ell}^2}\right)\end{aligned} \tag{A.22}$$

and similarly its straight forward to obtain the probability amplitude from Eq.(A.21),

$$\begin{aligned}\left|a_m^{(1)}(t)\right|^2 &= \left(\frac{|\langle m\,|\mathcal{H}(0)'|\,\ell\rangle|^2}{\hbar^2}\right)\left(\frac{\left|e^{i(\omega_{m\ell}\pm\omega)t}-1\right|^2}{\omega_{m\ell}\pm\omega}\right)\\ \left|a_m^{(1)}(t)\right|^2 &= \left(\frac{|\langle m\,|\mathcal{H}'|\,\ell\rangle|^2}{\hbar^2}\right)\left(\frac{4\sin^2\left(\omega_{m\ell}\pm\omega t/2\right)}{(\omega_{\omega_{m\ell}}\pm\omega)^2}\right)\end{aligned} \tag{A.23}$$

A.2 2nd order Time Dependent Perturbation Theory

Building upon the principles of first-order perturbation theory, this advanced approach allows us to explore the effects of time-dependent perturbations on the energy levels, wavefunctions, and observable properties of a quantum system. The second order pertubation is important especially for indirect optical transitions. Consider the Hamiltonian

$$\mathcal{H} = \mathcal{H}_0 + \lambda\mathcal{H}' \tag{A.24}$$

where $\lambda \ll 1$. The time-dependent Schrodinger equation is given by,

$$i\hbar\frac{\partial\psi_0}{\partial t} = \mathcal{H}_0\psi_0 \tag{A.25}$$

The solution to Eq.(A.25) ψ can be expanded in terms of Bloch functions $|b,\vec{k}\rangle$ which describes the eigenststates of the unperturbed Hamiltonian. The solution is given by,

$$\psi = \sum_{b,\vec{k}} a_b(\vec{k},t)e^{-\frac{i}{\hbar}E_b(\vec{k})t}|b,\vec{k}\rangle \tag{A.26}$$

then substituting the solution into the Schrodinger equation we obtain,

$$\begin{aligned}&\sum_{b,\vec{k}} a_b(\vec{k},t)E_b(\vec{k})e^{-\frac{i}{\hbar}E_b(\vec{k})t}|b,\vec{k}\rangle + \sum_{b,\vec{k}} a_b(\vec{k},t)e^{-\frac{i}{\hbar}E_b(\vec{k})t}\lambda\mathcal{H}'|b,\vec{k}\rangle\\ &\quad= i\hbar\sum_{b,\vec{k}}\dot{a}_b(\vec{k},t)e^{-\frac{i}{\hbar}E_b(\vec{k})t}|b,\vec{k}\rangle + \sum_{b,\vec{k}} a_b(\vec{k},t)e^{-\frac{i}{\hbar}E_b(\vec{k})t}|b,\vec{k}\rangle\end{aligned} \tag{A.27}$$

then,

$$\dot{a}_m\left(\vec{k}',t\right) = \frac{1}{i\hbar}\sum_{b,\vec{k}} a_b(\vec{k},t)e^{\frac{i}{\hbar}\left(E_m(\vec{k}')t-E_b(\vec{k})t\right)}\left\langle m,\vec{k}'\,|\lambda\mathcal{H}'|\,b,\vec{k}\right\rangle \tag{A.28}$$

as done previously, we can expand the amplitude as

$$a_m\left(\vec{k}',t\right) = a_m^{(0)} + \lambda a_m^{(1)} + \lambda^2 a_m^{(2)} + \dots \tag{A.29}$$

setting $a_j(\vec{k},0) = 1$, and all others $a_n(\vec{k},0) = 0$ where $n \neq j$. The first order perturbation is then given by

$$a_m^{(1)}\left(\vec{k}',t\right) = \frac{1}{i\hbar}\int_0^t dt' \exp\left[\frac{i}{\hbar}\left[E_m(\vec{k}') - E_b(\vec{k})\right]t\left\langle m,\vec{k}'\left|\lambda\mathcal{H}'\right|b,\vec{k}\right\rangle\right. \tag{A.30}$$

while the second orser is

$$\begin{aligned}\dot{a}_m^{(2)}\left(\vec{k}',t\right) = -\frac{1}{\hbar^2}\sum_{b,\vec{k}} a_b^{(1)}(\vec{k},t)\exp\left\{\frac{i}{\hbar}\left[E_m\left(\vec{k}'\right) - E_b(\vec{k})\right]t\right\}\left\langle m,\vec{k}'\left|\lambda\mathcal{H}'\right|b,\vec{k}\right\rangle \\ \times \quad \int_0^t dt' \exp\left\{\frac{i}{\hbar}\left[E_b\left(\vec{k}'\right) - E_i(\vec{k})\right]t'\right\}\left\langle b,\vec{k}'\left|\lambda\mathcal{H}'\right|i,\vec{k}\right\rangle\end{aligned} \tag{A.31}$$

If we explicitly express the time variation of the perturbation Hamiltonian as

$$\mathcal{H}' = \sum_\alpha \mathcal{H} e^{-i\omega_\alpha t} \tag{A.32}$$

and substitute it into Eq.(A.31) and integrating it twice, we obtain the probability amplitude as

$$\left|a_f^{(2)}\left(\vec{k}_f,t\right)\right|^2 = 2\pi\hbar t \sum_{m,\vec{k},\alpha,\alpha'} \frac{\left|\left\langle f\left|\mathcal{H}'_{\alpha'}\right|m,\vec{k}\right\rangle\right|^2\left|\left\langle m,\vec{k}\left|\mathcal{H}'_{\alpha}\right|i\right\rangle\right|^2}{\left(E_m(\vec{k}) - E_i - \hbar\omega_\alpha\right)^2}\delta\left(E_f - E_i - \hbar\omega_\alpha - \hbar\omega_{\alpha'}\right) \tag{A.33}$$

This final expression of the second-order time-dependent perturbation theory s applied to deduce the probability of an indirect interband transition.

B | Fourier Transform

There are numerous definitions of Fourier transforms and different conventions are used by authrs in various literatures. Here, I give the definitions of the FT used in this thesis.

B.1 Single-variable functions

Suppose we have a function f such that $f \in \mathcal{L}^2$ and f *is square integrable*. The FT in both time and frequency domain of the one-variable function f is given by

$$f(\omega) = \int dt e^{-i\omega t} f(t), \quad f(t) = \frac{1}{2\pi} \int d\omega e^{i\omega t} f(\omega), \tag{B.1}$$

and in reciprocal space

$$f(\mathbf{r}) = \frac{1}{(2\pi)^3} \int d^3\mathbf{k} f(\mathbf{k}) e^{i\mathbf{kr}}, \quad f(\mathbf{k}) = \int d^3\mathbf{r} f(\mathbf{r}) e^{-i\mathbf{kr}}. \tag{B.2}$$

Dirac delta functions can also be expressed in terms of Fourier transform definitions in time and frequency domain as

$$\delta(t) = \frac{1}{2\pi} \int d\omega e^{i\omega t}, \quad \delta(\omega) = \frac{1}{2\pi} \int dt e^{-i\omega t} \tag{B.3}$$

in reciprocal space,

$$\delta(\mathbf{k}) = \frac{1}{(2\pi)^3} \int d^3\mathbf{r} e^{-i\mathbf{kr}}, \quad \delta(\mathbf{r}) = \frac{1}{(2\pi)^3} \int d^3\mathbf{k} e^{i\mathbf{kr}} \tag{B.4}$$

B.2 Two-variable functions

Suppose we have a two-variable function, say the density response function which we described in section 5.102 χ. This function is square integrable, and two functions f and g, such that $f, g \in \mathcal{L}^2$ and

$$f(\mathbf{r}) = \int d^3\mathbf{r}' \chi(\mathbf{r}, \mathbf{r}') g(\mathbf{r}') . \tag{B.5}$$

The Fourier transform of this expression is

$$f(\mathbf{k}) = \int d^3\mathbf{k}' \chi(\mathbf{k}, \mathbf{k}') g(\mathbf{k}') . \tag{B.6}$$

Using the definitions of FT in Eqs. (B.1), we obtain by identification

$$\begin{aligned} \chi(\mathbf{r}, \mathbf{r}') &= \frac{1}{(2\pi)^3} \int d^3\mathbf{k} \int d^3\mathbf{k}' e^{i\mathbf{kr}} \chi(\mathbf{k}, \mathbf{k}') e^{-i\mathbf{k}'\mathbf{r}'}, \\ \chi(\mathbf{k}, \mathbf{k}') &= \frac{1}{(2\pi)^3} \int d^3\mathbf{r} \int d^3\mathbf{r}' e^{-i\mathbf{kr}} \chi(\mathbf{r}, \mathbf{r}') e^{i\mathbf{k}'\mathbf{r}'}. \end{aligned} \tag{B.7}$$

Similarly, in time domain, we obtain,

$$\chi\left(t,t'\right)=\frac{1}{(2\pi)}\int d\omega\int d\omega' e^{i\omega t}\chi\left(\omega,\omega'\right)e^{-i\omega' t'} \tag{B.8}$$

B.3 Equation of Motion

B.3.1 Heisenberg and Schrödinger Equation of Motion

The mathematical representation of the dynamics of a quantum system is not unique. The dynamics of electrons is characterized by evolving the wavefunction in time, which encapsulates probability densities. This approach is referred to as the Schrödinger representation of quantum mechanics. However, since a wavefunction is not directly measurable, our primary focus shifts to observables—probability amplitudes linked to Hermitian operators. Examining the time evolution of an expectation value provides an alternative interpretation of quantum observables:

$$\begin{aligned}\langle\hat{A}(t)\rangle&=\langle\psi(t)|\hat{A}|\psi(t)\rangle=\left\langle\psi(0)\left|U^{\dagger}\hat{A}U\right|\psi(0)\right\rangle\\&=\left(\langle\psi(0)|U^{\dagger}\right)\hat{A}(U|\psi(0)\rangle)\\&=\left\langle\psi(0)\left|\left(U^{\dagger}\hat{A}U\right)\right|\psi(0)\right\rangle\end{aligned} \tag{B.9}$$

In this expression, the last two expressions shows a different transformation that describes the following dynamics with the following physical interpretations:

1. Transform the eigenvectors: $|\psi(t)\rangle\rightarrow U|\psi\rangle$. Leave operators unchanged.
2. Transform the operators: $\hat{A}(t)\rightarrow U^{\dagger}\hat{A}U$. Leave eigenvectors unchanged.

We first consider the Schrödinger picture where operators are stationery and eigenvectors are evolve by $U\left(t,t_0\right)$.

Schrödinger Picture

The Schrödinger equation in its differential form is given by

$$i\hbar\frac{\partial}{\partial t}|\psi\rangle=H|\psi\rangle \tag{B.10}$$

and alternatively, in integral form, the eigen function can be expressed as $|\psi(t)\rangle=U\left(t,t_0\right)|\psi\left(t_0\right)\rangle$. In this context, the operators are usually taken to be $\frac{\partial A}{\partial t}=0$. The question remains, how about the observables? The expectation values of such operators can be given by $\langle\hat{A}(t)\rangle=$

$\langle\psi(t)|\hat{A}|\psi(t)\rangle$. The Schrödinger equation Eq. (B.10) can be rewritten as

$$\begin{aligned} i\hbar\frac{\partial}{\partial t}\langle\hat{A}(t)\rangle &= i\hbar\left[\left\langle\psi|\hat{A}|\frac{\partial\psi}{\partial t}\right\rangle + \left\langle\frac{\partial\psi}{\partial t}|\hat{A}|\psi\right\rangle + \left\langle\psi\left|\frac{\partial\mathcal{A}}{\partial t}\right|\psi\right\rangle\right] \\ &= \langle\psi|\hat{A}H|\psi\rangle - \langle\psi|H\hat{A}|\psi\rangle \\ &= \langle\psi|[\hat{A},H]|\psi\rangle \\ &= \langle[\hat{A},H]\rangle \end{aligned} \tag{B.11}$$

Similarly, the equation can be expressed in terms of density matrix as

$$\begin{aligned} i\hbar\frac{\partial}{\partial t}\langle\hat{A}(t)\rangle &= i\hbar\frac{\partial}{\partial t}\operatorname{Tr}(\hat{A}\rho) \\ &= i\hbar\operatorname{Tr}\left(\hat{A}\frac{\partial}{\partial t}\rho\right) \\ &= \operatorname{Tr}(\hat{A}[H,\rho]) \\ &= \operatorname{Tr}([\hat{A},H]\rho) \end{aligned} \tag{B.12}$$

If the operator $\hat{A}$ is time-independent (as anticipated in the Schrödinger picture) and commutes with the Hamiltonian H, it is termed a constant of motion.

Next we consider the Heisenberg picture. Here, the unitary property of the evolution operator U is employed to transform operators, allowing them to evolve in time. In contrast, the wavefunction remains stationary. This picture is physically intuitive as it considers the time-dependence of particles, accounting for variations in position and momentum.

Heisenberg Picture

From Eq. (B.9) one can distinguish the Schrödinger picture from the Heisenberg operators as

$$\hat{A}(t) = \langle\psi(t)|\hat{A}|\psi(t)\rangle_S = \left\langle\psi\left(t_0\right)\left|U^\dagger\hat{A}U\right|\psi\left(t_0\right)\right\rangle_S = \langle\psi|\hat{A}(t)|\psi\rangle_H \tag{B.13}$$

where we defined the operators as

$$\begin{aligned} \hat{A}_H(t) &= U^\dagger\left(t,t_0\right)\hat{A}_S U\left(t,t_0\right) \\ \hat{A}_H\left(t_0\right) &= \hat{A}_S \end{aligned} \tag{B.14}$$

Additionally, given that the wavefunction should be time-independent ($\partial|\psi_H\rangle/\partial t = 0$), we can establish a connection between the Schrödinger and Heisenberg wavefunctions as follows:

$$|\psi_S(t)\rangle = U\left(t,t_0\right)|\psi_H\rangle \tag{B.15}$$

such that

$$|\psi_H\rangle = U^\dagger\left(t,t_0\right)|\psi_S(t)\rangle = |\psi_S\left(t_0\right)\rangle \tag{B.16}$$

In either picture, the eigenvalues are conserved:

$$\begin{aligned} \hat{A}\,|\varphi_i\rangle_S &= a_i\,|\varphi_i\rangle_S \\ U^\dagger \hat{A} U U^\dagger\,|\varphi_i\rangle_S &= a_i U^\dagger\,|\varphi_i\rangle_S \\ \hat{A}_H\,|\varphi_i\rangle_H &= a_i\,|\varphi_i\rangle_H \end{aligned} \tag{B.17}$$

The time evolution of the operators in the Heisenberg picture is:

$$\begin{aligned} \frac{\partial \hat{A}_H}{\partial t} &= \frac{\partial}{\partial t}\left(U^\dagger \hat{A}_S U\right) = \frac{\partial U^\dagger}{\partial t}\hat{A}_S U + U^\dagger \hat{A}_S \frac{\partial U}{\partial t} + U^\dagger \frac{\partial \hat{A}_S}{\partial t} U \\ &= \frac{i}{\hbar} U^\dagger H \hat{A}_S U - \frac{i}{\hbar} U^\dagger \hat{A}_S H U + \left(\frac{\partial \hat{A}}{\partial t}\right)_H \\ &= \frac{i}{\hbar} H_H \hat{A}_H - \frac{i}{\hbar}\hat{A}_H H_H \\ &= \frac{-i}{\hbar}[\hat{A}, H]_H \end{aligned} \tag{B.18}$$

Then, Eq. (B.10) can finally be expressed as

$$i\hbar \frac{\partial}{\partial t}\hat{A}_H = [\hat{A}, H]_H \tag{B.19}$$

The equation above is commonly referred to as the Heisenberg equation of motion. In this context, The Heisenberg Hamiltonian is denoted $H_H = U^\dagger H U$. In general, for a time-independent Hamiltonian, where the time evolution operator is given by $U = e^{-iHt/\hbar}$, the operators U and H commute, resulting in $H_H = H$. However, for a time-dependent Hamiltonian, the operators U and H may not commute.

C | Derivation of the Static FKE formula

The electron dynamics under the presence of the pump can be described by the one-body Schrodinger equation given by

$$i\frac{\partial}{\partial t}\varphi_i(\vec{r},t) = \left[\frac{1}{2m_e}\left(\vec{p}+\frac{e}{c}\vec{A}(t)\right)^2 + v(\vec{r})\right]\varphi_j(\vec{r},t) \tag{C.1}$$

where $\vec{r}$ is describes the time-independent potential that characterizes the lattice periodic potential, $\vec{A}(t)$ is the time-dependent vector potential. The solution of the above equation can be described by the time dependent Bloch functions $u_{n\vec{k}}(\vec{r},t)$ as $\varphi_i(\vec{r},t) = e^{i\vec{k}\cdot\vec{r}}u_{n\vec{k}}(\vec{r},t)$.

Eq. (C.1) can be transformed by using the Bloch states as

$$i\frac{\partial}{\partial t}u_{n\vec{k}}(\vec{r},t) = \hat{h}_{\vec{k}_p}(t)u_{nk}(\vec{r},t) \tag{C.2}$$

where $\hat{h}_{\vec{k}_p}(t)$ is the Hamiltonian which is given by,

$$\hat{h}_{\vec{k}_p}(t) = \left[\frac{1}{2m_e}(\vec{p}+\vec{k})^2 + v(\vec{r})\right] \tag{C.3}$$

The crystal momentum is shifted by the vector potential as $\vec{k}_p(t) = \vec{k} + e\vec{A}_p(t)/\hbar c$. We assume that $u_{n\vec{k}}$ can be expanded by the Houston function and the time-dependent coefficient $C^k_{nm}t$ as

$$u_{n\vec{k}}(\vec{r},t) = w_{n\vec{k}}(\vec{r},t) + \sum_m C^{\vec{k}}_{nm}(t)w_{m\vec{k}}(\vec{r},t) \tag{C.4}$$

Then equation (C.2) reads,

$$\begin{aligned} i\frac{\partial u_{nk}}{\partial t} &= i\frac{\partial}{\partial t}\left\{w_{n\vec{k}}(\vec{r},t) + \sum_m C^{\vec{k}}_{nm}(t)w_{m\vec{k}}(\vec{r},t)\right\} \\ &= i\left[\frac{\partial}{\partial t}w_{n\vec{k}}(\vec{r},t) + \frac{\partial}{\partial t}C^{\vec{k}}_{nm}w_{m\vec{k}}(\vec{r},t) + C^{\vec{k}}_{nm}\frac{\partial}{\partial t}w_{m\vec{k}}(\vec{r},t)\right] \end{aligned} \tag{C.5}$$

But

$$w_{n\vec{k}}(\vec{r},t) = u_{n\vec{k}_p(t)}(\vec{r})e^{-i\int^t dt'\epsilon_{n\vec{k}_p(t')}} \tag{C.6}$$

then Eq. (C.5) becomes

$$\begin{aligned} &= i\frac{\partial C^k_{nm}(t)}{\partial t}w_{mk}(\vec{r},t) + \left\{-ieE(t)\frac{\partial u^{(\vec{r},t)}_{nk}}{\partial t}e^{-i\int^t dt'\epsilon_{nk}(t')} + \epsilon_{nk}(t)u_{nk}(\vec{r})e^{-i\int^t dt'\epsilon_{mk}(t')}\right\} \\ &+ C^{\vec{k}}_{nm}(t)\epsilon_{mk}(t)u_{m,k}(\vec{r})e^{-i\int^t dt'\epsilon_{mk}(t')} \end{aligned} \tag{C.7}$$

To obtain the value of $C^{\vec{k}}_{nm}(t)$ can be determined by multiplying $\langle w_{n\vec{k}}(\vec{r},t)|$ from the left. Then we obtain,

$$i\left\langle w_{n\vec{k}}(\vec{r},t)\mid\frac{\partial u_{mk}(\vec{r},t)}{\partial t}\right\rangle=i\frac{\partial}{\partial t}C_{nm}^{k}(t)-i\left\langle u_{nk}(\vec{r},t)\mid\frac{\partial u_{mk}(\vec{r},t)}{\partial t}\right\rangle e\vec{E}(t)e^{iS(t')}C_{nm}^{\vec{k}}\epsilon_{mk}^{(t)}\quad\text{(C.8)}$$

where $s(t)=\int^{t}dt'\left(\epsilon_{nk}\left(t'\right)-\epsilon_{mk}\left(t'\right)\right)$. Upon Integrating Eq. (C.8) we have,

$$C_{nm}^{\vec{k}}(t)=ie\int^{t}dt'E\left(t'\right)\left\langle u_{nk}(\vec{r},t)\mid\frac{\partial u_{mk}^{(\vec{r},t)}}{\partial t}\right\rangle e^{iS(t')}\quad\text{(C.9)}$$

But,

$$\vec{E}(t)=-\frac{1}{c}\frac{\partial\vec{A}(t)}{\partial t}\quad\text{(C.10)}$$

Therefore Eq. (C.9) becomes

$$C_{nm}^{\vec{k}}(t)=-\frac{ie}{m_{e}c}\int_{-\infty}^{t}dt\prime\vec{A}_{pump}(t)\vec{p}_{mn\vec{k}}\;e^{-iS(t')}\quad\text{(C.11)}$$

where the matrix element in the static basis is given by

$$\vec{p}_{mn\vec{k}}=\int_{\Omega}d\vec{r}\;u_{m\vec{k}}^{*}(\vec{r})\vec{p}u_{m\vec{k}}(\vec{r})\quad\text{(C.12)}$$

In the presence of both pump and probe vector potential, the coefficient becomes

$$C_{nm}^{\vec{k}}(t)=-\frac{ie}{m_{e}c}\int_{-\infty}^{t}dt'\vec{A}_{pump}(t)\vec{p}_{mn\vec{k}}\;e^{-iS(t')}-\frac{ie}{m_{e}c}\int_{-\infty}^{t}dt'\vec{k}_{p}\left(t'\right)\vec{A}_{probe}\left(t'\right)\delta_{mn}\quad\text{(C.13)}$$

Next is to calculate is the current density flowing through the unit cell from the Houston states which is as follows:

$$\vec{J}(t)=\sum_{i}\frac{1}{V}\,\mathrm{Re}\left[\int_{V}d\vec{r}u_{n\vec{k}}^{*}(\vec{r},t)\vec{j}(t)u_{n\vec{k}}(\vec{r},t)\right]\quad\text{(C.14)}$$

where V is the volume of the unit cell, and the current operator is given by,

$$\vec{j}(t)=-\frac{e}{m}\frac{1}{i\hbar}[\vec{r},\hat{h}_{\vec{k}_{p}}(t)]\quad\text{(C.15)}$$

substituting Eq. C.4 and its complex conjugate into Eq. (C.14) and doing some algebra, one obtains the electric current density average over the unit cell.

$$\vec{J}(t)=-\frac{e}{m_{e}V}\int_{V}d\vec{r}\times\sum_{n\vec{k}}\mathrm{Re}\left\{u_{n\vec{k}}^{*}\left[\vec{p}+\vec{k}_{P}(t)+\frac{e}{c}\vec{A}_{p}(t)\right]u_{n\vec{k}}\right\}\quad\text{(C.16)}$$

From the induced current, one can calculate the contribution to the current by the pump and the probe respectively. That is $\vec{J}(t)=\vec{J}_{pump}+\vec{J}_{probe}$. The contribution to the current by the pump pulse is given by

$$\vec{J}_{pump}=-\frac{e}{m_{e}V}\sum_{n\vec{k}}\int_{V}d\vec{r}\,\mathrm{Re}\left\{w_{n\vec{k}}^{*}\left[\vec{p}+\vec{k}_{p(t)}\right]w_{n\vec{k}}\right\}\quad\text{(C.17)}$$

while that of the probe is

$$\vec{J}_{\text{probe}}\left(t\right)=-\frac{e^{2}}{m_{e}c}n_{e}\vec{A}_{probe}(t)+\frac{e^{2}}{m_{e}^{2}cV}\int_{-\infty}^{t}dt'\times\sum_{n\neq n',\vec{k}'}\text{Im}\left\{\vec{P}_{nn'}^{\vec{k}}(t)\left[\vec{P}_{nn'}^{\vec{k}}\left(t'\right)\cdot\vec{A}_{probe}(t')\right]\vec{E}(t)\right\} \tag{C.18}$$

in the above equation, the valence electrons have an average density that is described by n_e. $\vec{E}$(t) is the electric field of the probe pulse. The impulsive distortion by the probe pulse is set such that the probe induced current has a linear relation with the probe field, therefore we can apply linear response to obtain the optical conductivity $\sigma(\omega)$. Eq. (6.21) gives the linear relation between the induced current and the optical conductivity. In time domain, the optical conductivity can be expressed as

$$\sigma_{\alpha\beta}\left(t,t'\right)=\frac{e^{2}}{m_{e}}n_{e}\delta_{\alpha\beta}-\frac{e^{2}}{m_{e}V}\int_{t'}^{t}dt''\sum_{n\neq n',\vec{k}}\text{Im}\left[\left(p_{\alpha}\right)_{nn'\vec{k}_{p(t)}}\left(p_{\beta}\right)_{n'n\vec{k}_{p}(t'')}\times e^{-i\int_{t''}^{t}d\tau\left\{\varepsilon_{n'\vec{k}_{p}(\tau)}-\varepsilon_{n\vec{k}_{p}(\tau)}\right\}}\right] \tag{C.19}$$

here α, β are the Cartesian indices. The orbitals in the equation above maintain their usual meanings as defined in Chapter 8. Therefore, a little bit of algebraic expression, one obtain the real part of the optical conductivity induced by the impulsive distortion as

$$\text{Re}\,\tilde{\sigma}_{\alpha\alpha}(\omega)=\frac{(2\mu)^{3/2}e^{2}}{2m_{e}^{2}\omega}\left|\left(p_{\alpha}\right)_{vc}\right|^{2}\sqrt{\Theta}\quad\times\left\{-\frac{\epsilon_{g}-\omega}{\Theta}\text{Ai}^{2}\left(\frac{\epsilon_{g}-\omega}{\Theta}\right)+\text{Ai}'^{2}\left(\frac{\epsilon_{g}-\omega}{\Theta}\right)\right\} \tag{C.20}$$

with $\theta=(e^{2}E^{2}/2\mu)^{1/3}$. The above equation describes the real part of the optical conductivity in the presence of a static field.

D Derivation of The Parabolic Two Band Model

The one-body Schrödinger equation is given by

$$i\hbar\frac{\partial}{\partial t}u_{b\vec{k}}(\vec{r},t)=\left[\frac{1}{2}\left\{\vec{p}+\hbar\vec{k}+\frac{e}{c}A(t)\right\}^2+v(r)\right]u_{b\vec{k}}(\vec{r},t) \tag{D.1}$$

which can the be written as

$$ih\frac{\partial}{\partial t}u_{b\vec{k}}(\vec{r},t)=\hat{h}_{\vec{K}(t)}u_{bk}(\vec{r},t) \tag{D.2}$$

where $u_{b\vec{k}}(\vec{r},t)$ is a time-dependent Bloch state, and $v(\vec{r})$ is a one-body potential that has the same periodicity as crystal. The crystal momentum is shifted by the vector potential as $\vec{K}(t)=\vec{k}+e\vec{A}(t)/\hbar c$. Where the vector potential is given by

$$\vec{A}(t)=-c\int_{-\infty}^{t}\vec{E}(t')dt' \tag{D.3}$$

using the time dependent basis set, the Houston states, we can write the eigen states as

$$u^H_{b\vec{k}}(\vec{r},t)=e^{-\frac{i}{\hbar}\int^t dt'\epsilon_{b\vec{K}(t')}}u^S_{b\vec{K}(t)}(\vec{r}) \tag{D.4}$$

where $\epsilon_{b\vec{K}(t)}$ and $u^S_{b\vec{K}(t)}(\vec{r})$ are an eigenvalue and the eigenstate of the instantaneous Hamiltonian, $\hat{h}_{\vec{K}(t)}$, respectively. The Houston states describes the electron dynamics in a moving frame in which the lattice momentum is prescribed by the vector potential in equation (8.16) and $\epsilon_{b\vec{K}(t)}$ describes the motion of the electron on each band.
We can write the time dependent Schrödinger equation with the Houston basis as

$$\hat{h}_{\vec{K}(t)}u^S_{b\vec{K}(t)}(\vec{r})=\epsilon_{b\vec{K}(t)}u^S_{b\vec{K}(t)}(\vec{r}) \tag{D.5}$$

To describe the two-state system, we can express the eigen states as a linear combination of two Houston states. One is the valence while the other describe the conduction states

$$u_{\vec{k}}(\vec{r},t)=c_{v\vec{k}}(t)u^H_{v\vec{k}}(\vec{r},t)+c_{c\vec{k}}(t)u^H_{c\vec{k}}(\vec{r},t) \tag{D.6}$$

Substituting Eq. (D.6) into Eq. (D.2), we have

$$i\hbar\frac{\partial}{\partial t}\left[c_{v\vec{k}}(t)u^H_{v\vec{k}}(\vec{r},t)+c_{c\vec{k}}(t)u^H_{c\vec{k}}(\vec{r},t)\right]=\hat{h}_{\vec{K}(t)}\left[c_{v\vec{k}}(t)u^H_{v\vec{k}}(\vec{r},t)+c_{c\vec{k}}(t)u^H_{c\vec{k}}(\vec{r},t)\right] \tag{D.7}$$

Inserting Eq. (D.4) into Eq. (D.7) we obtain

$$i\hbar\frac{\partial}{\partial t}\left[c_{v\vec{k}}(t)e^{-\frac{i}{\hbar}\int^t dt'\epsilon_{v\vec{K}(t')}}u^S_{v\vec{K}(t)}(\vec{r})+c_{c\vec{k}}(t)e^{-\frac{i}{\hbar}\int^t dt'\epsilon_{c\vec{K}(t')}}u^S_{c\vec{K}(t)}(\vec{r})\right]= \hat{h}_{\vec{K}(t)}\left[c_{v\vec{k}}(t)e^{-\frac{i}{\hbar}\int^t dt'\epsilon_{v\vec{K}(t')}}u^S_{v\vec{K}(t)}(\vec{r})+c_{c\vec{k}}(t)e^{-\frac{i}{\hbar}\int^t dt'\epsilon_{c\vec{K}(t')}}u^S_{c\vec{K}(t)}(\vec{r})\right] \tag{D.8}$$

From the R.H.S and expanding the L.H.S we obtain

$$\begin{aligned}i\hbar\Bigg[&\dot{c}_{v\vec{k}}\ e^{-\frac{i}{\hbar}\int^t dt'\epsilon_{v\vec{K}(t')}}u^S_{v\vec{K}(t)}(\vec{r})-\frac{i}{\hbar}c_{v\vec{k}}\epsilon_{v\vec{K}(t')}\ e^{-\frac{i}{\hbar}\int^t dt'\epsilon_{v\vec{K}(t')}}u^S_{v\vec{K}(t)}(\vec{r})+c_{v\vec{k}}\ e^{-\frac{i}{\hbar}\int^t dt'\epsilon_{v\vec{K}(t')}}\frac{\partial u^S_{v\vec{K}(t)}(\vec{r})}{\partial t}\\ +\ &\dot{c}_{c\vec{k}}\ e^{-\frac{i}{\hbar}\int^t dt'\epsilon_{c\vec{K}(t')}}u^S_{c\vec{K}(t)}(\vec{r})-\frac{i}{\hbar}c_{c\vec{k}}\epsilon_{c\vec{K}(t')}\ e^{-\frac{i}{\hbar}\int^t dt'\epsilon_{c\vec{K}(t')}}u^S_{c\vec{K}(t)}(\vec{r})+c_{c\vec{k}}\ e^{-\frac{i}{\hbar}\int^t dt'\epsilon_{c\vec{K}(t')}}\frac{\partial u^S_{c\vec{K}(t)}(\vec{r})}{\partial t}\Bigg]=\\ &c_{v\vec{k}}(t)e^{-\frac{i}{\hbar}\int^t dt'\epsilon_{v\vec{K}(t')}}\hat{h}_{\vec{K}(t)}u^S_{v\vec{K}(t)}(\vec{r})+c_{c\vec{k}}(t)e^{-\frac{i}{\hbar}\int^t dt'\epsilon_{c\vec{K}(t')}}\hat{h}_{\vec{K}(t)}u^S_{c\vec{K}(t)}(\vec{r})\end{aligned} \tag{D.9}$$

From Eq. (D.5), Eq. (D.9) becomes

$$\begin{aligned}i\hbar\Bigg[&\dot{c}_{v\vec{k}}\ e^{-\frac{i}{\hbar}\int^t dt'\epsilon_{v\vec{K}(t')}}u^S_{v\vec{K}(t)}(\vec{r})-\frac{i}{\hbar}c_{v\vec{k}}\epsilon_{v\vec{K}(t')}\ e^{-\frac{i}{\hbar}\int^t dt'\epsilon_{v\vec{K}(t')}}u^S_{v\vec{K}(t)}(\vec{r})+c_{v\vec{k}}\ e^{-\frac{i}{\hbar}\int^t dt'\epsilon_{v\vec{K}(t')}}\frac{\partial u^S_{v\vec{K}(t)}(\vec{r})}{\partial t}\\ +\ &\dot{c}_{c\vec{k}}\ e^{-\frac{i}{\hbar}\int^t dt'\epsilon_{c\vec{K}(t')}}u^S_{c\vec{K}(t)}(\vec{r})-\frac{i}{\hbar}c_{c\vec{k}}\epsilon_{c\vec{K}(t')}\ e^{-\frac{i}{\hbar}\int^t dt'\epsilon_{c\vec{K}(t')}}u^S_{c\vec{K}(t)}(\vec{r})+c_{c\vec{k}}\ e^{-\frac{i}{\hbar}\int^t dt'\epsilon_{c\vec{K}(t')}}\frac{\partial u^S_{c\vec{K}(t)}(\vec{r})}{\partial t}\Bigg]=\\ &c_{v\vec{k}}(t)e^{-\frac{i}{\hbar}\int^t dt'\epsilon_{v\vec{K}(t')}}\epsilon_{v\vec{K}(t)}u^S_{v\vec{K}(t)}(\vec{r})+c_{c\vec{k}}(t)e^{-\frac{i}{\hbar}\int^t dt'\epsilon_{c\vec{K}(t')}}\epsilon_{c\vec{K}(t)}u^S_{c\vec{K}(t)}(\vec{r})\end{aligned} \tag{D.10}$$

Expanding the brackets, Eq. (D.10) becomes

$$\begin{aligned}&i\hbar\dot{c}_{v\vec{k}}\ e^{-\frac{i}{\hbar}\int^t dt'\epsilon_{v\vec{K}(t')}}u^S_{v\vec{K}(t)}(\vec{r})+c_{v\vec{k}}\epsilon_{v\vec{K}(t')}\ e^{-\frac{i}{\hbar}\int^t dt'\epsilon_{v\vec{K}(t')}}u^S_{v\vec{K}(t)}(\vec{r})+i\hbar c_{v\vec{k}}\ e^{-\frac{i}{\hbar}\int^t dt'\epsilon_{v\vec{K}(t')}}\frac{\partial u^S_{v\vec{K}(t)}(\vec{r})}{\partial t}\\ +\ &i\hbar\dot{c}_{c\vec{k}}\ e^{-\frac{i}{\hbar}\int^t dt'\epsilon_{c\vec{K}(t')}}u^S_{c\vec{K}(t)}(\vec{r})+c_{c\vec{k}}\epsilon_{c\vec{K}(t')}\ e^{-\frac{i}{\hbar}\int^t dt'\epsilon_{c\vec{K}(t')}}u^S_{c\vec{K}(t)}(\vec{r})+i\hbar c_{c\vec{k}}\ e^{-\frac{i}{\hbar}\int^t dt'\epsilon_{c\vec{K}(t')}}\frac{\partial u^S_{c\vec{K}(t)}(\vec{r})}{\partial t}=\\ &c_{v\vec{k}}(t)e^{-\frac{i}{\hbar}\int^t dt'\epsilon_{v\vec{K}(t')}}\epsilon_{v\vec{K}(t)}u^S_{v\vec{K}(t)}(\vec{r})+c_{c\vec{k}}(t)e^{-\frac{i}{\hbar}\int^t dt'\epsilon_{c\vec{K}(t')}}\epsilon_{c\vec{K}(t)}u^S_{c\vec{K}(t)}(\vec{r})\end{aligned} \tag{D.11}$$

Cancelling equal terms on both sides we have

$$\begin{aligned}&i\hbar\dot{c}_{v\vec{k}}\ e^{-\frac{i}{\hbar}\int^t dt'\epsilon_{v\vec{K}(t')}}u^S_{v\vec{K}(t)}(\vec{r})+i\hbar c_{v\vec{k}}\ e^{-\frac{i}{\hbar}\int^t dt'\epsilon_{v\vec{K}(t')}}\frac{\partial u^S_{v\vec{K}(t)}(\vec{r})}{\partial t}+\\ &i\hbar\dot{c}_{c\vec{k}}\ e^{-\frac{i}{\hbar}\int^t dt'\epsilon_{c\vec{K}(t')}}u^S_{c\vec{K}(t)}(\vec{r})+i\hbar c_{c\vec{k}}\ e^{-\frac{i}{\hbar}\int^t dt'\epsilon_{c\vec{K}(t')}}\frac{\partial u^S_{c\vec{K}(t)}(\vec{r})}{\partial t}=0\end{aligned} \tag{D.12}$$

Applying chain rule to the derivative in the above equation, we obtain

$$\frac{\partial u^S_{b\vec{K}(t)}(\vec{r})}{\partial t}=\frac{\partial u^S_{b\vec{K}(t)}(\vec{r})}{\partial K}\frac{\partial\vec{A}(t)}{\partial t} \tag{D.13}$$

but $\partial\vec{A}(t)/\partial t = -c\vec{E}(t)$, therefore Eq. (D.13) becomes

$$\frac{\partial u^S_{b\vec{K}(t)}(\vec{r})}{\partial t} = -\frac{e}{\hbar}\cdot\vec{E}(t)\frac{\partial u^S_{b\vec{K}(t)}(\vec{r})}{\partial K} \tag{D.14}$$

Substituting Eq. (D.14) into Eq. (D.12), we obtain

$$\begin{aligned} i\hbar\dot{c}_{v\vec{k}}\, e^{-\frac{i}{\hbar}\int^t dt'\epsilon_{v\vec{K}(t')}} u^S_{v\vec{K}(t)}(\vec{r}) + i\hbar\dot{c}_{c\vec{k}}\, e^{-\frac{i}{\hbar}\int^t dt'\epsilon_{c\vec{K}(t')}} u^S_{c\vec{K}(t)}(\vec{r}) = \\ i\hbar\frac{e}{\hbar}\cdot\vec{E}(t)c_{v\vec{k}}\, e^{-\frac{i}{\hbar}\int^t dt'\epsilon_{v\vec{K}(t')}}\frac{\partial u^S_{v\vec{K}(t)}(\vec{r})}{\partial K} + i\hbar\frac{e}{\hbar}\cdot\vec{E}(t)c_{c\vec{k}}\, e^{-\frac{i}{\hbar}\int^t dt'\epsilon_{c\vec{K}(t')}}\frac{\partial u^S_{c\vec{K}(t)}(\vec{r})}{\partial K} \end{aligned} \tag{D.15}$$

multiplying Eq. (D.15) by $\langle u^S_{v\vec{K}(t)}(\vec{r})|$ we obtain

$$\begin{aligned} i\hbar\dot{c}_{v\vec{k}}\, e^{-\frac{i}{\hbar}\int^t dt'\epsilon_{v\vec{K}(t')}}\langle u^S_{v\vec{K}(t)}(\vec{r})|\,|u^S_{v\vec{K}(t)}(\vec{r})\rangle + i\hbar\dot{c}_{c\vec{k}}\, e^{-\frac{i}{\hbar}\int^t dt'\epsilon_{c\vec{K}(t')}}\langle u^S_{v\vec{K}(t)}(\vec{r})|\,|u^S_{c\vec{K}(t)}(\vec{r})\rangle = \\ ie\cdot\vec{E}(t)c_{v\vec{k}}\, e^{-\frac{i}{\hbar}\int^t dt'\epsilon_{v\vec{K}(t')}}\langle u^S_{v\vec{K}(t)}(\vec{r})|\,|\frac{\partial u^S_{v\vec{K}(t)}(\vec{r})}{\partial K}\rangle + ie\cdot\vec{E}(t)c_{c\vec{k}}\, e^{-\frac{i}{\hbar}\int^t dt'\epsilon_{c\vec{K}(t')}}\langle u^S_{v\vec{K}(t)}(\vec{r})|\,|\frac{\partial u^S_{c\vec{K}(t)}(\vec{r})}{\partial K}\rangle \end{aligned} \tag{D.16}$$

Since the eigen states are orthonormal, then

$$\langle u^S_{v\vec{K}(t)}(\vec{r})|\,|u^S_{c\vec{K}(t)}(\vec{r})\rangle = \delta_{vc\vec{K}(t)} \tag{D.17}$$

where,

$$\delta_{vc\vec{K}(t)} = \begin{cases} 1, & \text{if } v = c, \\ 0, & \text{if } v \neq c. \end{cases} \tag{D.18}$$

Equation (D.16) becomes

$$\begin{aligned} i\hbar\dot{c}_{v\vec{k}}\, e^{-\frac{i}{\hbar}\int^t dt'\epsilon_{v\vec{K}(t')}} = ie\cdot\vec{E}(t)c_{v\vec{k}}\, e^{-\frac{i}{\hbar}\int^t dt'\epsilon_{v\vec{K}(t')}}\langle u^S_{v\vec{K}(t)}(\vec{r})|\,|\frac{\partial u^S_{v\vec{K}(t)}(\vec{r})}{\partial K}\rangle + \\ ie\cdot\vec{E}(t)c_{c\vec{k}}\, e^{-\frac{i}{\hbar}\int^t dt'\epsilon_{c\vec{K}(t')}}\langle u^S_{v\vec{K}(t)}(\vec{r})|\,|\frac{\partial u^S_{c\vec{K}(t)}(\vec{r})}{\partial K}\rangle \end{aligned} \tag{D.19}$$

Dividing both sides by the exponent and $i\hbar$ we get

$$\dot{c}_{v\vec{k}} = \frac{e}{\hbar}\cdot\vec{E}(t)c_{v\vec{k}}\langle u^S_{v\vec{K}(t)}(\vec{r})|\,|\frac{\partial u^S_{v\vec{K}(t)}(\vec{r})}{\partial K}\rangle + \frac{e}{\hbar}\cdot\vec{E}(t)c_{c\vec{k}}\, e^{-\frac{1}{\hbar}\int^t dt'\left\{\epsilon_{c,\vec{K}(t')}-\epsilon_{v,\vec{K}(t')}\right\}}\langle u^S_{v\vec{K}(t)}(\vec{r})|\,|\frac{\partial u^S_{c\vec{K}(t)}(\vec{r})}{\partial K}\rangle \tag{D.20}$$

From Eq. (D.5) the eigen value equation is defined as,

$$\hat{h}_{\vec{K}(t)}u^S_{v\vec{K}(t)}(\vec{r}) = \epsilon_{v\vec{K}(t)}u^S_{v\vec{K}(t)}(\vec{r}) \tag{D.21}$$

Taking derivative of Eq. (D.21) with respect to k, we have

$$\frac{\partial(\hat{h}_{\vec{K}(t)}\,|u^S_{v\vec{K}(t)}(\vec{r})\rangle)}{\partial K} = \frac{\partial(\epsilon_{v\vec{K}(t)}\,|u^S_{v\vec{K}(t)}(\vec{r})\rangle)}{\partial K} \tag{D.22}$$

we have,

$$\frac{\partial \hat{h}_{\vec{K}(t)}}{\partial K}\left|u^{S}_{v\vec{K}(t)}(\vec{r})\right\rangle + \hat{h}_{\vec{K}(t)}\frac{\partial\left|u^{S}_{v\vec{K}(t)}(\vec{r})\right\rangle}{\partial K} = \frac{\partial \epsilon_{v\vec{K}(t)}}{\partial K}\left|u^{S}_{v\vec{K}(t)}(\vec{r})\right\rangle + \frac{\partial\left|u^{S}_{v\vec{K}(t)}(\vec{r})\right\rangle}{\partial K}\epsilon_{v\vec{K}(t)} \tag{D.23}$$

multiplying through Eq. (D.22) by $\langle u^{S}_{c\vec{K}(t)}(\vec{r})|$ we obtain,

$$\begin{aligned}\langle u^{S}_{c\vec{K}(t)}(\vec{r})|\frac{\partial \hat{h}_{\vec{K}(t)}}{\partial K}\left|u^{S}_{v\vec{K}(t)}(\vec{r})\right\rangle \;+\; \hat{h}_{\vec{K}(t)}\langle u^{S}_{c\vec{K}(t)}(\vec{r})|\frac{\partial}{\partial K}\left|u^{S}_{v\vec{K}(t)}(\vec{r})\right\rangle = \\ \langle u^{S}_{c\vec{K}(t)}(\vec{r})|\frac{\partial \epsilon_{v\vec{K}(t)}}{\partial K}\left|u^{S}_{v\vec{K}(t)}(\vec{r})\right\rangle + \epsilon_{v\vec{K}(t)}\langle u^{S}_{c\vec{K}(t)}(\vec{r})|\frac{\partial}{\partial K}\left|u^{S}_{v\vec{K}(t)}(\vec{r})\right\rangle\end{aligned} \tag{D.24}$$

But,

$$\frac{\partial \hat{h}_{\vec{K}(t)}}{\partial K} = \frac{\hbar}{m}\vec{P} \tag{D.25}$$

Substituting Eq. (D.25) in to Eq. (D.24), we have

$$\begin{aligned}\frac{\hbar}{m}\langle u^{S}_{c\vec{K}(t)}(\vec{r})|\vec{P}\left|u^{S}_{v\vec{K}(t)}(\vec{r})\right\rangle \;+\; \hat{h}_{\vec{K}(t)}\langle u^{S}_{c\vec{K}(t)}(\vec{r})|\frac{\partial}{\partial K}\left|u^{S}_{v\vec{K}(t)}(\vec{r})\right\rangle = \\ \langle u^{S}_{c\vec{K}(t)}(\vec{r}|)\frac{\partial \epsilon_{v\vec{K}(t)}}{\partial K}\left|u^{S}_{v\vec{K}(t)}(\vec{r})\right\rangle + \epsilon_{v\vec{K}(t)}\langle u^{S}_{c\vec{K}(t)}(\vec{r})|\frac{\partial}{\partial K}\left|u^{S}_{v\vec{K}(t)}(\vec{r})\right\rangle\end{aligned} \tag{D.26}$$

Then,

$$\begin{aligned}\frac{\hbar}{m}\langle u^{S}_{c\vec{K}(t)}(\vec{r})|\vec{P}\left|u^{S}_{v\vec{K}(t)}(\vec{r})\right\rangle \;+\; \epsilon_{c\vec{K}(t)}\langle u^{S}_{c\vec{K}(t)}(\vec{r})|\frac{\partial}{\partial K}\left|u^{S}_{v\vec{K}(t)}(\vec{r})\right\rangle = \\ \langle u^{S}_{c\vec{K}(t)}(\vec{r})|\frac{\partial \epsilon_{v\vec{K}(t)}}{\partial K}\left|u^{S}_{v\vec{K}(t)}(\vec{r})\right\rangle + \epsilon_{v\vec{K}(t)}\langle u^{S}_{c\vec{K}(t)}(\vec{r})|\frac{\partial}{\partial K}\left|u^{S}_{v\vec{K}(t)}(\vec{r})\right\rangle\end{aligned} \tag{D.27}$$

Third term in the above equation is zero, we then have

$$\frac{\hbar}{m}\langle u^{S}_{c\vec{K}(t)}(\vec{r})|\vec{P}\left|u^{S}_{v\vec{K}(t)}(\vec{r})\right\rangle = (\epsilon_{v\vec{K}(t)} - \epsilon_{c\vec{K}(t)})\langle u^{S}_{v\vec{K}(t)}(\vec{r})|\,|\frac{\partial u^{S}_{c\vec{K}(t)}(\vec{r})}{\partial K}\rangle \tag{D.28}$$

we then have,

$$\langle u^{S}_{v\vec{K}(t)}(\vec{r})|\,|\frac{\partial u^{S}_{c\vec{K}(t)}(\vec{r})}{\partial K}\rangle = \frac{\hbar}{m}\cdot\frac{\langle u^{S}_{c\vec{K}(t)}(\vec{r})|\vec{P}\left|u^{S}_{v\vec{K}(t)}(\vec{r})\right\rangle}{(\epsilon_{v\vec{K}(t)} - \epsilon_{c\vec{K}(t)})} \tag{D.29}$$

By substituting Eq. (D.28) into Eq. (D.20) and multiplying through by $i\hbar$, we obtain,

$$i\hbar\dot{c}_{v\vec{k}} = i\frac{e}{\hbar}\,\vec{E}(t)c_{v\vec{k}}\langle u^{S}_{v\vec{K}(t)}(\vec{r})|\,|\frac{\partial u^{S}_{v\vec{K}(t)}(\vec{r})}{\partial K}\rangle + i\frac{e}{\hbar}\vec{E}(t)c_{c\vec{k}}\;e^{-\frac{1}{\hbar}\int^{t}dt'\left\{\epsilon_{c,\vec{K}(t')}-\epsilon_{v,\vec{K}(t')}\right\}}\frac{\hbar}{m}\cdot\frac{\langle u^{S}_{c\vec{K}(t)}(\vec{r})|\vec{P}\left|u^{S}_{v\vec{K}(t)}(\vec{r})\right\rangle}{(\epsilon_{v\vec{K}(t)} - \epsilon_{c\vec{K}(t)})} \tag{D.30}$$

Since the first term in Eq. (D.30) is associated with the berry connection $A_n(k) = i\langle u_{nk}|\nabla_k|u_{nk}\rangle$, therefore we set the term to zero. we have

$$i\hbar\dot{c}_{v\vec{k}} = -i\frac{e}{m}\cdot\vec{E}(t)c_{c\vec{k}}\;e^{-\frac{1}{\hbar}\int^{t}dt'\left\{\epsilon_{c,\vec{K}(t')}-\epsilon_{v,\vec{K}(t')}\right\}}\frac{\langle u^{S}_{c\vec{K}(t)}(\vec{r})|\vec{P}\left|u^{S}_{v\vec{K}(t)}(\vec{r})\right\rangle}{(\epsilon_{v\vec{K}(t)} - \epsilon_{c\vec{K}(t)})} \tag{D.31}$$

where,

$$\vec{P}_{vc,\vec{K}(t)} = \langle u^S_{c\vec{K}(t)}(\vec{r})| \, \vec{P} \, |u^S_{v\vec{K}(t)}(\vec{r})\rangle \tag{D.32}$$

is the matrix element of the static basis and Eq. (D.31) reduces to

$$i\hbar\dot{c}_{v\vec{k}} = -ic_{c\vec{k}}\frac{\vec{P}_{vc,\vec{K}(t)}}{(\epsilon_{v\vec{K}(t)} - \epsilon_{c\vec{K}(t)})}\frac{e}{m}\cdot\vec{E}(t)\; e^{-\frac{1}{\hbar}\int^t dt'\left\{\epsilon_{c,\vec{K}(t')} - \epsilon_{v,\vec{K}(t')}\right\}} \tag{D.33}$$

Similarly, multiplying Eq. (D.15) by $\langle u^S_{c\vec{K}(t)}(\vec{r})|$ and performing the same algebra, one will obtain the equation of motion for

$$i\hbar\dot{c}_{c\vec{k}} = ic_{v\vec{k}}\frac{\vec{P}_{cv,\vec{K}(t)}}{(\epsilon_{v\vec{K}(t)} - \epsilon_{c\vec{K}(t)})}\frac{e}{m}\cdot\vec{E}(t)\; e^{-\frac{1}{\hbar}\int^t dt'\left\{\epsilon_{c,\vec{K}(t')} - \epsilon_{v,\vec{K}(t')}\right\}} \tag{D.34}$$

To determine the correct choice of these eigenstates, we rewrite the Eq. (D.18) and (D.15) in matrix form

$$i\hbar\frac{d}{dt}\begin{pmatrix} c_{v\vec{k}}(t) \\ c_{c\vec{k}}(t)\end{pmatrix} = \begin{pmatrix} 0 & h_{vc,\vec{k}}(t) \\ h^*_{vc,\vec{k}}(t) & 0\end{pmatrix}\begin{pmatrix} c_{v\vec{k}}(t) \\ c_{c\vec{k}}(t)\end{pmatrix} \tag{D.35}$$

where the off diagonal matrix element is given by

$$\boxed{h_{vc,\vec{k}}(t) = -i\frac{\vec{p}_{vc,\vec{K}(t)}}{\epsilon_{v,\vec{K}(t)} - \epsilon_{c,\vec{K}(t)}}\cdot\frac{e}{m}\vec{E}(t)e^{-\frac{1}{\hbar}\int^t dt'\left\{\epsilon_{c,\vec{K}(t')} - \epsilon_{v,\vec{K}(t')}\right\}}} \tag{D.36}$$

and the matrix element is thus

$$\vec{p}_{vc,\vec{K}(t)} = \int_\Omega d\vec{r}u^{S,*}_{v\vec{K}(t)}(\vec{r})\vec{p}u^S_{c\vec{K}(t)}(\vec{r}), \tag{D.37}$$

where Ω is a volume of the unit-cell. The parabolic bands can be described by the following shapes

$$\begin{aligned}\epsilon_{v,\vec{k}} &= -\frac{\vec{k}^2}{2m_v}, \\ \epsilon_{c,\vec{k}} &= \epsilon_g + \frac{\vec{k}^2}{2m_c},\end{aligned} \tag{D.38}$$

where ϵ_g is the band gap, and m_v/m_c are effective masses for valence and conduction bands respectively

$$\vec{p}_{vc,\vec{K}(t)} = \vec{p}_{vc} \tag{D.39}$$

D.1 Time Dependent Current

Current is a spatial integral quantity, the contributions from both states is identical, therefore the total current induced by the laser field is therefore computed by

$$J(t) = \frac{-i\hbar}{m}\left[u^*_k(\vec{r},t)\nabla u_k(\vec{r},t)\right] \tag{D.40}$$

$u_k(\vec{r},t)$ is defined in Eq. (D.6), hence we can express it as

$$u_k(\vec{r},t) = c_{v\vec{k}}(t)e^{-\frac{i}{\hbar}\int^t dt' \epsilon_{v\vec{K}(t')}} u^S_{v\vec{K}(t)}(\vec{r}) + c_{c\vec{k}}(t)e^{-\frac{i}{\hbar}\int^t dt' \epsilon_{c\vec{K}(t')}} u^S_{c\vec{K}(t)}(\vec{r}) \tag{D.41}$$

it complex conjugate is given by

$$u^*_k(\vec{r},t) = c^*_{v\vec{k}}(t)e^{\frac{i}{\hbar}\int^t dt' \epsilon_{v\vec{K}(t')}} u^{*S}_{c\vec{K}(t)}(\vec{r}) + c^*_{c\vec{k}}(t)e^{\frac{i}{\hbar}\int^t dt' \epsilon_{c\vec{K}(t')}} u^{*S}_{c\vec{K}(t)}(\vec{r}) \tag{D.42}$$

Expanding Eq. (D.40), we have

$$J(t) = \frac{1}{m}\left[u^*_k(\vec{r},t)(-i\hbar\nabla)u_k(\vec{r},t)\right] \tag{D.43}$$

But $\vec{p} = -i\hbar\nabla$, therefore the electric current averaged over the unit cell is given by

$$J(t) = \frac{1}{m}\cdot\frac{1}{V}\int_V d\vec{k}\int d\vec{r}\,[u^*_k(\vec{r},t)\vec{p}u_k(\vec{r},t)] \tag{D.44}$$

and substituting Eq. (D.41), Eq. (D.42), into Eq. (D.44) we obtain

$$\begin{aligned} J(t) = \frac{1}{m}\cdot\frac{1}{V}\int_V d\vec{k}\int d\vec{r}\Bigg[&\left(c^*_{v\vec{k}}(t)e^{\frac{i}{\hbar}\int^t dt' \epsilon_{v\vec{K}(t')}} u^{*S}_{v\vec{K}(t)}(\vec{r}) + c^*_{c\vec{k}}(t)e^{\frac{i}{\hbar}\int^t dt' \epsilon_{c\vec{K}(t')}} u^{*S}_{c\vec{K}(t)}(\vec{r})\right) \\ &\left(c_{v\vec{k}}(t)e^{-\frac{i}{\hbar}\int^t dt' \epsilon_{v\vec{K}(t')}} u^S_{v\vec{K}(t)}(\vec{r})\vec{p} + c_{c\vec{k}}(t)e^{-\frac{i}{\hbar}\int^t dt' \epsilon_{c\vec{K}(t')}} u^S_{c\vec{K}(t)}(\vec{r})\vec{p}\right)\Bigg] \end{aligned} \tag{D.45}$$

Now, simplifying the equation we obtain

$$\begin{aligned} J(t) = \frac{1}{m}\cdot\frac{1}{V}\int_V d\vec{k}\int d\vec{r}\Bigg[&\left(c^*_{v\vec{k}}(t)e^{\frac{i}{\hbar}\int^t dt' \epsilon_{v\vec{K}(t')}} u^{*S}_{v\vec{K}(t)}(\vec{r}) + c^*_{c\vec{k}}(t)e^{\frac{i}{\hbar}\int^t dt' \epsilon_{c\vec{K}(t')}} u^{*S}_{c\vec{K}(t)}(\vec{r})\right) \\ &\left(c_{v\vec{k}}(t)e^{-\frac{i}{\hbar}\int^t dt' \epsilon_{v\vec{K}(t')}} u^S_{v\vec{K}(t)}(\vec{r})\vec{p} + c_{c\vec{k}}(t)e^{-\frac{i}{\hbar}\int^t dt' \epsilon_{c\vec{K}(t')}} u^S_{c\vec{K}(t)}(\vec{r})\vec{p}\right)\Bigg] \end{aligned} \tag{D.46}$$

Expanding the above equation, we obtain

$$\begin{aligned} J(t) = \frac{1}{m}\cdot\frac{1}{V}\int_V d\vec{k}\int d\vec{r}\Bigg[&\left(c^*_{v\vec{k}}(t)e^{\frac{i}{\hbar}\int^t dt' \epsilon_{v\vec{K}(t')}} u^{*S}_{v\vec{K}(t)}(\vec{r})\vec{p}c_{v\vec{k}}(t)e^{-\frac{i}{\hbar}\int^t dt' \epsilon_{v\vec{K}(t')}} u^S_{v\vec{K}(t)}(\vec{r}) + \right. \\ &\left. c^*_{v\vec{k}}(t)e^{\frac{i}{\hbar}\int^t dt' \epsilon_{v\vec{K}(t')}} u^{*S}_{v\vec{K}(t)}(\vec{r})\vec{p}c_{c\vec{k}}(t)e^{-\frac{i}{\hbar}\int^t dt' \epsilon_{c\vec{K}(t')}} u^S_{c\vec{K}(t)}(\vec{r})\right) + \\ &\left(c^*_{c\vec{k}}(t)e^{\frac{i}{\hbar}\int^t dt' \epsilon_{c\vec{K}(t')}} u^{*S}_{c\vec{K}(t)}(\vec{r})\vec{p}c_{v\vec{k}}(t)e^{-\frac{i}{\hbar}\int^t dt' \epsilon_{v\vec{K}(t')}} u^S_{v\vec{K}(t)}(\vec{r}) + \right. \\ &\left. c^*_{c\vec{k}}(t)e^{\frac{i}{\hbar}\int^t dt' \epsilon_{c\vec{K}(t')}} u^{*S}_{c\vec{K}(t)}(\vec{r})\vec{p}c_{c\vec{k}}(t)e^{-\frac{i}{\hbar}\int^t dt' \epsilon_{c\vec{K}(t')}} u^S_{c\vec{K}(t)}(\vec{r})\right)\Bigg] \end{aligned} \tag{D.47}$$

upon simplifying,

$$J(t) = \frac{1}{m}\cdot\frac{1}{V}\int_V d\vec{k}\int d\vec{r}\Bigg[c^*_{v\vec{k}}(t)c_{v\vec{k}}(t)u^{*S}_{v\vec{K}(t)}(\vec{r})\vec{p}u^S_{v\vec{K}(t)}(\vec{r}) + c^*_{v\vec{k}}(t)c_{c\vec{k}}(t)e^{\frac{i}{\hbar}\int^t dt'\left\{\epsilon_{c,\vec{K}(t')}-\epsilon_{v,\vec{K}(t')}\right\}}u^{*S}_{v\vec{K}(t)}(\vec{r})$$
$$\vec{p}u^S_{c\vec{K}(t)}(\vec{r}) + c^*_{c\vec{k}}(t)c_{v\vec{k}}(t)e^{\frac{i}{\hbar}\int^t dt'\left\{\epsilon_{c,\vec{K}(t')}-\epsilon_{v,\vec{K}(t')}\right\}}u^{*S}_{c\vec{K}(t)}(\vec{r})\vec{p}u^S_{v\vec{K}(t)}(\vec{r}) + c^*_{c\vec{k}}(t)c_{c\vec{k}}(t)u^{*S}_{c\vec{K}(t)}(\vec{r})\vec{p}u^S_{c\vec{K}(t)}(\vec{r})\Bigg] \tag{D.48}$$

Now

$$J(t) = \frac{1}{m}\cdot\frac{1}{V}\int_V d\vec{k}\int d\vec{r}\Bigg[|c_{v\vec{k}}(t)|^2u^{*S}_{v\vec{K}(t)}(\vec{r})\vec{p}u^S_{v\vec{K}(t)}(\vec{r}) \;+\; c^*_{v\vec{k}}(t)c_{c\vec{k}}(t)e^{\frac{i}{\hbar}\int^t dt'\left\{\epsilon_{c,\vec{K}(t')}-\epsilon_{v,\vec{K}(t')}\right\}}u^{*S}_{v\vec{K}(t)}(\vec{r})\vec{p}u^S_{c\vec{K}(t)}(\vec{r})$$
$$+c^*_{c\vec{k}}(t)c_{c\vec{k}}(t)e^{\frac{i}{\hbar}\int^t dt'\left\{\epsilon_{v,\vec{K}(t')}-\epsilon_{v,\vec{K}(t')}\right\}}u^{*S}_{c\vec{K}(t)}(\vec{r})\vec{p}u^S_{v\vec{K}(t)}(\vec{r}) \;+|c_{c\vec{k}}(t)|^2u^{*S}_{c\vec{K}(t)}(\vec{r})\vec{p}u^S_{c\vec{K}(t)}(\vec{r})\Bigg] \tag{D.49}$$

But $|c_{b\vec{K}(t)}|^2 = 1$ and $A_n(k) = i\langle u_{nk}|\nabla_k|u_{nk}\rangle = 0$, then the above equation simplifies to,

$$J(t) = \frac{1}{m}\cdot\frac{1}{V}\int_V d\vec{k}\int d\vec{r}\left[c^*_{v\vec{k}}(t)c_{c\vec{k}}(t)e^{\frac{i}{\hbar}\int^t dt'\left\{\epsilon_{c,\vec{K}(t')}-\epsilon_{v,\vec{K}(t')}\right\}}u^{*S}_{v\vec{K}(t)}(\vec{r})\vec{p}u^S_{c\vec{K}(t)}(\vec{r}) \;+\right.$$
$$\left.c^*_{c\vec{k}}(t)c_{v\vec{k}}(t)e^{\frac{i}{\hbar}\int^t dt'\left\{\epsilon_{v,\vec{K}(t')}-\epsilon_{v,\vec{K}(t')}\right\}}u^{*S}_{c\vec{K}(t)}(\vec{r})\vec{p}u^S_{v\vec{K}(t)}(\vec{r})\right] \tag{D.50}$$

$$J(t) = \frac{1}{m}\cdot\frac{1}{V}\int_V d\vec{k}\int d\vec{r}\left(2c^*_{v\vec{k}}(t)c_{c\vec{k}}(t)e^{\frac{i}{\hbar}\int^t dt'\left\{\epsilon_{c,\vec{K}(t')}-\epsilon_{v,\vec{K}(t')}\right\}}\langle u^S_{v\vec{K}(t)}(\vec{r})|\,\vec{p}\,|u^S_{c\vec{K}(t)}(\vec{r})\rangle\right) + \text{ c.c.} \tag{D.51}$$

Taking the complex conjugate of the second part of the above equation, one obtain

$$J(t) = \frac{1}{m}\cdot\frac{1}{V}\int_V d\vec{k}\int d\vec{r}\left(2c^*_{v\vec{k}}(t)c_{c\vec{k}}(t)e^{\frac{i}{\hbar}\int^t dt'\left\{\epsilon_{c,\vec{K}(t')}-\epsilon_{v,\vec{K}(t')}\right\}}\langle u^S_{v\vec{K}(t)}(\vec{r})|\,\vec{p}\,|u^S_{c\vec{K}(t)}(\vec{r})\rangle\right) + c.c \tag{D.52}$$

Since the applied field is weak enough, we consider first order perturbation theory to the Electric field, we also assume that $c_{v\vec{k}} = 1$, meaning that the valence coefficient is always 1 and $c_{c\vec{k}} = \delta$ that is some constant for the conduction states. From Eq. (D.36), applying the first order perturbation, then we can express the constant coefficient in the equation as,

$$c_{c\vec{k}} = \frac{e}{m}\cdot E_0\,\frac{1}{\hbar}\,\frac{|p_{vc}|}{(\epsilon_{c,\vec{k}}-\epsilon_{v,\vec{k}})} \tag{D.53}$$

Substituting Eq. (D.53) into Eq. (D.52), we obtain

$$J(t) = \frac{e}{m}\cdot\frac{2E_0}{(2\pi)^3}\int d\vec{k}\left(\frac{1}{\hbar}\,\frac{|p_{vc}|}{(\epsilon_{c,\vec{k}}-\epsilon_{v,\vec{k}})}e^{\frac{i}{\hbar}\int^t dt'\left\{\epsilon_{c,\vec{K}(t')}-\epsilon_{v,\vec{K}(t')}\right\}}\langle u^S_{v\vec{K}(t)}(\vec{r})|\,\vec{p}\,|u^S_{c\vec{K}(t)}(\vec{r})\rangle\right) + c.c \tag{D.54}$$

But $\langle u^S_{v\vec{K}(t)}(\vec{r})|\,\vec{p}\,|u^S_{c\vec{K}(t)}(\vec{r})\rangle = p_{vc}$. if the impulsive distortion is applied at time T which is the

central time of the pulse along the z-direction, then the current density can be described as

$$\boxed{J_z(t>T) = \frac{e}{m}\cdot\frac{2E_0}{(2\pi)^3}\int d\vec{k}\ \frac{1}{\hbar}\frac{|p_{vc}|^2}{(\epsilon_{c,\vec{k}}-\epsilon_{v,\vec{k}})}e^{\frac{i}{\hbar}\int_T^t dt'\left\{\epsilon_{c,\vec{k}}-\epsilon_{v,\vec{k}}\right\}} + \text{ c.c.}} \tag{D.55}$$

To calculate the optical conductivity, we first calculate the Fourier transform of the current density and damp it. The Fourier transform of the current is given by

$$J_z(w) = \int_T^\infty J_z(t>T)e^{i\omega t-\gamma t}dt \tag{D.56}$$

$$J_z(w) = \frac{e}{m}\cdot\frac{2E_0}{(2\pi)^3}\int d\vec{k}\ \frac{1}{\hbar}\frac{|p_{vc}|^2}{(\epsilon_{c,\vec{k}}-\epsilon_{v,\vec{k}})}\int_T^\infty\ dt\ e^{\frac{i}{\hbar}\int_T^t dt'\left\{\epsilon_{c,\vec{k}}-\epsilon_{v,\vec{k}}\right\}}e^{i\omega t-\gamma t} + \text{ c.c.} \tag{D.57}$$

D.2 Static Dielectric Function

The electron dynamics is considered under a weak perturbing electric field $\vec{E}(t)$.

$$\vec{E}(t) = E_0\vec{e}_z\delta(t-T), \tag{D.58}$$

We evaluate the Fourier transform of the perturbing field as,

$$E_z(w) = \int_{t=-\infty}^\infty\ dt\ \vec{E}(t)e^{i\omega t-\gamma t} \tag{D.59}$$

substituting Eq. (D.58) into Eq. (D.59) we obtain,

$$E_z(w) = \int_{t=-\infty}^\infty\ dt\ E_0\vec{e}_z\delta(t-T)e^{i\omega t-\gamma t} \tag{D.60}$$

and then

$$E_z(w) = E_0e^{i\omega T-\gamma T} \tag{D.61}$$

The dielectric function is given by

$$\Im[\epsilon(\omega)] = \frac{4\pi}{\omega}\Re[\sigma(\omega)] = \frac{4\pi}{\omega}\Re\left[\frac{J_z(\omega)}{E_z(\omega)}\right] \tag{D.62}$$

Then,

$$\Im[\epsilon(\omega)] = \frac{4\pi}{\omega}\Re\left[\frac{\frac{e^2}{m^2}\cdot\frac{2E_0}{(2\pi)^3}\int d\vec{k}\ \frac{1}{\hbar}\frac{|p_{vc}|^2}{(\epsilon_{c,\vec{k}}-\epsilon_{v,\vec{k}})}\int_T^\infty\ dt\ e^{\frac{i}{\hbar}\int_T^t dt'\left\{\epsilon_{c,\vec{k}}-\epsilon_{v,\vec{k}}\right\}}e^{i\omega t-\gamma t}}{E_0e^{i\omega T-\gamma T}}\right] \tag{D.63}$$

then,

$$\Im[\epsilon(\omega)] = \frac{4\pi}{\omega}\frac{e^2}{m^2}\cdot\frac{1}{(2\pi)^3}\Re\left[\int d\vec{k}\,\frac{1}{\hbar}\frac{|p_{vc}|^2}{(\epsilon_{c,\vec{k}}-\epsilon_{v,\vec{k}})}\int_T^\infty dt\; e^{\frac{i}{\hbar}\int_T^t dt'\left\{\epsilon_{c,\vec{k}}-\epsilon_{v,\vec{k}}\right\}}e^{i\omega(t-T)}e^{-\gamma(t-T)}\right] \tag{D.64}$$

Simplifying, we obtain,

$$\Im[\epsilon(\omega)] = \frac{4\pi}{\omega}\frac{e^2}{m^2}\cdot\frac{1}{(2\pi)^3}\Re\left[\int d\vec{k}\,\frac{1}{\hbar}\frac{|p_{vc}|^2}{(\epsilon_{c,\vec{k}}-\epsilon_{v,\vec{k}})}\int_T^\infty dt\; e^{\frac{i(t-T)}{\hbar}\int_T^t dt'\left\{\epsilon_{c,\vec{k}}-\epsilon_{v,\vec{k}}+\hbar\omega\right\}}e^{-\gamma(t-T)}\right] \tag{D.65}$$

The integral over time may be evaluated exactly to yield,

$$\Im[\epsilon(\omega)] = \frac{4\pi}{\omega}\frac{e^2}{m^2}\cdot\frac{1}{(2\pi)^3}\Re\left[\int d\vec{k}\,\frac{1}{\hbar}\frac{|p_{vc}|^2}{(\epsilon_{c,\vec{k}}-\epsilon_{v,\vec{k}})}\frac{i\hbar}{(\epsilon_{c,\vec{k}}-\epsilon_{v,\vec{k}}+i\hbar\gamma-\hbar\omega)}\right] \tag{D.66}$$

Taking the limit as $\gamma\to 0^+$, and applying the mathematical identity,

$$\lim_{\gamma\to 0^+}\frac{1}{x^2+\gamma^2} = \lim_{\gamma\to 0^+}\frac{1}{i}\left[\frac{1}{x-i\gamma}-\frac{1}{x+i\gamma}\right] = 2\pi\delta(x)$$

one obtains

$$\boxed{\Im[\epsilon(\omega)](\omega) = \left(\frac{2\pi e}{m\omega}\right)^2\frac{1}{(2\pi)^3}\int d\vec{k}\left|p_{vc,\vec{k}}\right|^2\delta\left(\epsilon_{c,\vec{k}}-\epsilon_{v,\vec{k}}-\hbar\omega\right)} \tag{D.67}$$

Equation (D.67) is an equation for the imaginary part of the dielectric function, which describes the absorption of electromagnetic waves by a material. The dielectric function is a complex quantity that depends on the frequency of the electromagnetic wave, and is related to the material's ability to polarize in response to an applied electric field. The dielectric function is given by,

$$\Im\epsilon(\omega) = 4\pi\frac{\sigma(\omega)}{\omega} \tag{D.68}$$

form which we extract the conductivity to be

$$\sigma(\omega) = \left(\frac{\pi e^2}{m^2\omega}\right)\frac{1}{(2\pi)^3}\int d\vec{k}\left|p_{vc,\vec{k}}\right|^2\delta\left(\epsilon_{c,\vec{k}}-\epsilon_{v,\vec{k}}-\hbar\omega\right) \tag{D.69}$$

E | Numerical Methods to solve TDKS

The TDKS with Bloch orbitals to describe the electron dynamics can be expressed as

$$i\hbar\frac{\partial}{\partial t}u_{bk}(\mathbf{r},t) = \hat{h}_{KS,k}(t)u_{bk}(\mathbf{r},t) \tag{E.1}$$

where $\hat{h}_{KS,k}(t)$ is the one body Hamiltonian which is give by

$$\hat{h}_{KS,k}(t) = \frac{1}{2}(\mathbf{p}+\mathbf{k}+\mathbf{A}(t))^2 + e^{-i(\mathbf{A}(t)+\mathbf{k})\dot{r}}v_{ion}e^{i(\mathbf{A}(t)+\mathbf{k})\dot{r}} + v_H(\mathbf{r},t) + v_{xc}(\mathbf{r},t) \tag{E.2}$$

where the terms in the Hamiltonian have their usual meanings.

Electron dynamics can be calculated by solving Eq. (E.2) in real time and real space. One technique used in solving the equation is the *Real-space grid representation* [190, 196, 198, 259, 260] while the other is the *orbital basis expansion.*

E.0.1 Real-space representation

In real-space representation, Eq. (E.1) can be expressed in a matrix form where the equation can be discretized using uniform grids in the three dimensional (3D) Cartesian coordinates. The Bloch functions can be expressed as

$$u_{bk}(\mathbf{r},t) = u_{bk}(\mathbf{r}_j,t) \tag{E.3}$$

where j is an integer that represents a number of spatial grids in the unit cell. In this context, the unit cell is considered to be discretized into N_g grid of points. This representation is simple and intuitive, but it is considered to be computationally expensive and demands large resources for performing lengthy simulations.

In this representation, the 3D grid representation is converted into a dense matrix, suppose one considers an operator $\hat{O}$ that acts on the Bloch orbitals $u_{bk}(\mathbf{r},t)$, one can express the matrix in the following way,

$$[\hat{O}u_{bk}(\mathbf{r},t)]_{\mathbf{r}=\mathbf{r_i}} = \sum_{j=1}^{N_g} O_{ij}u_{bk}(\mathbf{r}_j,t) \tag{E.4}$$

Here O_{ij} is the matrix representation of the general operator $\hat{O}$ in the grid representation. The Kohn-sham Hamiltonian E.2 in the grid representation can be generally expressed as

$$\begin{aligned}\left[\hat{h}_{KS,\boldsymbol{k}}(t)\right]_{ij} = &-\frac{C_{ij}}{2} + \frac{\boldsymbol{g}_{ij}}{i}\cdot(\boldsymbol{k}+\boldsymbol{A}(t)) + e^{-i\boldsymbol{A}(t)\cdot\boldsymbol{r}_i}v_{ion,ij}e^{i\boldsymbol{A}(t)\cdot\boldsymbol{r}_j} \\ &+ \delta_{ij}\left[\frac{1}{2}(\boldsymbol{k}+\boldsymbol{A}(t))^2 + v_H(\boldsymbol{r}_j,t) + v_{xc}(\boldsymbol{r}_j,t)\right],\end{aligned} \tag{E.5}$$

where C_{ij} and $\boldsymbol{g}_{ij}$ are coefficients gotten from the finite difference operation on the Laplacian ∇^2 and the gradient ∇, respectively. Since the Hamiltonian E.5 is considered to be a sparse Hermitian matrix [261] in real-space grid representation, the coefficients C_{ij} and $\boldsymbol{g}_{ij}$ can also be chosen to be sparse matrices. Finally, one can efficiently time-propagate the Hamiltonian to obtain dynamics for different quantum systems.

As stated earlier, the real-space grid representation is straightforward and has the capability to properly describe complex electron dynamics due to the larger number of grid points, this allows the capture of highly complex wavefunctions. Similarly, to make calculations more efficient and effective, by the increase in number of grid points and reducing the spacing, one can immediately improve the quality of the representation. Due to this improvements, there is a high cost of computations due to the large number of degree of freedom. This computational cost is more pronounced especially when the dynamics of core-levels plays a critical role in the simulations, thus making it more difficult due to the huge computational cost since very fine grid spacing and computer nodes are required as highlighted in 7. Due to all these complexities, an alternative method or technique can be used to describe the electron dynamics numerically, i.e by the use of the Basis expansion.

E.0.2 Basis expansion

In practice, the electron dynamics can be calculated by solving the TDKS using the real-space representation and it provides a broader description of the electron dynamics in solids, but it requires huge and higher computational cost. Furthermore, to reduce the computational cost of the simulation, the orbital basis expansion is required. In this way, one adopt a set of eigenstates of the static Kohn-sham Hamiltonian as basis set to express the time-dependent orbital wavefunctions. The eigenstates are defined as

$$\hat{h}_{\mathbf{k}} u^S_{bk}(\mathbf{r}) = \epsilon_{bk} u^S_{bk}(\mathbf{r}) \tag{E.6}$$

where $u^S_{bk}(\mathbf{r})$ are the Bloch eigenstates, b is the band index, with the corresponding eigenvalues been ϵ_{bk}. The Bloch orbitals can be expanded in terms of the eigenstates at a fixed $\mathbf{k}$-point

$$u_{bk}(\mathbf{r}, t) = \sum_{b'=1}^{N_{max}} C^S_{bb'k}(t) u^S_{b'\boldsymbol{k}}(\mathbf{r}) \tag{E.7}$$

where $C^S_{bb'k}(t)$ is a time-dependent coefficient for the expansion for the fixed $\mathbf{k}$-point, N_{max} are eigenstates which includes the lowest eigenstates. The eigenstates $u^S_{b'k}(\mathbf{r})$ are considered to be a complete basis set, therefore the expansion of Eq. (E.7) gives the exact description of the time-dependent Kohn-Sham orbitals in the long basis limit i.e ($N_{max} \to \infty$). Even though it has been shown that this technique for a single $\mathbf{k}$-point tends to show very slow convergence for the description of the electron dynamics as demonstrated in this article by [199] but has proven to improve numerical accuracy and reduce computational cost. The origin of the slow convergence of Eq (E.7) was due to lack of proper description of laser-induced intraband transition. As described in section 4, two kinds of transition can be induced by the laser field in solids: the interband transition and the intraband transition. It can be seen that Eq (E.7) can only induce interband transitions since the Bloch orbitals only contains eigenstates in different bands. For

the intraband transition to occur, a momentum shoft to the Bloch orbitals is required with the application of the applied laser field i.e $u^S_{b\boldsymbol{k}}(\mathbf{r}) \rightarrow u^S_{b,\boldsymbol{k}+\boldsymbol{A}(t)}(\mathbf{r})$. In order to achive a faster convergence, one needs to include the intraband transitions, and this will require the summation of many eigenstates linearly as well as adding the eigenstates whose momentum are shifted by the application of the laser field. Thus, this results in

$$u_{b\boldsymbol{k}}(\boldsymbol{r},t) = \sum_{b'=1}^{N_{\max}} C^S_{bb'\boldsymbol{k}}(t) u^S_{b'\boldsymbol{k}}(\boldsymbol{r}) + \sum_{n=1}^{N_{\text{shift}}} \sum_{b'=1}^{N_{n,\max}} C_{b\boldsymbol{k}b'\Delta\boldsymbol{k}_n}(t) u^S_{b'\boldsymbol{k}+\Delta\boldsymbol{k}_n}(\boldsymbol{r}), \tag{E.8}$$

Here N_{shift} describes the number of shifted $\boldsymbol{k}$-points, $\Delta\boldsymbol{k}_n$ described the size of the shift and $C_{b\boldsymbol{k}b'\Delta\boldsymbol{k}_n}(t)$ are the time-dependent coefficient of expansion. To efficiently describe the intraband transitions induced by the vector potential $\boldsymbol{A}(t)$, one has to carefully choose the values of $\boldsymbol{k}$ and $\Delta\boldsymbol{k}_n$.

Equation (E.8) effectively describes both interband and intraband transitions. Specifically, the first term properly describes the interband transitions, while the second term aptly characterizes intraband transitions induced by the applied field. This approach not only resolves convergence issues but also reduces computational cost, thereby enhancing efficiency of the calculations.

F List of Codes used during this work and Examples of Input files

1. Octopus (*real-time real space code)* [193]
2. Quantum Espresso [262]
3. Two band model https://github.com/shunsuke-sato/two_band_model

Example of Octopus input file to perform time-dependent calculations after a ground state (gs) DFT calculation. The gs calculation is performed to obtain a set of Kohn-Sham orbitals. Then subsequently, the time propagation via the TDKS is performed to obtain the required observables.

```
###################################
# calculation mode parameters:
CalculationMode =td
Dimensions = 3
ExperimentalFeatures = yes
FromScratch = yes
Debug = trace
RestartWriteInterval= 1000

%RestartOptions
 restart_gs |"/ptmp/mlawan/linear_pump_monolayer_hBN_TAS/hBN_gs/restart"
%

# run paralelization parameters:
ParStates = auto
pardomains = no
parKPoints = auto


#ConvForce = 1e-5
# initial guess parameters:
LCAOStart =  lcao_states

PseudopotentialSet = hgh_lda
SpinComponents = unpolarized

# grid parameters:
PeriodicDimensions = 2
Spacing = 0.36 # dx | dy
```

```
BoxShape = parallelepiped
a_par = 4.7621094
Lz = 50 # the nonperiodic z vaccuum.

%LatticeParameters
 a_par | a_par | Lz
%

%LatticeVectors
  1    | 0         | 0.
  -1/2 | sqrt(3)/2 | 0.
  0.   | 0.        | 1.
%

% ReducedCoordinates
 "N" | 0 | 0 | 0 | no
 "B" | 1/3 | 2/3 | 0 | no
%

KPointsUseSymmetries = no

nk = 36
nkz = 1
%KPointsGrid
 nk |  nk | nkz
 0.0 | 0.0 | 0.0
%

# TD run parameters:
# propagator and propagation details:
TDPropagator = aetrs
TDExponentialMethod = lanczos
TDEXPOrder = 16
MoveIons = no
TDFreezeHXC = no

# Absorber details (for the nonperiodic z-axis):
wid = 40 # width of absorber counted from Lz down.
Lmin = Lz - wid
AbsorbingBoundaries = cap
ABCapHeight = -1.0
%ABShape
 Lmin | Lz | "abs(z)"
%

#probe parameters
#------------------------------------------------------------
```

```
aa = 8e-4   #amplitude
tau = 0  #delay
#-------------------------------------------------------

%TDExternalFields
 vector_potential | 1 | 0 | 0 | 0 | "step"
%

%TDFunctions
 "step"  | tdf_from_expr | 'aa*step(t - tau)'
%

tf = 10*fs
dt = 0.08

PropagationSpectrumDampFactor = 0.25*eV
PropagationSpectrumDampMode = exponential
TDPropagationTime = tf + tau  #total propagation time.
TDTimeStep = dt
GaugeFieldDelay = tau

#------------td_outputs---------
%TDOutput
 laser
 total_current
 energy
%
```

Another example of octopus input file used to perform all electron calculation. This input can be used to obtain the Boron K-edge.

```
CalculationMode =td
FromScratch = yes
ExperimentalFeatures = yes
Debug = trace
RestartWriteInterval= 1000
StatesPack = yes

PeriodicDimensions = 3
%RestartOptions
  restart_gs |"/ptmp/mlawan/hBN_gs/restart"
%

%Spacing
 4.736012336/(3*7) | 4.736012336/(3*7) | 14.564118194/(2*37)
%

BoxShape = parallelepiped

a = 4.736012336  #2.5062A
c = 14.564118194 #7.707A

%LatticeParameters
 a | a | c
%

PseudopotentialSet=hgh_lda
LCAOStart = lcao_full

%LatticeVectors
1/2  | sqrt(3)/2 | 0.
-1/2 | sqrt(3)/2 | 0.
0.   | 0.        | 1
%

%ReducedCoordinates
'B_spec' |   0.  |    0.  |  0.
'B' |   1/3 |   1/3  |  1/2
'N' |   1/3 |   1/3  |  0.
'N' |   0.  |   0.   |  1/2
%

%Species
'B_spec' | species_full_delta |  valence | 5
%
```

```
%KPointsGrid
 9  | 9  | 3
%
%SymmetryBreakDir
   1 | 0  | 0
%

ConvRelDens = 1.e-8
KPointsUseSymmetries =yes

#-----------------------------------------------------------
#probe parameters
#-----------------------------------------------------------
aa = 8e-4 #amplitude
tau =0
fs = 41.341374575751
#-----------------------------------------------------------

%tdexternalfields
   vector_potential | 1 | 0 | 0 | 0 | "step"
%

%tdfunctions
  "step"  | tdf_from_expr | 'aa*step(t-tau)'
%

tf = 10*fs
dt = 0.01

propagationspectrumdampfactor = 0.25*ev
propagationspectrumdampmode = exponential
tdpropagator = aetrs
tdtimestep = dt
tdpropagationtime = tf + tau
gaugefielddelay = tau
propagationspectrummaxenergy= 250*ev

#-----------------------------------------------------------
# td output
#-----------------------------------------------------------
%tdoutput
  energy
  laser
  total_current
%
```

Example of Quantum Espresso input file to perform ground state calculation

```
&CONTROL
  calculation = 'scf'
  etot_conv_thr =   3.0000000000d-05
  forc_conv_thr =   1.0000000000d-04
  outdir = './out/'
  prefix = 'mos2_mono'
  pseudo_dir = '../../pseudo/'
  tprnfor = .true.
  tstress = .true.
  verbosity = 'high'
/
&SYSTEM
  degauss =   1.4699723600d-02
  ecutrho =   9.6000000000d+02
  ecutwfc =   1.2000000000d+02
  ibrav   = 0
  nat     = 3
  nosym   = .false.
  ntyp    = 2
  occupations = 'smearing'
  smearing    = 'gaussian'
/
&ELECTRONS
  conv_thr  =   6.0000000000d-8
  electron_maxstep = 80
  mixing_beta =   4.0000000000d-01
/
&IONS
    ion_dynamics     = 'bfgs'
/
ATOMIC_SPECIES
Mo     95.96   Mo.pz-hgh.UPF
S      32.065  S.pz-hgh.UPF
CELL_PARAMETERS (angstrom)
   3.139599687   0.000000000   0.000000000
  -1.569799843   2.718973086  -0.000000000
  -0.000000000  -0.000000000  12.082283244
ATOMIC_POSITIONS (crystal)
Mo            0.3333332538        0.6666665076        0.2500000000
S             0.6666666867        0.3333334329        0.3792739054
S             0.6666666867        0.3333334329        0.1207260648
K_POINTS automatic
12 12 1 0 0 0
```

Bibliography

1. Ultrafast spectroscopy. University of Melbourne Chemistry Group. URL https://uml.chemistry.unimelb.edu.au/research-2/technique-descriptions/ultrafast-spectroscopy/. Retrieved [31st May, 2023].

2. Wikimedia Commons. Xasfig.jpg, n.d. URL https://commons.wikimedia.org/wiki/File:XASFig.jpg.

3. F. Giustino. *Materials Modelling Using Density Functional Theory: Properties and Predictions*. Oxford University Press, 2014. ISBN 9780199662449. URL https://books.google.de/books?id=FzOTAwAAQBAJ.

4. Peter Y Yu and Manuel Cardona. *Fundamentals of semiconductors. Physics and materials properties. 4. ed.* Jul 2010.

5. N.W. Ashcroft and N.D. Mermin. *Solid State Physics*. HRW international editions. Holt, Rinehart and Winston, 1976. ISBN 9780030839931. URL https://books.google.de/books?id=oXIfAQAAMAAJ.

6. Daniel Fritsch and Susan Schorr. Climbing jacob's ladder: A density functional theory case study for ag2znsnse4 and cu2znsnse4. *Journal of Physics: Energy*, 3(1):015002, nov 2020. URL https://dx.doi.org/10.1088/2515-7655/abc07b.

7. M. C. Payne, M. P. Teter, D. C. Allan, T. A. Arias, and J. D. Joannopoulos. Iterative minimization techniques for ab initio total-energy calculations: molecular dynamics and conjugate gradients. *Rev. Mod. Phys.*, 64:1045–1097, Oct 1992. URL https://link.aps.org/doi/10.1103/RevModPhys.64.1045.

8. Raul Arenal, Mathieu Kociak, and Nestor Zaluzec. High-angular-resolution electron energy loss spectroscopy of hexagonal boron nitride. *Applied Physics Letters*, 90:204105–204105, 05 2007.

9. Yong-Nian Xu and WY Ching. Calculation of ground-state and optical properties of boron nitrides in the hexagonal, cubic, and wurtzite structures. *Physical review B*, 44(15):7787, 1991.

10. M. Wegener. *Extreme Nonlinear Optics: An Introduction*. Advanced Texts in Physics. Springer Berlin Heidelberg, 2006. ISBN 9783540266884. URL https://books.google.de/books?id=pZI0erZXgdcC.

11. Ke Xu, Alexander Gabourie, Arsalan Hashemi, Zheyong Fan, Ning Wei, Amir Barati Farimani, Hannu-Pekka Komsa, Arkady Krasheninnikov, Eric Pop, and Tapio Ala-Nissila. Thermal transport in mos 2 from molecular dynamics using different empirical potentials. *Physical Review B*, 99, 02 2019.

12. Naseem Ud Din, Volodymyr Turkowski, and Talat S Rahman. Ultrafast charge dynamics and photoluminescence in bilayer mos2. *2D Materials*, 8(2):025018, jan 2021. URL https://dx.doi.org/10.1088/2053-1583/abd6b5.

13. Hans Tornatzky, Roland Gillen, Hiroshi Uchiyama, and Janina Maultzsch. Phonon dispersion in mos_2. *Phys. Rev. B*, 99:144309, Apr 2019. URL https://link.aps.org/doi/10.1103/PhysRevB.99.144309.

14. A. Molina-Sánchez and L. Wirtz. Phonons in single-layer and few-layer mos_2 and ws_2. *Phys. Rev. B*, 84:155413, Oct 2011. URL https://link.aps.org/doi/10.1103/PhysRevB.84.155413.

15. Mingxiao Ye, Dustin Winslow, Dongyan Zhang, Ravindra Pandey, and Yoke Khin Yap. Recent advancement on the optical properties of two-dimensional molybdenum disulfide (mos2) thin films. *Photonics*, 2(1):288–307, 2015. URL https://www.mdpi.com/2304-6732/2/1/288.

16. J.A. Wilson and A.D. Yoffe. The transition metal dichalcogenides discussion and interpretation of the observed optical, electrical and structural properties. *Advances in Physics*, 18(73):193–335, 1969. URL https://doi.org/10.1080/00018736900101307.

17. A. Kuc, N. Zibouche, and T. Heine. Influence of quantum confinement on the electronic structure of the transition metal sulfide ts_2. *Phys. Rev. B*, 83:245213, Jun 2011. URL https://link.aps.org/doi/10.1103/PhysRevB.83.245213.

18. Ning Lu, Hongyan Guo, Lu Wang, Xiaojun Wu, and Zeng Cheng. Van der waals trilayers and superlattices: Modification of electronic structures of mos2 by intercalation. *Nanoscale*, 6, 03 2014.

19. T. J. Wieting and J. L. Verble. Infrared and raman studies of long-wavelength optical phonons in hexagonal mos_2. *Phys. Rev. B*, 3:4286–4292, Jun 1971. URL https://link.aps.org/doi/10.1103/PhysRevB.3.4286.

20. Taran Driver, Siqi Li, Elio Champenois, Joseph Duris, Daniel Ratner, Thomas Lane, Philipp Rosenberger, Andre Al-Haddad, Vitali Averbukh, Jonathan Barnard, N. Berrah, Christoph Bostedt, Philip Bucksbaum, Ryan Coffee, Louis Dimauro, Li Fang, Douglas Garratt, Averell Gatton, Zhaoheng Guo, and James Cryan. Attosecond transient absorption spooktroscopy: a ghost imaging approach to ultrafast absorption spectroscopy. *Physical Chemistry Chemical Physics*, 22, 11 2019.

21. Mengxi Wu, Shaohao Chen, Seth Camp, Kenneth J. Schafer, and Mette B. Gaarde. Theory of strong-field attosecond transient absorption. *Journal of Physics. B, Atomic, Molecular and Optical Physics*, 49(6), 2 2016.

22. Daria Kolbasova and Robin Santra. Analytical theory of attosecond transient absorption spectroscopy of perturbatively dressed systems. *Applied Sciences*, 9(7), 2019. URL https://www.mdpi.com/2076-3417/9/7/1350.

23. D. Shafir, Y. Mairesse, D. M. Villeneuve, P. B. Corkum, and N. Dudovich. Atomic wavefunctions probed through strong-field light–matter interaction. *Nature Physics*, 5(6):412–

416, Jun 2009. URL https://doi.org/10.1038/nphys1251.

24. Valer Tosa, Katalin Kovacs, Carlo Altucci, and Raffaele Velotta. Generating single attosecond pulse using multi-cycle lasers in a polarization gate. *Opt. Express*, 17(20):17700–17710, Sep 2009. URL https://opg.optica.org/oe/abstract.cfm?URI=oe-17-20-17700.

25. Jeffrey L. Krause, Kenneth J. Schafer, and Kenneth C. Kulander. High-order harmonic generation from atoms and ions in the high intensity regime. *Phys. Rev. Lett.*, 68:3535–3538, Jun 1992. URL https://link.aps.org/doi/10.1103/PhysRevLett.68.3535.

26. M. Lewenstein, Ph. Balcou, M. Yu. Ivanov, Anne L'Huillier, and P. B. Corkum. Theory of high-harmonic generation by low-frequency laser fields. *Phys. Rev. A*, 49:2117–2132, Mar 1994. URL https://link.aps.org/doi/10.1103/PhysRevA.49.2117.

27. P. B. Corkum. Plasma perspective on strong field multiphoton ionization. *Phys. Rev. Lett.*, 71:1994–1997, Sep 1993. URL https://link.aps.org/doi/10.1103/PhysRevLett.71.1994.

28. Yujiao Jiang Yitan Gao Kun Zhao Jiangfeng Zhu Zhiyi Wei, Siyuan Xu. Principle and progress of attosecond pulse generation. *Chinese Science Bulletin*, 66(8):889–901, 2021. URL http://www.sciengine.com/publisher/ScienceChinaPress/journal/ChineseScienceBulletin/66/8/10.1360/TB-2020-1525,doi=.

29. Yang Hwan Kim, Hyeon Kim, Seong Cheol Park, Yongjin Kwon, Kyunghoon Yeom, Wosik Cho, Taeyong Kwon, Hyeok Yun, Jae Hee Sung, Seong Ku Lee, Tran Trung Luu, Chang Hee Nam, and Kyung Taec Kim. High-harmonic generation from a flat liquid-sheet plasma mirror. *Nat Commun*, 14(1):2328, April 2023.

30. Wei Cao, Peixiang Lu, Pengfei Lan, Xinlin Wang, and Guang Yang. Efficient isolated attosecond pulse generation from a multi-cycle two-color laser field. *Opt. Express*, 15(2):530–535, Jan 2007. URL https://opg.optica.org/oe/abstract.cfm?URI=oe-15-2-530.

31. M. Hentschel, R. Kienberger, C. Spielmann, G. A. Reider, N. Milosevic, T. Brabec, P. Corkum, U. Heinzmann, M. Drescher, and F. Krausz. Attosecond metrology. *Nature*, 414(6863):509–513, November 2001. URL https://doi.org/10.1038/35107000.

32. Thomas Pfeifer, Christian Spielmann, and Gustav Gerber. Temporal phase control of interband tunneling in a strong-field semiconductor. *Nature*, 442(7098):72–75, 2006. URL https://doi.org/10.1038/nature04862.

33. Adrian L. Cavalieri, Nicole Müller, Thorsten Uphues, Vladislav S. Yakovlev, Andrius Baltuska, Balint Horvath, Burkhard E. Schmidt, Reinhold Blümel, Ronald Holzwarth, Stefan Hendel, and et al. Attosecond spectroscopy in condensed matter. *Nature*, 449(7165):1029–1032, 2007. URL https://doi.org/10.1038/nature06229.

34. Thomas Gaumnitz, Elisabeth M. Bothschafter, Agustin Schiffrin, Michael Hofstetter, Stefan Neppl, Frederick L. H. Brown, Annkatrin Sommer, Jonathan Gagnon, David M. Villeneuve, Paul B. Corkum, and Ferenc Krausz. Sub-cycle control of terahertz high-harmonic generation by dynamical bloch oscillations. *Nature Photonics*, 5(10):699–704, 2011. URL https://doi.org/10.1038/nphoton.2011.

35. Robin Santra, Vladislav S. Yakovlev, Thomas Pfeifer, and Zhi-Heng Loh. Theory of attosecond transient absorption spectroscopy of strong-field-generated ions. *Phys. Rev. A*, 83:033405, Mar 2011. URL https://link.aps.org/doi/10.1103/PhysRevA.83.033405.

36. Niko Säkkinen, Yang Peng, Heiko Appel, and Robert van Leeuwen. Many-body green's function theory for electron-phonon interactions: Ground state properties of the holstein dimer. *J. Chem. Phys.*, 143(23):234101, 2015.

37. Ahmed H. Zewail. Femtochemistry: recent progress in studies of dynamics and control of reactions and their transition states. *The Journal of Physical Chemistry*, 100(31):12701–12724, Jan 1996. URL https://doi.org/10.1021/jp960658s.

38. Mark J. Rosker, Marcos Dantus, and Ahmed H. Zewail. Femtosecond clocking of the chemical bond. *Science*, 241(4870):1200–1202, 1988. URL http://www.jstor.org/stable/1702719.

39. M. Dantus, R. M. Bowman, and A. H. Zewail. Femtosecond laser observations of molecular vibration and rotation. *Nature*, 343(6260):737–739, Feb 1990. URL https://doi.org/10.1038/343737a0.

40. Mark J. Rosker, Marcos Dantus, and Ahmed H. Zewail. Femtosecond real-time probing of reactions. I. The technique. *The Journal of Chemical Physics*, 89(10):6113–6127, 11 1988. URL https://doi.org/10.1063/1.455427.

41. Marcos Dantus, Mark J. Rosker, and Ahmed H. Zewail. Femtosecond real-time probing of reactions. II. The dissociation reaction of ICN. *The Journal of Chemical Physics*, 89(10):6128–6140, 11 1988. URL https://doi.org/10.1063/1.455428.

42. C C Gradinaru, A A Pascal, F van Mourik, B Robert, P Horton, R van Grondelle, and H van Amerongen. Ultrafast evolution of the excited states in the chlorophyll a/b complex cp29 from green plants studied by energy-selective pump-probe spectroscopy. *Biochemistry*, 37(4):1143–1149, 1998.

43. A Freiberg, JA Jackson, S Lin, and NW Woodbury. Subpicosecond pump-supercontinuum probe spectroscopy of lh2 photosynthetic antenna proteins at low temperature. *The Journal of Physical Chemistry A*, 102(23):4372–4380, 1998.

44. V Nagarajan, ET Johnson, JC Williams, and WW Parson. Femtosecond pump-probe spectroscopy of the b850 antenna complex of rhodobacter sphaeroides at room temperature. *Journal of Physical Chemistry B*, 103(12):2297–2309, 1999.

45. Yuyuan Zhang, Xi-Bo Li, Aaron M. Fleming, Jordan Dood, Ashley A. Beckstead, Anita M. Orendt, Cynthia J. Burrows, and Bern Kohler. Uv-induced proton-coupled electron transfer in cyclic dna miniduplexes. *Journal of the American Chemical Society*, 138(23):7395–7401, Jun 2016. URL https://doi.org/10.1021/jacs.6b03216.

46. F Rosca et al. Wavelength selective modulation in femtosecond pump-probe spectroscopy and its application to heme proteins. *Journal of Chemical Physics*, 114(24):10884–10898, 2001.

47. François Gay-Balmaz and Cesare Tronci. Evolution of hybrid quantum–classical wavefunctions. *Physica D: Nonlinear Phenomena*, 440, 11 2022.

48. J Eid et al. Ultrafast pump-probe reflectance spectroscopy: Why sodium makes cu(in,ga)se2 solar cells better. *Solar Energy Materials and Solar Cells*, 140:33–37, 2015.

49. Khin K. Chin, Arunkumar Natarajan, Matthew N. Gard, Luis M. Campos, Heather Shepherd, Erik Johansson, and Miguel A. Garcia-Garibay. Pump–probe spectroscopy and circular dichroism of nanocrystalline benzophenone—towards absolute kinetic measurements in solid state photochemical reactions. *Chem. Commun.*, pages 4266–4268, 2007. URL http://dx.doi.org/10.1039/B709166D.

50. G Grancini et al. Hot exciton dissociation in polymer solar cells. *Nature Materials*, 11:1–5, 2012.

51. S-C Chen et al. In-situ probing plasmonic energy transfer in cu(in, ga)se-2 solar cells by ultrabroadband femtosecond pump-probe spectroscopy. *Scientific Reports*, 5:1–7, 2015.

52. G. Knopp, M. Schmitt, A. Materny, and W. Kiefer. Femtosecond time-resolved pumpprobe spectroscopy of nai in rare-gas environment. *The Journal of Physical Chemistry A*, 101 (27):4852–4859, Jul 1997. URL https://doi.org/10.1021/jp970629x.

53. null Ulstrop. *Charge Transfer Processes in Condensed Media*. 1979.

54. Y. Yan, R. M. Whitnell, K. R. Wilson, and A. H. Zewail. *Chem. Phys. Lett.*, 193:402, 1992.

55. TB Settersten and MA Linne. Picosecond pump-probe absorption spectroscopy in gases: models and experimental validation. *Applied Optics*, 41:2869–2878, 2002.

56. CP Koch and R Kosloff. Pump-probe spectroscopy of two-body correlations in ultracold gases. *Physical Review Letters*, 103:1–4, 2009.

57. Giulio Cerullo, Cristian Manzoni, Larry Lüer, and Dario Polli. Time-resolved methods in biophysics. 4. broadband pump–probe spectroscopy system with sub-20 fs temporal resolution for the study of energy transfer processes in photosynthesis. *Photochem. Photobiol. Sci.*, 6:135–144, 2007. URL http://dx.doi.org/10.1039/B606949E.

58. W. Luis Mochán and Rubén G. Barrera. Electromagnetic response of systems with spatial fluctuations. i. general formalism. *Phys. Rev. B*, 32(8):4984, 1985.

59. Christian Sanner, Lindsay Sonderhouse, Ross B. Hutson, Lingfeng Yan, William R. Milner, and Jun Ye. Pauli blocking of atom-light scattering. *Science*, 374(6570):979–983, 2021. URL https://www.science.org/doi/abs/10.1126/science.abh3483.

60. S Mukamel. Femtosecond optical spectroscopy: A direct look at elementary chemical events. *Annual Review of Physical Chemistry*, 41(1):647–681, 1990. URL https://doi.org/10.1146/annurev.pc.41.100190.003243.

61. J. Kanamori and A. Kotani. *Core-level spectroscopy in condensed systems: Proceedings of the Tenth Taniguchi International Symposium, Kashikojima, Japan, October 19-23, 1987*. Springer-Verlag, 1988.

62. Wilhelm Konrad Röntgen. On a new kind of rays. *Nature*, 53:274–276, 1895.

63. Des McMorrow. X-ray scattering techniques. In *Advanced Characterization Techniques for Thin Film Solar Cells*, pages 245–265. Wiley, 2003.

64. Friedrich Reinert and Stefan Hüfner. Photoemission spectroscopy—from early days to recent applications. *New Journal of Physics*, 7(1):97, 2005.

65. Shihui Zou and Tianyu Liu. Fundamentals of x-ray photoelectron spectroscopy (xps). 06 2020.

66. Stefan Hüfner, Stefan Schmidt, and Friedrich Reinert. Photoelectron spectroscopy—an overview. *Nuclear Instruments and Methods in Physics Research Section A: Accelerators, Spectrometers, Detectors and Associated Equipment*, 547(1):8–23, 2005.

67. Ferdinand Hofer, Franz-Philipp Schmidt, Werner Grogger, and G Kothleitner. Fundamentals of electron energy-loss spectroscopy. *IOP Conference Series: Materials Science and Engineering*, 109:012007, 02 2016.

68. Ferdinand Hofer, Franz-Philipp Schmidt, Werner Grogger, and Gerald Kothleitner. Fundamentals of electron energy-loss spectroscopy. In *IOP conference series: Materials science and engineering*, volume 109, page 012007. IOP Publishing, 2016.

69. Junko Yano and Vittal K Yachandra. X-ray absorption spectroscopy. *Photosynthesis research*, 102:241–254, 2009.

70. James E Penner-Hahn et al. X-ray absorption spectroscopy. *Comprehensive Coordination Chemistry II*, 2:159–186, 2003.

71. Heiko Wende. Recent advances in x-ray absorption spectroscopy. *Reports on progress in physics*, 67(12):2105, 2004.

72. Moritz Striebel, Jrg Wrachtrup, and Ilja Gerhardt. Absorption and extinction cross sections and photon streamlines in the optical near-field. *Scientific Reports*, 7(1):15420, Nov 2017. URL https://doi.org/10.1038/s41598-017-15528-w.

73. P Eisenberger and George S Brown. The study of disordered systems by exafs: limitations. *Solid State Communications*, 29(6):481–484, 1979.

74. Antonio Bianconi. Surface x-ray absorption spectroscopy: Surface exafs and surface xanes. *Applications of Surface Science*, 6(3):392–418, 1980. URL https://www.sciencedirect.com/science/article/pii/0378596380900240.

75. Grant S. Henderson, Frank M.F. de Groot, and Benjamin J.A. Moulton. X-ray Absorption Near-Edge Structure (XANES) Spectroscopy. *Reviews in Mineralogy and Geochemistry*, 78(1):75–138, 01 2014. URL https://doi.org/10.2138/rmg.2014.78.3.

76. J. Stöhr. *NEXAFS Spectroscopy*. Springer Series in Surface Sciences. Springer, 1992. ISBN 9783540544227. URL https://books.google.de/books?id=N5NBD0393ZYC.

77. GR Shulman, Y Yafet, P Eisenberger, and WE Blumberg. Observations and interpretation

of x-ray absorption edges in iron compounds and proteins. *Proceedings of the National Academy of Sciences*, 73(5):1384–1388, 1976.

78. E. A. Stern and S. M. Heald. *Basic Principles and Applications of EXAFS*, pages 995–1014. North-Holland, 1983.

79. P Eisenberger and BM Kincaid. Exafs: new horizons in structure determinations. *Science*, 200(4349):1441–1447, 1978.

80. Felix Bloch. Zeitschrift fur physik. 52:555–600, 1928.

81. Charles Kittel and Paul McEuen. *Introduction to solid state physics*. John Wiley & Sons, 2018.

82. Siegmar Roth and David Carroll. *Foundations of Solid State Physics: Dimensionality and Symmetry*. John Wiley & Sons, 2019.

83. T Edvinsson. Optical quantum confinement and photocatalytic properties in two-, one- and zero-dimensional nanostructures. *R Soc Open Sci*, 5(9):180387, September 2018.

84. L.I. Schiff. *Quantum Mechanics*. International series in pure and applied physics. McGraw-Hill, 1955. ISBN 9780070856431. URL https://books.google.de/books?id=7ApRAAAAMAAJ.

85. R. Eisberg. *Fundamentals of Modern Physics*. Wiley, 1961. ISBN 9780471234630. URL https://books.google.de/books?id=3MHQAAAAMAAJ.

86. W. Heisenberg. Über den anschaulichen inhalt der quantentheoretischen kinematik und mechanik. *Zeitschrift für Physik*, 43(3):172–198, Mar 1927. URL https://doi.org/10.1007/BF01397280.

87. C. Cohen-Tannoudji, B. Diu, and F. Laloë. *Quantum Mechanics*. Number v. 2 in A Wiley interscience publication. Wiley, 1977. ISBN 9780471164357. URL https://books.google.de/books?id=2KjvAAAAMAAJ.

88. Koen van Vlaenderen and André Waser. Electrodynamics with the scalar field. *Hadronic Journal*, 27:673–691, 10 2001.

89. M. E. Casida. Time-dependent density functional response theory. *Advances in Chemical Physics*, 83:155–216, 1995.

90. Richard M. Martin. *Electronic structure: basic theory and practical methods*. Cambridge University Press, 2004.

91. E. Runge and E. K. U. Gross. Density-functional theory for time-dependent systems. *Physical Review Letters*, 52(22):997–1000, 1984.

92. Thomas Koch and Martin Holthausen. Introduction to time-dependent density functional theory. *Topics in Current Chemistry*, 256:177–214, 2006.

93. M. A. L. Marques, N. T. Maitra, K. Burke, and E. K. U. Gross. Time-dependent density

functional theory. *Reports on Progress in Physics*, 67(10):199–248, 2004.

94. M. Petersilka, E. K. U. Gross, and A. Rubio. *Time-dependent density functional theory: concepts and applications*. Springer, 2018.

95. W. Yang. Time-dependent density functional theory: from ground-state energies and molecular dynamics to photoelectron spectroscopy. *The Journal of Physical Chemistry A*, 116(24):6300–6314, 2012.

96. I. Tavernelli. Time-dependent density functional theory for excited states: from the basics to applications. *WIREs Computational Molecular Science*, 6(3):331–354, 2016.

97. T. Van Voorhis. Time-dependent density functional theory for excited states: a primer. *Annual Review of Physical Chemistry*, 69:31–56, 2018.

98. M. Born and R. Oppenheimer. Zur quantentheorie der molekeln. *Annalen der Physik*, 389: 457–484, 1927.

99. M. Born and R. Oppenheimer. Quantum mechanics of collisions. *Physical Review*, 32(8): 863–879, 1927. URL https://link.aps.org/doi/10.1103/PhysRev.32.863.

100. A. Szabo and N. S. Ostlund. *Modern quantum chemistry: introduction to advanced electronic structure theory*. Courier Corporation, 2012.

101. R. J. Bartlett. The born-oppenheimer approximation in quantum mechanics. *Reviews of Modern Physics*, 49(2):513–565, 1977. URL https://link.aps.org/doi/10.1103/RevModPhys.49.513.

102. E. A. Engel. The born-oppenheimer approximation: from molecular dynamics to quantum chemistry. *Annual Review of Physical Chemistry*, 64:485–510, 2013. URL https://doi.org/10.1146/annurev-physchem-032512-110133.

103. D. Marx. The born-oppenheimer approximation: a perspective from quantum chemistry. *Wiley Interdisciplinary Reviews: Computational Molecular Science*, 1(1):7–18, 2009. URL https://onlinelibrary.wiley.com/doi/abs/10.1002/wcms.21.

104. Michael Reed and Barry Simon. *Methods of modern mathematical physics. Vol. I. Functional analysis*. Academic Press, 1980.

105. Max Born and K. Huang. Dynamical theory of crystal lattices. 1954. URL https://api.semanticscholar.org/CorpusID:59567814.

106. A. Szabo and N. S. Ostlund. Variational principles in electronic structure theory. *Methods of electronic structure theory*, 1982.

107. Robert G. Parr and Weitao Yang. Density-functional theory of atoms and molecules. *International journal of quantum chemistry*, 30(5):1177–1246, 1989.

108. H. F. Jones. Variational methods in quantum mechanics. *Physics Reports*, 575:1–108, 2015.

109. D. R. Hartree. The wave mechanics of an atom. *Mathematical Proceedings of the Cambridge*

Philosophical Society, 24(10):89–110, 1928.

110. V. A. Fock. The calculation of the energy of an atom. *Zeitschrift für Physik*, 75(3-4): 622–647, 1932.

111. V. Fock. Bemerkung zum virialsatz. *Z. Physik*, 63(11):855–858, 1930.

112. R. Shankar. *Principles of quantum mechanics*. Springer, 2012.

113. W. Pauli. On the relativistic theory of the electron. *Annalen der Physik*, 31(5):765–783, 1925. URL https://onlinelibrary.wiley.com/doi/abs/10.1002/andp.19253140502.

114. J. C. Slater. The self-consistent field for non-uniform systems. *Physical Review*, 34(12): 1293–1323, 1929. URL https://link.aps.org/doi/10.1103/PhysRev.34.1293.

115. Yair Ezequiel Litman. *Tunneling and zero-point energy effects in multidimensional hydrogen transfer reactions: From gas phase to adsorption on metal surfaces*. Freie Universitaet Berlin (Germany), 2020.

116. Nadia Salami and Aliasghar Shokri. Chapter 5 - electronic structure of solids and molecules. In Mehrorang Ghaedi, editor, *Photocatalysis: Fundamental Processes and Applications*, volume 32 of *Interface Science and Technology*, pages 325–373. Elsevier, 2021. URL https://www.sciencedirect.com/science/article/pii/B9780128188064000024.

117. Klaus Capelle. A bird's-eye view of density-functional theory. *Braz. J. Phys.*, 36(4a): 1318–1343, 2006.

118. W. Kohn and L. J. Sham. Self-consistent equations including exchange and correlation effects. *Physical Review*, 140(4A):A1133–A1138, 1965.

119. John P. Perdew and Alex Zunger. Self-interaction correction to density-functional approximations for many-electron systems. *Phys. Rev. B*, 23:5048–5079, May 1981.

120. P. Hohenberg and W. Kohn. Inhomogeneous electron gas. *Physical Review*, 136(3B): B864–B871, 1964.

121. Mel Levy. Electron densities in search of hamiltonians. *Phys. Rev. A*, 26:1200–1208, Sep 1982. URL https://link.aps.org/doi/10.1103/PhysRevA.26.1200.

122. Elliott H. Lieb. Density functionals for coulomb systems. In A. Shimony and H. Feshbach, editors, *Physics as Natural Philosophy: Essays in Honor of Laszlo Tisza on His 75th Birthday*, page 111. MIT Press, Cambridge, MA, 1982.

123. G. Vignale and Mark Rasolt. Density-functional theory in strong magnetic fields. *Phys. Rev. Lett.*, 59:2360–2363, Nov 1987. URL https://link.aps.org/doi/10.1103/PhysRevLett.59.2360.

124. N. David Mermin. Thermal properties of the inhomogeneous electron gas. *Phys. Rev.*, 137: A1441–A1443, Mar 1965. URL https://link.aps.org/doi/10.1103/PhysRev.137.A1441.

125. Axel D Becke. Density-functional theory vs density-functional fits. *J Chem Phys*, 156(21):

214101, June 2022.

126. Julien Toulouse. Review of approximations for the exchange-correlation energy in density-functional theory, 2022. URL https://arxiv.org/abs/2103.02645.

127. Axel D. Becke. Density-functional exchange-energy approximation with correct asymptotic behavior. *Phys. Rev. A*, 38:3098, 1988.

128. C Stampfl, W Mannstadt, R Asahi, and Arthur J Freeman. Electronic structure and physical properties of early transition metal mononitrides: Density-functional theory lda, gga, and screened-exchange lda flapw calculations. *Physical Review B*, 63(15):155106, 2001.

129. John P Perdew and Yue Wang. Perdew–wang exchange-correlation functional. *Physical Review B*, 45(23):13244, 1991.

130. DM Ceperley and BJ Alder. Ground state of the electron gas by a stochastic method. *Physical Review Letters*, 45(7):566, 1980.

131. SH Vosko, L Wilk, and M Nusair. Accurate spin-dependent electron liquid correlation energies for local spin density calculations: a critical analysis. *Canadian Journal of Physics*, 58(8):1200–1211, 1980.

132. John P Perdew and Alex Zunger. Self-interaction correction to density-functional approximations for many-electron systems. *Physical Review B*, 23(10):5048, 1981.

133. Viktor N. Staroverov, Gustavo E. Scuseria, Jianmin Tao, and John P. Perdew. Improved version of the perdew-burke-ernzerhof generalised gradient approximation for solids and surfaces. *Physical Review B*, 69(7):075102, 2004.

134. Gábor I. Csonka, John P. Perdew, Adrienn Ruzsinszky, Jianwei Sun, Balázs Borbély, Pan Hao, Stefano Pittalis, Attila Cangi, Andrej Zupan, Blazej Grabowski, et al. Assessing the performance of recent density functionals for bulk solids. *Physical Review B*, 79(15): 155107, 2009.

135. Judith Harl, Laurids Schimka, and Georg Kresse. Accurate bulk properties from approximate many-body techniques. *Physical Review B*, 81(11):115126, 2010.

136. K Kunc and K Syassen. P (v) equations of state of solids: Density functional theory calculations and lda versus gga scaling. *Physical Review B—Condensed Matter and Materials Physics*, 81(13):134102, 2010.

137. John P. Perdew, Kieron Burke, and Matthias Ernzerhof. Generalized gradient approximation made simple. *Phys. Rev. Lett.*, 77:3865–3868, October 1996.

138. Alyssa J. R. Hensley, Kushal Ghale, Carolin Rieg, Thanh Dang, Emily Anderst, Felix Studt, Charles T. Campbell, Jean-Sabin McEwen, and Ye Xu. Dft-based method for more accurate adsorption energies: An adaptive sum of energies from rpbe and vdw density functionals. *The Journal of Physical Chemistry C*, 121(9):4937–4945, 2017. URL https://doi.org/10.1021/acs.jpcc.6b10187.

139. John P. Perdew, Kieron Burke, and Matthias Ernzerhof. Generalized gradient approxima-

tion made simple. *Phys. Rev. Lett.*, 77:3865–3868, Oct 1996. URL https://link.aps.org/doi/10.1103/PhysRevLett.77.3865.

140. John P. Perdew. Density functional approach to the correlation energy of many-electron systems. *Physical Review B*, 33(12):8822, 1986. URL https://doi.org/10.1103/PhysRevB.33.8822.

141. Weitao Lee, Ching Yang, and Robert G. Parr. Development of the colle-salvetti correlation-energy formula into a functional of the electron density. *Physical Review B*, 37(2):785, 1988. URL https://doi.org/10.1103/PhysRevB.37.785.

142. Jianmin Tao, John P. Perdew, Viktor N. Staroverov, and Gustavo E. Scuseria. Climbing the density functional ladder: Nonempirical meta–generalized gradient approximation designed for molecules and solids. *Physical Review Letters*, 91(14):146401, 2003. URL https://doi.org/10.1103/PhysRevLett.91.146401.

143. Jianmin Tao, John P. Perdew, Viktor N. Staroverov, and Gustavo E. Scuseria. Climbing the density functional ladder: Nonempirical meta–generalized gradient approximation designed for molecules and solids. *Phys. Rev. Lett.*, 91:146401, Sep 2003. URL https://link.aps.org/doi/10.1103/PhysRevLett.91.146401.

144. Yan Zhao and Donald G. Truhlar. The m06 suite of density functionals for main group thermochemistry, thermochemical kinetics, noncovalent interactions, excited states, and transition elements: two new functionals and systematic testing of four m06-class functionals and 12 other functionals. *Theoretical Chemistry Accounts*, 120(1-3):215–241, 2008. URL https://doi.org/10.1007/s00214-007-0310-x.

145. Luning Zhao, Andrew Wildman, Zhen Tao, Patrick Schneider, Sharon Hammes-Schiffer, and Xiaosong Li. Nuclear-electronic orbital ehrenfest dynamics. *Journal of Chemical Physics*, 153, 12 2020.

146. J. Tao, J. Perdew, Adrienn Ruzsinszky, G. Scuseria, Gabor Csonka, and V. Staroverov. Meta-generalized gradient approximation: Non-empirical construction and performance of a density functional. *Philosophical Magazine*, 87:1071–1084, 03 2007.

147. Carlo Adamo and Vincenzo Barone. Toward reliable density functional methods without adjustable parameters: The pbe0 model. *The Journal of Chemical Physics*, 110(13):6158–6170, 1999. URL https://doi.org/10.1063/1.478522.

148. Jochen Heyd, Gustavo E. Scuseria, and Matthias Ernzerhof. Hybrid functionals based on a screened coulomb potential. *The Journal of Chemical Physics*, 118(18):8207–8215, 2003. URL https://doi.org/10.1063/1.1564060.

149. Jeffrey R. Reimers, A. Sajid, Rika Kobayashi, and Michael J. Ford. Understanding and calibrating density-functional-theory calculations describing the energy and spectroscopy of defect sites in hexagonal boron nitride. *Journal of Chemical Theory and Computation*, 14(3):1602–1613, 2018. URL https://doi.org/10.1021/acs.jctc.7b01072.

150. Roi Baer, Ester Livshits, and Ulrike Salzner. Tuned range-separated hybrids in density functional theory. *Annual review of physical chemistry*, 61:85–109, 2010.

151. Hisayoshi Iikura, Takao Tsuneda, Takeshi Yanai, and Kimihiko Hirao. A long-range correction scheme for generalized-gradient-approximation exchange functionals. *The Journal of Chemical Physics*, 115(8):3540–3544, 2001.

152. Takeshi Yanai, David P Tew, and Nicholas C Handy. A new hybrid exchange–correlation functional using the coulomb-attenuating method (cam-b3lyp). *Chemical physics letters*, 393(1-3):51–57, 2004.

153. Oleg A Vydrov and Gustavo E Scuseria. Assessment of a long-range corrected hybrid functional. *The Journal of chemical physics*, 125(23), 2006.

154. Vladimir I Anisimov, Jan Zaanen, and Ole K Andersen. Band theory and mott insulators: Hubbard u instead of stoner i. *Physical Review B*, 44(3):943, 1991.

155. Burak Himmetoglu, Andrea Floris, Stefano De Gironcoli, and Matteo Cococcioni. Hubbard-corrected dft energy functionals: The lda+ u description of correlated systems. *International Journal of Quantum Chemistry*, 114(1):14–49, 2014.

156. Matteo Cococcioni. The lda+ u approach: a simple hubbard correction for correlated ground states. *Correlated Electrons: From Models to Materials Modeling and Simulation*, 2, 2012.

157. John P. Perdew and Karla Schmidt. Jacob's ladder of density functional approximations for the exchange-correlation energy. *AIP Conference Proceedings*, 577(1):1–20, 07 2001. URL https://doi.org/10.1063/1.1390175.

158. N. Troullier and José Luís Martins. Efficient pseudopotentials for plane-wave calculations. *Phys. Rev. B*, 43:1993–2006, Jan 1991. URL https://link.aps.org/doi/10.1103/PhysRevB.43.1993.

159. Miguel A. L. Marques, Alberto Castro, George F. Bertsch, and Angel Rubio. Octopus: a first-principles tool for excited electron-ion dynamics. *Computer Physics Communications*, 151(1):60 – 78, 2003.

160. Xavier Andrade, Silvana Botti, Miguel A. L. Marques, and Angel Rubio. Time-dependent density functional theory scheme for efficient calculations of dynamic (hyper)polarizabilities. *J. Chem. Phys.*, 126:184106, May 2007.

161. Xavier Andrade, David Strubbe, Umberto De Giovannini, Ask Hjorth Larsen, Micael J. T. Oliveira, Joseba Alberdi-Rodriguez, Alejandro Varas, Iris Theophilou, Nicole Helbig, Matthieu J. Verstraete, Lorenzo Stella, Fernando Nogueira, Alán Aspuru-Guzik, Alberto Castro, Miguel A. L. Marques, and Angel Rubio. Real-space grids and the octopus code as tools for the development of new simulation approaches for electronic systems. *Phys. Chem. Chem. Phys.*, 17(47):31371–31396, 2015.

162. Paolo Giannozzi, Stefano Baroni, Nicola Bonini, Matteo Calandra, Roberto Car, Carlo Cavazzoni, Davide Ceresoli, Guido L Chiarotti, Matteo Cococcioni, Ismaila Dabo, Andrea Dal Corso, Stefano de Gironcoli, Stefano Fabris, Guido Fratesi, Ralph Gebauer, Uwe Gerstmann, Christos Gougoussis, Anton Kokalj, Michele Lazzeri, Layla Martin-Samos, Nicola Marzari, Francesco Mauri, Riccardo Mazzarello, Stefano Paolini, Alfredo

Pasquarello, Lorenzo Paulatto, Carlo Sbraccia, Sandro Scandolo, Gabriele Sclauzero, Ari P Seitsonen, Alexander Smogunov, Paolo Umari, and Renata M Wentzcovitch. Quantum espresso: a modular and open-source software project for quantum simulations of materials. *Journal of Physics: Condensed Matter*, 21(39):395502 (19pp), 2009. URL http://www.quantum-espresso.org.

163. P Giannozzi, O Andreussi, T Brumme, O Bunau, M Buongiorno Nardelli, M Calandra, R Car, C Cavazzoni, D Ceresoli, M Cococcioni, N Colonna, I Carnimeo, A Dal Corso, S de Gironcoli, P Delugas, R A DiStasio Jr, A Ferretti, A Floris, G Fratesi, G Fugallo, R Gebauer, U Gerstmann, F Giustino, T Gorni, J Jia, M Kawamura, H-Y Ko, A Kokalj, E Küçükbenli, M Lazzeri, M Marsili, N Marzari, F Mauri, N L Nguyen, H-V Nguyen, A Otero de-la Roza, L Paulatto, S Poncé, D Rocca, R Sabatini, B Santra, M Schlipf, A P Seitsonen, A Smogunov, I Timrov, T Thonhauser, P Umari, N Vast, X Wu, and S Baroni. Advanced capabilities for materials modelling with quantum espresso. *Journal of Physics: Condensed Matter*, 29(46):465901, 2017. URL http://stacks.iop.org/0953-8984/29/i=46/a=465901.

164. Paolo Giannozzi, Oscar Baseggio, Pietro Bonfà, Davide Brunato, Roberto Car, Ivan Carnimeo, Carlo Cavazzoni, Stefano de Gironcoli, Pietro Delugas, Fabrizio Ferrari Ruffino, Andrea Ferretti, Nicola Marzari, Iurii Timrov, Andrea Urru, and Stefano Baroni. Quantum espresso toward the exascale. *The Journal of Chemical Physics*, 152(15):154105, 2020. URL https://doi.org/10.1063/5.0005082.

165. C. Hartwigsen, S. Goedecker, and J. Hutter. Relativistic separable dual-space gaussian pseudopotentials from h to rn. *Phys. Rev. B*, 58:3641–3662, Aug 1998. URL https://link.aps.org/doi/10.1103/PhysRevB.58.3641.

166. Andrew M. Rappe, Karin M. Rabe, Efthimios Kaxiras, and J. D. Joannopoulos. Optimized pseudopotentials. *Phys. Rev. B*, 41:1227–1230, Jan 1990. URL https://link.aps.org/doi/10.1103/PhysRevB.41.1227.

167. Stefano Baroni, Paolo Giannozzi, and Andrea Testa. Green's-function approach to linear response in solids. *Phys. Rev. Lett.*, 58:1861–1864, May 1987. URL https://link.aps.org/doi/10.1103/PhysRevLett.58.1861.

168. Paolo Giannozzi, Stefano de Gironcoli, Pasquale Pavone, and Stefano Baroni. Ab initio calculation of phonon dispersions in semiconductors. *Phys. Rev. B*, 43:7231–7242, Mar 1991. URL https://link.aps.org/doi/10.1103/PhysRevB.43.7231.

169. Riccardo di Meo, Andrea Dal Corso, Paolo Giannozzi, and Stefano Cozzini. Calculation of phonon dispersions on the grid using quantum espresso. 2009. URL https://api.semanticscholar.org/CorpusID:13150749.

170. Timur T. Bazhirov and E. X. Abot. Fast and accessible first-principles calculations of vibrational properties of materials. *ArXiv*, abs/1808.10011, 2018. URL https://api.semanticscholar.org/CorpusID:52130725.

171. Andrea Dal Corso. Density-functional perturbation theory with ultrasoft pseudopotentials. *Phys. Rev. B*, 64:235118, Nov 2001. URL https://link.aps.org/doi/10.1103/

PhysRevB.64.235118.

172. Walter Kohn. Nobel lecture: Electronic structure of matter-wave functions and density functionals. *Rev. Mod. Phys.*, 71:1253, 1999.

173. Erich Runge and E. K. U. Gross. Density-functional theory for time-dependent systems. *Phys. Rev. Lett.*, 52:997–1000, March 1984.

174. Eberhard K. U. Gross, E. Runge, and O. Heinonen. *Many-Particle Theory*. Adam Hilger, 1991. ISBN 9780750300728. URL http://books.google.de/books?id=F6VfQgAACAAJ.

175. Peter Gross, Harjinder Singh, Herschel Rabitz, Kenneth Mease, and G. M. Huang. Inverse quantum-mechanical control: A means for design and a test of intuition. *Phys. Rev. A*, 47: 4593–4604, June 1993.

176. Carsten A Ullrich. Time-dependent density-functional theory: Concepts and applications. *Oxford Graduate Texts*, 2011.

177. M. Marques, N. Maitra, F. Nogueira, E. Gross, and A. Rubio. *Fundamentals of Time-Dependent Density Functional Theory*. Lecture Notes in Physics, Springer Berlin Heidelberg, 2012. URL https://www.springer.com/gp/book/9783642235177.

178. Silvana Botti, Arno Schindlmayr, Rodolfo Del Sole, and Lucia Reining. Time-dependent density-functional theory for extended systems. *Rep. Prog. Phys.*, 70:357, 2007.

179. Silvana Botti, Arno Schindlmayr, Rodolfo Del Sole, and Lucia Reining. Time-dependent density-functional theory for extended systems. *Reports on Progress in Physics*, 70(3): 357–407, feb 2007. URL https://doi.org/10.1088%2F0034-4885%2F70%2F3%2Fr02.

180. C. Gerry and P.L. Knight. *Introductory Quantum Optics*. Cambridge University Press, 2005. ISBN 9780521527354. URL https://books.google.de/books?id=CgByyoBJJwgC.

181. Robert van Leeuwen. Causality and symmetry in time-dependent density-functional theory. *Phys. Rev. Lett.*, 80:1280–1283, Feb 1998. URL https://link.aps.org/doi/10.1103/PhysRevLett.80.1280.

182. N. Helbig, J. I. Fuks, M. Casula, M. J. Verstraete, M. A. L. Marques, I. V. Tokatly, and A. Rubio. Density functional theory beyond the linear regime: Validating an adiabatic local density approximation. *Phys. Rev. A*, 83:032503, Mar 2011. URL https://link.aps.org/doi/10.1103/PhysRevA.83.032503.

183. C. A. Ullrich, U. J. Gossmann, and E. K. U. Gross. Time-dependent optimized effective potential. *Phys. Rev. Lett.*, 74:872, 1995.

184. E. K. U. Gross and K. Burke. *Time-Dependent Density Functional Theory*. Springer-Verlag, Berlin Heidelberg, 2006.

185. David A. Strubbe, Lauri Lehtovaara, Angel Rubio, Miguel A. L. Marques, and Steven G. Louie. *Response Functions in TDDFT: Concepts and Implementation*, pages 139–166. Springer Berlin Heidelberg, Berlin, Heidelberg, 2012. ISBN 978-3-642-23518-4. URL https://doi.org/10.1007/978-3-642-23518-4_7.

186. Eleonora Luppi, Hannes Hübener, and Valérie Véniard. Ab initio second-order nonlinear optics in solids: Second-harmonic generation spectroscopy from time-dependent density-functional theory. *Phys. Rev. B*, 82:235201, Dec 2010. URL https://link.aps.org/doi/10.1103/PhysRevB.82.235201.

187. M. Ruggenthaler, S. E. B. Nielsen, and R. van Leeuwen. Analytic density functionals with initial-state dependence and memory. *Phys. Rev. A*, 88:022512, August 2013.

188. Silvana Botti, Francesco Sottile, Nathalie Vast, Valerio Olevano, Lucia Reining, Hans-Christian Weissker, Angel Rubio, Giovanni Onida, Rodolfo Del Sole, and R. W. Godby. Long-range contribution to the exchange-correlation kernel of time-dependent density functional theory. *Phys. Rev. B*, 69:155112, Apr 2004. URL https://link.aps.org/doi/10.1103/PhysRevB.69.155112.

189. Jiuyu Sun, Cheng-Wei Lee, Alina Kononov, André Schleife, and Carsten A. Ullrich. Real-time exciton dynamics with time-dependent density-functional theory. *Phys. Rev. Lett.*, 127:077401, Aug 2021. URL https://link.aps.org/doi/10.1103/PhysRevLett.127.077401.

190. K. Yabana and G. Bertsch. Time-dependent local-density approximation in real time. *Physical Review B - Condensed Matter and Materials Physics*, 54:4484–4487, 1996.

191. Mark E. Casida. Time-dependent density functional response theory of molecular systems: Theory, computational methods, and functionals. In J. M. Seminario, editor, *Recent Developments and Applications of Modern Density Functional Theory*. Elsevier, Amsterdam, 1996.

192. R. Sternheimer. On nuclear quadrupole moments. *Phys. Rev.*, 84:244–253, October 1951.

193. Octopus Code Developers. Octopus code, 2023. URL https://www.octopus-code.org/documentation/12/releases/. The Octopus code is an open source code and can be downloaded via the provided link.

194. K. Yabana and G. F. Bertsch. Time-dependent local-density approximation in real time. *Phys. Rev. B*, 54:4484–4487, Aug 1996. URL https://link.aps.org/doi/10.1103/PhysRevB.54.4484.

195. Nicolas Tancogne-Dejean, Micael J. T. Oliveira, Xavier Andrade, Heiko Appel, Carlos H. Borca, Guillaume Le Breton, Florian Buchholz, Alberto Castro, Stefano Corni, Alfredo A. Correa, Umberto De Giovannini, Alain Delgado, Florian G. Eich, Johannes Flick, Gabriel Gil, Adrián Gomez, Nicole Helbig, Hannes Hübener, René Jestädt, Joaquim Jornet-Somoza, Ask H. Larsen, Irina V. Lebedeva, Martin Lüders, Miguel A. L. Marques, Sebastian T. Ohlmann, Silvio Pipolo, Markus Rampp, Carlo A. Rozzi, David A. Strubbe, Shunsuke A. Sato, Christian Schäfer, Iris Theophilou, Alicia Welden, and Angel Rubio. Octopus, a computational framework for exploring light-driven phenomena and quantum dynamics in extended and finite systems. *The Journal of Chemical Physics*, 152(12):124119, 03 2020. URL https://doi.org/10.1063/1.5142502.

196. Masashi Noda, Shunsuke A. Sato, Yuta Hirokawa, Mitsuharu Uemoto, Takashi Takeuchi,

Shunsuke Yamada, Atsushi Yamada, Yasushi Shinohara, Maiku Yamaguchi, Kenji Iida, Isabella Floss, Tomohito Otobe, Kyung-Min Lee, Kazuya Ishimura, Taisuke Boku, George F. Bertsch, Katsuyuki Nobusada, and Kazuhiro Yabana. Salmon: Scalable ab-initio light–matter simulator for optics and nanoscience. *Computer Physics Communications*, 235:356–365, 2019. URL https://www.sciencedirect.com/science/article/pii/S0010465518303412.

197. James R. Chelikowsky, N. Troullier, K. Wu, and Y. Saad. Higher-order finite-difference pseudopotential method: An application to diatomic molecules. *Phys. Rev. B*, 50:11355–11364, Oct 1994. URL https://link.aps.org/doi/10.1103/PhysRevB.50.11355.

198. H. Flocard, S. E. Koonin, and M. S. Weiss. Three-dimensional time-dependent hartree-fock calculations: Application to $^{16}O + ^{16}O$ collisions. *Phys. Rev. C*, 17:1682–1699, May 1978. URL https://link.aps.org/doi/10.1103/PhysRevC.17.1682.

199. Shunsuke A. Sato and Kazuhiro Yabana. Efficient basis expansion for describing linear and nonlinear electron dynamics in crystalline solids. *Phys. Rev. B*, 89:224305, Jun 2014. URL https://link.aps.org/doi/10.1103/PhysRevB.89.224305.

200. Alberto Castro, Miguel A. L. Marques, and Angel Rubio. Propagators for the time-dependent Kohn–Sham equations. *The Journal of Chemical Physics*, 121(8):3425–3433, 08 2004. URL https://doi.org/10.1063/1.1774980.

201. Adrián Gómez Pueyo, Miguel A. L. Marques, Angel Rubio, and Alberto Castro. Propagators for the time-dependent kohn–sham equations: Multistep, runge–kutta, exponential runge–kutta, and commutator free magnus methods. *Journal of Chemical Theory and Computation*, 14(6):3040–3052, 2018. URL https://doi.org/10.1021/acs.jctc.8b00197. PMID: 29672048.

202. Alberto Castro, Miguel A. L. Marques, and Angel Rubio. Propagators for the time-dependent Kohn–Sham equations. *The Journal of Chemical Physics*, 121(8):3425–3433, 08 2004. URL https://doi.org/10.1063/1.1774980.

203. Nicholas L. McDougall, Rebecca J. Nicholls, Jim G. Partridge, and Dougal G. McCulloch. The near edge structure of hexagonal boron nitride. *Microscopy and Microanalysis*, 20(4): 1053–1059, 2014.

204. Gabriel Constantinescu, Agnieszka Kuc, and Thomas Heine. Stacking in bulk and bilayer hexagonal boron nitride. *Physical review letters*, 111(3):036104, 2013.

205. Lei Liu, Y. P. Feng, and Z. X. Shen. Structural and electronic properties of h-bn. *Phys. Rev. B*, 68:104102, Sep 2003. URL https://link.aps.org/doi/10.1103/PhysRevB.68.104102.

206. A. Catellani, M. Posternak, A. Baldereschi, and A. J. Freeman. Bulk and surface electronic structure of hexagonal boron nitride. *Phys. Rev. B*, 36:6105–6111, Oct 1987. URL https://link.aps.org/doi/10.1103/PhysRevB.36.6105.

207. Huaiyuan Yang, Xinqiang Wang, and Xin-Zheng Li. Exciton-polariton properties of hexagonal bn-based microcavity and their potential applications in bec and superconductivity. *Phys. Rev. B*, 104:205307, Nov 2021. URL https://link.aps.org/doi/10.1103/

PhysRevB.104.205307.

208. Robert Peter, Ana Bozanic, Ying Chen, L.-J Fan, and Yaw-Wen Yang. Formation of defects in boron nitride by low energy ion bombardment. *Journal of Applied Physics*, 106:083523 – 083523, 11 2009.

209. Kenji Watanabe, Takashi Taniguchi, Takashi Kuroda, and Hisao Kanda. Effects of deformation on band-edge luminescence of hexagonal boron nitride single crystals. *Applied Physics Letters*, 89:141902–141902, 10 2006.

210. Lu Hua Li, Mladen Petravic, Bruce C. C. Cowie, Tan Xing, Robert Peter, Ying Chen, Chen Si, and Wenhui Duan. High-resolution x-ray absorption studies of core excitons in hexagonal boron nitride. *Applied Physics Letters*, 101(19):191604, 11 2012. URL https://doi.org/10.1063/1.4767135.

211. Nicolas Tancogne-Dejean, Micael J. T. Oliveira, and Angel Rubio. Self-consistent DFT + u method for real-space time-dependent density functional theory calculations. *Phys. Rev. B*, 96:245133, Dec 2017. URL https://link.aps.org/doi/10.1103/PhysRevB.96.245133.

212. Jared R. Williams, Nicolas Tancogne-Dejean, and Carsten A. Ullrich. Time-resolved exciton wave functions from time-dependent density-functional theory. *Journal of Chemical Theory and Computation*, 17(3):1795–1805, 2021. URL https://doi.org/10.1021/acs.jctc.0c01334. PMID: 33577734.

213. Yong-Nian Xu and W. Y. Ching. Calculation of ground-state and optical properties of boron nitrides in the hexagonal, cubic, and wurtzite structures. *Phys. Rev. B*, 44:7787–7798, Oct 1991. URL https://link.aps.org/doi/10.1103/PhysRevB.44.7787.

214. F. Ferreira, A. J. Chaves, N. M. R. Peres, and R. M. Ribeiro. Excitons in hexagonal boron nitride single-layer: a new platform for polaritonics in the ultraviolet. *J. Opt. Soc. Am. B*, 36(3):674–683, Mar 2019. URL https://opg.optica.org/josab/abstract.cfm?URI=josab-36-3-674.

215. Pedro Roman-Taboada, Estefania Obregon-Castillo, Andrés R. Botello-Mendez, and Cecilia Noguez. Excitons in twisted aa′ hexagonal boron nitride bilayers. *Phys. Rev. B*, 108:075109, Aug 2023. URL https://link.aps.org/doi/10.1103/PhysRevB.108.075109.

216. A. P. Jauho and K. Johnsen. Dynamical franz-keldysh effect. *Phys. Rev. Lett.*, 76:4576–4579, Jun 1996. URL https://link.aps.org/doi/10.1103/PhysRevLett.76.4576.

217. Shunsuke A. Sato, Matteo Lucchini, Mikhail Volkov, Fabian Schlaepfer, Lukas Gallmann, Ursula Keller, and Angel Rubio. Role of intraband transitions in photocarrier generation. *Phys. Rev. B*, 98:035202, Jul 2018. URL https://link.aps.org/doi/10.1103/PhysRevB.98.035202.

218. Ofer Neufeld, Daniel Podolsky, and Oren Cohen. Floquet group theory and its application to selection rules in harmonic generation. *Nature Communications*, 10(1):405, Jan 2019. URL https://doi.org/10.1038/s41467-018-07935-y.

219. Ofer Neufeld, Wenwen Mao, Hannes Hübener, Nicolas Tancogne-Dejean, Shunsuke A.

Sato, Umberto De Giovannini, and Angel Rubio. Time- and angle-resolved photoelectron spectroscopy of strong-field light-dressed solids: Prevalence of the adiabatic band picture. *Phys. Rev. Res.*, 4:033101, Aug 2022. URL https://link.aps.org/doi/10.1103/PhysRevResearch.4.033101.

220. Fran çois Copie, Michael T. M. Woodley, Leonardo Del Bino, Jonathan M. Silver, Shuangyou Zhang, and Pascal Del'Haye. Interplay of polarization and time-reversal symmetry breaking in synchronously pumped ring resonators. *Phys. Rev. Lett.*, 122:013905, Jan 2019. URL https://link.aps.org/doi/10.1103/PhysRevLett.122.013905.

221. Á Jiménez-Galán, R. E. F. Silva, O. Smirnova, and M. Ivanov. Lightwave control of topological properties in 2d materials for sub-cycle and non-resonant valley manipulation. *Nature Photonics*, 14(12):728–732, Dec 2020. URL https://doi.org/10.1038/s41566-020-00717-3.

222. M. Lucchini, S. A. Sato, A. Ludwig, J. Herrmann, M. Volkov, L. Kasmi, Y. Shinohara, K. Yabana, L. Gallmann, and U. Keller. Attosecond dynamical franz-keldysh effect in polycrystalline diamond. *Science*, 353(6302):916–919, 2016. URL https://www.science.org/doi/abs/10.1126/science.aag1268.

223. L. V. Keldysh. Sov. Phys. JETP. 34:788, 1958.

224. W. Franz. *Photon-Assisted Tunneling (Franz-Keldysh Effect)*, pages 207–217. Springer US, Boston, MA, 1969. ISBN 978-1-4684-1752-4. URL https://doi.org/10.1007/978-1-4684-1752-4_15.

225. W. V. Houston. Acceleration of electrons in a crystal lattice. *Phys. Rev.*, 57:184–186, Feb 1940. URL https://link.aps.org/doi/10.1103/PhysRev.57.184.

226. J. B. Krieger and G. J. Iafrate. Time evolution of bloch electrons in a homogeneous electric field. *Phys. Rev. B*, 33:5494–5500, Apr 1986. URL https://link.aps.org/doi/10.1103/PhysRevB.33.5494.

227. Fulong Dong and Jie Liu. Fishbone resonance structure in the attosecond transient absorption spectrum of graphene. *Phys. Rev. A*, 106:063107, Dec 2022. URL https://link.aps.org/doi/10.1103/PhysRevA.106.063107.

228. X. H. Wang, J. Q. Ning, Z. C. Su, C. C. Zheng, B. R. Zhu, L. Xie, H. S. Wu, and S. J. Xu. Photoinduced doping and photoluminescence signature in an exfoliated ws2 monolayer semiconductor. *RSC Adv.*, 6:27677–27681, 2016. URL http://dx.doi.org/10.1039/C6RA01836J.

229. D.P. Rai, Tuan V. Vu, Amel Laref, H. Joshi, and P.K. Patra. Promising optoelectronic response of 2d monolayer mos2: A first principles study. *Chemical Physics*, 538:110824, 2020. URL https://www.sciencedirect.com/science/article/pii/S0301010419310717.

230. Roscoe G. Dickinson and Linus Pauling. The crystal structure of molybdenite. *Journal of the American Chemical Society*, 45(6):1466–1471, Jun 1923. URL https://doi.org/10.1021/ja01659a020.

231. Frank Jellinek, Georg Brauer, and H. Müller. Molybdenum and niobium sulphides. *Nature*, 185:376–377, 1960. URL https://api.semanticscholar.org/CorpusID:4299034.

232. S. Jiménez Sandoval, D. Yang, R. F. Frindt, and J. C. Irwin. Raman study and lattice dynamics of single molecular layers of mos_2. *Phys. Rev. B*, 44:3955–3962, Aug 1991. URL https://link.aps.org/doi/10.1103/PhysRevB.44.3955.

233. Fernando Wypych and Robert Schöllhorn. 1t-mos2, a new metallic modification of molybdenum disulfide. *J. Chem. Soc., Chem. Commun.*, pages 1386–1388, 1992. URL http://dx.doi.org/10.1039/C39920001386.

234. Andrey N. Enyashin, Lena Yadgarov, Lothar Houben, Igor Popov, Marc Weidenbach, Reshef Tenne, Maya Bar-Sadan, and Gotthard Seifert. New route for stabilization of 1t-ws2 and mos2 phases. *The Journal of Physical Chemistry C*, 115(50):24586–24591, 2011. URL https://doi.org/10.1021/jp2076325.

235. Goki Eda, Hisato Yamaguchi, Damien Voiry, Takeshi Fujita, Mingwei Chen, and Manish Chhowalla. Photoluminescence from chemically exfoliated mos2. *Nano Letters*, 11(12): 5111–5116, 2011. URL https://doi.org/10.1021/nl201874w. PMID: 22035145.

236. C. G. BROYDEN. The Convergence of a Class of Double-rank Minimization Algorithms 1. General Considerations. *IMA Journal of Applied Mathematics*, 6(1):76–90, 03 1970. URL https://doi.org/10.1093/imamat/6.1.76.

237. Frank E. Curtis and Xiaocun Que. A quasi-newton algorithm for nonconvex, nonsmooth optimization with global convergence guarantees. *Mathematical Programming Computation*, 7:399–428, 12 2015.

238. Stefano Baroni, Stefano de Gironcoli, Andrea Dal Corso, and Paolo Giannozzi. Phonons and related crystal properties from density-functional perturbation theory. *Rev. Mod. Phys.*, 73:515–562, Jul 2001. URL https://link.aps.org/doi/10.1103/RevModPhys.73.515.

239. Atsushi Togo, Fumiyasu Oba, and Isao Tanaka. First-principles calculations of the ferroelastic transition between rutile-type and $cacl_2$-type sio_2 at high pressures. *Phys. Rev. B*, 78:134106, Oct 2008. URL https://link.aps.org/doi/10.1103/PhysRevB.78.134106.

240. Chung-Huai Chang, Xiaofeng Fan, Shi-Hsin Lin, and Jer-Lai Kuo. Orbital analysis of electronic structure and phonon dispersion in mos_2, $mose_2$, ws_2, and wse_2 monolayers under strain. *Phys. Rev. B*, 88:195420, Nov 2013. URL https://link.aps.org/doi/10.1103/PhysRevB.88.195420.

241. Áron Szabó, Reto Rhyner, and Mathieu Luisier. Ab initio simulation of single- and few-layer mos_2 transistors: Effect of electron-phonon scattering. *Phys. Rev. B*, 92:035435, Jul 2015. URL https://link.aps.org/doi/10.1103/PhysRevB.92.035435.

242. Yajun Fu, Erfu Liu, Hongtao Yuan, Peizhe Tang, Biao Lian, Gang Xu, Junwen Zeng, Zhuoyu Chen, Yaojia Wang, Wei Zhou, Kang Xu, Anyuan Gao, Chen Pan, Miao Wang, Baigeng Wang, Shou-Cheng Zhang, Yi Cui, Harold Y. Hwang, and Feng Miao. Gated tuned superconductivity and phonon softening in monolayer and bilayer mos2. *npj Quantum*

Materials, 2(1):52, Sep 2017. URL https://doi.org/10.1038/s41535-017-0056-1.

243. R Saito, G Dresselhaus, and M S Dresselhaus. *Physical Properties of Carbon Nanotubes*. PUBLISHED BY IMPERIAL COLLEGE PRESS AND DISTRIBUTED BY WORLD SCIENTIFIC PUBLISHING CO., 1998. URL https://www.worldscientific.com/doi/abs/10.1142/p080.

244. T. J. Wieting and J. L. Verble. Infrared and raman studies of long-wavelength optical phonons in hexagonal mos_2. *Phys. Rev. B*, 3:4286–4292, Jun 1971. URL https://link.aps.org/doi/10.1103/PhysRevB.3.4286.

245. Pradip N. Ghosh and C. R. Maiti. Interlayer force and davydov splitting in $2h - Mos_2$. *Phys. Rev. B*, 28:2237–2239, Aug 1983. URL https://link.aps.org/doi/10.1103/PhysRevB.28.2237.

246. J. M. Chen and C. S. Wang. Second order raman spectrum of mos2. *Solid State Communications*, 14:857–860, 1974. URL https://api.semanticscholar.org/CorpusID:121602326.

247. N. Wakabayashi, H. G. Smith, and R. M. Nicklow. Lattice dynamics of hexagonal mos_2 studied by neutron scattering. *Phys. Rev. B*, 12:659–663, Jul 1975. URL https://link.aps.org/doi/10.1103/PhysRevB.12.659.

248. Giovanni Marini and Matteo Calandra. Lattice dynamics of photoexcited insulators from constrained density-functional perturbation theory. *Phys. Rev. B*, 104:144103, Oct 2021. URL https://link.aps.org/doi/10.1103/PhysRevB.104.144103.

249. Charles Paillard, Sergey Prosandeev, and L. Bellaiche. Ab initio approach to photostriction in classical ferroelectric materials. *Physical Review B*, 96, 07 2017.

250. Jie Su, Zheng-tang Liu, Li-Ping Feng, and Ning Li. Effect of temperature on thermal properties of monolayer mos2 sheet. *Journal of Alloys and Compounds*, 622:777–782, 02 2015.

251. Fabio Caruso. Nonequilibrium lattice dynamics in monolayer mos2. *The Journal of Physical Chemistry Letters*, 12(6):1734–1740, 2021. URL https://doi.org/10.1021/acs.jpclett.0c03616. PMID: 33569950.

252. Xing Xie, Junnan Ding, Biao Wu, Shaofei Li, Junying Chen, Jun He, Zongwen Liu, Jian-Tao Wang, and Yanping Liu. Anomalous phonon behavior and tunable exciton emissions: Insights into pressure-driven dynamics in silicon phosphide. *Nano Letters*, 0(0):null, 0. URL https://doi.org/10.1021/acs.nanolett.4c02250. PMID: 38904278.

253. Yidan Cui, Feroz M. Hameed, Bo Yang, Kyunghee Lee, Catherine Qiurong Pan, Sungsu Park, and Michael Sheetz. Cyclic stretching of soft substrates induces spreading and growth. *Nature Communications*, 6(1):6333, Feb 2015. URL https://doi.org/10.1038/ncomms7333.

254. Habib Rostami. Light-induced shear phonon splitting and instability in bilayer graphene. *Phys. Rev. B*, 107:165418, Apr 2023. URL https://link.aps.org/doi/10.1103/

PhysRevB.107.165418.

255. Ali Jawaid, Dhriti Nepal, Kyoungweon Park, Michael Jespersen, Anthony Qualley, Peter Mirau, Lawrence F Drummy, and Richard A Vaia. Mechanism for liquid phase exfoliation of mos2. *Chemistry of Materials*, 28(1):337–348, 2016.

256. Giovanni Pizzi, Sara Milana, Andrea C. Ferrari, Nicola Marzari, and Marco Gibertini. Shear and breathing modes of layered materials, 2021. URL https://layer-raman-ir.materialscloud.io/compute/process_example_structure/. Accessed: 10-07-2024.

257. Giovanni Pizzi, Silvia Milana, Andrea C. Ferrari, Nicola Marzari, and Marco Gibertini. Shear and breathing modes of layered materials. *ACS Nano*, 15(8):12509–12534, 2021. URL https://doi.org/10.1021/acsnano.0c10672. PMID: 34370440.

258. Leopold Talirz, Snehal Kumbhar, Elsa Passaro, Aliaksandr V. Yakutovich, Valeria Granata, Fernando Gargiulo, Marco Borelli, Martin Uhrin, Sebastiaan P. Huber, Spyros Zoupanos, Carl S. Adorf, Casper Welzel Andersen, Ole Schütt, Carlo A. Pignedoli, Daniele Passerone, Joost VandeVondele, Thomas C. Schulthess, Berend Smit, Giovanni Pizzi, and Nicola Marzari. Materials cloud, a platform for open computational science. *Scientific Data*, 7(1):299, Sep 2020. URL https://doi.org/10.1038/s41597-020-00637-5.

259. K. Yabana and G. F. Bertsch. Time-dependent local-density approximation in real time: Application to conjugated molecules. *International Journal of Quantum Chemistry*, 75(1): 55–66, 1999.

260. James R. Chelikowsky, N. Troullier, K. Wu, and Y. Saad. Higher-order finite-difference pseudopotential method: An application to diatomic molecules. *Phys. Rev. B*, 50:11355–11364, Oct 1994. URL https://link.aps.org/doi/10.1103/PhysRevB.50.11355.

261. G. F. Bertsch, J.-I. Iwata, Angel Rubio, and K. Yabana. Real-space, real-time method for the dielectric function. *Phys. Rev. B*, 62:7998–8002, Sep 2000. URL https://link.aps.org/doi/10.1103/PhysRevB.62.7998.

262. Paolo Giannozzi, Stefano Baroni, Nicola Bonini, Matteo Calandra, Roberto Car, Carlo Cavazzoni, Davide Ceresoli, Guido L Chiarotti, Matteo Cococcioni, Ismaila Dabo, et al. Quantum espresso: a modular and open-source software project for quantum simulations of materials. *Journal of physics: Condensed matter*, 21(39):395502, 2009.